Collected LWA Engineering Memos from the Development of the Antenna Subsystem (ANT)

2007 October 29 – 2009 September 11

Editor: Paul S. Ray (NRL)

Table of Contents

Acknowledgements

Basic research in radio astronomy at the Naval Research Lab is supported by NRL/ONR.

LWA Engineering Memo ANT0004
Big Blade Measurement Plots
April 10, 2008

Nagini Paravastu (NRL/ASEE)

Abstract

We report on field measurements of the Big Blade antenna performed at the LWDA site in the 10 – 100 MHz frequency band. The Big Blade antenna prototypes were tested over three ground conditions – Earth ground, a 3mx3m ground screen, and a 10mx10m ground screen. The data collected during this campaign were used to make impedance, sky noise dominance, and drift curve plots that can be used to compare the performance of a Big Blade antenna, in isolation, over the three ground conditions. All measurements are compared with simulated data based on NEC4 models. Our analysis shows that the presence of the large ground screen results in higher beam pattern sidelobe levels at frequencies above ∼50 MHz, resulting in undesirable distortions in the drift curves at these frequencies. The Big Blade over the smaller ground screen yields lower sidelobe levels and better beam pattern symmetry than the Big Blade over large ground screen case, making the smaller ground screen a more attractive design choice than the large ground screen for an LWA station.

I. INTRODUCTION

In February 2008, measurements were performed at the LWDA site by Henrique Schmitt, Frank Schinzel and me on candidate antenna designs for LWA-1 [1]. Part of this campaign involved testing the baseline Big Blade antenna over three ground conditions – Earth ground, a 3mx3m ground screen, and a 10mx10m ground screen – in order to better understand how the performance of this antenna differs as a function of these ground conditions. Table I shows the designations used for each antenna/ground screen case.

TABLE I

ANTENNA DESIGNATIONS

Antenna	Ground	Designation
Big Blade	Earth	BBEG
Big Blade	3mx3m ground screen	BBSGS
Big Blade	10mx10m ground screen	BBLGS
Big Blade	3mx3m ground screen on 10mx10m ground screen	BBSGSLGS

A. The Ground Screen

Galvanized welded wire mesh was used as the ground screen material for the measurements. The wire diameter was 2 mm, and the mesh cell size was 5cmx10cm. The mesh material was purchased in 1.5mx210m rolls. Each ground screen consisted of 2 layers of mesh material, with one later oriented East-West, and the other oriented North-South, so that the wire density could be kept approximately equal in both directions. Pieces of rebar (one every ∼50 cm on each ground screen) were used to pin down the screen and ensure good electrical connections throughout. Further information on the ground screens can be found in Engineering Memo GND0001 [2].

Fig. 1. Close-up of the 10mx10m ground screen. Two rebar pieces used to pin the ground screen down can be seen near the center of the image.

B. The Big Blade Antenna and Active Balun

Photographs and the NEC4 models of BBEG, BBSGS, and BBLGS are shown in Figures 2, 3, and 4. A dimensioned drawing of a Big Blade element is shown in Figure 5. The Big Blade antenna feedpoint is 9 cm wide and stands 1.5 m off the ground. The elements are drooped 45°. All antennas were positioned North-South/East-West, and all measurements were done on the East-West antenna elements.

All NEC4 models, even the ones with ground screens, were assumed to be over Earth ground with a dielectric constant of 13 and a conductivity of 0.005 S/m. All wires in the models were set to be lossless conductors. The wires in the ground screen were spaced 0.1λ center-to-center at 100 MHz and were 3.25 mm thick. The wires were therefore tangentially connected, simulating a continuous, conducting surface. This was done to simplify the model since using the actual wire diameter, metal properties, and spacing of the mesh material used in field testing would have resulted in a model with many more wires, requiring greatly increased simulation times.

The G250R active balun was used as the front-end low noise amplifier during spectral sky power measurements [3]. Figure 6 shows pictures of the balun board mounted onto a Big Blade antenna.

II. ANTENNA IMPEDANCES

Antenna impedance measurements were performed using a Tele-tech hybrid power combiner and an Array Solutions AIM 4170 impedance analyzer. The raw measurement and simulated impedance data for BBEG, BBSGS, and BBLGS are shown in Figure 7 (the impedance of BBSGSLGS was not measured since it was assumed that the result would be the same as BBLGS). We believe the significant difference between the measurements and simulations are due primarily to the presence of the hybrid in the measurement, which must either be calibrated out prior to measurement, or extracted in post-processing in order to determine the true measured antenna impedance. Previous impedance measurements on the LWDA Small Blade antenna performed by R. Bradley and me made use of a method to calibrate out the hybrid prior to measurement [4]. Measurements performed by A. Kerkhoff on Inverted-V antennas employed a post-measurement extraction method [5]. In both cases, the measured antenna impedances showed good agreement with simulations based on NEC4 antenna models. Attempts have been made to use the post-measurement extraction method on the measured impedances taken during the February 2008 field trip, but did not yield a significant improvement in the comparison with simulation. The reasons for this are being investigated, but will require considerable time and additional ANT tasks in the project work plan.

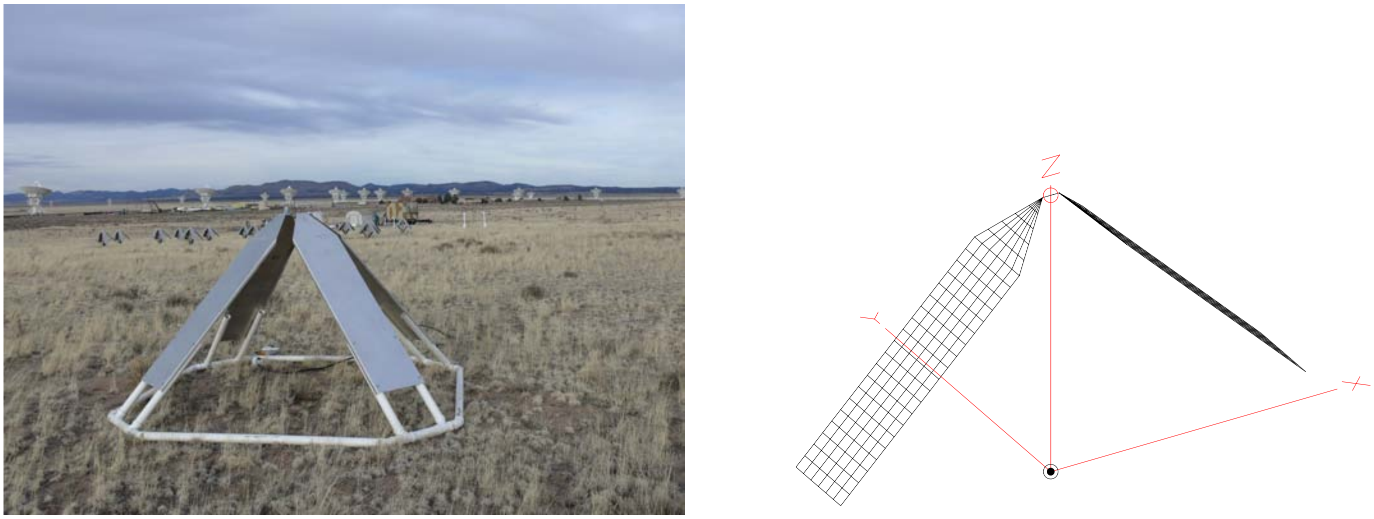

Fig. 2. Photograph and NEC4 model of BBEG.

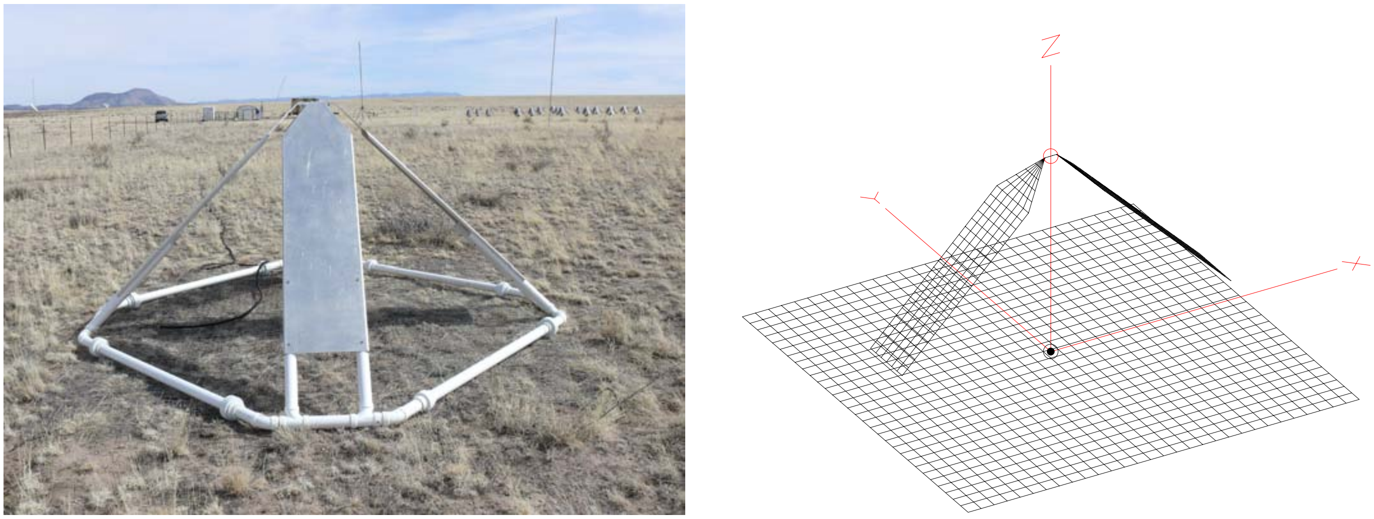

Fig. 3. Photograph and NEC4 model of BBSGS.

III. SKY NOISE DOMINANCE

Figure 8 shows plots of simulated and measured sky noise dominances for BBEG, BBSGS, BBLGS, and BBSGSLGS. The measured data in Figure 8 are plotted on one axis for direct comparison in Figure 9. BBLGS and BBSGSLGS exhibit the highest levels of sky noise dominance, which is to be expected given that the ground losses are lower in the large ground screen cases. The BBEG plot in Figure 8 shows the poorest agreement between measurement and simulation, indicating that the ground models are in need of improvement. The agreement is greatly improved for BBSGS, BBLGS and BBSGSLGS, indicating that the ground screens dominate the overall ground properties in these cases.

IV. DRIFT CURVES

Figures 10, 11, 12, and 13 show measured and simulated drift curves for BBEG, BBSGS, BBLGS and BBSGSLGS respectively. The drift curve models do not currently take into account the impedance mismatch between the antenna and the active balun. The reduced amplitude of the measured curve compared to the simulated curve is therefore a direct indication of the decreased sky noise dominance resulting from that impedance mismatch.

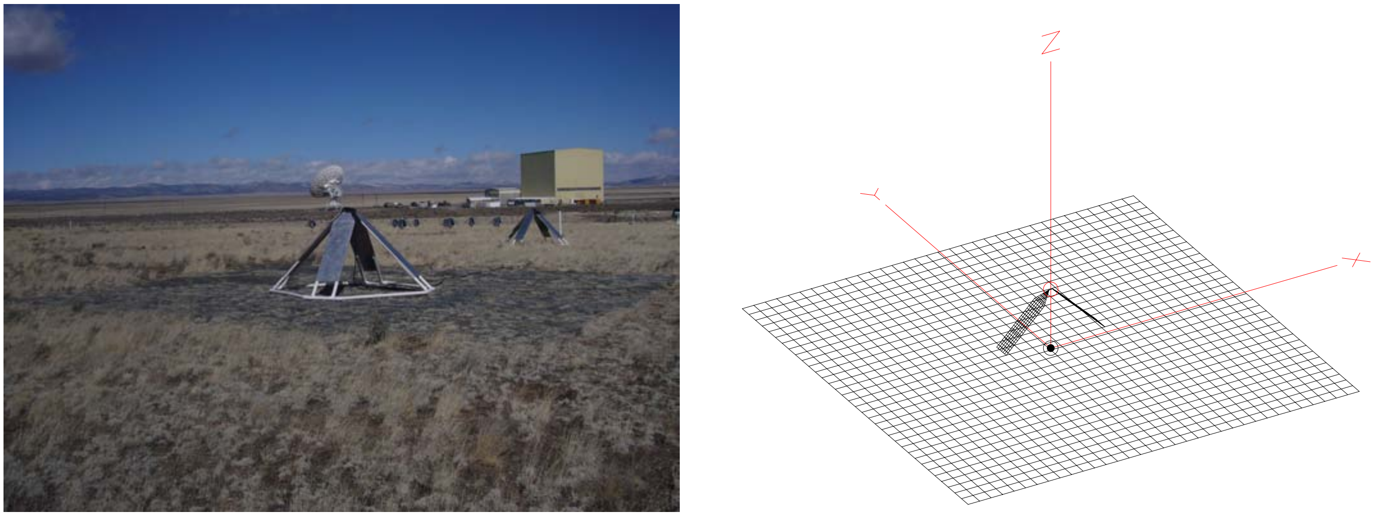

Fig. 4. Photograph and NEC4 model of BBLGS.

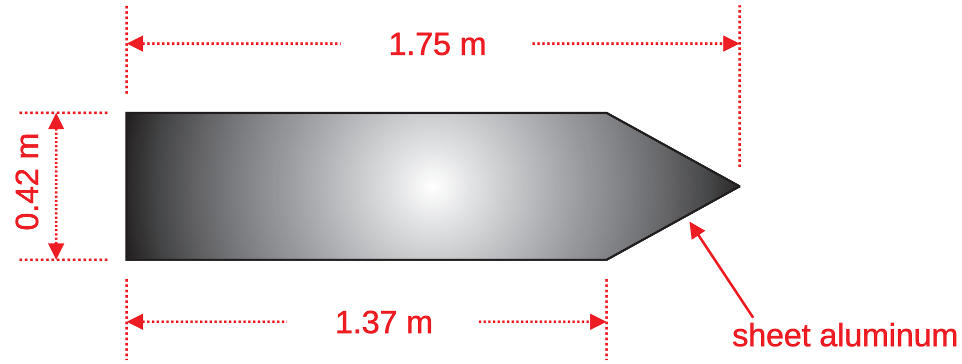

Fig. 5. Big Blade element dimensions (drawing not to scale).

Of particular interest are the drift curve plots for BBLGS and BBSGSLGS at 74 MHz and 80 MHz, which seem to indicate deteriorating beam patterns at these frequencies in the presence of a large ground screen. This is corroborated by the simulated beam patterns shown in Figure 14. The BBLGS beam pattern exhibits a drop in Zenith gain at 50 MHz, and strong sidelobes and poor axial symmetry at higher frequencies. BBSGS would therefore appear to be more desirable for satisfying the scientific and technical requirements for the LWA.

V. SUMMARY

In this report we have presented impedance, sky noise dominance and drift curve measurements taken of the Big Blade antenna over Earth ground, a 3mx3m ground screen, and a 10mx10m ground screen at the LWDA site in February 2008. All of the measured data were compared with simulations based on NEC4 antenna models. While decent agreement between measurement and simulation is achieved for sky noise dominance and drift curves, further investigation is needed to understand the reasons for the discrepancies between the simulated and measured impedances. Since this will take some time, additional tasks must be added to the ANT work plan for this investigation.

A comparison of the BBSGS, BBLGS and BBSGSLGS drift curves brings to light some very interesting differences in the behavior of the Big Blade antenna over these three ground conditions. In both measurement and simulation, the large ground screen cases show signs of degradation at higher frequencies. This is most likely to due to deteriorating beam patterns at these frequencies. An examination of simulated

Fig. 6. The G250R balun mounted on a Big Blade antenna.

beam patterns show that when the Big Blade antenna is placed over the large ground screen, the resultant beam pattern shows a decrease in Zenith gain at 50 MHz, and highly pronounced sidelobes at higher frequencies compared to the small ground screen case. In addition, BBSGS beam patterns have better axial symmetry than BBLGS. Based on these findings, I recommend that small ground screens be used in LWA-1.

REFERENCES

[1] N. Paravastu, “LWA Engineering Memo ANT0003 - Measurement Trip Notes,” *LWA Engineering Memo Series (ANT0003)*, February 2008.

[2] H. Schmitt, “LWA Engineering Memo GND0001 - Baseline Design of Station Ground Screen,” *LWA Engineering Memo Series (GND0001)*, March 2008.

[3] B. Hicks and N. Paravastu, “The Rapid Test Array Balun (G250R),” *LWA Memo Series (Memo 120)*, January 2008.

[4] N. Paravastu, B. Hicks, R. Bradley, and et al., “Characterizing Active Antennas for the Long Wavelength Array,” *Bulletin of the American Astronomical Society*, vol. 37, p. 1388, December 2005.

[5] A. Kerkhoff, “Multi-Objective Optimization of Antennas for Ultra-Wideband Applications,” *Ph.D. Dissertation, University of Texas at Austin*, May 2008.

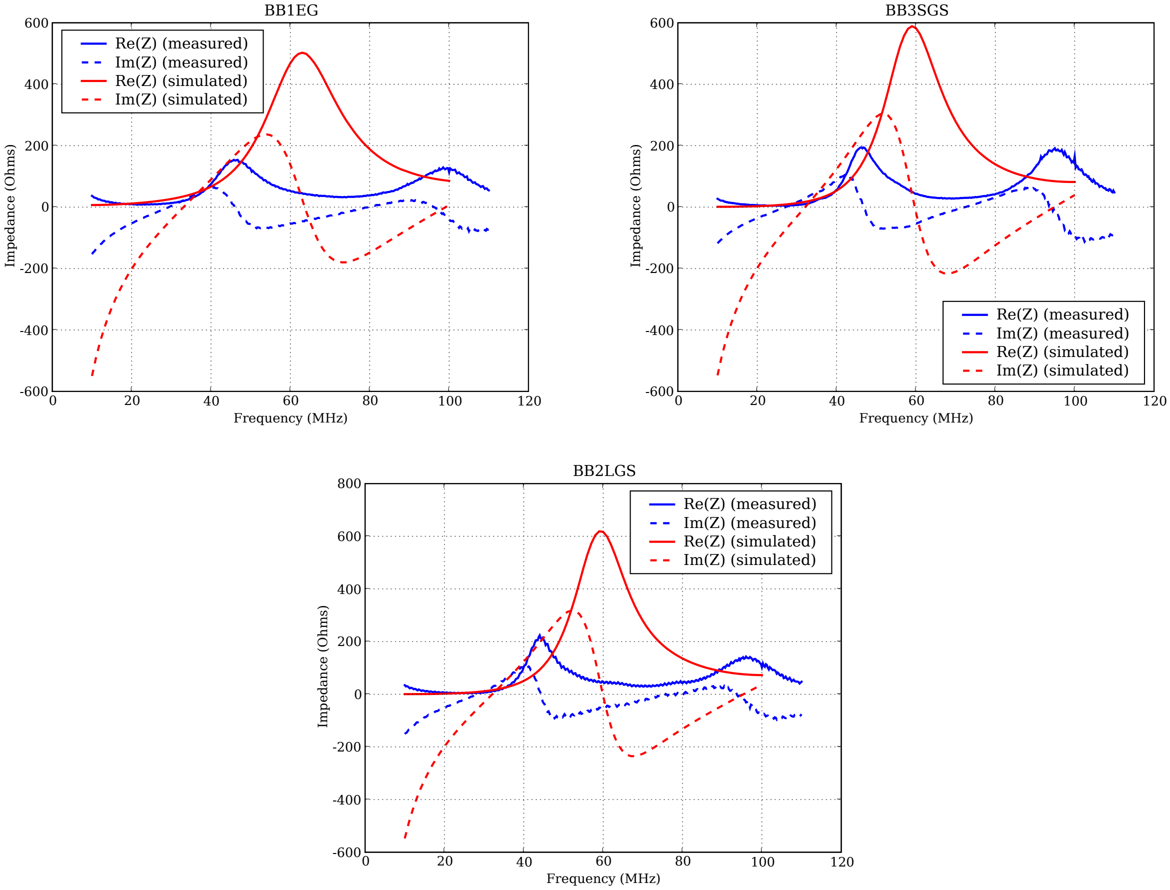

Fig. 7. Measured and simulated impedances for the Big Blade antenna on Earth ground (BB1EG), 3mx3m ground screen (BB3SGS), and 10mx10m ground screen (BB2LGS). The impedance measurements were taken using a connectorized hybrid power combiner, but these plots do not include the correction for the effect of the hybrid.

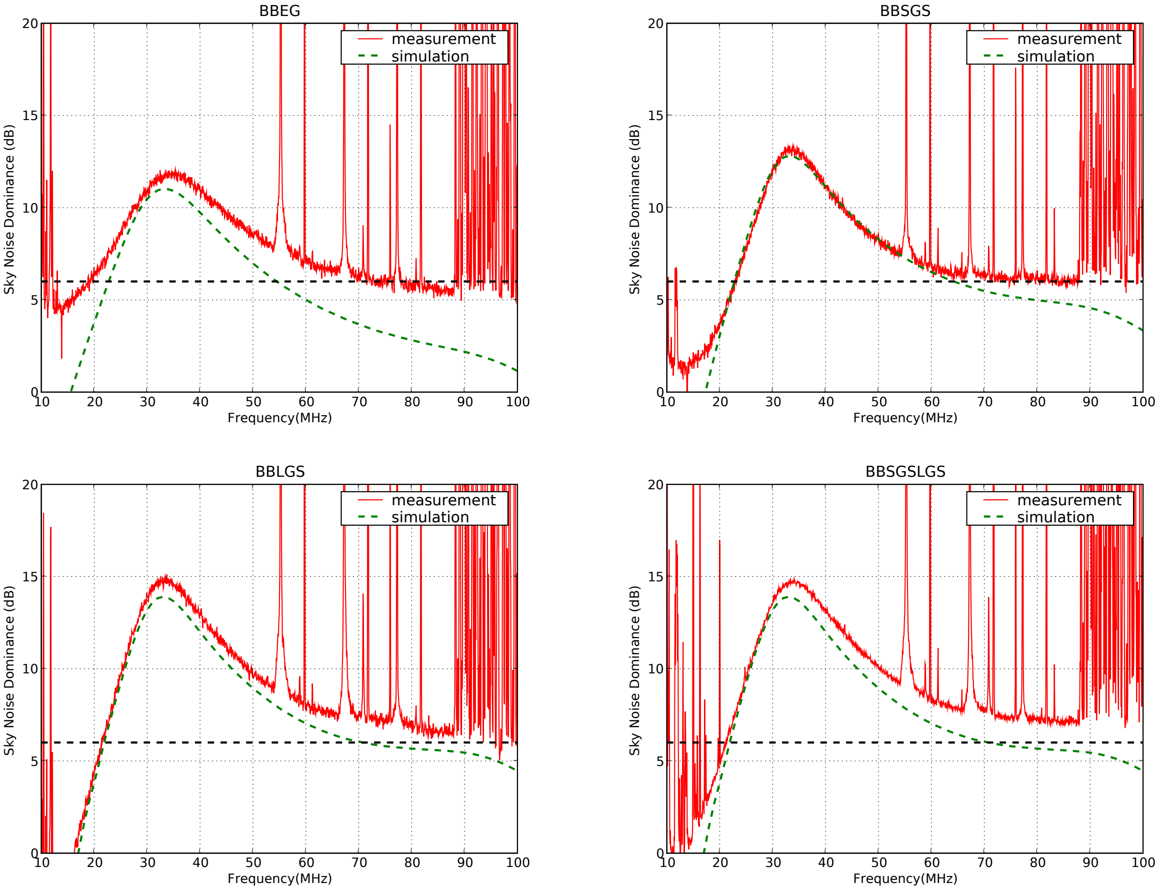

Fig. 8. Measured and simulated sky noise dominances for the Big Blade antenna on Earth ground (BBEG), 3mx3m ground screen (BBSGS), 10mx10m ground screen (BBLGS), and 3mx3m ground screen on 10mx10m ground screen. Data shown here for all antennas were taken at Galactic minimum (10 hrs LST).

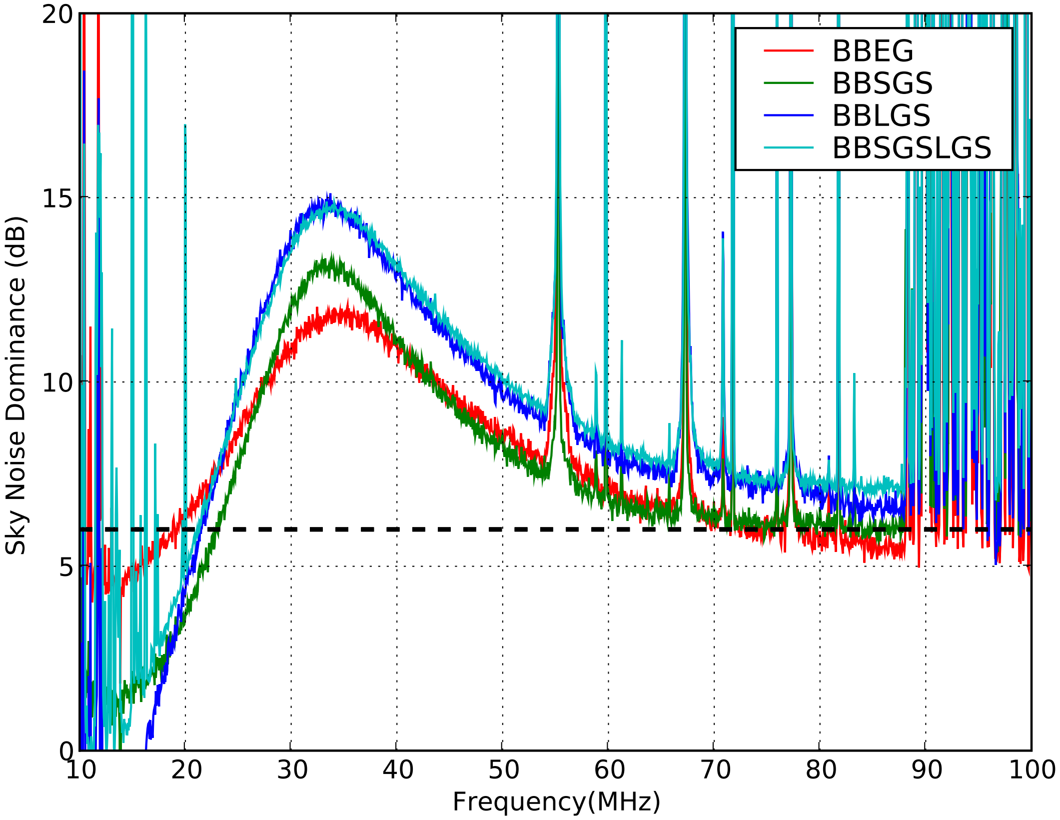

Fig. 9. Measured sky noise dominances for the Big Blade antenna on Earth ground (BBEG), 3mx3m ground screen (BBSGS), 10mx10m ground screen (BBLGS), and 3mx3m ground screen on 10mx10m ground screen. Data shown here for all antennas were taken at Galactic minimum (10 hrs LST).

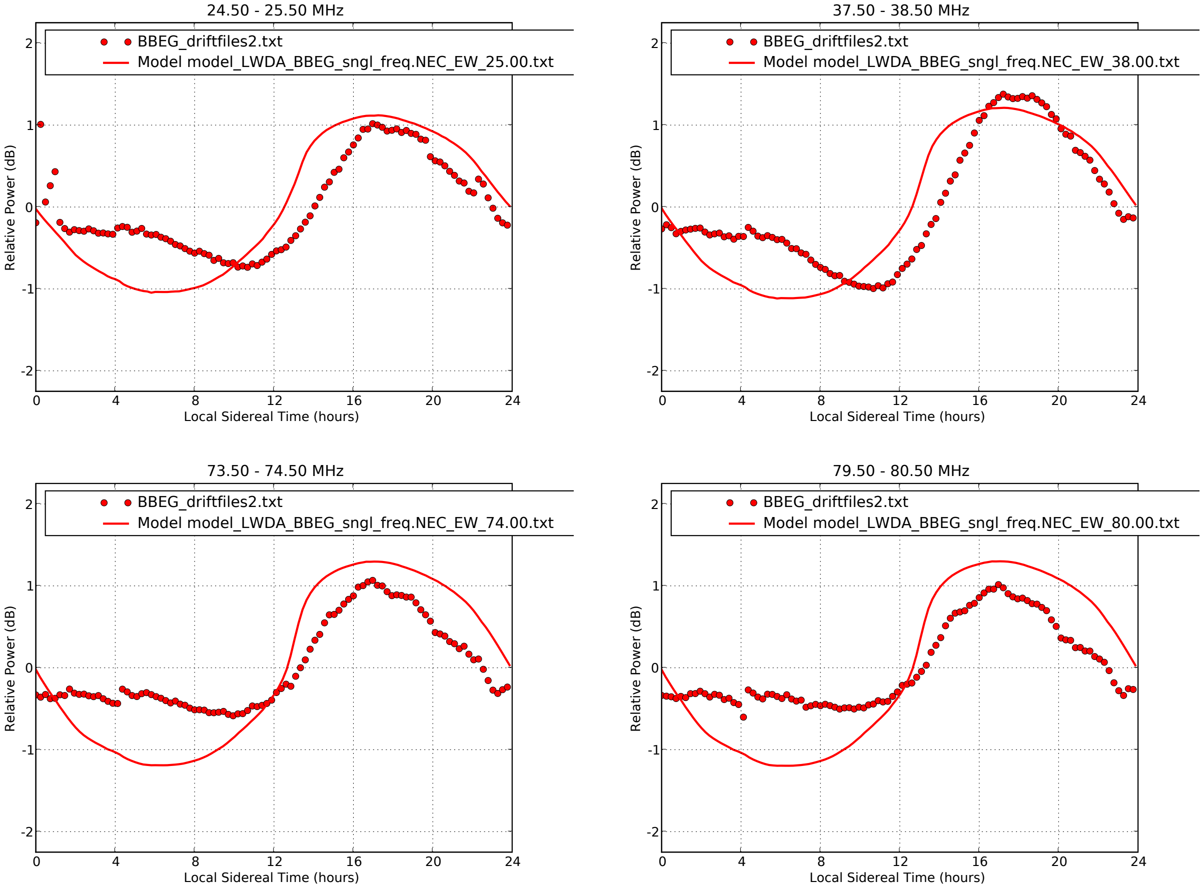

Fig. 10. Measured and simulated drift curves for the Big Blade antenna on Earth ground (BBEG) at 25 MHz, 38 MHz, 74 MHz, and 80 MHz.

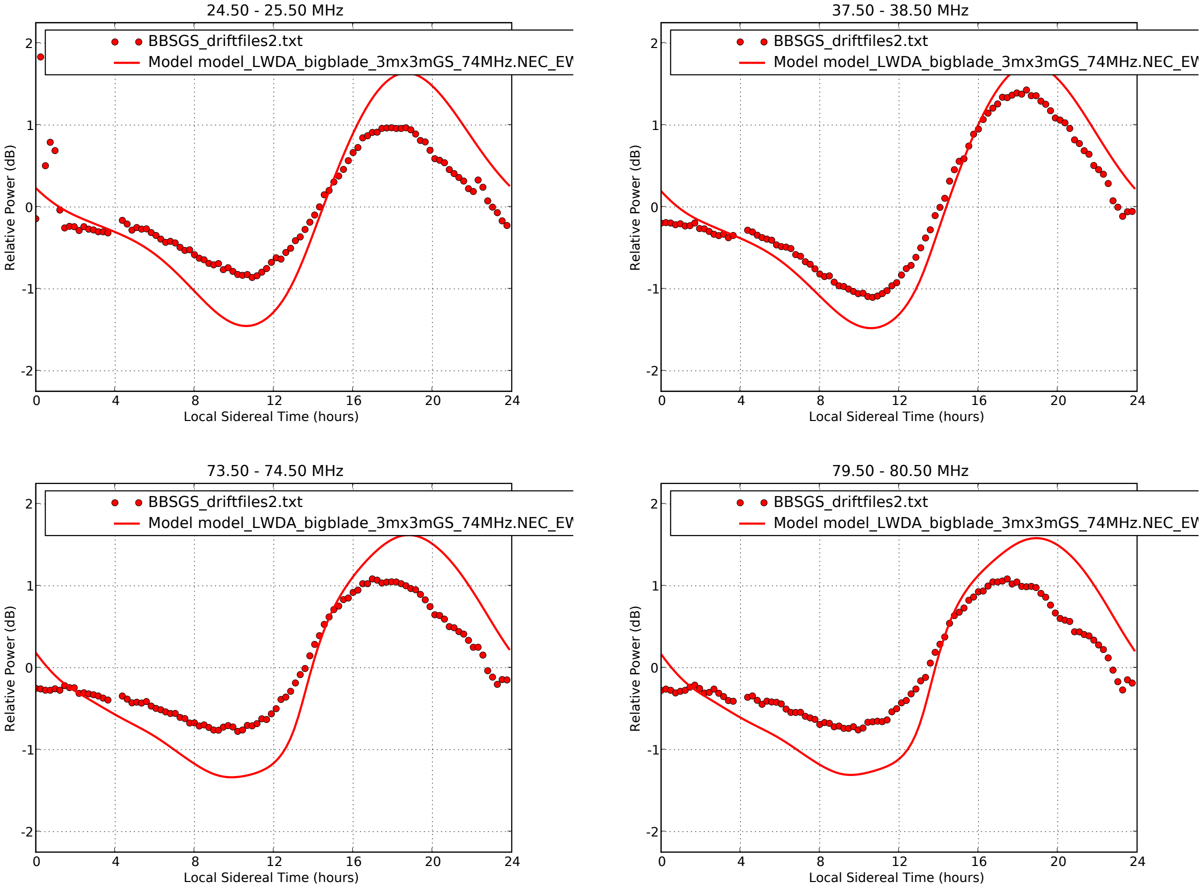

Fig. 11. Measured and simulated drift curves for the Big Blade antenna on 3mx3m ground screen (BBSGS) at 25 MHz, 38 MHz, 74 MHz, and 80 MHz.

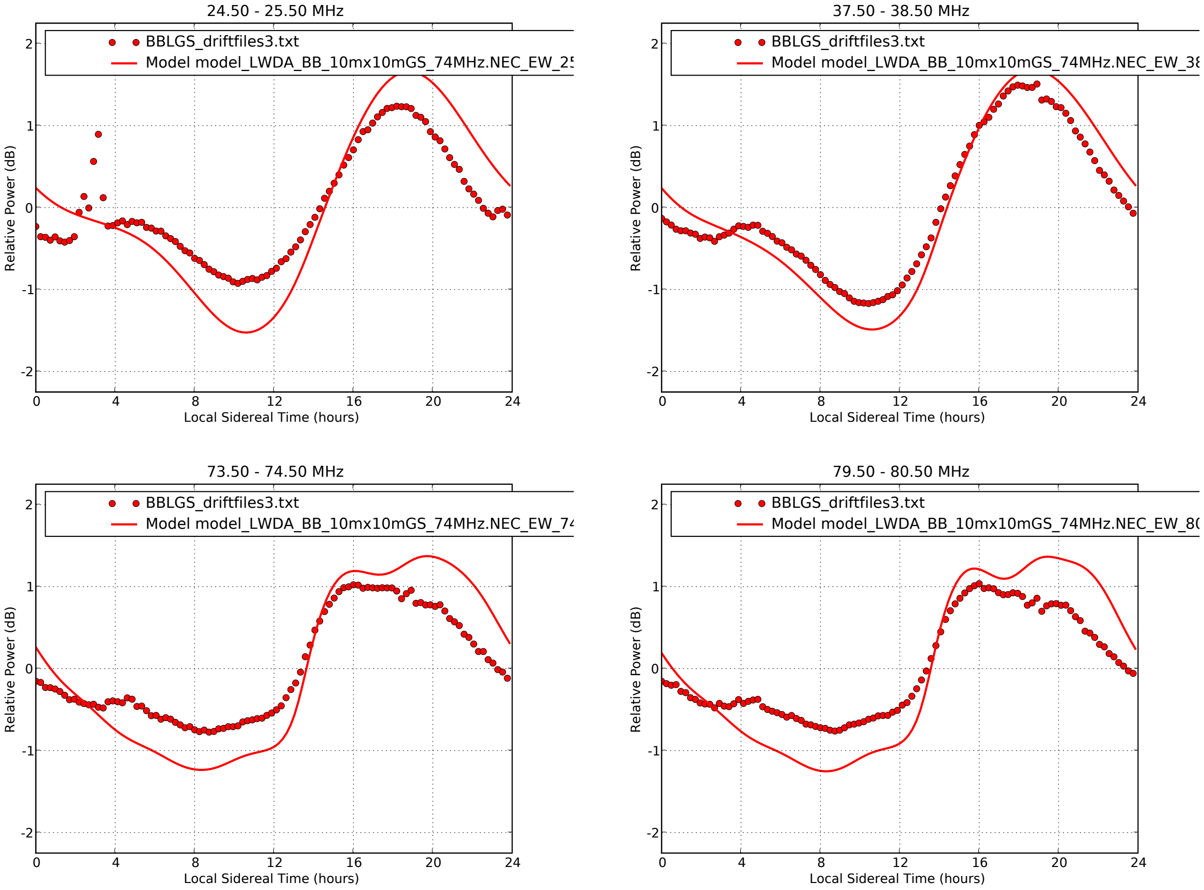

Fig. 12. Measured and simulated drift curves for the Big Blade antenna on 10mx10m ground screen (BBLGS) at 25 MHz, 38 MHz, 74 MHz, and 80 MHz.

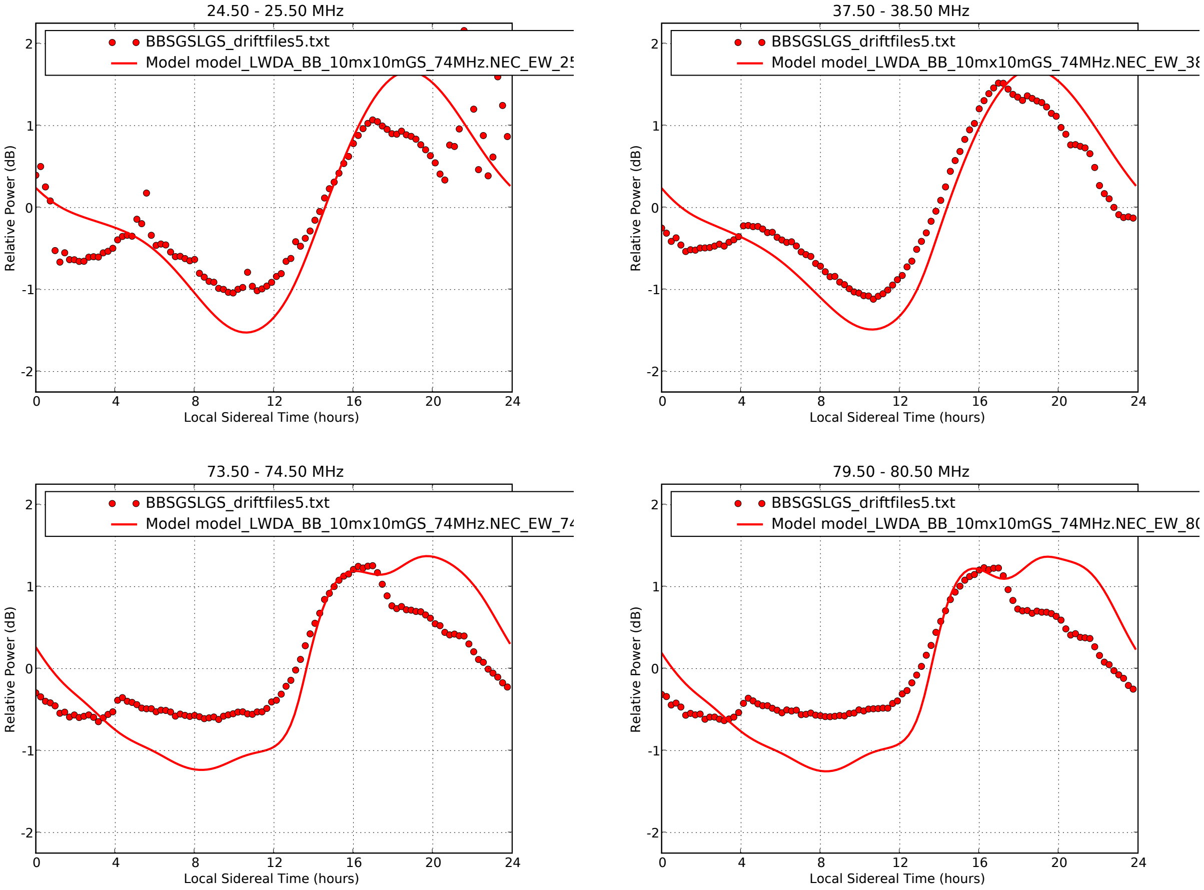

Fig. 13. Measured and simulated drift curves for the Big Blade antenna on 3mx3m ground screen on 10mx10m ground screen (BBSGSLGS) at 25 MHz, 38 MHz, 74 MHz, and 80 MHz.

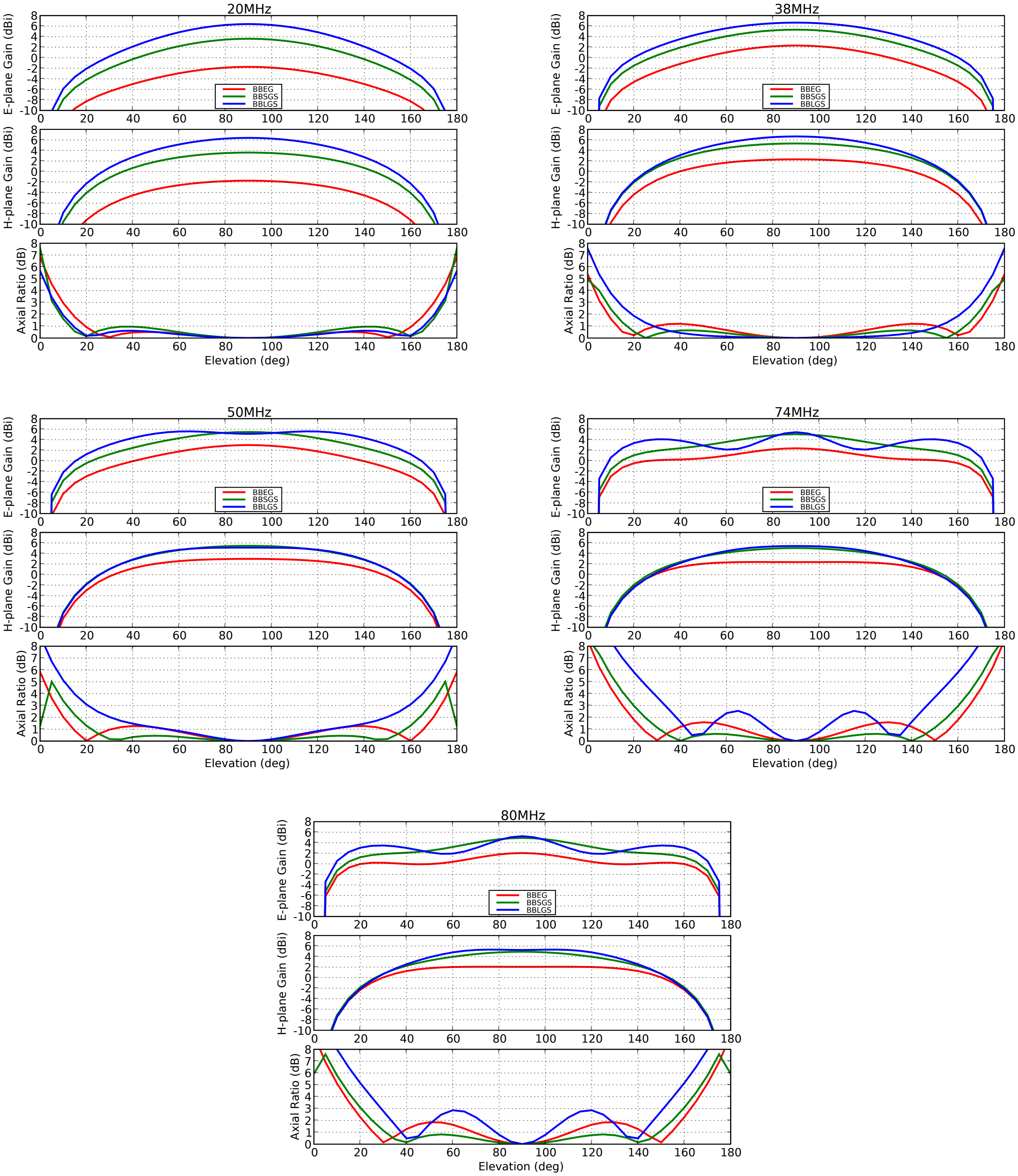

Fig. 14. Simulated beam patterns for the Big Blade antenna on Earth ground (BBEG), 3mx3m ground screen (BBSGS), and 10mx10m ground screen (BBLGS) at 25 MHz, 38 MHz, 50 MHz, 74 MHz, and 80 MHz.

LWA Engineering Memo ANT0005
Measurement and Simulation of 38 MHz and 74 MHz Resonant Dipoles

Nagini Paravastu (NRL/ASEE)

April 16, 2008

Abstract

We report on summer 2007 field measurements on half-wave resonant 38 MHz and 74 MHz dipoles. Data collected on these antennas were used to generate spectral power plots, sky noise dominance plots and drift curves. We also compare the measured sky noise dominances and drift curves to simulated results.

I. INTRODUCTION

During the summer of 2007, half-wave resonant dipoles at 38 MHz and 74 MHz were constructed at the LWDA site, the intent being to compare field measurements made on these dipoles to simulated results in order to gain confidence in modeling techniques currently being used on LWA antenna candidate designs. Sky measurements that were performed using these antennas were used to generate spectral, sky noise dominance and diurnal power plots. We present those plots in this report, and we also compare the measured results to simulation. It should be noted that measurements were performed on these dipoles during late July/early August of 2007 and then again in February 2008. Unfortunately, technical difficulties with the active baluns used in the measurements prevented valid sky data from being taken during the February 2008 trip. We therefore present in this report data that were taken during the summer 2007 trip.

II. THE ANTENNAS AND ACTIVE BALUN

A G250R balun was used as the active balun for these measurements [1]. The dipoles were modeled in NEC4 as shown in Figure 1. Antenna dimensions, height over ground and wire thickness used in the models are indicated in Figures 2 and 3.The ground screen dimensions, as well the antennas' orientation over it are shown in Figure 4. All NEC4 models were assumed to be over Earth ground with a dielectric constant of 13 and a conductivity of 0.005 S/m. All wires in the models were set to be lossless conductors. The wires in the ground screen were spaced 0.1λ center-to-center at 100 MHz and were 3.25 mm thick. The wires were therefore tangentially connected, simulating a continuous, conducting surface. This was done to simplify the model since using the actual wire diameter, metal properties, and spacing of the mesh material used in field testing would have resulted in a model with more wires and increased complexity, requiring greatly increased simulation times.

III. DRIFT CURVES

Measured and simulated drift curves for the 38 MHz dipole at 25 MHz, 38 MHz, 50 MHz, 74 MHz, and 80 MHz are shown in Figure 5, and drift curves for the 74 MHz dipole at 25 MHz, 38 MHz, 50 MHz, 74 MHz, and 80 MHz are shown in Figure 6. As expected, the measured data show that the dipoles display the greatest dynamic ranges at their resonant frequencies. The model used to generate the simulated curves assumes that the system is fully sky noise dominated, and that there is no impedance mismatch between the antenna and active balun. The differences in amplitude between the simulation and measurement is therefore an indication of how poor the sky noise dominance is at a given frequency.

IV. SKY NOISE DOMINANCE

Measured spectral powers and sky noise dominances are shown in Figure 7, and the calculation of the quantities in these plots is described in detail in another report that is currently in preparation [2].

Figure 8 compares the measured sky noise dominances from Figure 7 with simulated results. For the 38 MHz dipole, the simulated and measured sky noise dominances peak at the resonant frequency as expected, but the measured curve is narrower than simulation. For the 74 MHz dipole, the simulated sky noise dominance peaks at ∼74 MHz, but the measured sky noise dominance peaks at ∼69 MHz and the overall curve is narrower than simulation. The reason for these discrepancies must be investigated.

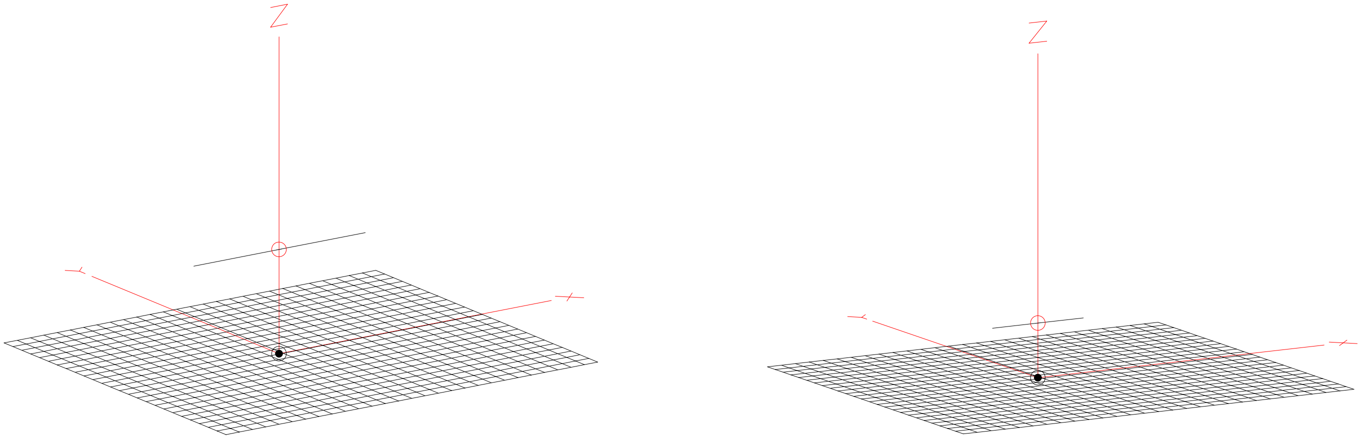

Fig. 1. NEC4 models of the 38 MHz dipole over ground screen (left) and the 74 MHz dipole over ground screen (right). The dimensions of the antennas, orientation and height over the ground screen and ground screen dimensions are shown in Figures 2, 3, and 4.

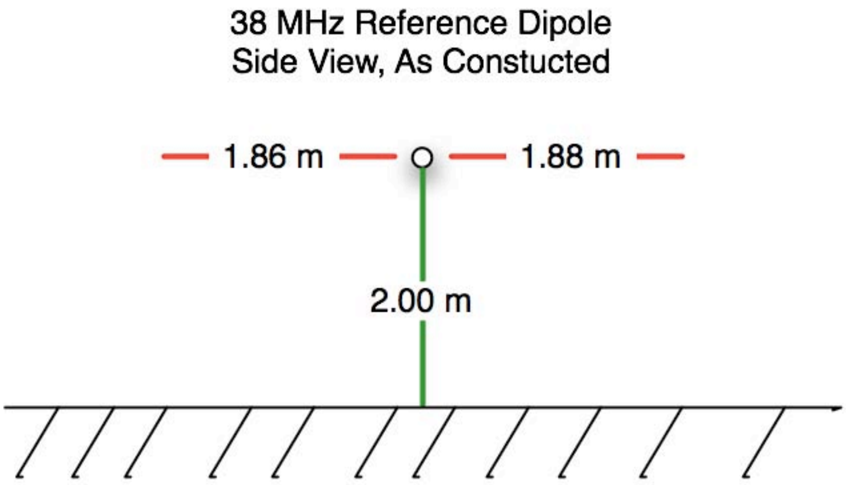

Fig. 2. Diagram of the 38 MHz reference dipole over ground screen.

REFERENCES

[1] B. Hicks and N. Paravastu, “The Rapid Test Array Balun (G250R),” *LWA Memo Series (Memo 120)*, January 2008.

[2] N. Paravastu, P. Ray, B. Hicks, W. Erickson, et al., “Comparison of Field Measurments on Active Antenna Prototypes on Ground Screens for the Long Wavelength Array,” *LWA Memo Series (In Prep)*, February 2008.

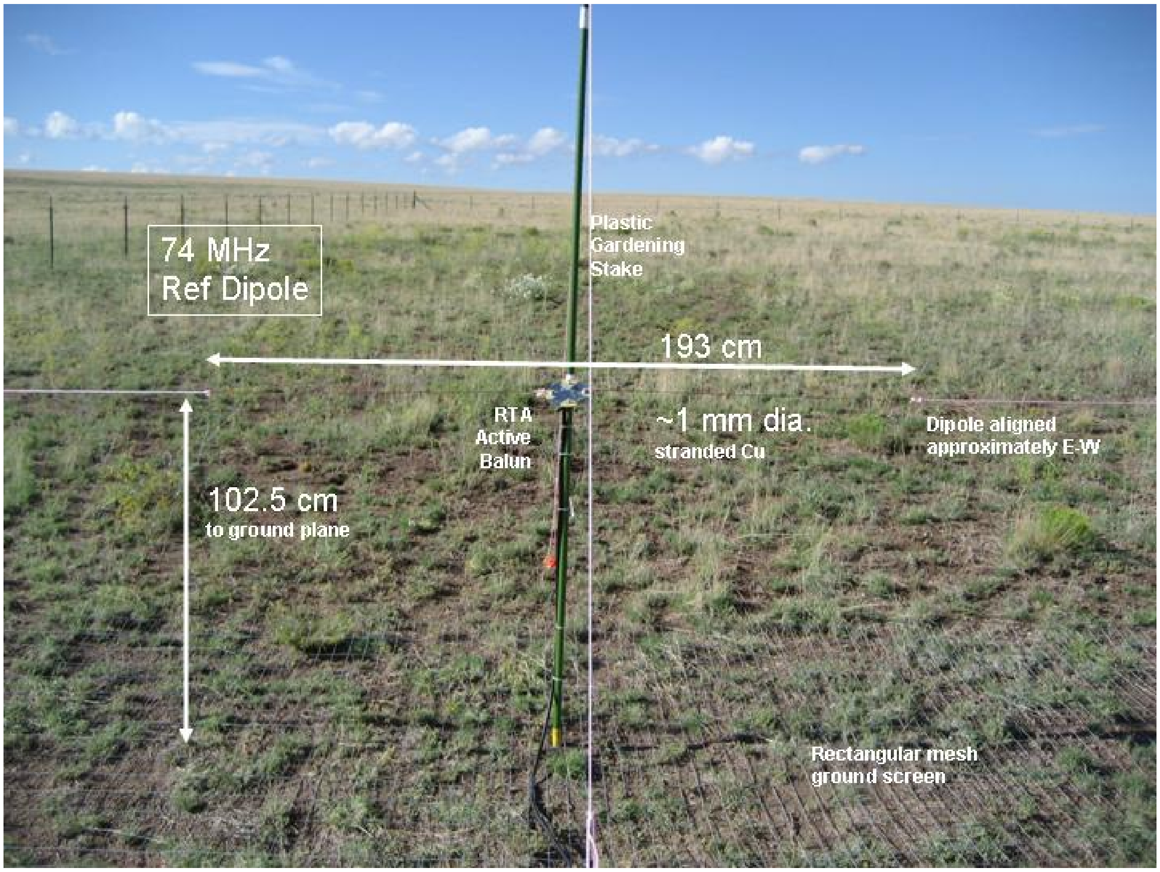

Fig. 3. Photograph of the 74 MHz reference dipole.

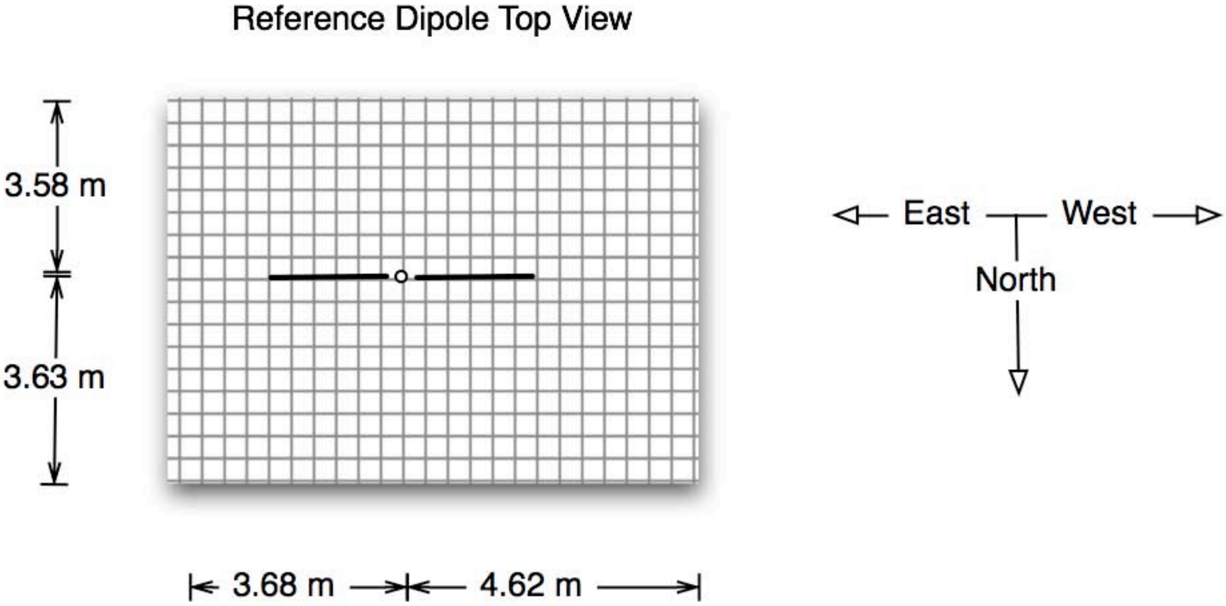

Fig. 4. Diagram of the dipoles' position over the ground screen.

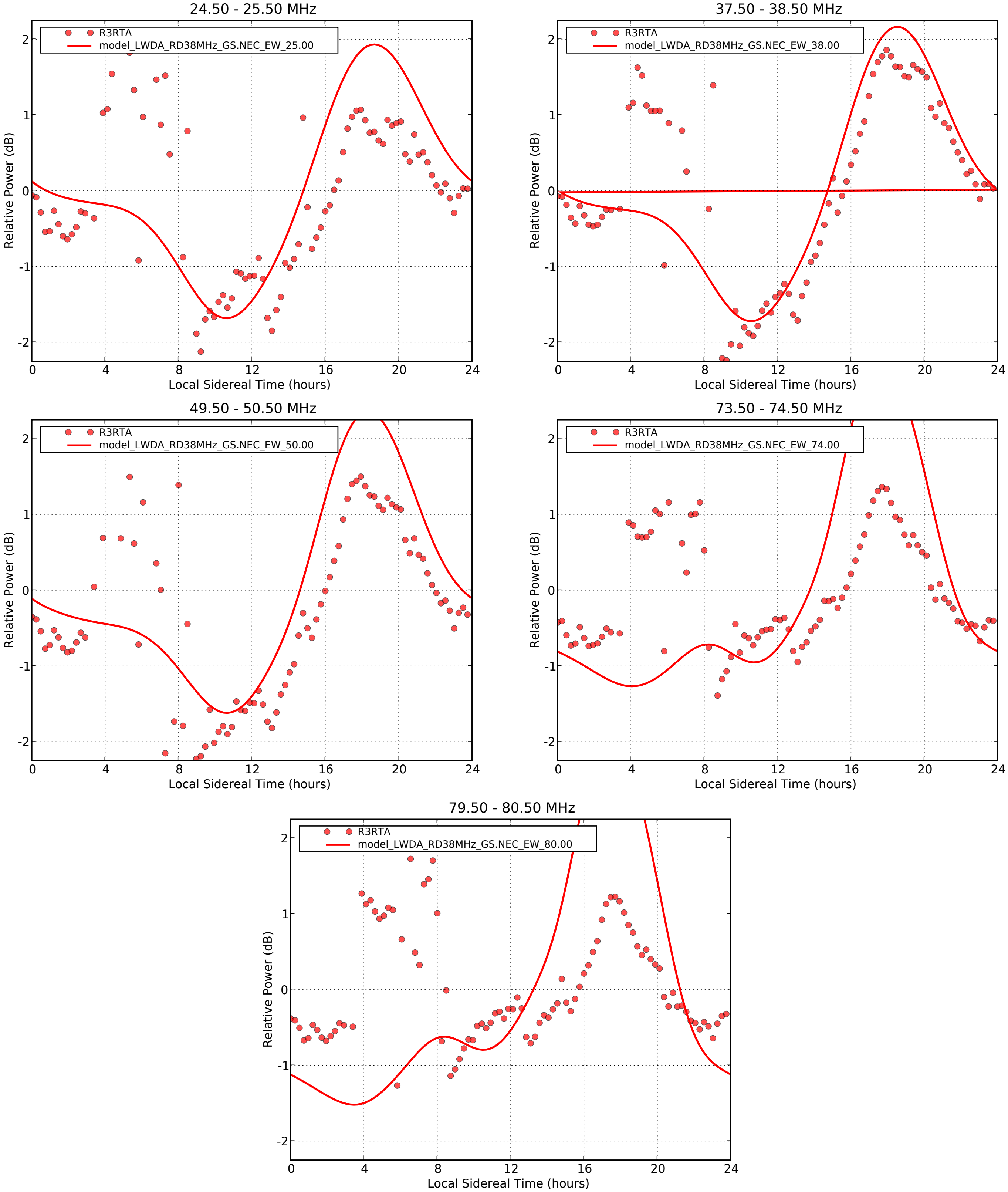

Fig. 5. Measured and simulated drift curves for the 38 MHz dipole/RTA balun at 25 MHz, 38 MHz, 50 MHz, 74 MHz, and 80 MHz.

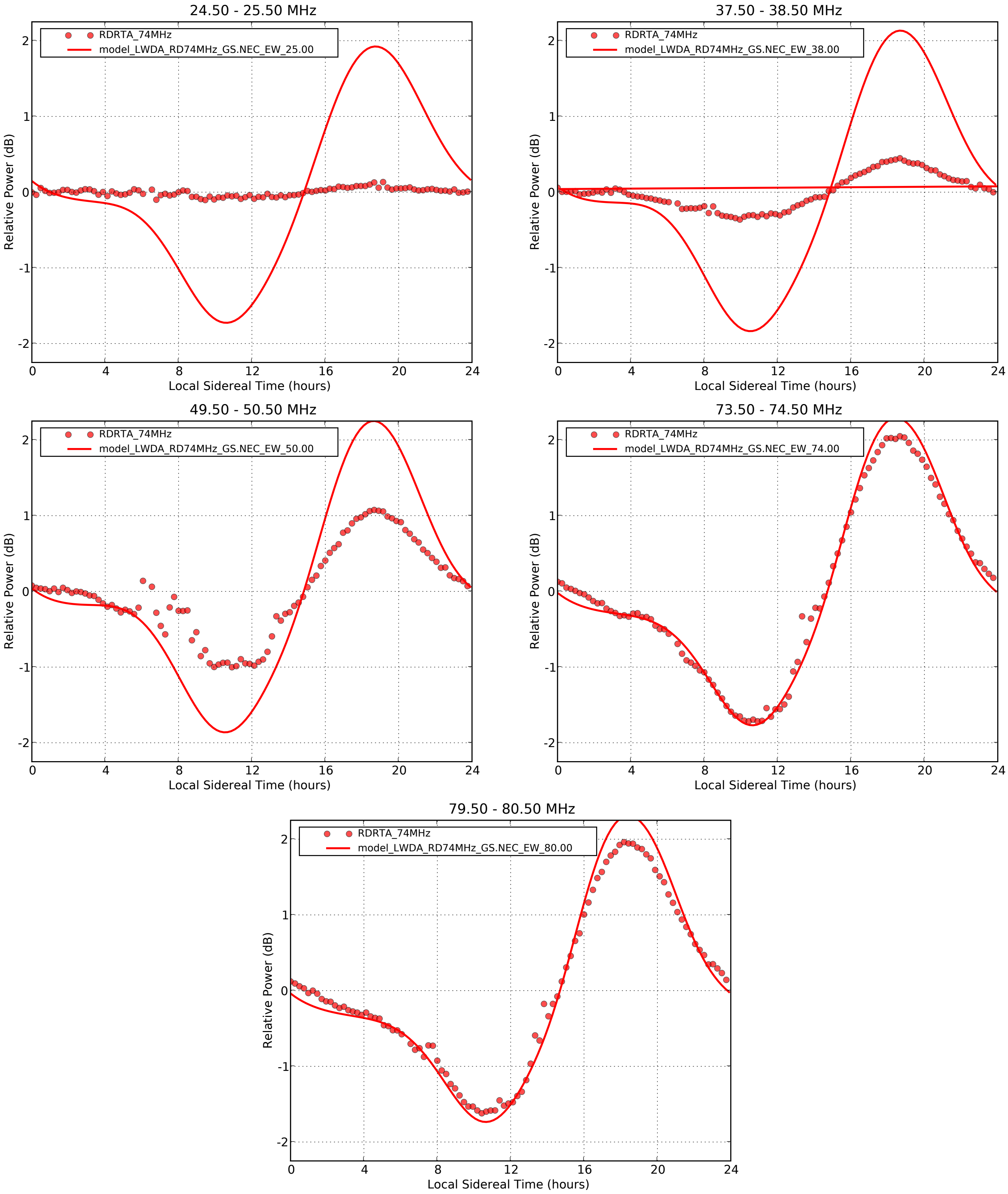

Fig. 6. Measured and simulated drift curves for the 74 MHz dipole/RTA balun at 25 MHz, 38 MHz, 50 MHz, 74 MHz, and 80 MHz.

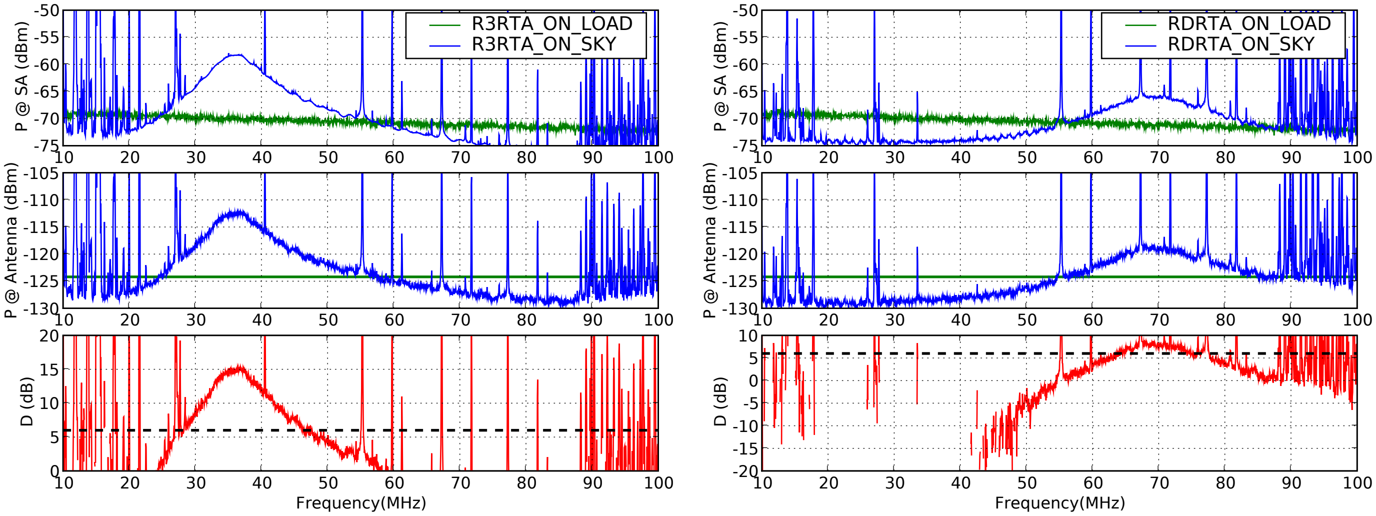

Fig. 7. Measured powers for the 34 MHz dipole/RTA balun (R3RTA) (left) and the 74 MHz dipole/RTA balun (RDRTA) (right). The power measured at the spectrum analyzer input (P @ SA) is shown on top. The power measured at the antenna feed point (P @ Antenna) is shown in the middle, and the sky noise dominance is shown on the bottom. Also on the bottom plots, D = 6 dB is indicated with a black dashed line.

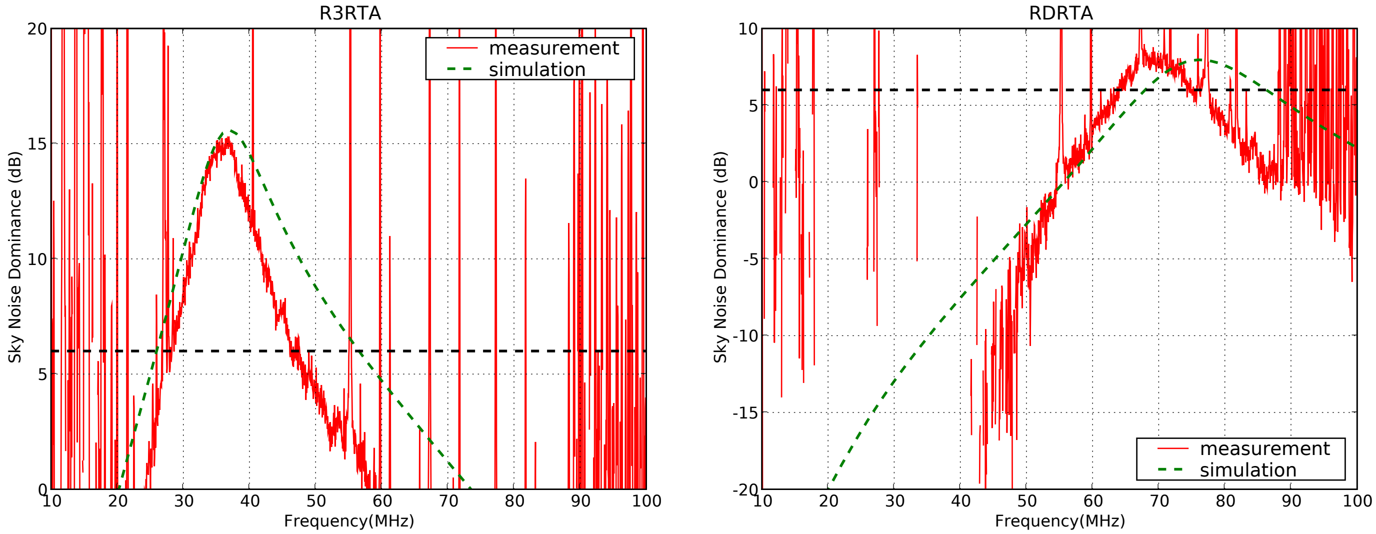

Fig. 8. Measured and simulated sky noise dominances for the 38 MHz dipole/RTA balun (R3RTA) (left) and the 74 MHz dipole/RTA balun (RDRTA) (right). D = 6 dB is indicated with a black dashed line.

LWA Engineering Memo ANT0006
Field Measurements of
Candidate Antenna Designs for LWA-1
April 22, 2008

Nagini Paravastu (NRL/ASEE)

Abstract

We report on field measurements taken in the 10 – 100 MHz frequency range on antenna design candidates for LWA-1 – the Blade Frame, the Tied Fork, the Screen Blade Frame, and the Screen Tied Fork. All antennas were tested in isolation over 3mx3m ground screens at the LWDA site in New Mexico. The data collected were used to calculate sky noise dominance and drift curve plots for each antenna. We also show simulated beam patterns and axial ratios of all antennas candidates. We use these plots to perform a side-by-side comparison of the performance of each antenna. Based on these comparisons, we find that the Screen Blade Frame antenna exhibits the broadest sky noise dominance bandwidth, but the Tied Fork and Screen Tied Fork beam patterns maintain axial ratios of 1.5 dB or less over a larger portion of the sky, particularly at higher frequencies.

I. INTRODUCTION

In February 2008, field measurements were performed on candidate antenna designs for LWA-1 by Henrique Schmitt, Frank Schinzel and me. We collected sky data on the baseline Big Blade antenna that facilitated a better understanding of the performance of the Big Blade antenna over a small 3mx3m ground screen, a larger 10mx10m ground screen and Earth ground. Our findings from these measurements are detailed in [1], [2], and [3]. In addition, we performed measurements on antenna designs that could serve as alternatives to the baseline Big Blade in LWA-1. Preliminary cost estimates obtained from Blonder Tongue Laboratories on the Big Blade antenna indicated that it may be too expensive for LWA-1. This motivated the exploration of other antenna designs that might be cheaper alternatives. More recent estimates from Burns Industries, Inc. indicate that the Big Blade may be more affordable than originally anticipated [4]. Nevertheless, characterization of these alternative designs has proceeded since the Burns Industries estimates are also preliminary and will most likely change once finer details on the balun, hub and element support structure designs have been finalized. In this report, we present sky noise dominance and drift curve plots made from the field measurements on these alternative antenna design candidates.

A. *Candidate Antenna Designs*

The four designs tested were named the Blade Frame, the Tied Fork, the Screen Blade Frame, and the Screen Tied Fork. The elements on all alternative antenna designs are made primarily of angled aluminum, the purpose being to realize an element similar in both shape and size the to the Big Blade that would require less metal to fabricate, be lighter and less susceptible to wind loading, and require a simpler and less expensive support structure. Photographs and NEC4 models of these antennas are shown in Figures 1, 2, 3, and 4 (the model for SBDSG is the same as that which was used for BBSGS in [2]). Dimensions of these elements are shown Figure 5. The Screen Blade Frame and Screen Tied Fork elements have the same dimensions as their frame element counterparts, with the only difference being that metal mesh has been bolted to the angled aluminum frames. The intent with the screen elements was to increase the available metal surface area to achieve performance more closely approaching the Big Blade while at the same time maintaining all of the advantages of the frame element designs. The mesh material used for this purpose is the same as that which was used for the ground screens. Further details on these antenna designs are also provided in [5] and [6].

All antennas were tested in isolation with the G250R balun over 3mx3m ground screens. Additional information on ground screen material and construction, antenna modeling, and the G250R balun used in the field tests are given in [2] and [7]. Each antenna was given a short designation, as shown in Table I, to facilitate data collection and record keeping. The antennas will be referred to by these designations in subsequent sections of this report.

II. SKY NOISE DOMINANCE

Figure 6 shows the measured sky noise dominance at Galactic minimum (10 hrs LST) of all four antennas. SBDSG shows the broadest frequency response and remains $\geq$ 6 dB sky noise dominated over almost the entire 20 – 80 MHz frequency band. STFSG exhibits similar properties, but has a smaller overall 6 dB bandwidth. It should be noted that the upturn in the the BDSGS and STFSG curves is unexpected since simulations predict a steady decrease in sky noise dominance at lower frequencies as demonstrated in the TFSGS and SBDSG data. The same balun was used to measure BDSGS and STFSG, and there is a possibility that it was defective. It is therefore highly recommended that BDSGS and STFSG be remeasured before any solid conclusions can be made on the most appropriate antenna design for LWA-1.

Figure 7 compares the SBDSG sky noise dominance response to BBSGS from [2]. While it was expected that the two curves would be very similar, the SBDSG curve appears to be shifted $\sim$5 MHz lower in frequency, while at the same time, maintaining $\geq$6 dB sky noise dominant performance up to 80 MHz. Figure 8 shows how the measured sky noise dominances for all four antennas compare to NEC4-based simulations.

III. DRIFT CURVES

Simulated and measured drift curves at 25 MHz, 38 MHz, 74 MHz and 80 MHz for the for antennas under consideration are shown in Figures 9, 10, 11, 12. As was the case with the drift curves presented in [2], the model used to generate the simulated curves does not take into account the antenna-active balun impedance mismatch. This feature will be integrated into the model in the near future.

Figure 13 shows the simulated beam patterns for five frequencies in the 20 – 80 MHz frequency band. Although SBDSG exhibited the broadest frequency response in sky noise dominance, the simulated beam patterns show that it has the poorest axial symmetry of the four antennas under consideration.

IV. SUMMARY

In this report, we have provided sky noise dominance and drift curve plots based on field measurement data and simulated beam patterns for alternative antenna designs for LWA-1. We have shown that in isolation, SBDSG has the broadest frequency response, but the poorest axial symmetry of the four candidate antenna designs. Tradeoffs such as these will have to be taken into consideration in the process of choosing the final LWA-1 antenna design.

In addition, there are suspicious features in the sky noise dominance curves for BDSGS and STFSG at low frequencies that could have been caused by the use of a defective active balun during measurement. These two antennas should be remeasured before any final conclusions can be drawn about their performance.

REFERENCES

[1] N. Paravastu, "LWA Engineering Memo ANT0003 - Measurement Trip Notes," *LWA Engineering Memo Series (ANT0003)*, February 2008.

[2] ——, "LWA Engineering Memo ANT0004 - Big Blade Measurement Plots," *LWA Engineering Memo Series (ANT0004)*, April 2008.

[3] H. Schmitt, "LWA Engineering Memo GND0001 - Baseline Design of Station Ground Screen," *LWA Engineering Memo Series (GND0001)*, March 2008.

TABLE I

ANTENNA DESIGNATIONS

Antenna	Ground	Designation
Blade Frame	3mx3m ground screen	BDSGS
Tied Fork	3mx3m ground screen	TFSGS
Screen Blade Frame	3mx3m ground screen	SBDSG
Screen Tied Fork	3mx3m ground screen	STFSG
Big Blade	3mx3m ground screen	BBSGS

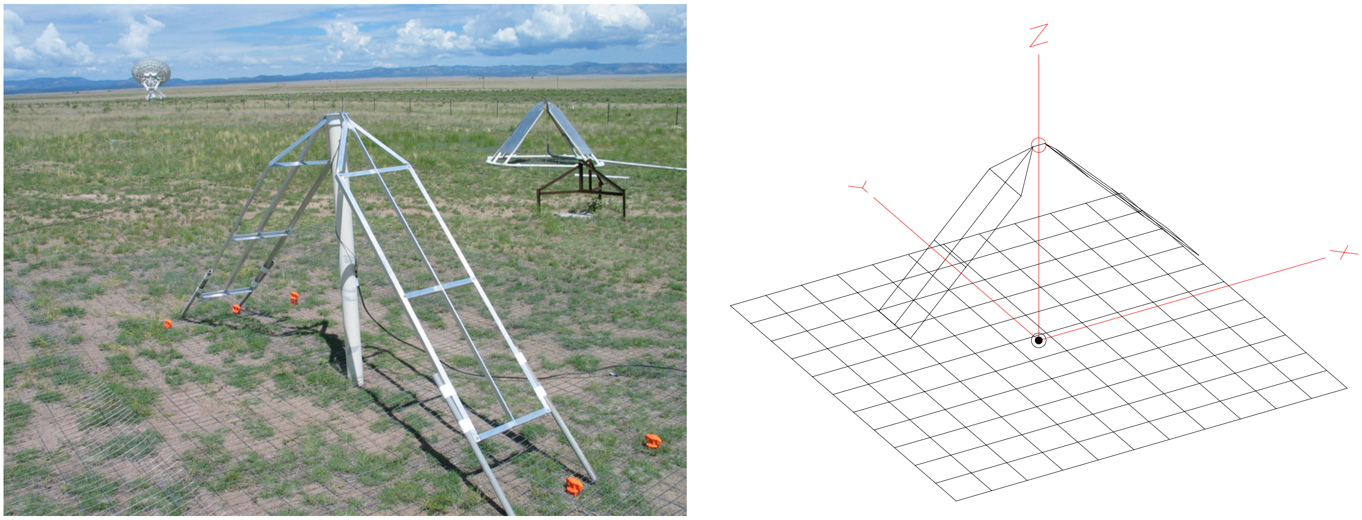

Fig. 1. Photograph and NEC4 model of BDSGS.

[4] N. Paravastu, "LWA Engineering Memo STD0001 - Burns Industries Antenna Cost Estimates," *LWA Engineering Memo Series (STD0001)*, April 2008.

[5] N. Paravastu, W. Erickson, and B. Hicks, "Comparison of Antenna Designs on Ground Screens for the Long Wavelength Array," *LWA Memo Series (In Prep)*.

[6] N. Paravastu, B. Hicks, P. Ray, and W. Erickson, "A New Candidate Active Antenna Design for the Long Wavelength Aray," *LWA Memo Series (Memo 88)*, May 2007.

[7] B. Hicks and N. Paravastu, "The Rapid Test Array Balun (G250R)," *LWA Memo Series (Memo 120)*, January 2008.

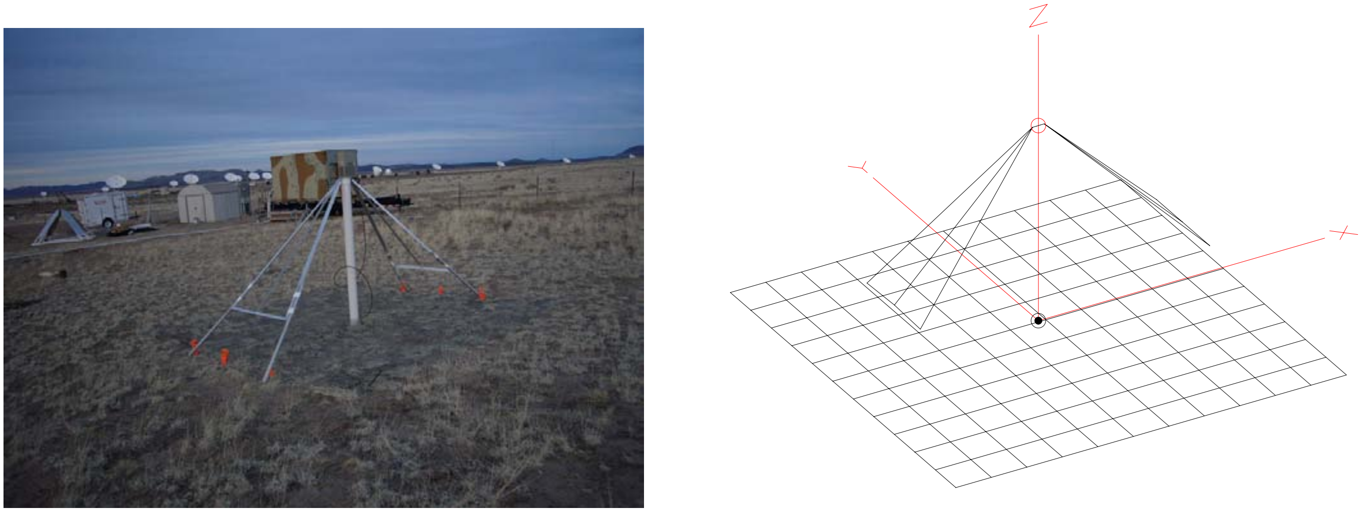

Fig. 2. Photograph and NEC4 model of TFSGS.

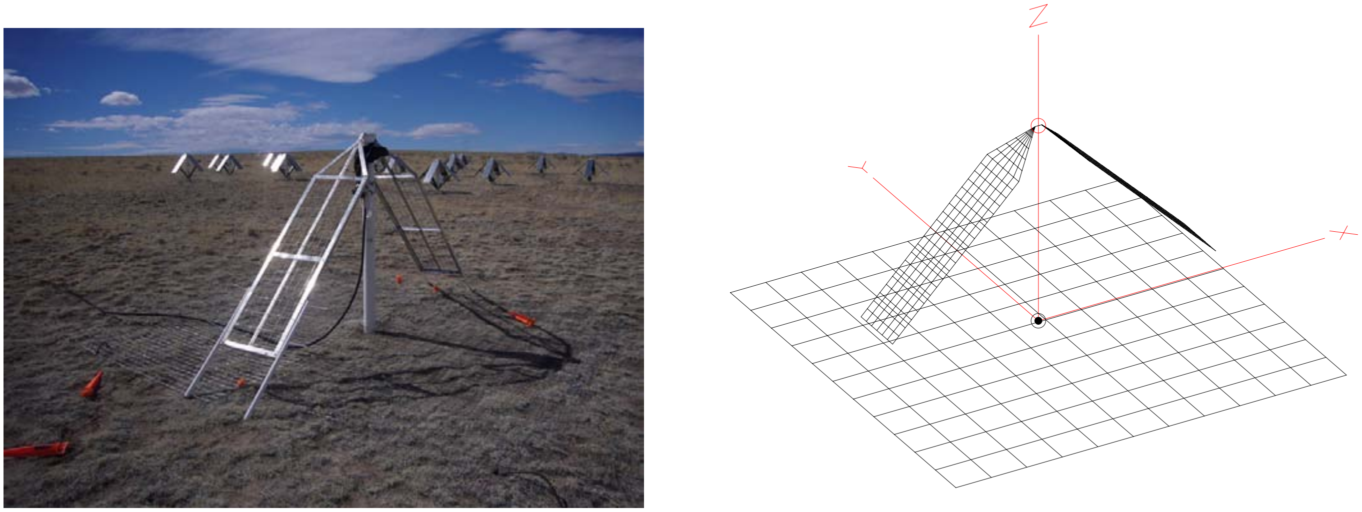

Fig. 3. Photograph and NEC4 model of SBDSG. The NEC4 model is the same as that which was used for BBSGS in [2].

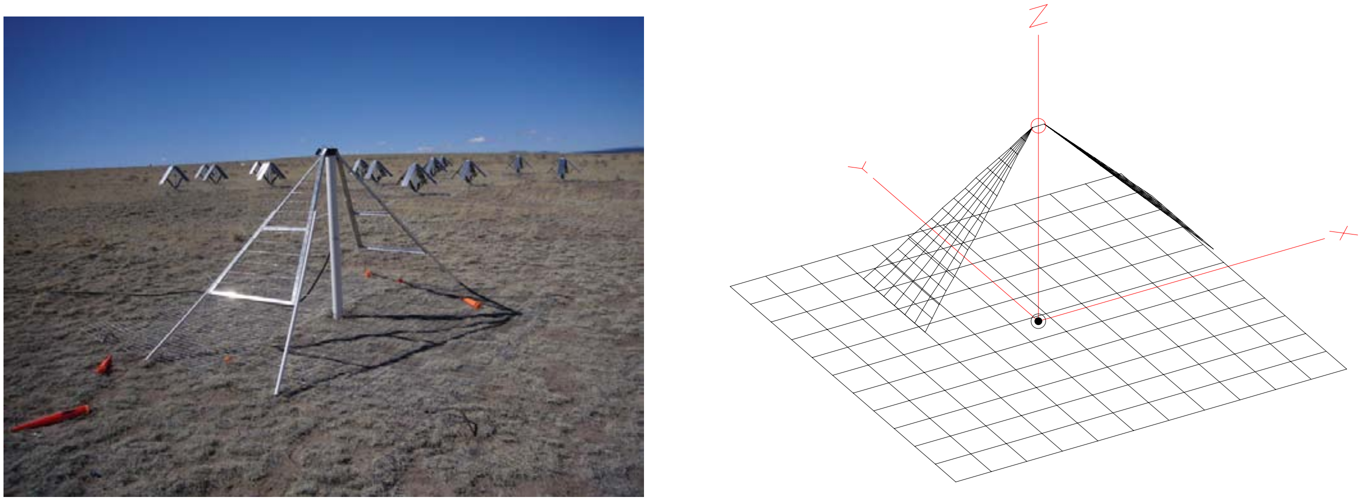

Fig. 4. Photograph and NEC4 model of STFSG.

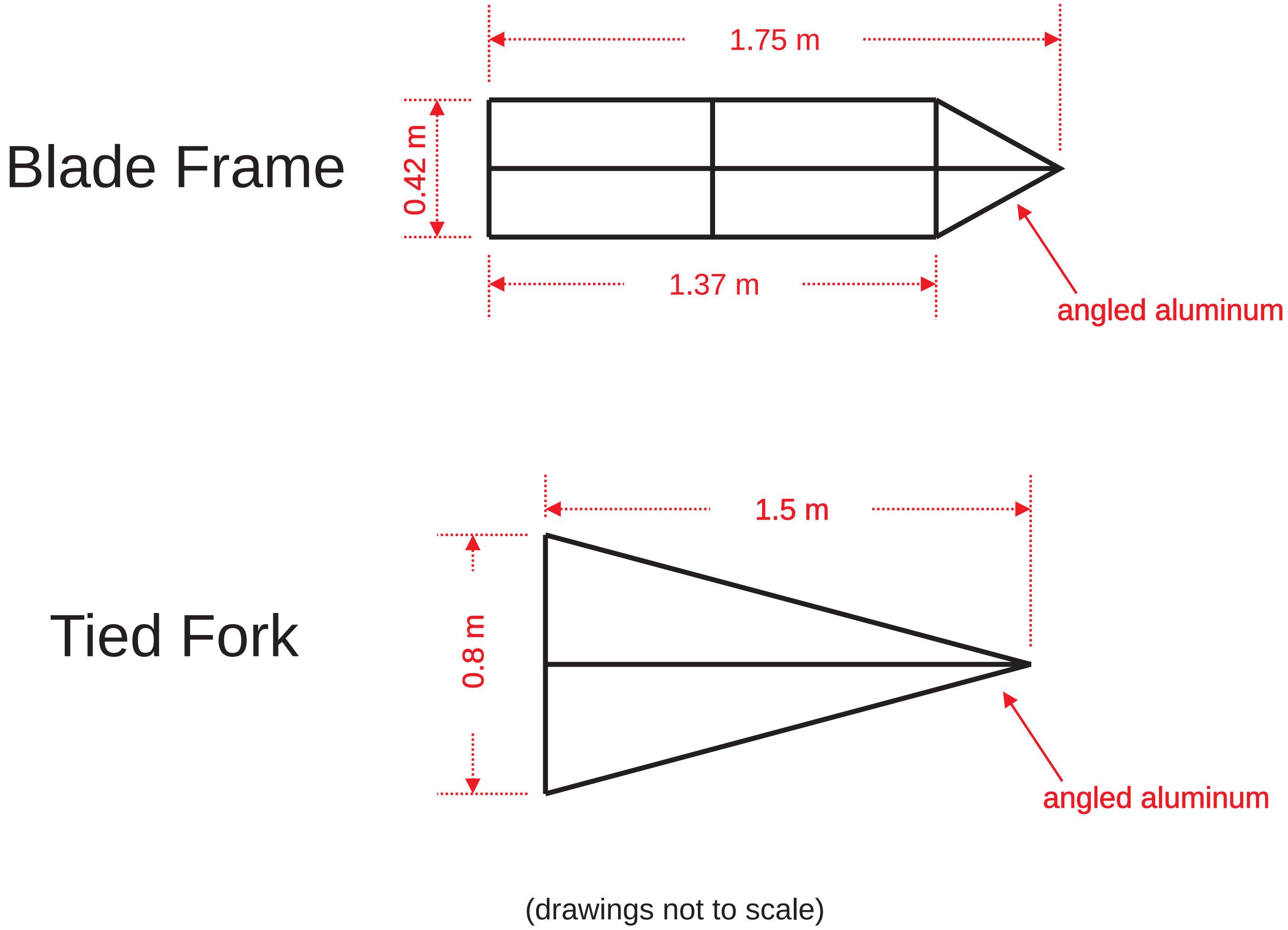

Fig. 5. Element dimensions (drawing not to scale). The Screen Blade Frame and Screen Tied Fork have the same dimensions as their non-screen counterparts.

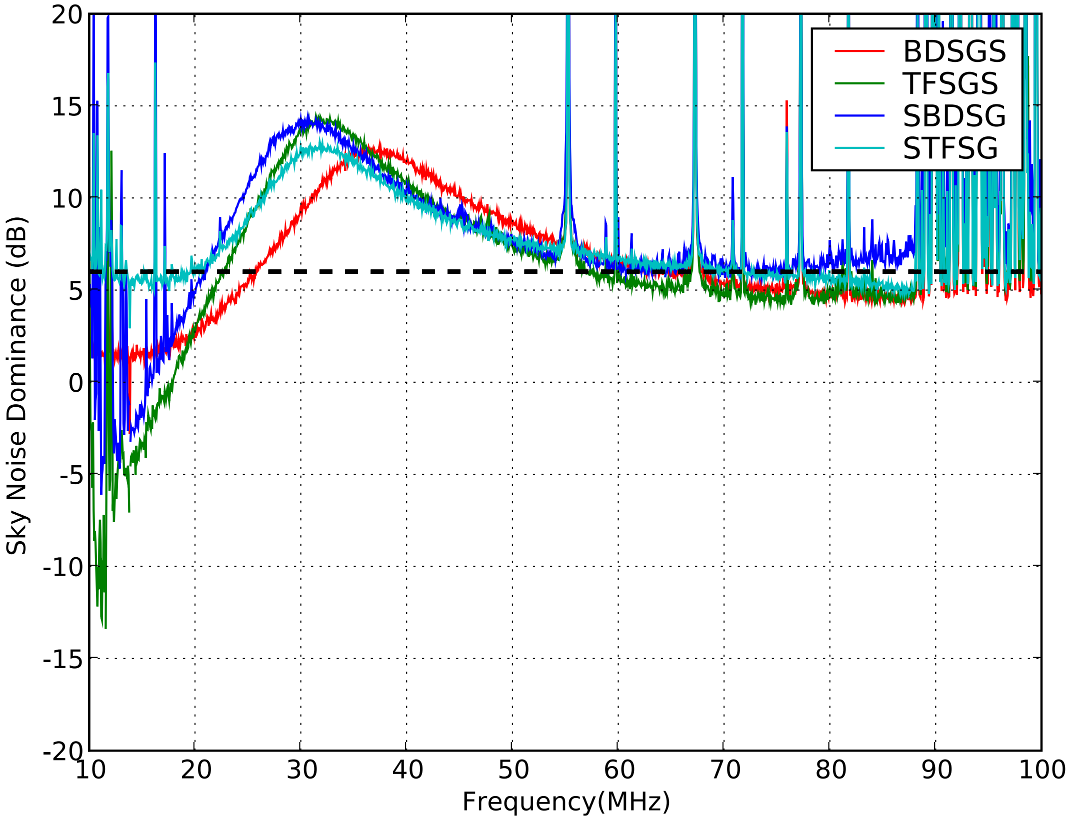

Fig. 6. Measured sky noise dominances of BDSGS, TFSGS, SBDSG, STFSG. Data shown here for all antennas were taken at Galactic minimum (10 hrs LST).

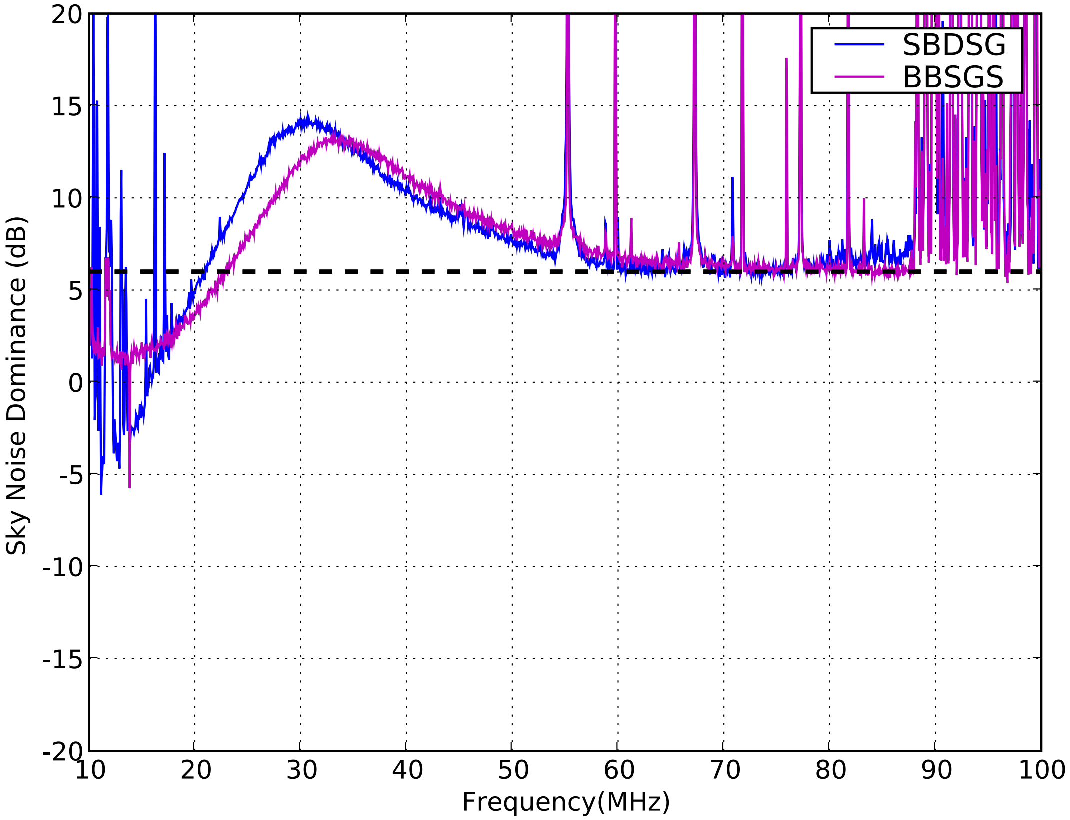

Fig. 7. Measured sky noise dominances for SBDSG and BBSGS. Data shown here for all antennas were taken at Galactic minimum (10 hrs LST).

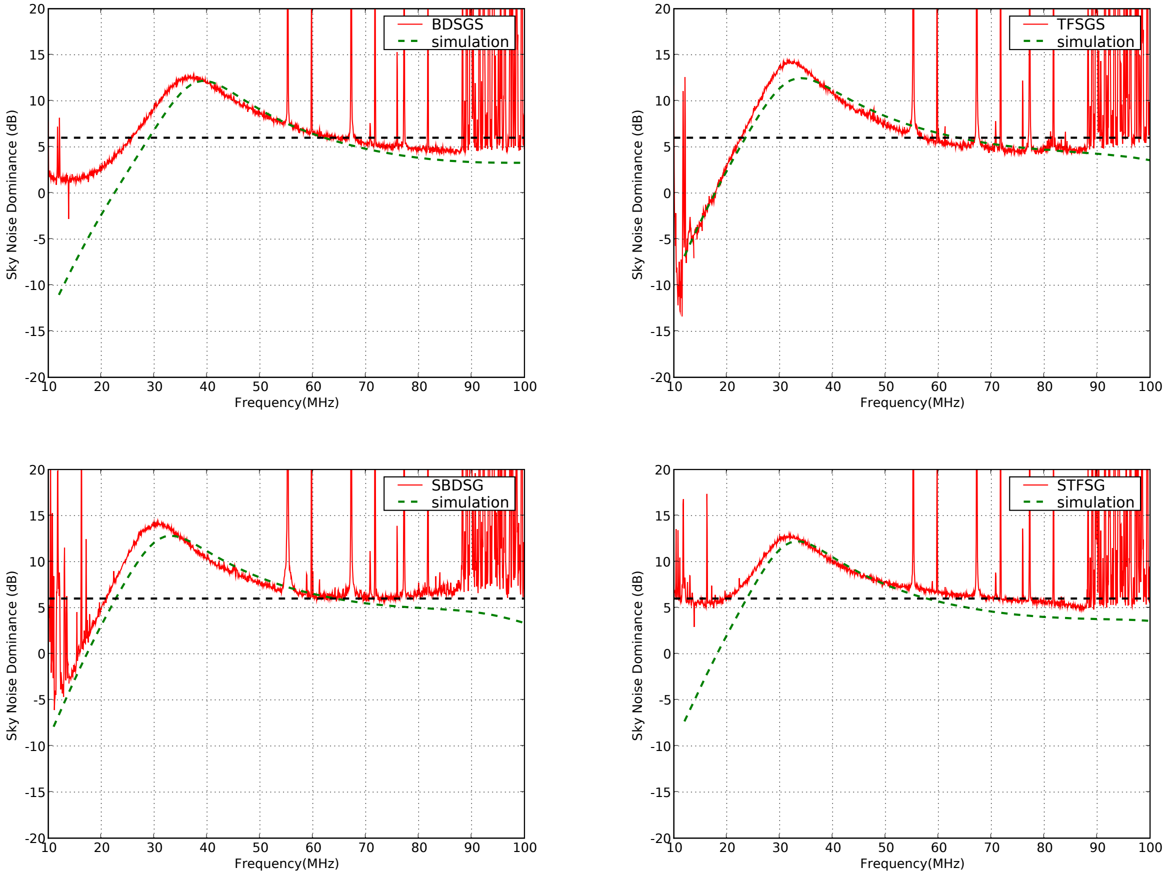

Fig. 8. Measured and simulated sky noise dominances for BDSGS, TFSGS, SBDSG, STFSG. Data shown here for all antennas were taken at Galactic minimum (10 hrs LST).

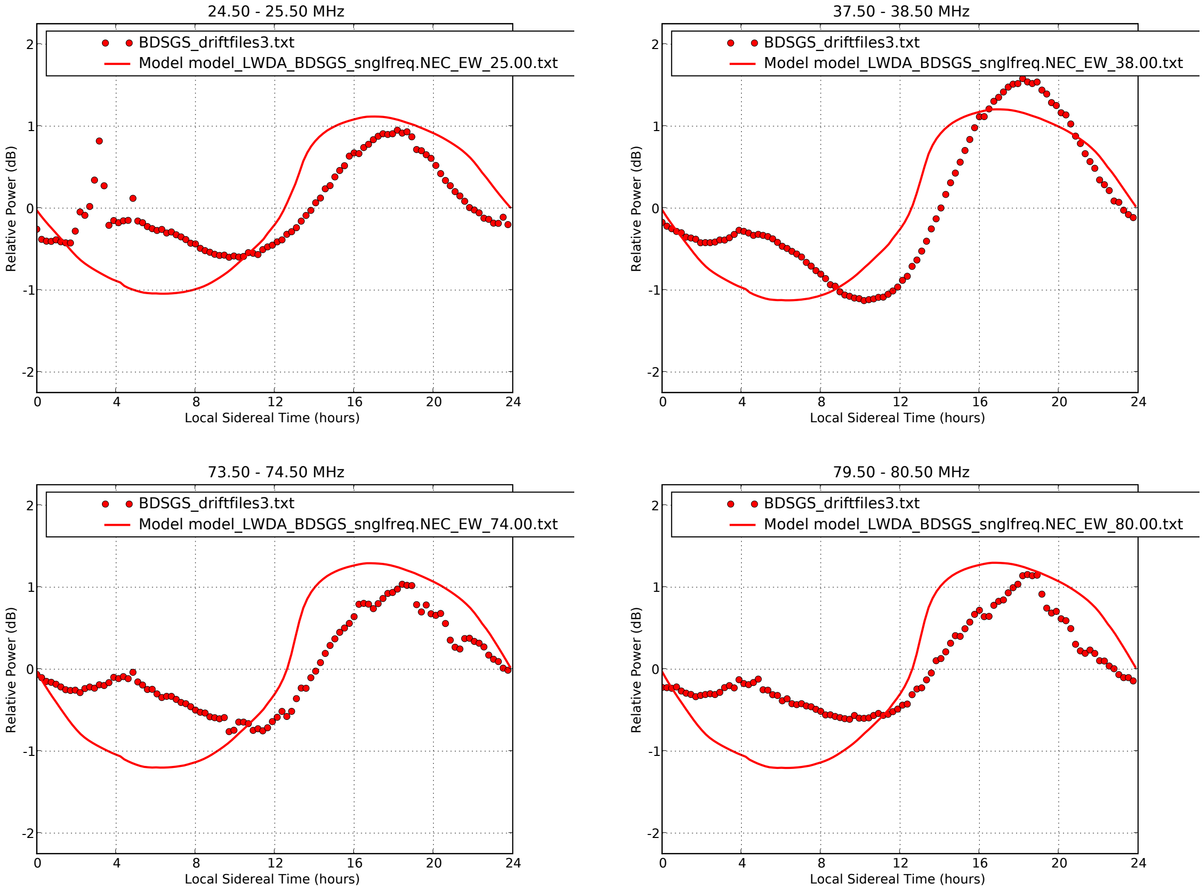

Fig. 9. Measured and simulated drift curves for BDSGS at 25 MHz, 38 MHz, 74 MHz, and 80 MHz.

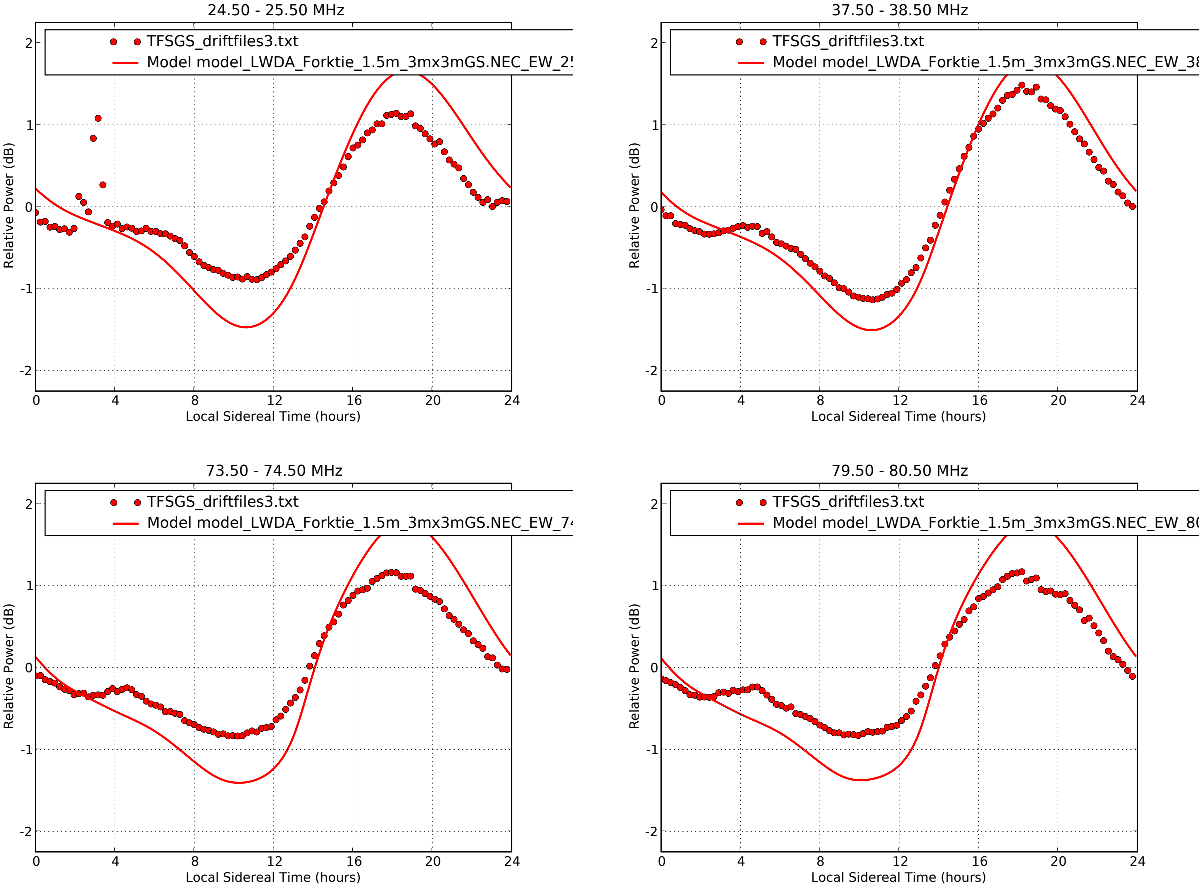

Fig. 10. Measured and simulated drift curves for TFSGS at 25 MHz, 38 MHz, 74 MHz, and 80 MHz.

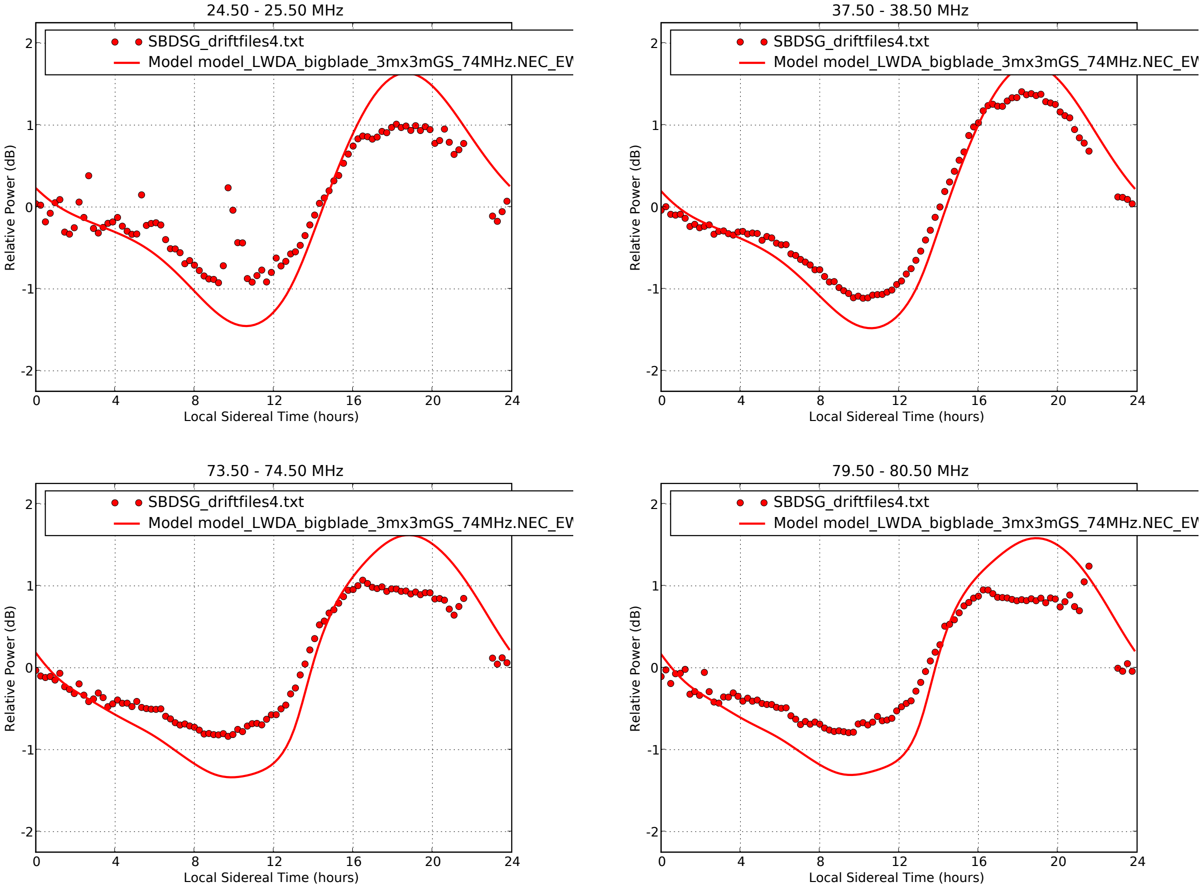

Fig. 11. Measured and simulated drift curves for SBDSG at 25 MHz, 38 MHz, 74 MHz, and 80 MHz.

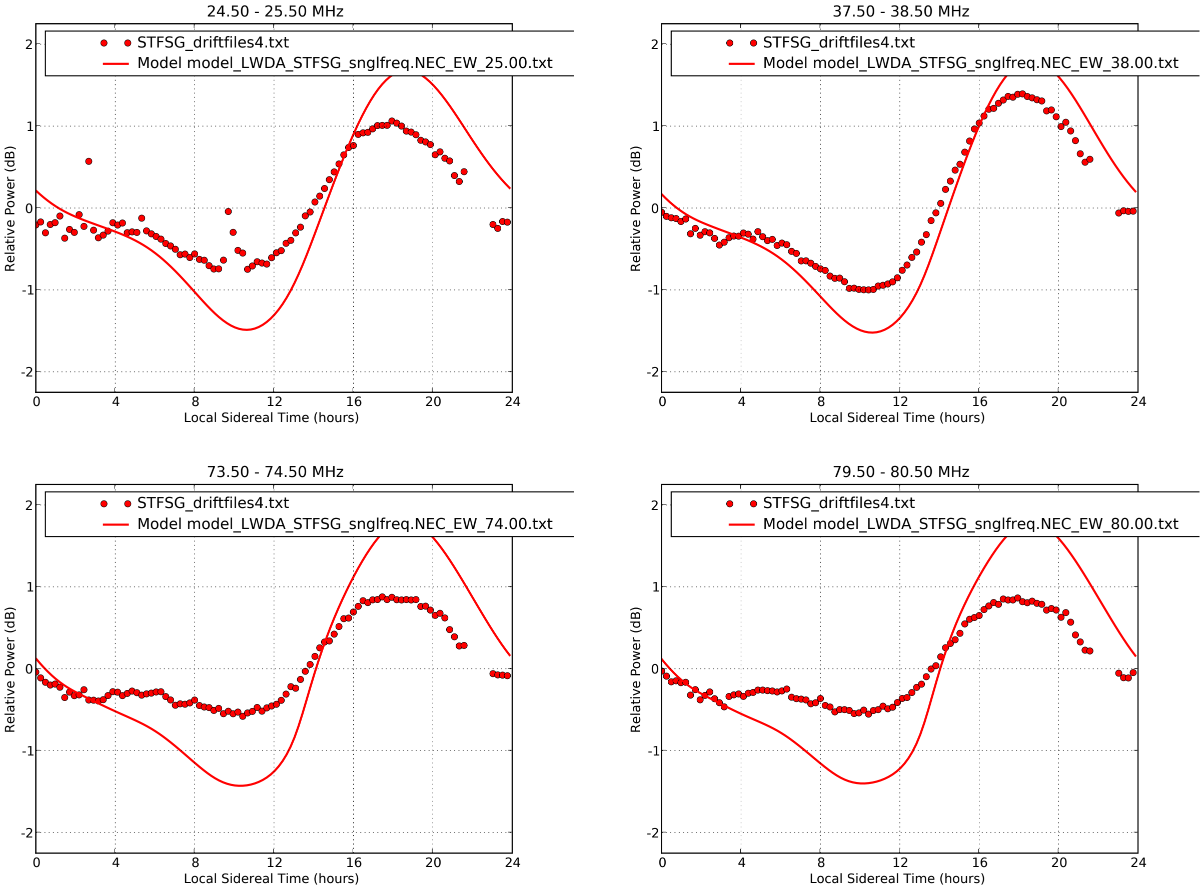

Fig. 12. Measured and simulated drift curves for STFSG at 25 MHz, 38 MHz, 74 MHz, and 80 MHz.

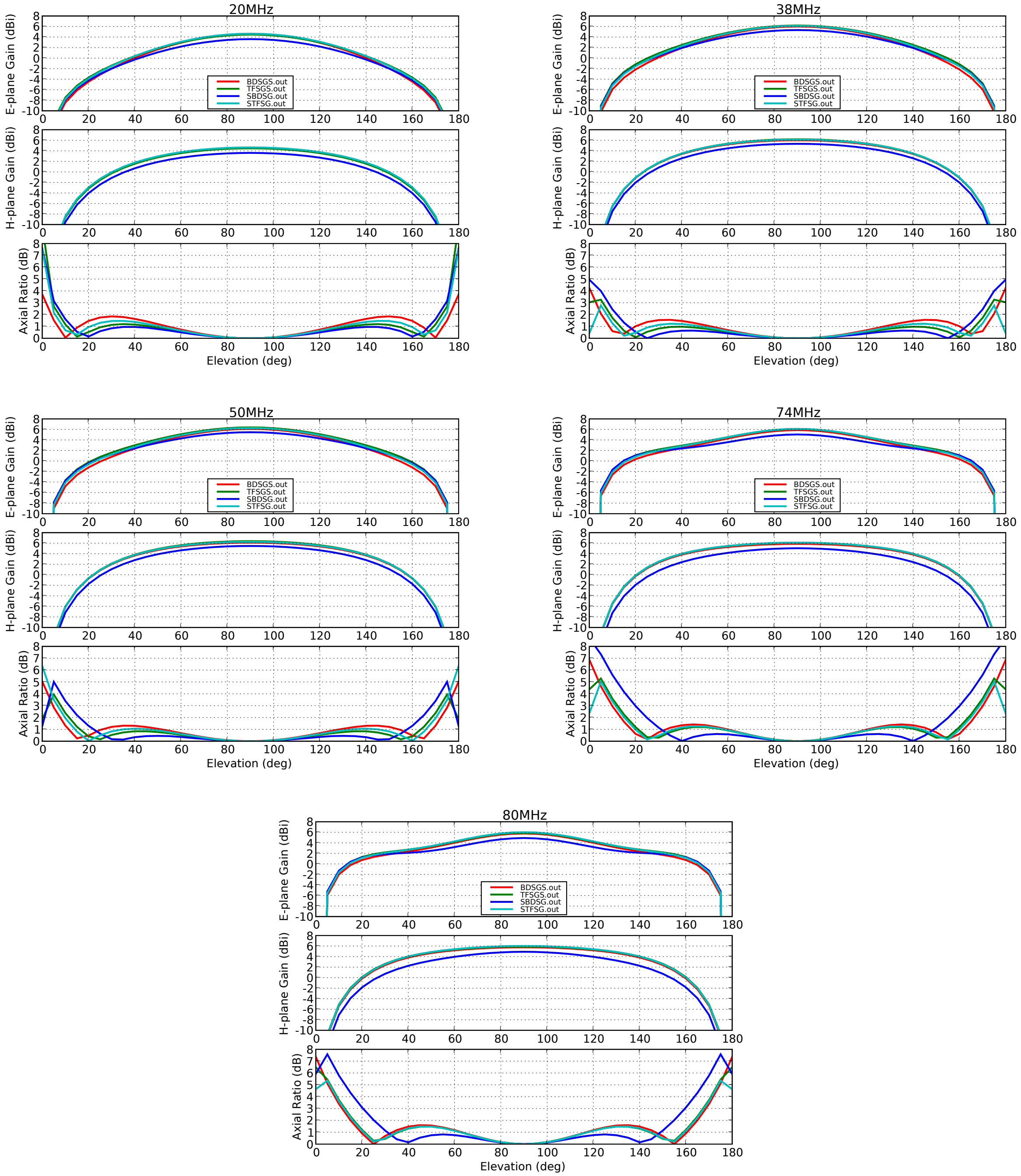

Fig. 13. Simulated beam patterns for BDSGS, TFSGS, SBDSG, and STFSG at 25 MHz, 38 MHz, 50 MHz, 74 MHz, and 80 MHz.

LWA Engineering Memo ANT0007
Antenna Design for LWA-1
August 29, 2008

Nagini Paravastu (NRL/ASEE)

Abstract

We review the LWA antenna design and development effort that has taken place over the past few years which has included simulation and field measurements of several potential antenna designs. Based on our results, we recommend that the Screen Tied Fork be used as the antenna design for the first LWA station. The Tied Fork antenna, which performs comparably to the Screen Tied Fork, can be used as an alternative design. The current status of work being done with Burns Industries to finalize a mechanical design for the antennas is also discussed.

I. INTRODUCTION

One of the critical aspects in the Long Wavelength Array project has been to develop an antenna for the first station (LWA-1). Over the past few years, the task of designing the LWA-1 antenna has been accomplished using extensive electromagnetic simulation and field testing of prototypes made at NRL. In this report, we briefly review the findings of that work and use the lessons learned to make a recommendation on an antenna design for LWA-1.

II. ANTENNA DESIGN REQUIREMENTS

The LWA-1 antennas were developed with the goal of satisfying the following key requirements:

1) The antenna must exhibit stable, sky noise dominant performance (preferably 6 dB or greater) in the 20 – 80 MHz frequency band.
2) The antenna must exhibit good beam pattern E/H plane symmetry and a wide ($\sim 100^\circ$) half-power beam width for good sky coverage.
3) The antenna must be a simple topology that can be easily constructed in large quantity.
4) The antenna must be affordable ($\sim \$100$ per antenna) in quantities of 5000 or more.
5) The antenna and support structure must be easy to assemble. It must also survive for ~ 15 years in the New Mexico environment. This includes resistance to temperature variations, and high wind speeds that are characteristic of the New Mexico desert.

III. ANTENNA DESIGN PROCESS

The baseline design for the LWA-1 antenna was the Big Blade antenna [1], [2]. The Big Blade topology is based on that of the LWDA Small Blade antenna, but is scaled for use over the full 20 – 80 MHz frequency range of the LWA. Although the Big Blade did satisfy requirements 1 and 2 mentioned in Section II, preliminary cost estimates indicated that it may not meet requirements 3 – 5. The Big Blade antenna elements are made of sheet aluminum, which is costly. They are also very heavy and would therefore likely require a substantial and prohibitively expensive support structure. Our efforts therefore focused on designing an antenna that would have RF properties that are comparable to the Big Blade, but would be lighter and cheaper.

All antennas were designed using NEC-4, a standard antenna simulation package [1]. For the purposes of simulation, a dielectric constant of 13 and a conductivity of 0.005 S/m were assumed for the ground properties. All antennas were also assumed to have a G250R active balun ,with a 100Ω input impedance and a 250 K noise temperature, installed at the feed points [6].

The most promising designs were prototyped and tested at the LWDA site in New Mexico. These field tests included antenna impedance measurements as well as power spectral measurements from which drift curves and antenna sky noise dominance could be plotted [3], [4]. All antennas were simulated and field tested in isolation (i.e. - mutual coupling effects were not considered). Furthermore, it was determined through experimentation in the field that a ground screen would be required in order to stabilize the RF properties of the antennas in the presence of varying ground conditions [5]. In light of this finding, all antennas designs included a 3mx3m ground screen.

IV. ANTENNA DESIGN RECOMMENDATION

Based on simulation and field measurement results summarized in Section III, we recommend that the Screen Tied Fork antenna design be chosen for LWA-1. Of all the designs considered, the Screen Tied Fork antenna has the most preferable combination of sky noise dominance and beam pattern properties [4]. The Screen Tied Fork maintains 6 dB or greater sky noise dominant performance over most of the 20 – 80 MHz frequency band. In addition, its beam pattern has an axial symmetry of 2 dB or less for elevation angles down to 65° from Zenith.

As future field test results and pricing information become available on the Screen Tied Fork, the LWA project should continue to evaluate if this antenna design is the best option for the project. In the event that the Screen Tied Fork is judged to be undesirable, the Tied Fork antenna, which has comparable RF properties but with a simpler topology, should be the alternative (details on the Tied Fork are given in [1], and [4]).

V. MECHANICAL DESIGN DEVELOPMENT

In order to prepare for mass production, we have been working with Steve Burns of Burns Industries, Inc. to develop a mechanical design package for the LWA-1 antennas. The Screen Tied Fork antenna, as it was prototyped at NRL, is shown in Figure 1. In this design, a metal mesh material is bolted to an angle aluminum frame. The Screen Tied Fork antenna, as it was prototyped by Burns Industries, is shown in Figure 2. A CAD drawing of the antenna elements as provided by Burns Industries is shown in Figure 3. In the Burns Industries prototype, the metal screen has been replaced with segments of angle aluminum. Steve Burns proposed this concept as a way to facilitate antenna element fabrication and minimize cost. As shown in Figures 4 and 5, the simulated sky noise dominances and beam patterns of the NRL and Burns Industries prototypes are comparable.

Burns Industries has produced three prototypes of a Screen Tied Fork such as the one pictured in Figure 2. This prototype will be tested at the LWDA site in September. The Burns prototypes and the field test results will be described more in detail in later reports.

VI. SUMMARY

In this report, we have given a brief summary of the LWA antenna development program that has been in progress over the past few years. As a culmination of this work, we recommend the Screen Tied Fork as the antenna design of choice for the first LWA station (LWA-1), with the Tied Fork as second alternative.

We also describe the work we have begun in collaboration with Burns Industries, an antenna manufacturer, to develop a mechanical design package for the Screen Tied Fork that can be produced in mass quantity at low cost for future LWA stations. Burns Industries has recently produced a first round of antenna prototypes, which will be field tested in September.

REFERENCES

[1] N. Paravastu, W. Erickson, and B. Hicks, “Comparison of Antenna Designs on Ground Screens for the Long Wavelength Array,” *LWA Memo Series (In Prep)*.

[2] N. Paravastu, “LWA Engineering Memo ANT0004 - Big Blade Measurement Plots,” *LWA Engineering Memo Series (ANT0004)*, April 2008.

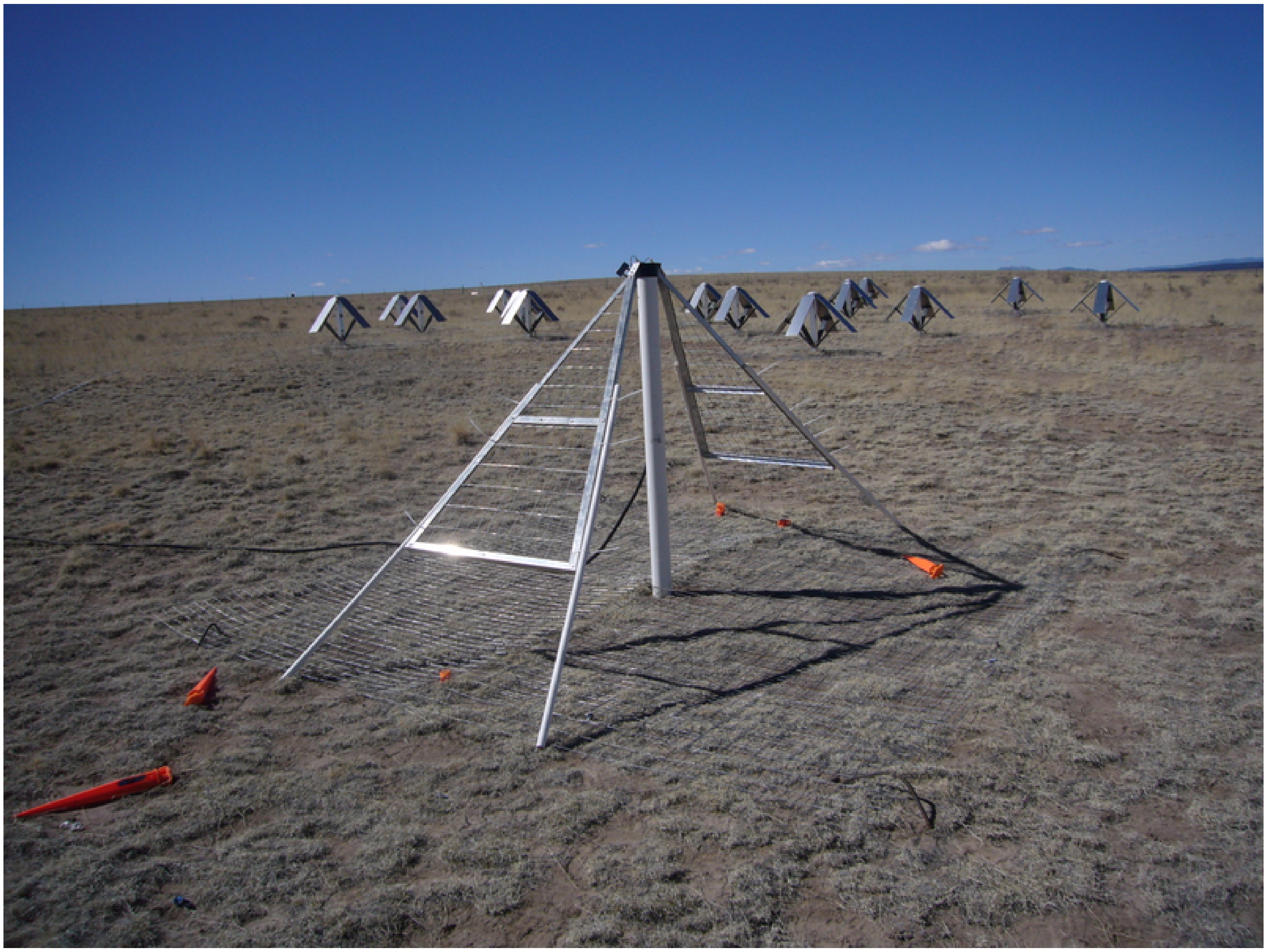

Fig. 1. Photograph of a Screen Tied Fork prototype constructed at NRL.

[3] N. Paravastu, P. Ray, B. Hicks, W. Erickson, et al. "Comparison of Field Measurments on Active Antenna Prototypes on Ground Screens for the Long Wavelength Array," *LWA Memo Series (In Prep)*, February 2008.

[4] N. Paravastu, "LWA Engineering Memo ANT0006 - Field Measurements of Candidate Antenna Designs for LWA-1," *LWA Engineering Memo Series (ANT0006)*, April 2008.

[5] N. Paravastu, B. Hicks, E. Aguilera, et al. "Impedance Measurements of the Big Blade and Fork Antennas on Ground Screens at the LWDA Site,"*LWA Memo Series (Memo 90)*, June 2007.

[6] B. Hicks and N. Paravastu, "The Rapid Test Array Balun (G250R)," *LWA Memo Series (Memo 120)*, January 2008.

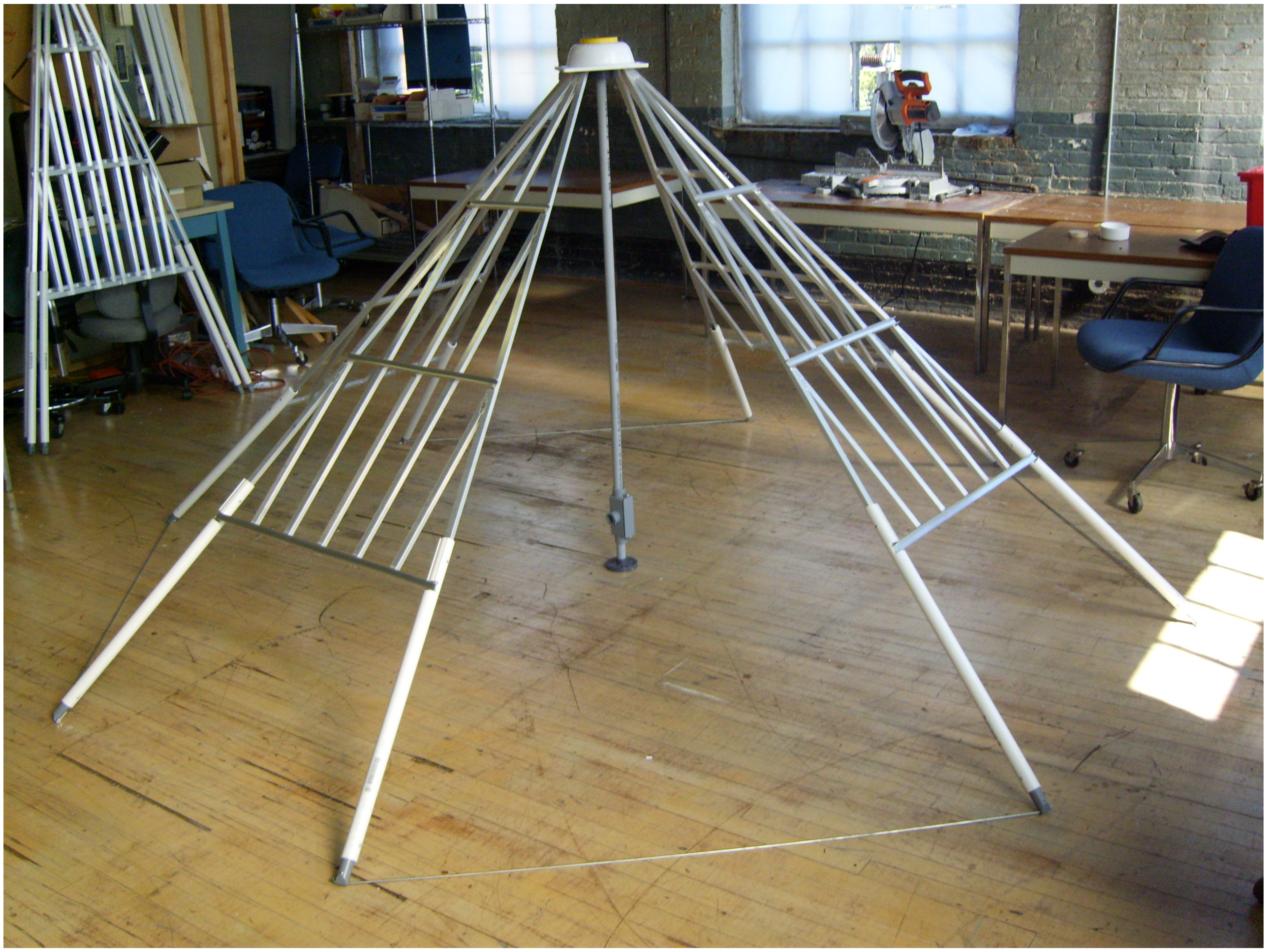

Fig. 2. Photograph of a modified Screen Tied Fork prototype constructed by Burns Industries.

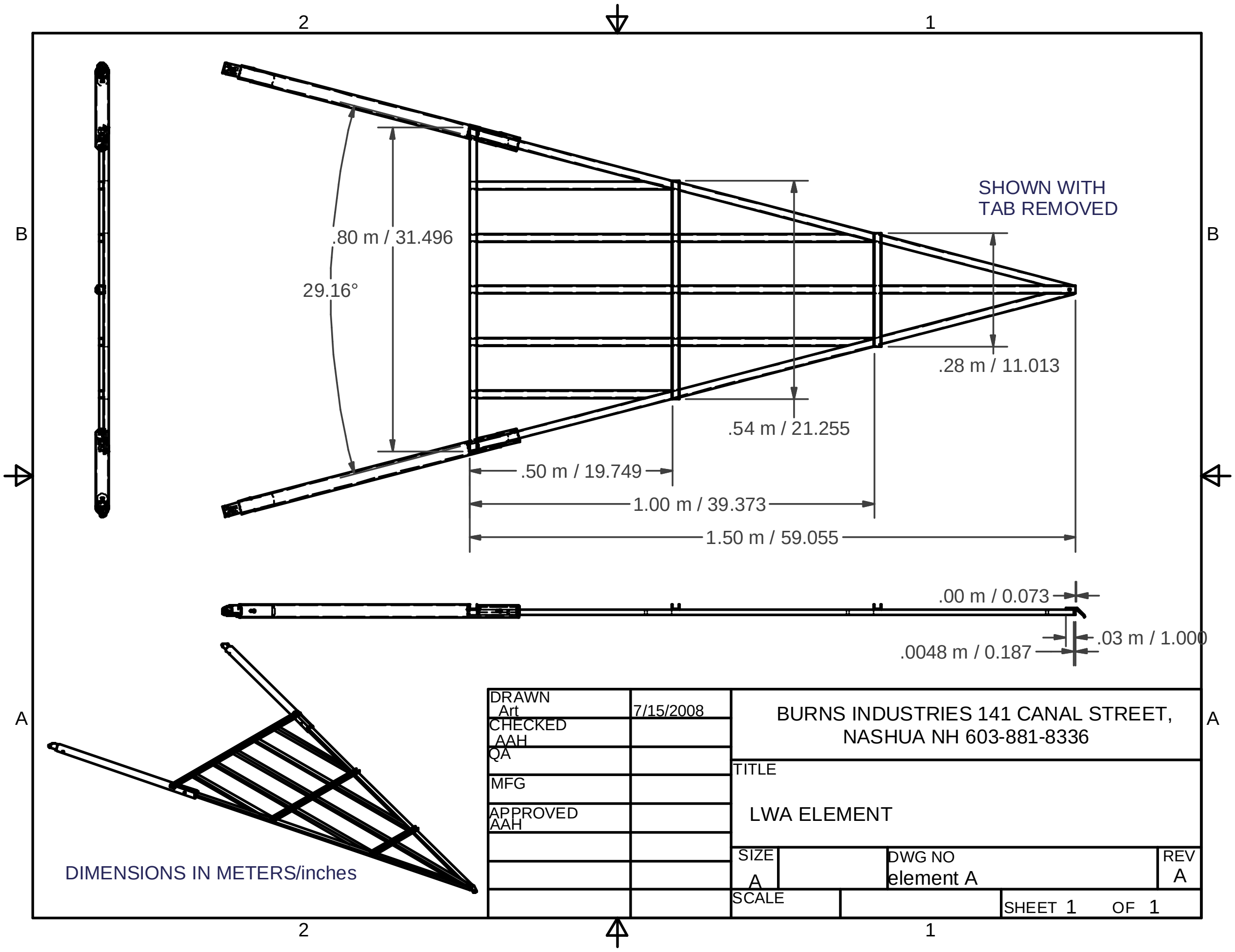

Fig. 3. CAD drawing of a Screen Tied Fork prototype element constructed by Burns Industries.

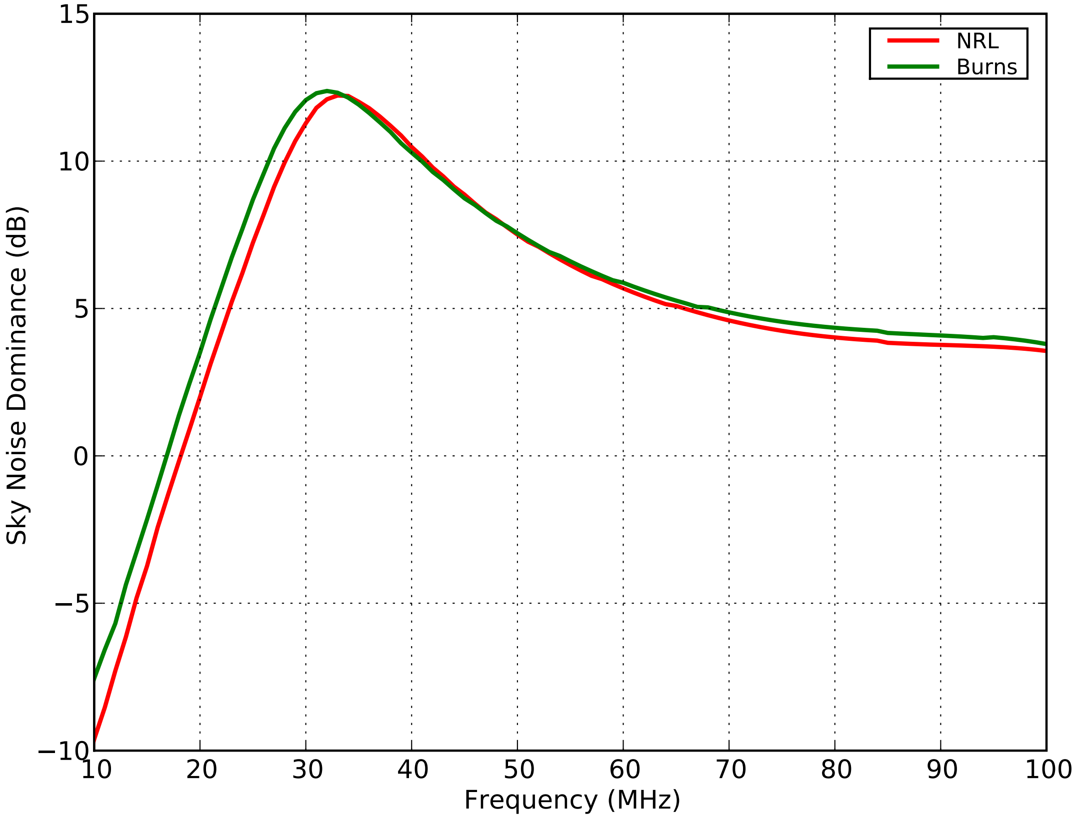

Fig. 4. Simulated sky noise dominances for the NRL and Burns Industries Screen Tied Fork prototypes.

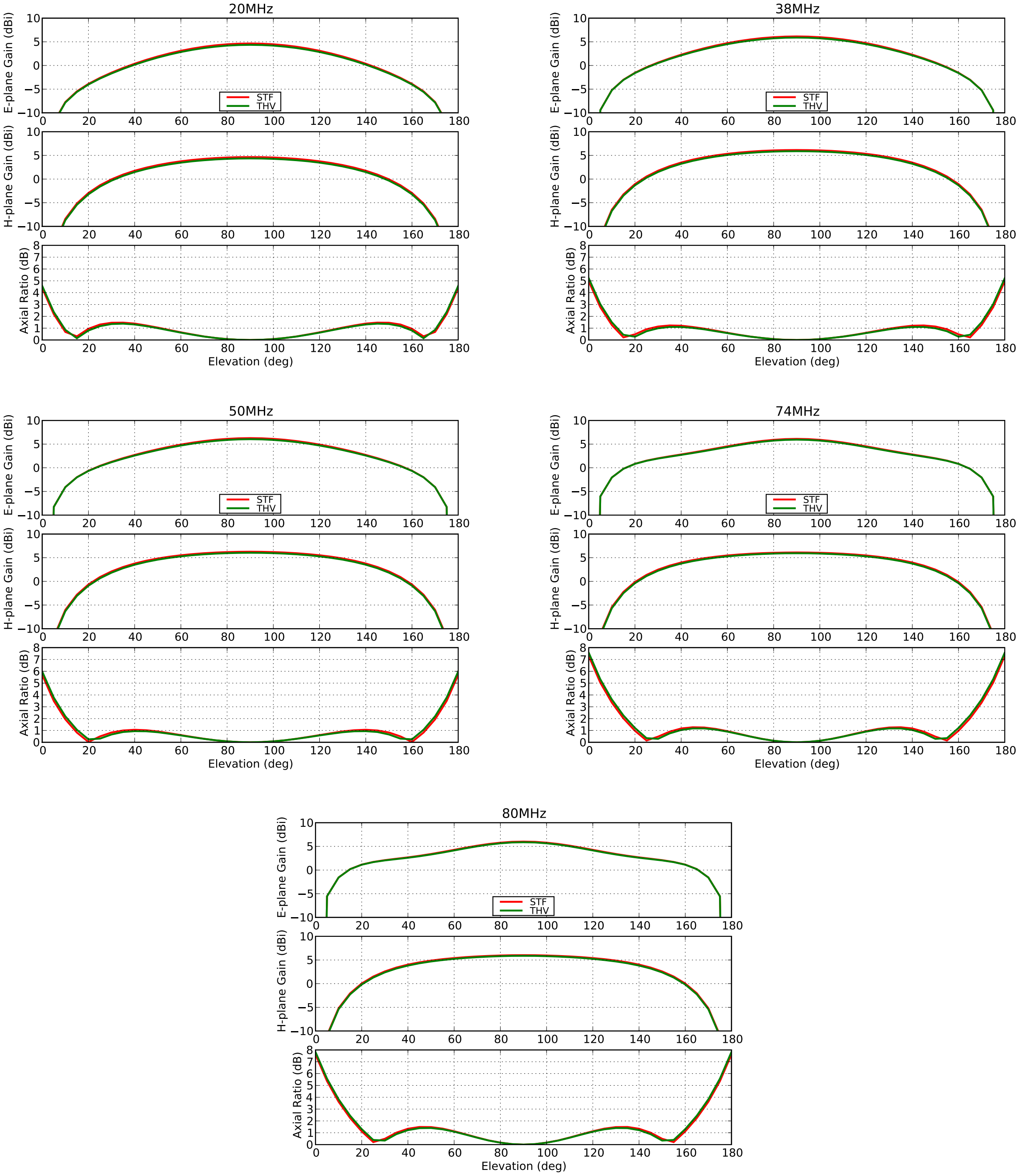

Fig. 5. Simulated beam patterns for the NRL and Burns Industries Screen Tied Fork prototypes.

Comparison of Antenna Designs on Groundscreens for the Long Wavelength Array

Nagini Paravastu (NRL/ASEE), William Erickson (UMD), Brian Hicks (NRL)

October 29, 2007

Abstract

In this report, we compare six antenna design candidates for the first Long Wavelength Array station – the single wire inverted-V antenna, the scaled MWA bowtie antenna, the Burns dipole antenna, the tied fork antenna, the filled fork antenna, and the big blade antenna. We provide simulated beam pattern and axial ratio plots, as well as plots of sky noise dominances achieved when each of these antennas is paired with a Hicks active balun, the baseline active balun for the LWA. In addition, we explore the effects on sky noise dominance for each of these antennas if the input impedance of the active balun were to be increased from the current 100Ω design by taking into account the higher input impedance as well as the anticipated increase in balun noise temperature. All antennas in this report were simulated on 3mx3m ground screens sitting on Earth ground.

I. INTRODUCTION

Over the past several months, work has been progressing on finalizing an antenna design for the first Long Wavelength Array Station, LWA-1. Simulations, prototyping and field measurements have been used to narrow the list of possibilities down to a few likely candidates. Recent field testing done on antenna prototypes included impedance measurements in wet and dry ground conditions, as well as over ground screens [1]. This work lead to the finding that antenna properties vary dramatically with changing ground conditions, but can be stabilized with the use of ground screens. Furthermore, it was found that a small, square ground screen, approximately the size of the footprint of the antenna support frame, would be sufficient for this purpose.

A report recently produced by A. Kerkhoff provides an initial comparison of LWA antenna candidates based on simulations over a ground screen of infinite extent [2]. We go a step further in this report by exploring antenna properties over a small ground screen on Earth ground to more closely reflect the likely ground conditions for an LWA station. All simulations were performed in NEC4. A dielectric constant, ϵ_r, of 13 and a conductivity, σ, of 0.005 S/m were assumed for the Earth ground properties, and 3mx3m ground screens were used in all simulations. ***It is important to note that as in [2], all results in this document are based purely on simulations. Impedance measurements recently performed in the field on antenna prototypes disagree significantly with these simulations. The cause of this disagreement must be determined and corrected before any final design decisions can be made on the LWA antenna.***

This is the first in a series of reports that will compare the performance of the leading antenna designs for LWA-1 – the big blade, the Burns, and the tied fork – over ground screens. In addition, we include three other designs – an inverted-V antenna similar to that being used as the low-band antenna in the LOFAR project, a version of the MWA antenna that has been scaled to work at LWA frequencies, and a filled fork antenna made by welding a metal mesh material to the tied fork antenna element frame. Three follow-on reports are planned, the first of which will detail drift scans and sky noise dominance measurements recently done at the LWDA site on prototypes of many of the antennas described in this report. The second will compare antenna impedance measurements done in the field on antenna prototypes to simulations. The third will address collecting area, sensitivity, and beam pattern as a function of ground screen size.

Section I-A defines the metrics by which the antennas are compared in this report. Sections II – VII contain photographs and descriptions of each antenna, as well as plots and charts of each metric. Section VIII contains plots directly comparing all the antenna candidates and some conclusions.

A. Description of Metrics

Simulated beam patterns and axial ratios, and sky noise dominance will be the primary metrics focused upon in this report. The simulated E- and H- plane beam patterns and axial ratio, $AR(\theta)$, are plotted for each antenna at 20MHz, 38MHz, 50MHz, 74MHz, and 80MHz. The axial ratio is given by equation 1,

$$AR(\theta) = |G_E(\theta) - G_H(\theta)| \tag{1}$$

where G_E and G_H are the E-plane and H-plane gains respectively, expressed in dB, and θ is the elevation angle. Charts are included for each antenna summarizing the E- and H-plane half power beamwidths and the maximum axial ratios for $20^\circ \leq \theta \leq 160^\circ$ at each of the frequencies for which beam patterns are shown. The half power beamwidth is given by equation 2,

$$HPBW = 2(90^\circ - \theta|_{G(\theta=90^\circ)-3dB}) \tag{2}$$

where θ is the elevation angle and $G(\theta)$ is the power gain in either the E- or the H-plane.

The sky noise dominance, D, is also plotted for each antenna for different noise temperatures and input impedances. The Hicks balun, the baseline active balun for the LWA, has a noise temperature, T_{balun}, of 250K and an input impedance, Z_{balun}, of 100Ω [3]. Improving the sky noise dominance by increasing the input impedance of the LWA active balun has recently been under consideration, and is investigated in this report. A higher balun input impedance can be realized by placing impedance transformers at the balun inputs. However, this would also result in the unfortunate side effect of a higher balun noise temperature because of transformer loss. Impedance transformers currently available for purchase have minimum loss values of 0.6dB at LWA frequencies [4]. Using these transformers in the Hicks balun would translate to an increase in noise temperature of at least 80K. We assume a conservative noise temperature increase of 100K in our calculations.

In this report, we compare the sky noise dominance characteristics of each antenna when combined with the baseline Hicks balun ($T_{balun} = 250K$, $Z_{balun} = 100\Omega$), higher impedance baluns ($T_{balun} = 250K$, $Z_{balun} = 100\Omega, 200\Omega, 400\Omega$), and higher noise temperature/higher impedance baluns ($T_{balun} = 350K$, $Z_{balun} = 100\Omega, 200\Omega, 400\Omega$). We also include charts indicating the 0dB, 3dB and 6dB frequency ranges for each of these cases.

The sky noise dominance is defined by equation 3.

$$D = \frac{T_{antenna}}{T_{balun}} \tag{3}$$

$T_{antenna}$ is given by equation 4,

$$T_{antenna} = T_{sky}\frac{(1 - |\Gamma|^2)}{L_g} \tag{4}$$

where T_{sky} is the Galactic noise temperature calculated using the Cane model, T_{balun} is the active balun noise temperature, $(1 - |\Gamma|^2)$ is the simulated impedance mismatch efficiency, and L_g is the simulated ground loss factor [5].

II. THE INVERTED-V ANTENNA

The first antenna considered in this report is the inverted-V dipole antenna. Each element in this antenna consists of a single wire, drooped $45°$ from horizontal. The feed point stands 1.5m off the ground. The antenna is similar to the LOFAR low-band antenna, designed to work in the 30 – 80 MHz frequency band. Further details on the dimensions of the inverted-V antenna are given in the Appendix.

Figure 1 shows the inverted-V antenna model as it was simulated in NEC4 over a 3mx3m ground screen. A photograph of LOFAR inverted-V antennas are shown in Figure 2. Figure 3 shows plots of sky noise dominance, and Table I gives the 0dB, 3dB, and 6dB frequency ranges for all of the balun noise temperature and input impedance combinations simulated. Figures 4 – 8 show the E- and H-plane beam patterns and axial ratios for five frequencies across the LWA frequency band. Half power beamwidths and maximum axial ratios at all of these frequencies are summarized in Tables II and III.

When paired with the baseline Hicks balun ($T_{balun} = 250K$, $Z_{balun} = 100\Omega$), the inverted V antenna exhibits 6dB sky noise dominance bandwidth over the 39MHz–57MHz frequency band – much less than what is desired for the LWA. Simulations show, however, that a higher balun input impedance improves the impedance mismatch efficiency between the antenna and balun, thereby increasing the range of frequencies over which the antenna and balun are sky noise dominated. For balun input impedances of 200Ω and 400Ω, the 6dB bandwidths increase significantly. This, however, assumes that the balun noise temperature stays the same with the increase in balun input impedance, which in reality, is not the case. Taking into account the $\sim 100K$ increase in balun noise temperature ($T_{balun} = 350K$), the 6dB bandwidths for the $Z_{balun} = 200\Omega$ and $Z_{balun} = 400\Omega$ cases are comparable to the bandwidth originally achieved with the baseline Hicks balun. These calculations therefore show that the bandwidth that is gained by increasing the balun input impedance is lost because of the resulting higher noise temperature.

The beam patterns of the inverted-V antenna maintain a relatively constant shape at lower frequencies, and then start widening in the H-plane at higher frequencies. Beam patterns at all frequencies exhibit nulls at the horizon, which results from the use of small ground screens over lossy ground.

TABLE I

FREQUENCY RANGES (IN MHZ) OVER WHICH THE INVERTED-V ANTENNA ACHIEVES 0DB, 3DB AND 6DB SKY NOISE DOMINANCES (D) FOR DIFFERENT BALUN INPUT IMPEDANCES (Z_{balun}) AND NOISE TEMPERATURES (T_{preamp})

	$T_{preamp} = 250K$			$T_{preamp} = 350K$		
	$D > 0dB$	$D > 3dB$	$D > 6dB$	$D > 0dB$	$D > 3dB$	$D > 6dB$
$Z_{preamp} = 100\Omega$	33-79	36-65	39-57			
$Z_{preamp} = 200\Omega$	30-95	34-76	38-62	32-85	36-69	40-57
$Z_{preamp} = 400\Omega$	28-98	33-90	39-70	30-98	36-80	43-61

TABLE II

E- AND H-PLANE HALF POWER BEAMWIDTHS AT DIFFERENT FREQUENCIES FOR THE INVERTED-V ANTENNA

Frequency (MHz)	E-plane HPBW (deg)	H-plane HPBW (deg)
20	80	100
38	80	100
50	80	100
74	80	120
80	80	120

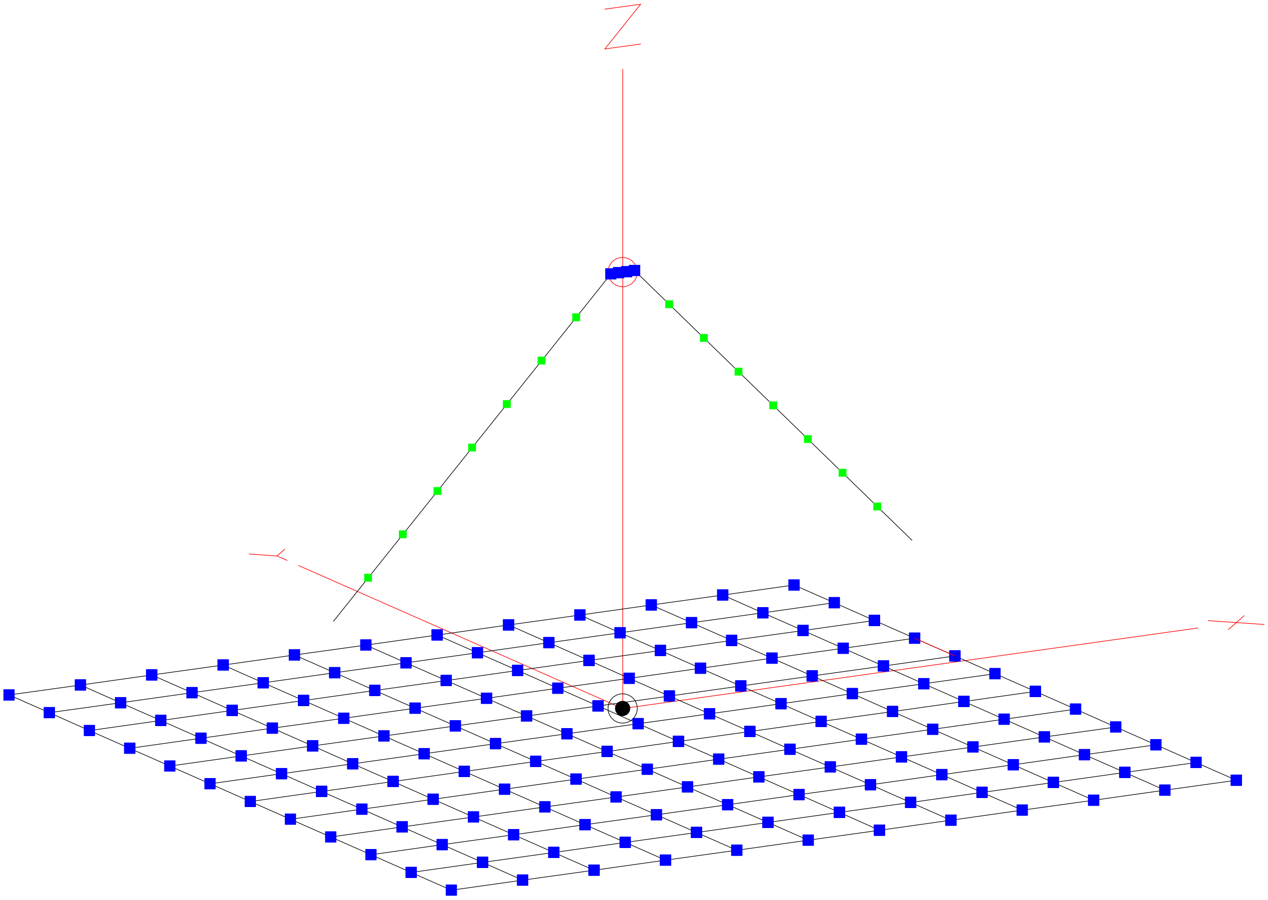

Fig. 1. The NEC4 model of the inverted-V antenna over a 3mx3m ground screen.

TABLE III

MAXIMUM AXIAL RATIO FOR $20^\circ \leq \theta \leq 160^\circ$ FOR THE INVERTED-V ANTENNA

Frequency (MHz)	Maximum Axial Ratio (dB)
20	1.82
38	1.73
50	1.67
74	2.19
80	2.52

Fig. 2. A photograph of LOFAR low-band antennas similar to the inverted-V antenna modelled in Figure 1.

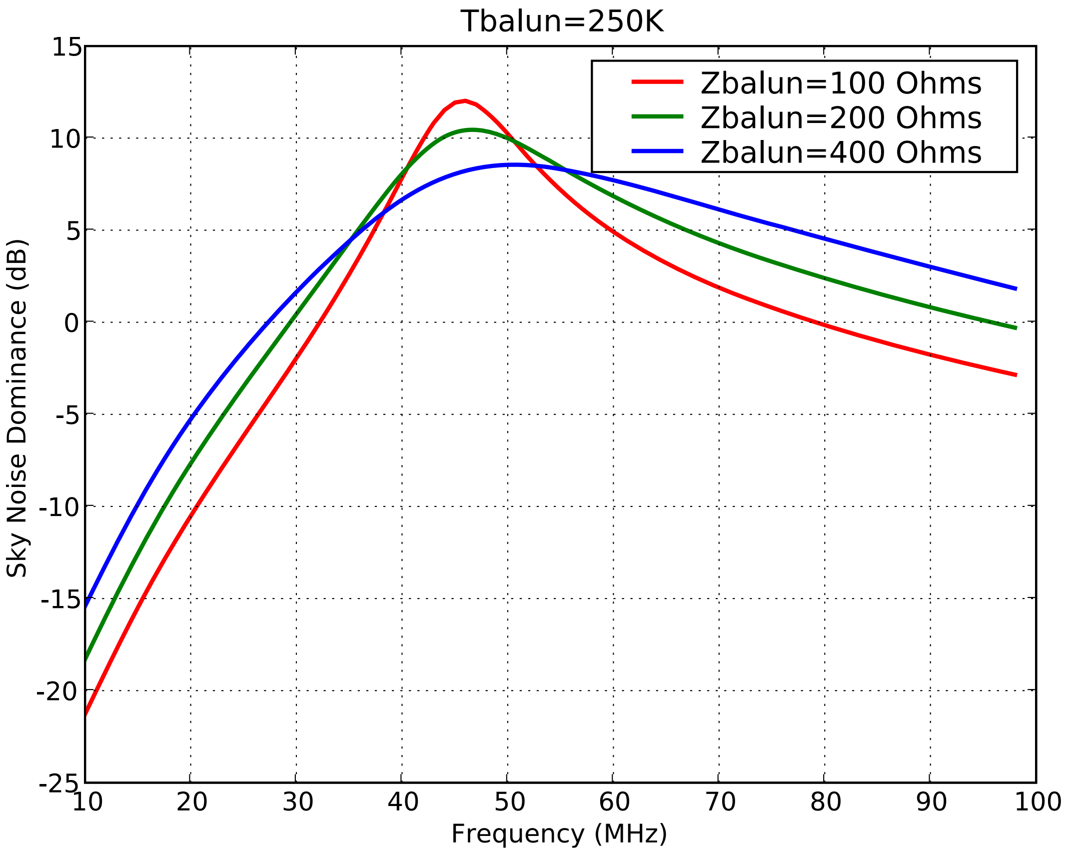

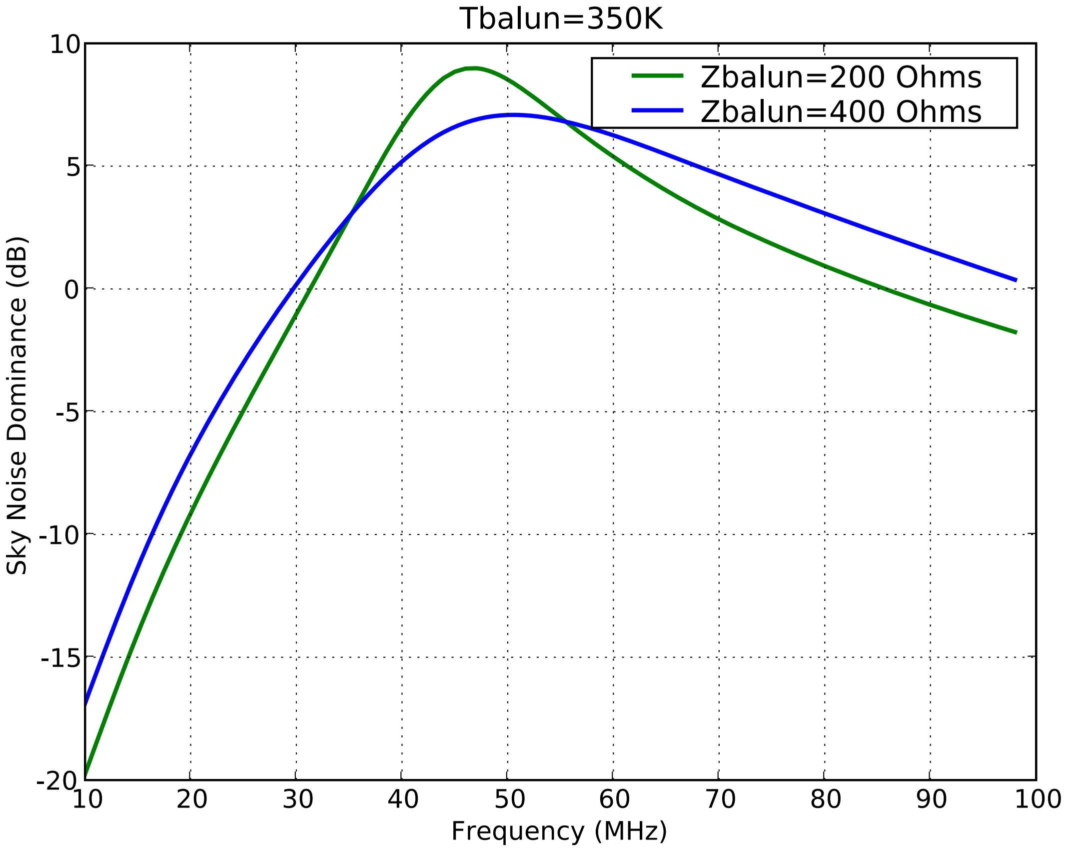

Fig. 3. Simulated sky noise dominance for the inverted-V antenna for a 250K noise temperature balun with different input impedances (top). Simulated sky noise dominance for the inverted-V antenna for a 350K noise temperature balun with different input impedances (bottom).

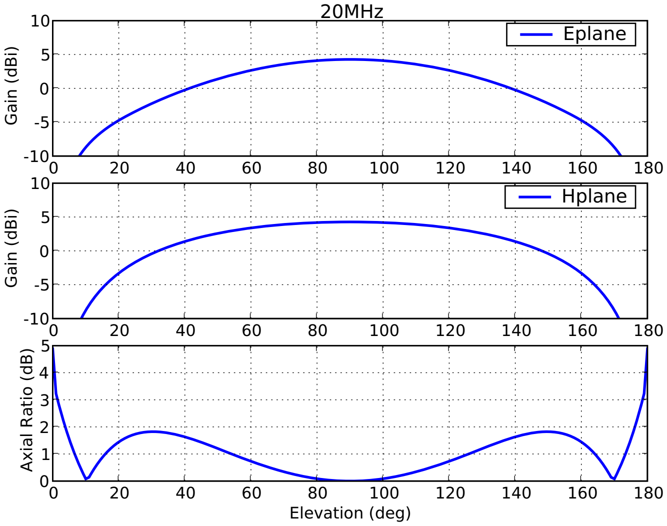

Fig. 4. E- and H- plane beam pattern slices and axial ratios of the inverted-V antenna at 20 MHz.

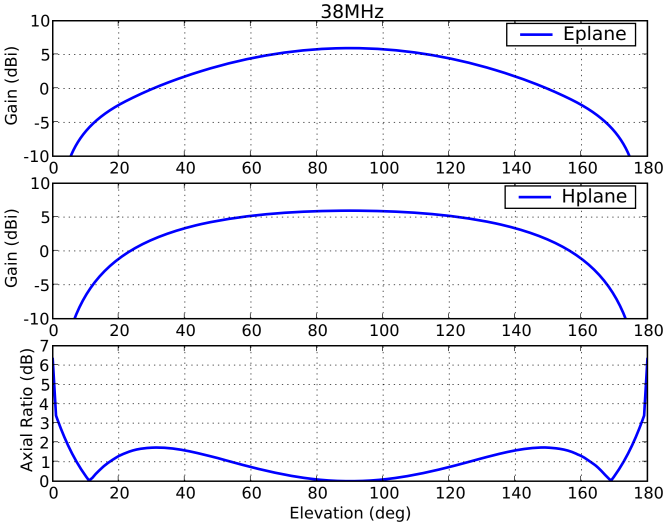

Fig. 5. E- and H- plane beam pattern slices and axial ratios of the inverted-V antenna at 38 MHz.

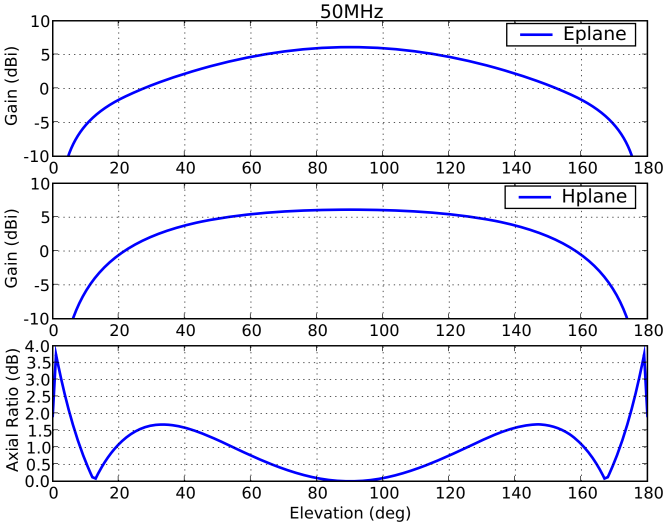

Fig. 6. E- and H- plane beam pattern slices and axial ratios of the inverted-V antenna at 50 MHz.

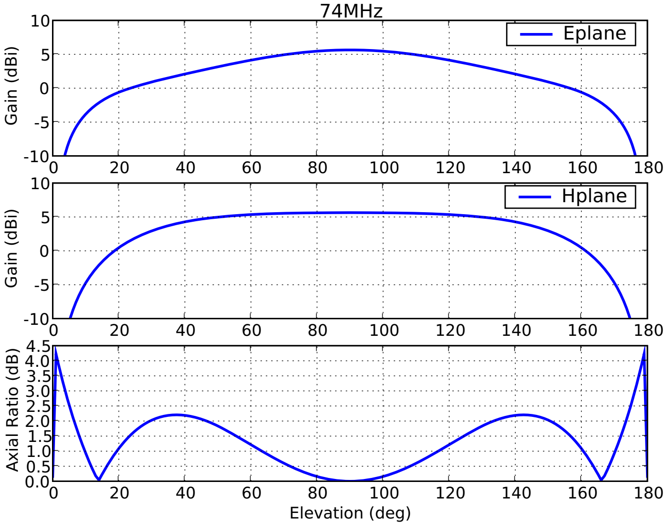

Fig. 7. E- and H- plane beam pattern slices and axial ratios of the inverted-V antenna at 74 MHz.

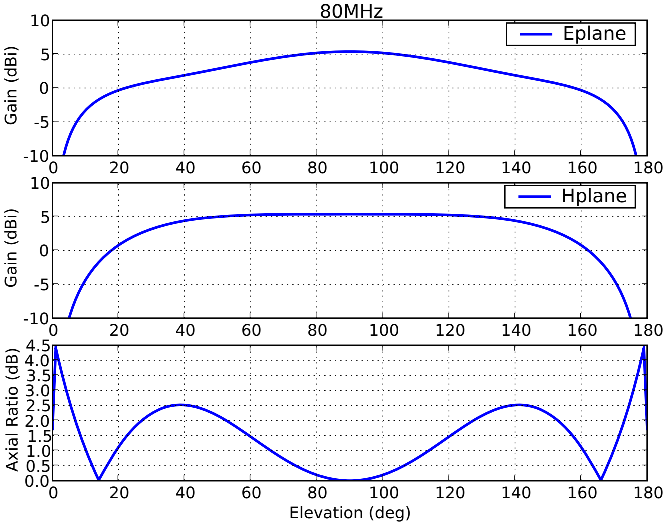

Fig. 8. E- and H- plane beam pattern slices and axial ratios of the inverted-V antenna at 80 MHz.

III. THE BOWTIE ANTENNA

The next antenna considered in this report is a bowtie antenna. Each element in this antenna is triangular in shape, and oriented perpendicular to the ground. The feed point stands 1.26m off the ground. This antenna is the MWA antenna, scaled up in size by a factor of 3, as was presented in [2]. Further details on the dimensions of the bowtie antenna are given in the Appendix.

Figure 9 shows the bowtie antenna model as it was simulated in NEC4 over a 3mx3m ground screen. A photograph of an MWA antenna is shown in Figure 10. Figure 11 shows plots of sky noise dominance, and Table IV gives the 0dB, 3dB, and 6dB frequency ranges for all of the balun noise temperature and input impedance combinations simulated. Figures 12 – 16 show the E- and H-plane beam patterns and axial ratios for five frequencies across the LWA frequency band. Half power beamwidths and maximum axial ratios at all of these frequencies are summarized in Tables V and VI.

When paired with the baseline Hicks balun ($Z_{balun} = 100\Omega, T_{balun} = 250K$), the bowtie antenna has a 6dB sky noise dominance frequency range of 22MHz–72MHz, which is a significant improvement over the inverted-V antenna. Increasing the balun input impedance and taking into account the higher noise temperature results in similar 6dB bandwidths. There is therefore no advantage gained by increasing the balun input impedance for the bowtie antenna.

The beam patterns and axial ratios reflect the greatest disadvantage offered by the bowtie antenna. The E-plane beamwidths of the bowtie antenna are significantly smaller than the corresponding H-plane beamwidths at all frequencies across the LWA frequency band, resulting in high axial ratios. Good beam pattern symmetry is a requirement of the LWA for forming circular polarization. The qualities of the bowtie antenna beam patterns are therefore not favorable for this project.

TABLE IV

FREQUENCY RANGES (IN MHZ) OVER WHICH THE BOWTIE ANTENNA ACHIEVES 0DB, 3DB AND 6DB SKY NOISE DOMINANCES (D) FOR DIFFERENT BALUN INPUT IMPEDANCES (Z_{balun}) AND NOISE TEMPERATURES (T_{preamp})

	$T_{preamp} = 250K$			$T_{preamp} = 350K$		
	$D > 0dB$	$D > 3dB$	$D > 6dB$	$D > 0dB$	$D > 3dB$	$D > 6dB$
$Z_{preamp} = 100\Omega$	16-100	19-100	22-72			
$Z_{preamp} = 200\Omega$	14-100	17-100	21-83	16-100	19-92	23-73
$Z_{preamp} = 400\Omega$	13-100	18-94	25-85	16-100	21-91	29-77

TABLE V

E- AND H-PLANE HALF POWER BEAMWIDTHS AT DIFFERENT FREQUENCIES FOR THE BOWTIE ANTENNA

Frequency (MHz)	E-plane HPBW (deg)	H-plane HPBW (deg)
20	60	100
38	70	110
50	80	120
74	90	140
80	90	140

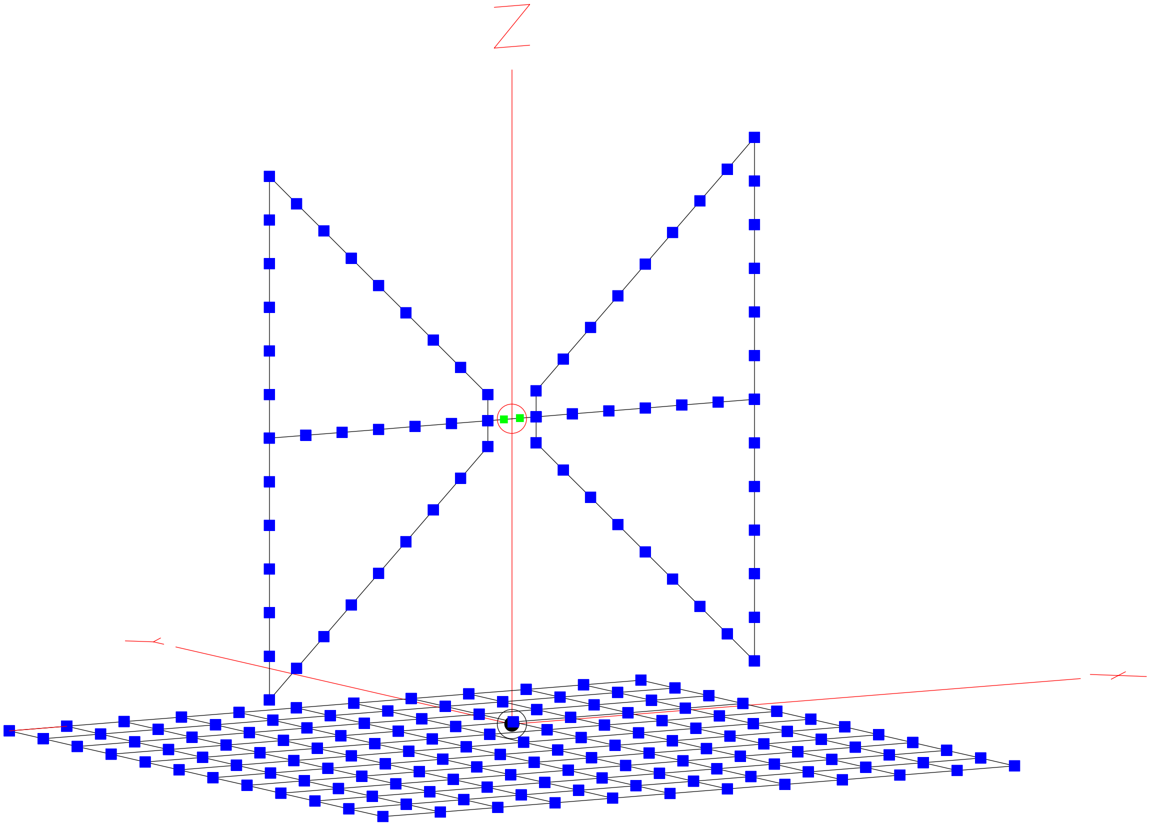

Fig. 9. The NEC4 model of the bowtie antenna over a 3mx3m ground screen. This antenna is the MWA antenna scaled up in size by a factor of 3.

TABLE VI

MAXIMUM AXIAL RATIO FOR $20^\circ \leq \theta \leq 160^\circ$ FOR THE BOWTIE ANTENNA

Frequency (MHz)	Maximum Axial Ratio (dB)
20	6.01
38	6.40
50	3.90
74	12.80
80	13.34

Fig. 10. A photograph of an MWA antenna. The bowtie antenna modelled in Figure 9 is this antenna scaled up in size by a factor of 3.

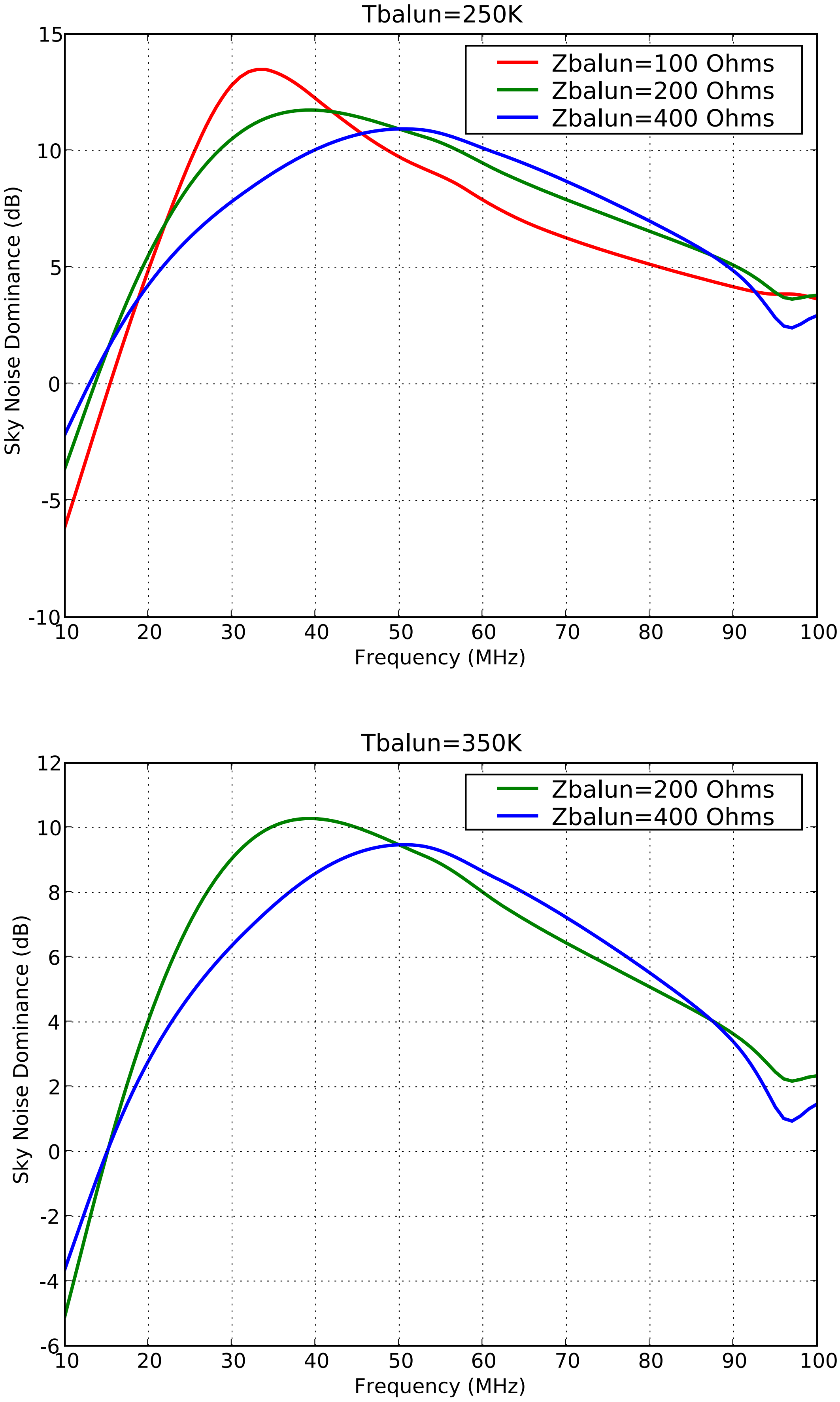

Fig. 11. Simulated sky noise dominance for the bowtie antenna for a 250K noise temperature balun with different input impedances (top). Simulated sky noise dominance for the bowtie antenna for a 350K noise temperature balun with different input impedances (bottom).

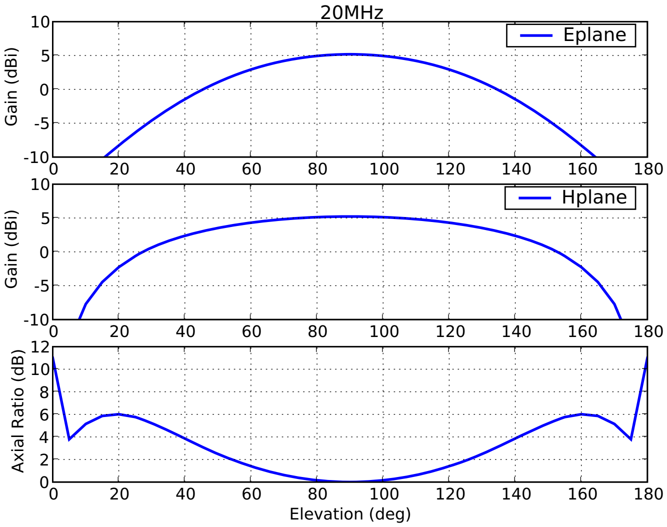

Fig. 12. E- and H- plane beam pattern slices and axial ratios of the bowtie antenna at 20 MHz.

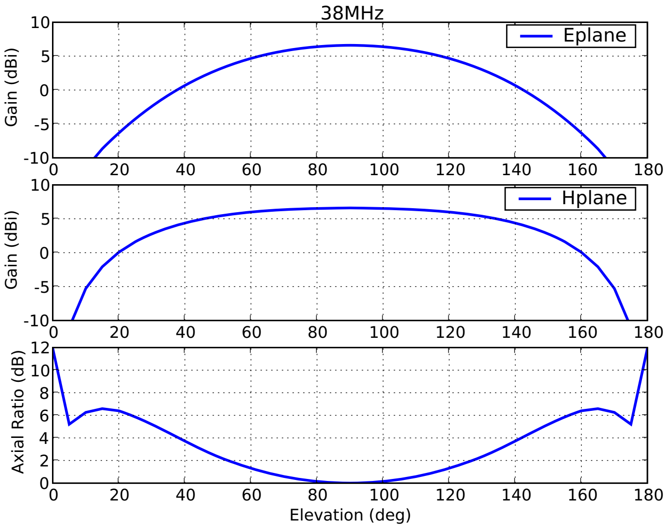

Fig. 13. E- and H- plane beam pattern slices and axial ratios of the bowtie antenna at 38 MHz.

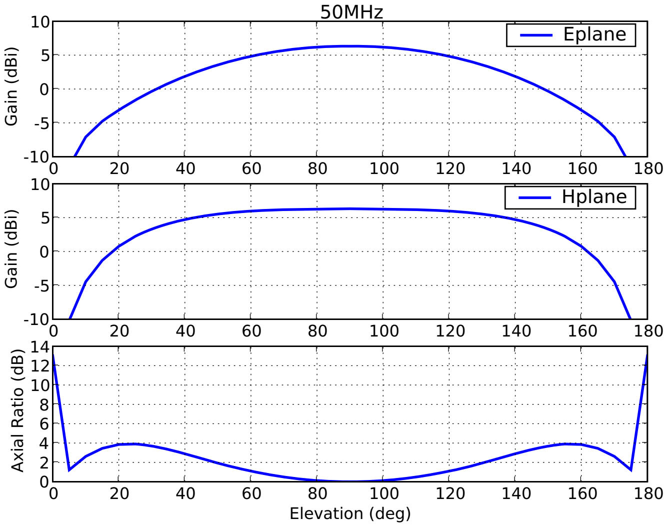

Fig. 14. E- and H- plane beam pattern slices and axial ratios of the bowtie antenna at 50 MHz.

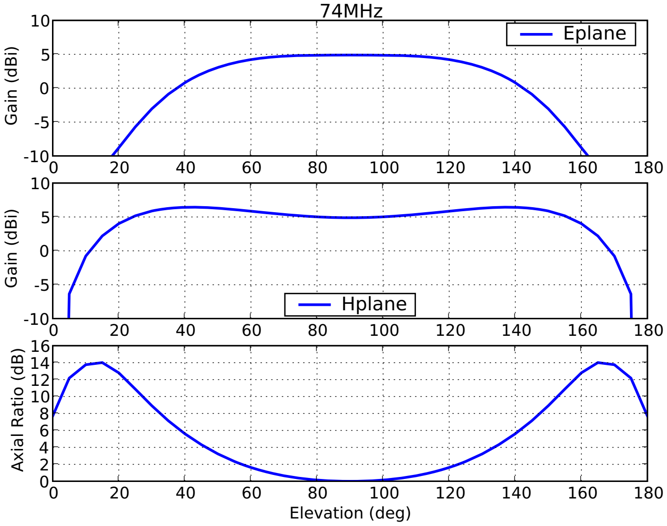

Fig. 15. E- and H- plane beam pattern slices and axial ratios of the bowtie antenna at 74 MHz.

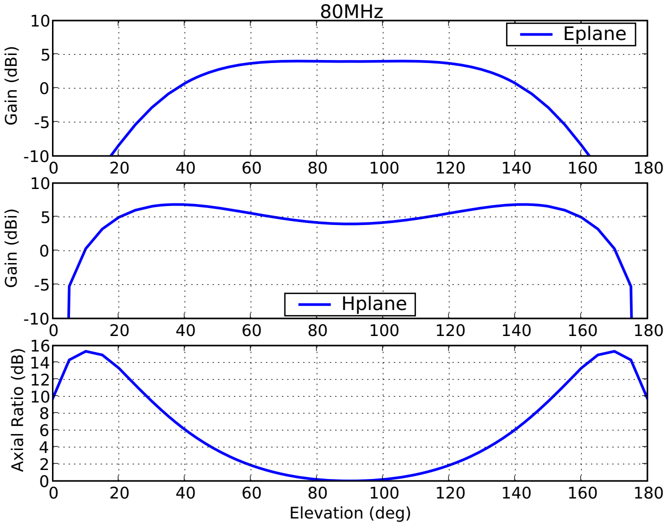

Fig. 16. E- and H- plane beam pattern slices and axial ratios of the bowtie antenna at 80 MHz.

IV. THE BURNS ANTENNA

This section focuses on the Burns antenna. This antenna was conceived of by Steve Burns of Burns Industries, Inc. and is meant to be a low cost substitute for the LWA baseline big blade antenna, which will be described in section VII [6]. In this design, strips of angled aluminum are used to make the outline shape of the big blade element. All elements are drooped 45° from horizontal, and the feed point stands 1.5m off the ground. Further details on the dimensions of the Burns antenna are given in the Appendix.

Figure 17 shows the Burns antenna model as it was simulated in NEC4 over a 3mx3m ground screen. A photograph of a prototype Burns antenna is shown in Figure 18. Figure 19 shows plots of sky noise dominance, and Table VII gives the 0dB, 3dB, and 6dB frequency ranges for all of the balun noise temperature and input impedance combinations simulated. Figures 20 – 24 show the E- and H-plane beam patterns and axial ratios for five frequencies across the LWA frequency band. Half power beamwidths and maximum axial ratios at all of these frequencies are summarized in Tables VIII and IX.

Pairing the Burns antenna with the baseline Hicks balun ($Z_{balun} = 100\Omega, T_{balun} = 250K$) results in a 23MHz–65MHz 6dB sky noise dominance frequency range. Although simply increasing the balun input impedance initially appears to improve this result, taking into account the higher balun noise temperature gives 6dB bandwidths similar to that originally obtained with the baseline Hicks balun. As with the inverted-V and bowtie antennas, simulations on the Burns antenna show that increasing the balun input impedance is not advantageous because of the unavoidable simultaneous increase in balun noise temperature.

Beam patterns of the Burns antenna maintain a consistent shape at lower frequencies, and then become wider in the E-plane at higher frequencies. The 74MHz and 80MHz patterns in particular show signs of developing sidelobes, but all beam patterns have horizon nulls at all frequencies because of the small ground screens.

TABLE VII

FREQUENCY RANGES (IN MHZ) OVER WHICH THE BURNS ANTENNA ACHIEVES 0DB, 3DB AND 6DB SKY NOISE DOMINANCES (D) FOR DIFFERENT BALUN INPUT IMPEDANCES (Z_{balun}) AND NOISE TEMPERATURES (T_{preamp}).

	$T_{preamp} = 250K$			$T_{preamp} = 350K$		
	$D > 0dB$	$D > 3dB$	$D > 6dB$	$D > 0dB$	$D > 3dB$	$D > 6dB$
$Z_{preamp} = 100\Omega$	18-98	20-98	23-65			
$Z_{preamp} = 200\Omega$	16-98	19-97	23-75	18-98	21-85	25-65
$Z_{preamp} = 400\Omega$	16-98	20-86	27-73	18-95	23-79	31-68

TABLE VIII

E- AND H-PLANE HALF POWER BEAMWIDTHS AT DIFFERENT FREQUENCIES FOR THE BURNS ANTENNA

Frequency (MHz)	E-plane HPBW (deg)	H-plane HPBW (deg)
20	80	100
38	90	100
50	100	100
74	120	100
80	120	100

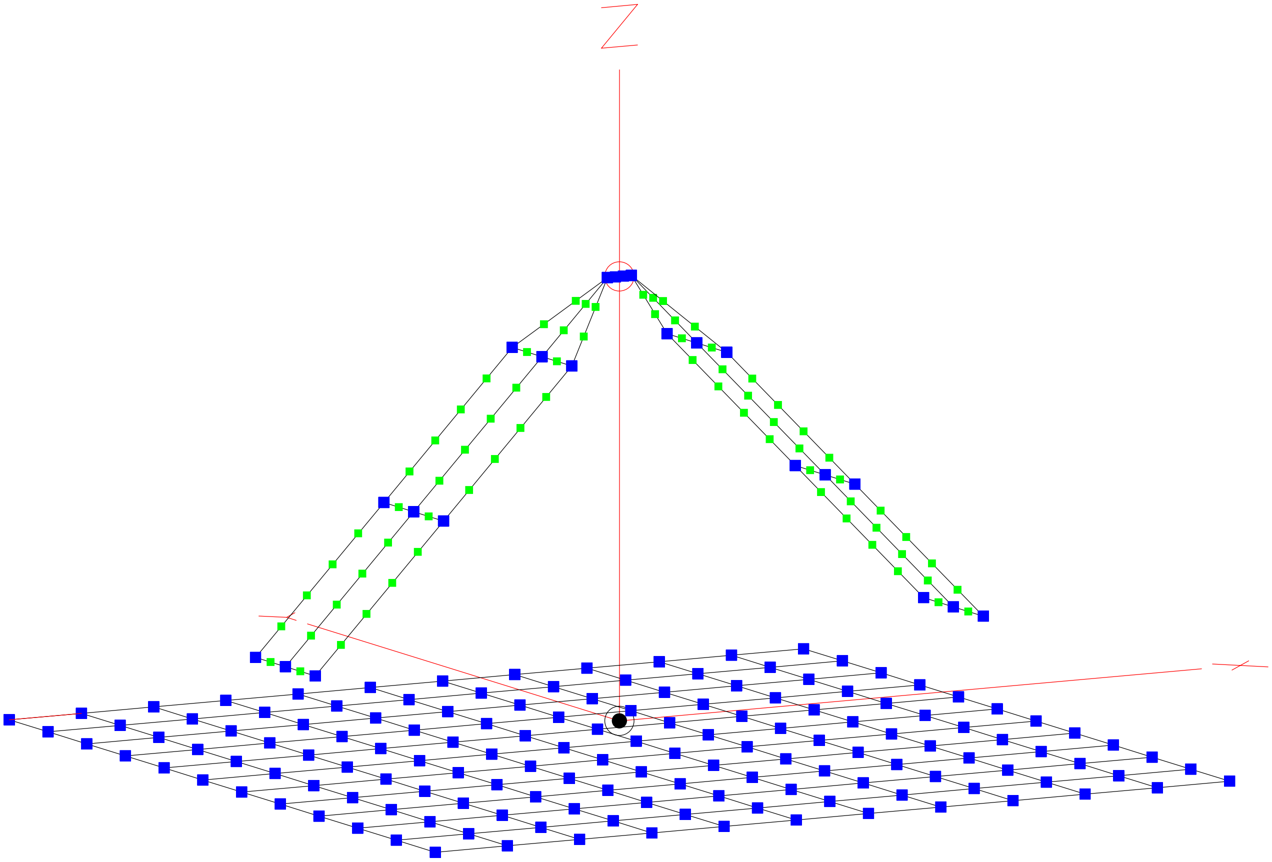

Fig. 17. The NEC4 model of the Burns antenna over a 3mx3m ground screen.

TABLE IX

Maximum Axial Ratio for $20^\circ \leq \theta \leq 160^\circ$ for the Burns Antenna

Frequency (MHz)	Maximum Axial Ratio (dB)
20	0.89
38	0.74
50	1.58
74	3.33
80	3.33

Fig. 18. A photograph of a Burns antenna prototype, modelled in Figure 17.

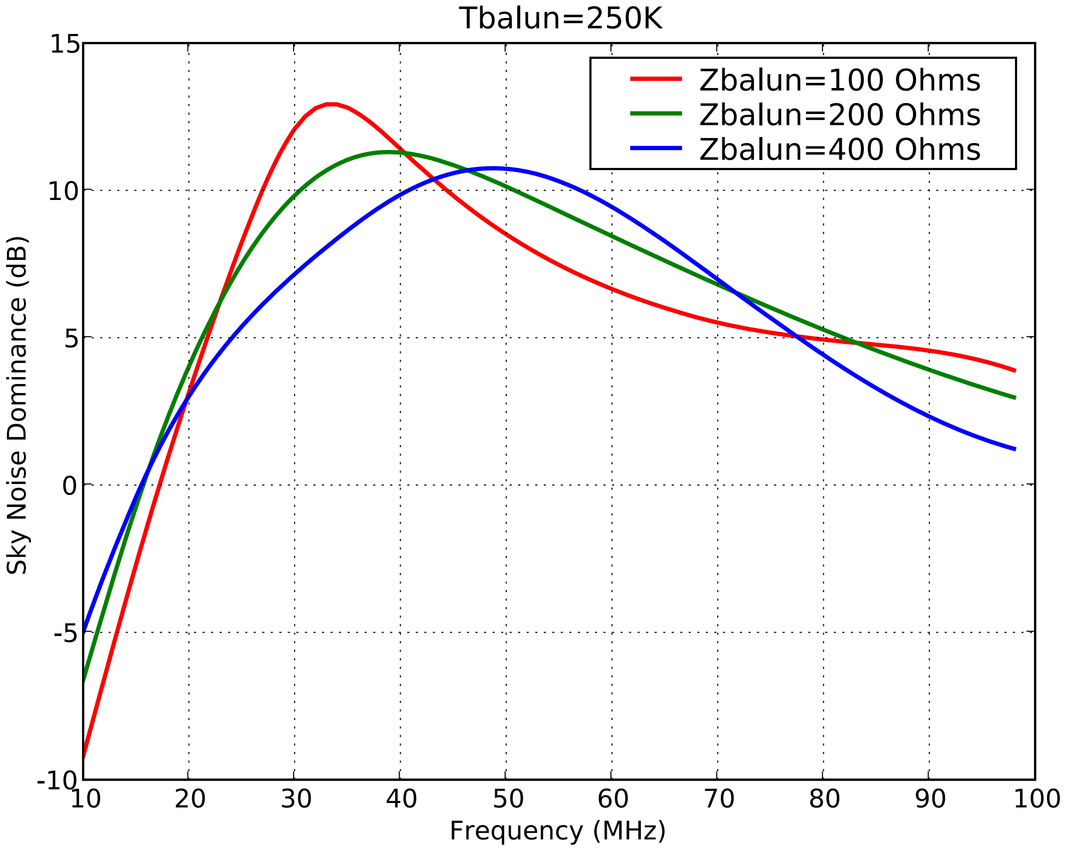

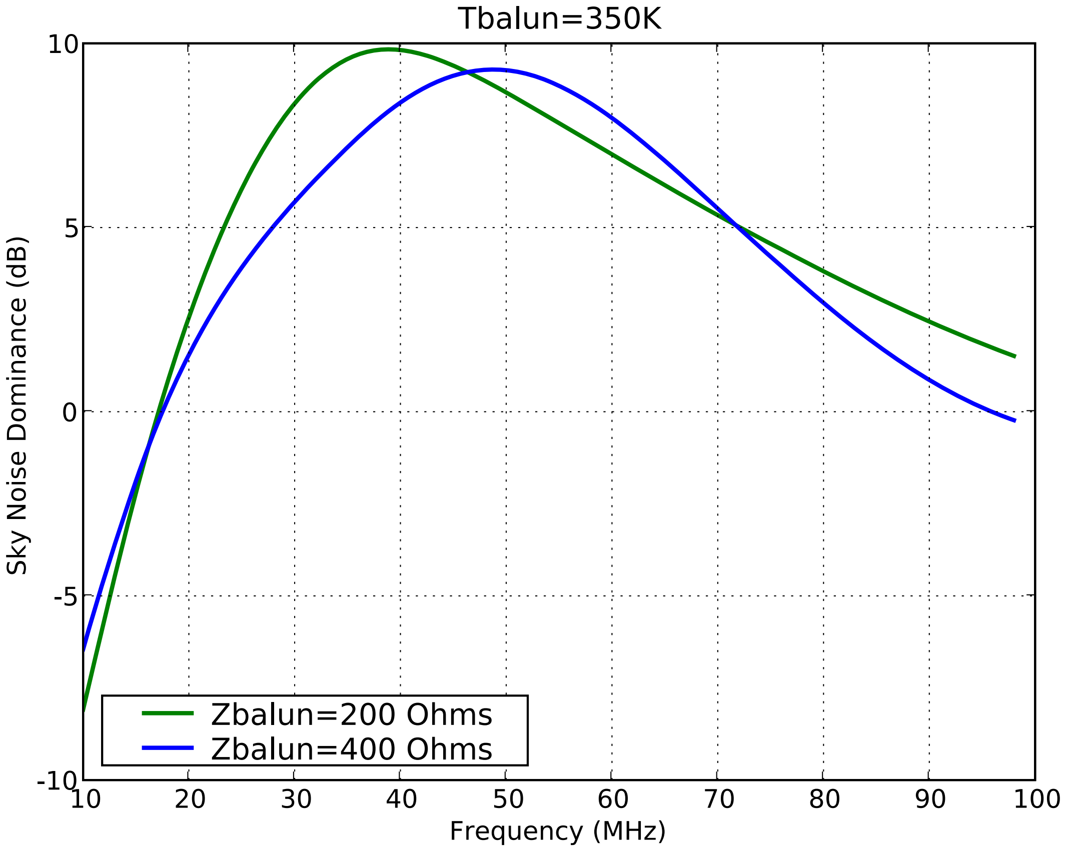

Fig. 19. Simulated sky noise dominance for the Burns antenna for a 250K noise temperature balun with different input impedances (top). Simulated sky noise dominance for the Burns antenna for a 350K noise temperature balun with different input impedances (bottom).

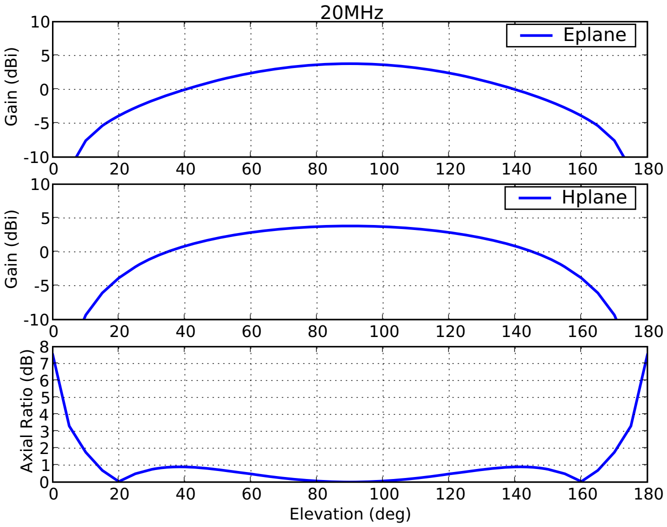

Fig. 20. E- and H- plane beam pattern slices and axial ratios of the Burns antenna at 20 MHz.

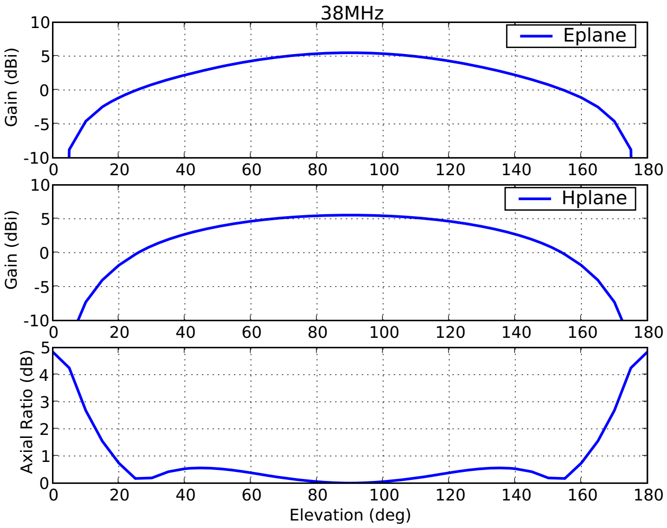

Fig. 21. E- and H- plane beam pattern slices and axial ratios of the Burns antenna at 38 MHz.

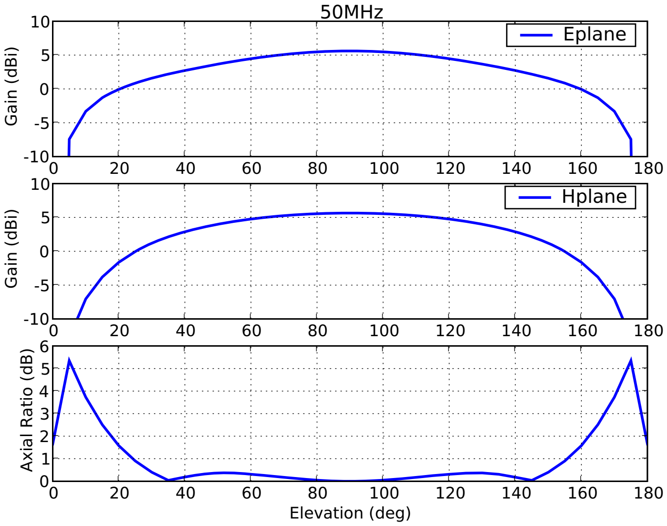

Fig. 22. E- and H- plane beam pattern slices and axial ratios of the Burns antenna at 50 MHz.

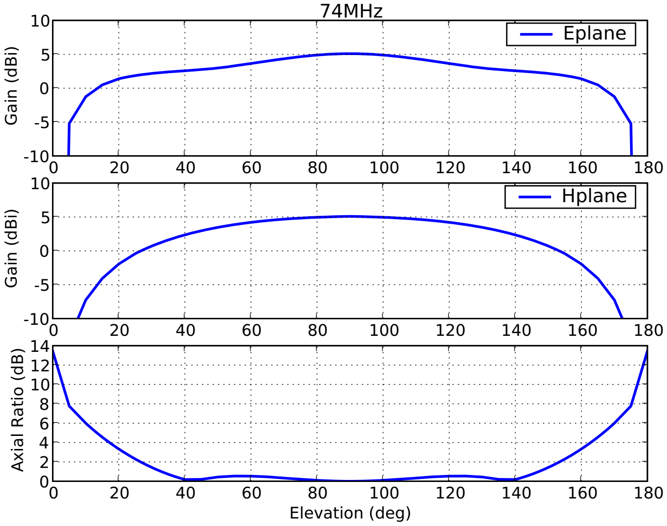

Fig. 23. E- and H- plane beam pattern slices and axial ratios of the Burns antenna at 74 MHz.

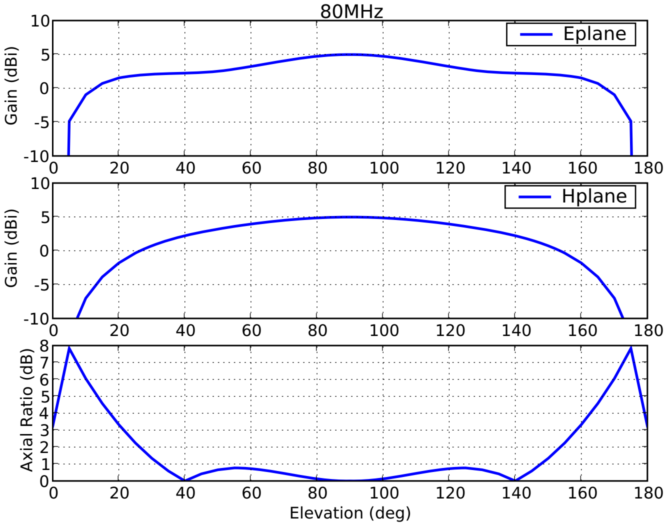

Fig. 24. E- and H- plane beam pattern slices and axial ratios of the Burns antenna at 80 MHz.

V. THE TIED FORK ANTENNA

This section focuses on the tied fork antenna. This antenna was originally simply called the fork antenna and was introduced in a previous LWA memo [7]. Like the Burns antenna in section IV, the tied fork antenna is meant to be a low cost substitute for the LWA baseline big blade antenna, which will be described in section VII. The elements in this antenna are also made of strips of angled aluminum. An additional 0.8m segment of angled aluminum has been added to the fork antenna design since its introduction to eliminate an extraneous 60MHz resonance that appeared in impedance measurements of the fork antenna prototype. All elements are drooped $45°$ from horizontal, and the feed point stands 1.5m off the ground. Further details on the dimensions of the tied fork antenna are given in the Appendix.

Figure 25 shows the tied fork antenna model as it was simulated in NEC4 over a 3mx3m ground screen. A photograph of a prototype tied fork antenna is shown in Figure 26. Figure 27 shows plots of sky noise dominance, and Table X gives the 0dB, 3dB, and 6dB frequency ranges for all of the balun noise temperature and input impedance combinations simulated. Figures 28 – 32 show the E- and H-plane beam patterns and axial ratios for five frequencies across the LWA frequency band. Half power beamwidths and maximum axial ratios at all of these frequencies are summarized in Tables XI and XII.

When the tied fork antenna is paired with the baseline Hicks balun ($Z_{balun} = 100\Omega, T_{balun} = 100K$) a minimum of 6dB sky noise dominance is achieved over the 24MHz–63MHz frequency band. A simple increase in balun input impedance from 100Ω to 200Ω would appear to improve the power coupling between antenna and balun, and increase the 6dB sky noise dominance bandwidth. However, as with the other antennas in this report, properly accounting for the increase in balun noise temperature with increasing balun input impedance results in little or no overall improvement in sky noise dominance bandwidth.

Tied fork antenna beam patterns exhibit qualities similar to those of the Burns antenna. Patterns maintain a fairly consistent shape at lower frequencies, with sidelobes forming at higher frequencies. Axial ratios for the tied fork antenna remain close to 1dB at all frequencies, indicating that the tied fork beam patterns have better E-/H-plane symmetry than the burns antenna, making it a more attractive candidate for the LWA.

TABLE X

FREQUENCY RANGES (IN MHZ) OVER WHICH THE TIED FORK ANTENNA ACHIEVES 0DB, 3DB AND 6DB SKY NOISE DOMINANCES (D) FOR DIFFERENT PREAMP INPUT IMPEDANCES (Z_{balun}) AND NOISE TEMPERATURES (T_{preamp}).

	$T_{preamp} = 250K$			$T_{preamp} = 350K$		
	$D > 0dB$	$D > 3dB$	$D > 6dB$	$D > 0dB$	$D > 3dB$	$D > 6dB$
$Z_{preamp} = 100\Omega$	18-100	21-100	24-63			
$Z_{preamp} = 200\Omega$	17-100	20-100	24-80	18-100	22-95	27-66
$Z_{preamp} = 400\Omega$	16-100	21-100	29-81	19-100	25-91	34-73

TABLE XI

E- AND H-PLANE HALF POWER BEAMWIDTHS AT DIFFERENT FREQUENCIES FOR THE TIED FORK ANTENNA

Frequency (MHz)	E-plane HPBW (deg)	H-plane HPBW (deg)
20	80	100
38	80	100
50	90	100
74	90	110
80	90	110

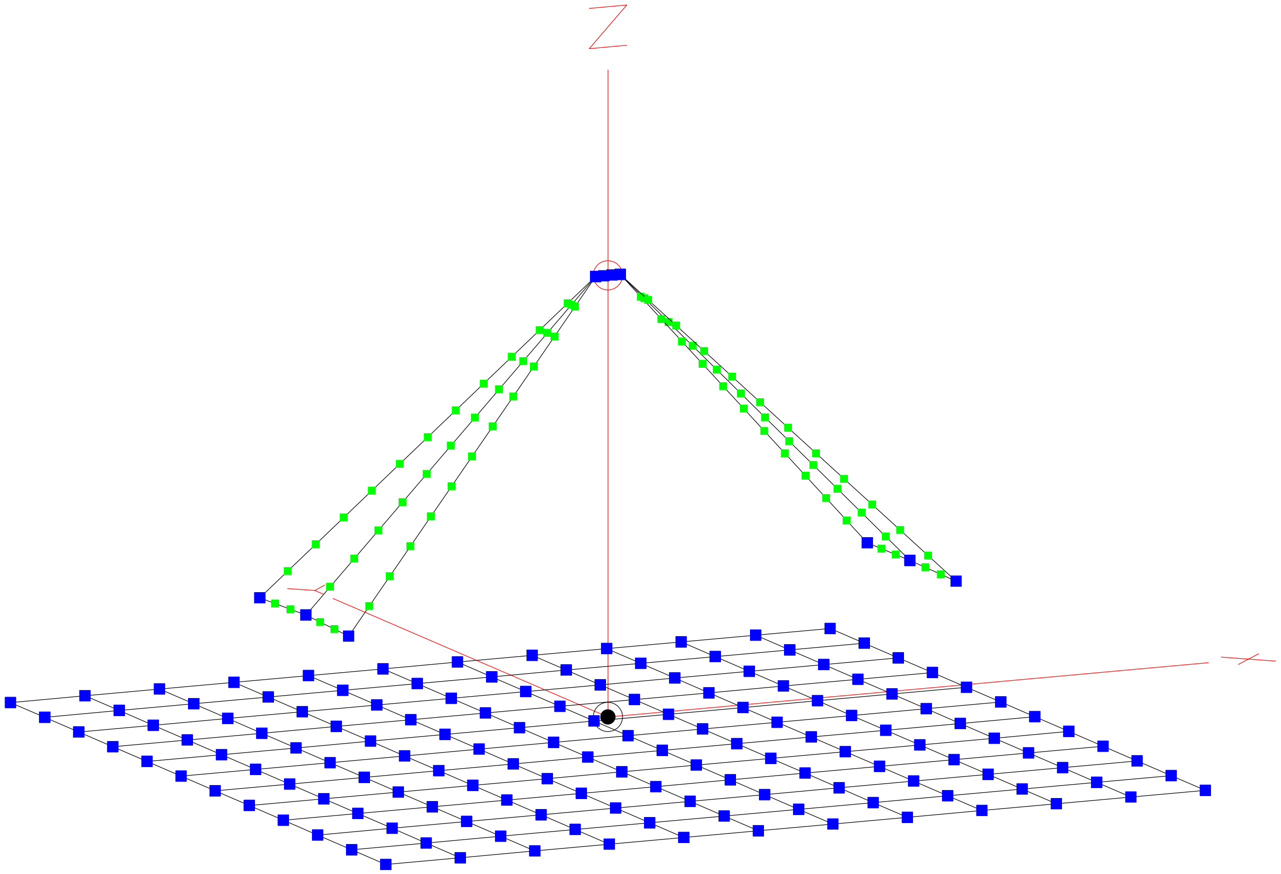

Fig. 25. The NEC4 model of the tied fork antenna over a 3mx3m ground screen.

TABLE XII

MAXIMUM AXIAL RATIO FOR $20^\circ \leq \theta \leq 160^\circ$ FOR THE TIED FORK ANTENNA

Frequency (MHz)	Maximum Axial Ratio (dB)
20	1.20
38	0.98
50	0.84
74	1.19
80	1.48

Fig. 26. A photograph a tied fork antenna prototype, modelled in Figure 25.

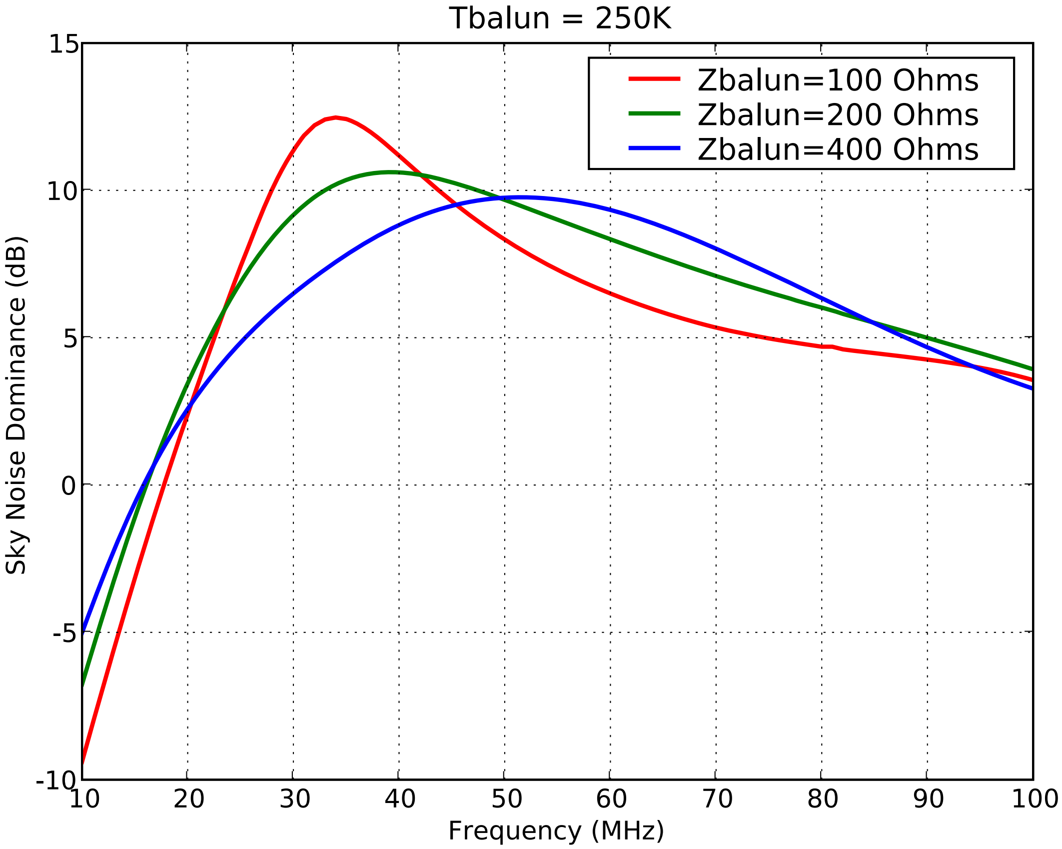

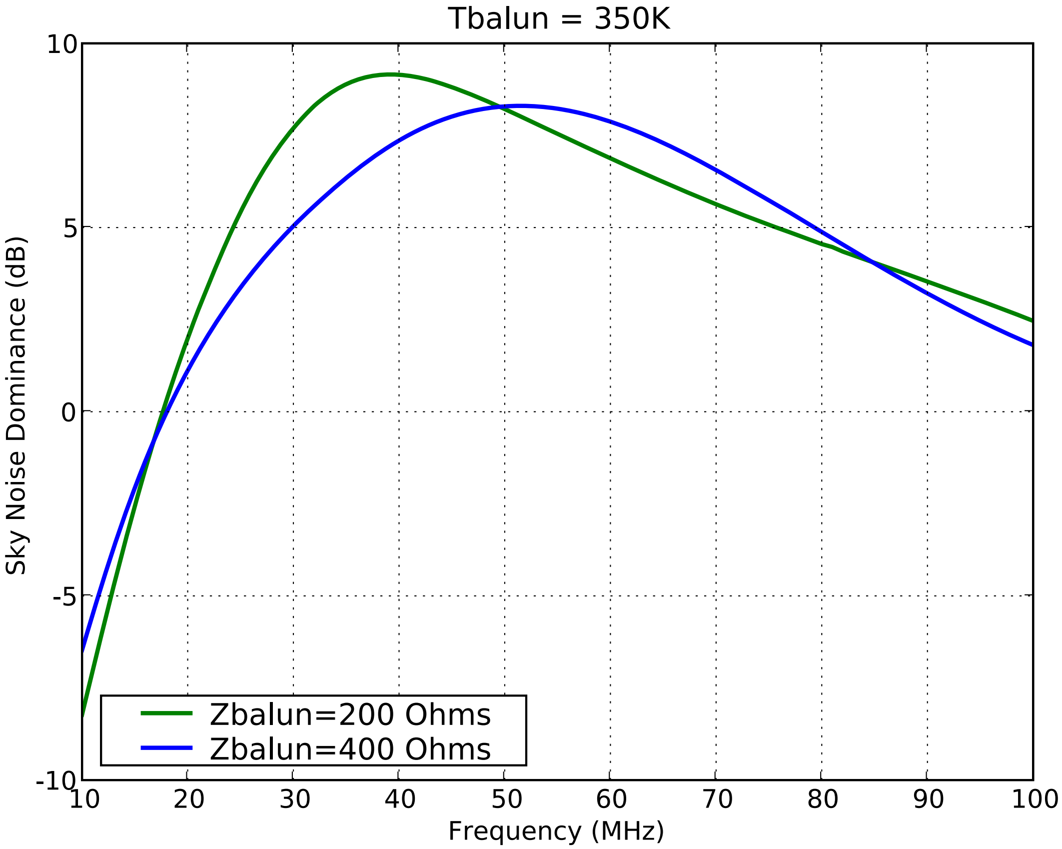

Fig. 27. Simulated sky noise dominance for the tied fork antenna for a 250K noise temperature balun with different input impedances (top). Simulated sky noise dominance for the tied fork antenna for a 350K noise temperature balun with different input impedances (bottom).

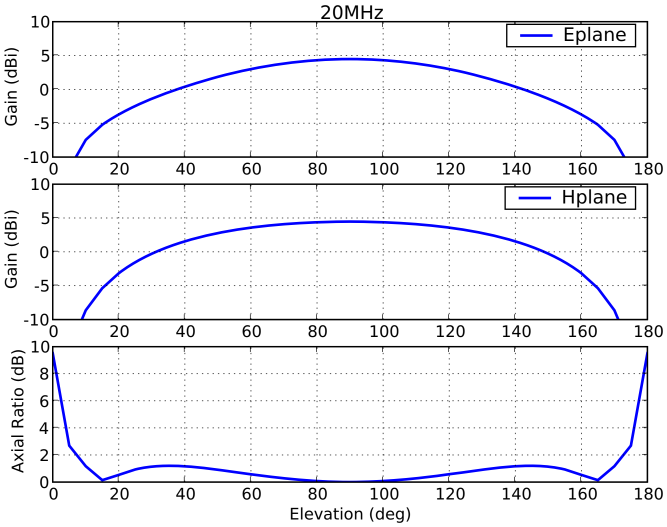

Fig. 28. E- and H- plane beam pattern slices and axial ratios of the tied fork antenna at 20 MHz.

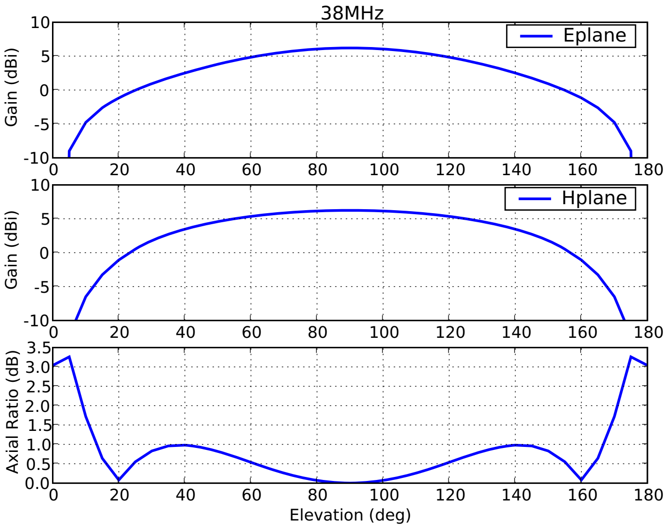

Fig. 29. E- and H- plane beam pattern slices and axial ratios of the tied fork antenna at 38 MHz.

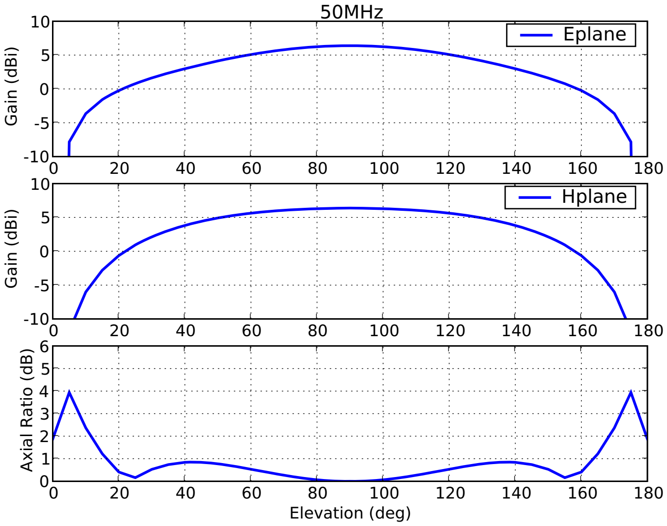

Fig. 30. E- and H- plane beam pattern slices and axial ratios of the tied fork antenna at 50 MHz.

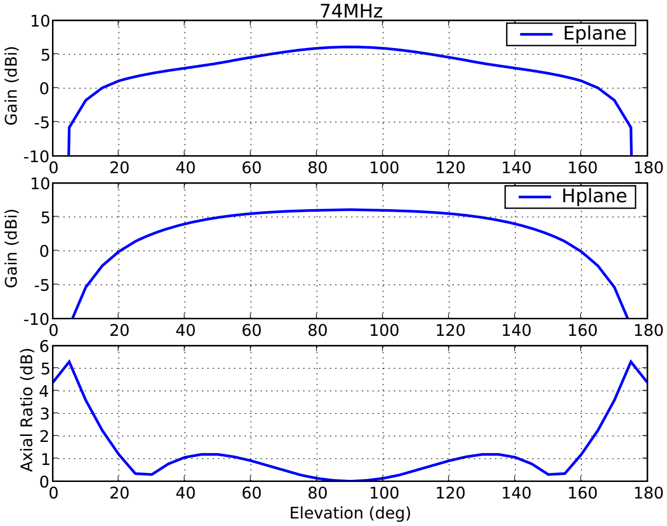

Fig. 31. E- and H- plane beam pattern slices and axial ratios of the tied fork antenna at 74 MHz.

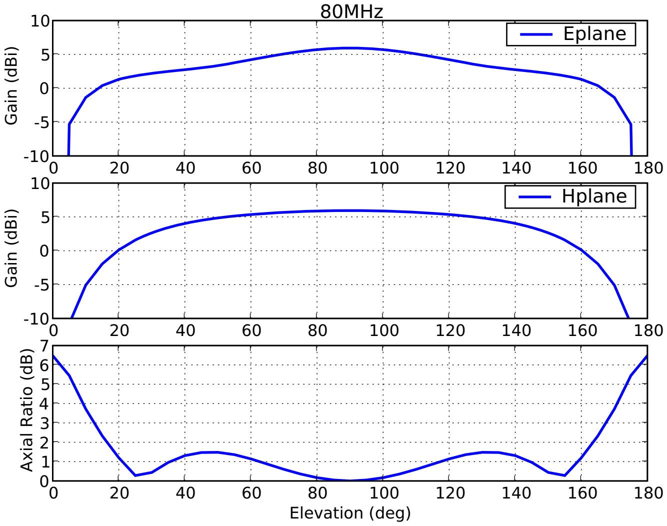

Fig. 32. E- and H- plane beam pattern slices and axial ratios of the tied fork antenna at 80 MHz.

VI. THE FILLED FORK ANTENNA

In this section, we focus on the filled fork antenna. This antenna can be made by welding a conducting mesh material to the frame of the tied fork antenna elements. The filled fork antenna elements would then have the same outer dimensions as the tied fork antenna described in section V, and the mesh material would approximate a continuous conducting surface at LWA frequencies. As with the tied fork antenna, the elements would be drooped 45° from horizontal and the feed point would stand 1.5m off the ground (see dimensions of tied fork antenna in Appendix).

Figure 33 shows a model of the filled fork antenna as it was simulated in NEC4 over a 3mx3m ground screen. No photograph is available for this antenna as it has not yet been prototyped. Figure 34 shows simulated plots of sky noise dominance for the filled fork antenna for different active balun noise temperatures and input impedances. Table XIII gives the frequency ranges over which the filled fork antenna achieves 0dB, 3dB and 6dB sky noise dominance for all of the different balun noise temperatures and input impedances simulated. Figures 35 – 39 show simulated E- and H-plane beam patterns and axial ratios for five frequencies in the LWA frequency band. Tables XIV and XV summarize half power beamwidths and maximum axial ratios at these five frequencies.

As with the other antennas in this report, pairing the filled fork antenna with the baseline Hicks balun ($Z_{balun} = 100\Omega, T_{balun} = 100K$) results in a limited 6dB bandwidth (24MHz–57MHz). Increasing the balun input impedance without properly accounting for the increase in balun noise temperature would seem to result in an increase in bandwidth. However, raising the balun noise temperature as well brings the 6dB sky noise dominance bandwidth back down, making it comparable that which was originally obtained with the baseline balun, once again indicating that there is no advantage in increasing the input impedance of the balun.

Beam patterns of the filled fork antenna have roughly the same shape as the tied fork antenna, with maximum axial ratios being slightly higher.

TABLE XIII

FREQUENCY RANGES (IN MHZ) OVER WHICH THE FILLED FORK ANTENNA ACHIEVES 0DB, 3DB AND 6DB SKY NOISE DOMINANCES (D) FOR DIFFERENT PREAMP INPUT IMPEDANCES (Z_{balun}) AND NOISE TEMPERATURES (T_{preamp}).

	$T_{preamp} = 250K$			$T_{preamp} = 350K$		
	$D > 0dB$	$D > 3dB$	$D > 6dB$	$D > 0dB$	$D > 3dB$	$D > 6dB$
$Z_{preamp} = 100\Omega$	19-100	21-100	24-57			
$Z_{preamp} = 200\Omega$	17-100	20-100	24-76	19-100	22-96	27-61
$Z_{preamp} = 400\Omega$	17-100	22-100	30-83	19-100	25-93	35-73

TABLE XIV

E- AND H-PLANE HALF POWER BEAMWIDTHS AT DIFFERENT FREQUENCIES FOR THE FILLED FORK ANTENNA

Frequency (MHz)	E-plane HPBW (deg)	H-plane HPBW (deg)
20	80	100
38	80	100
50	90	100
74	90	110
80	90	110

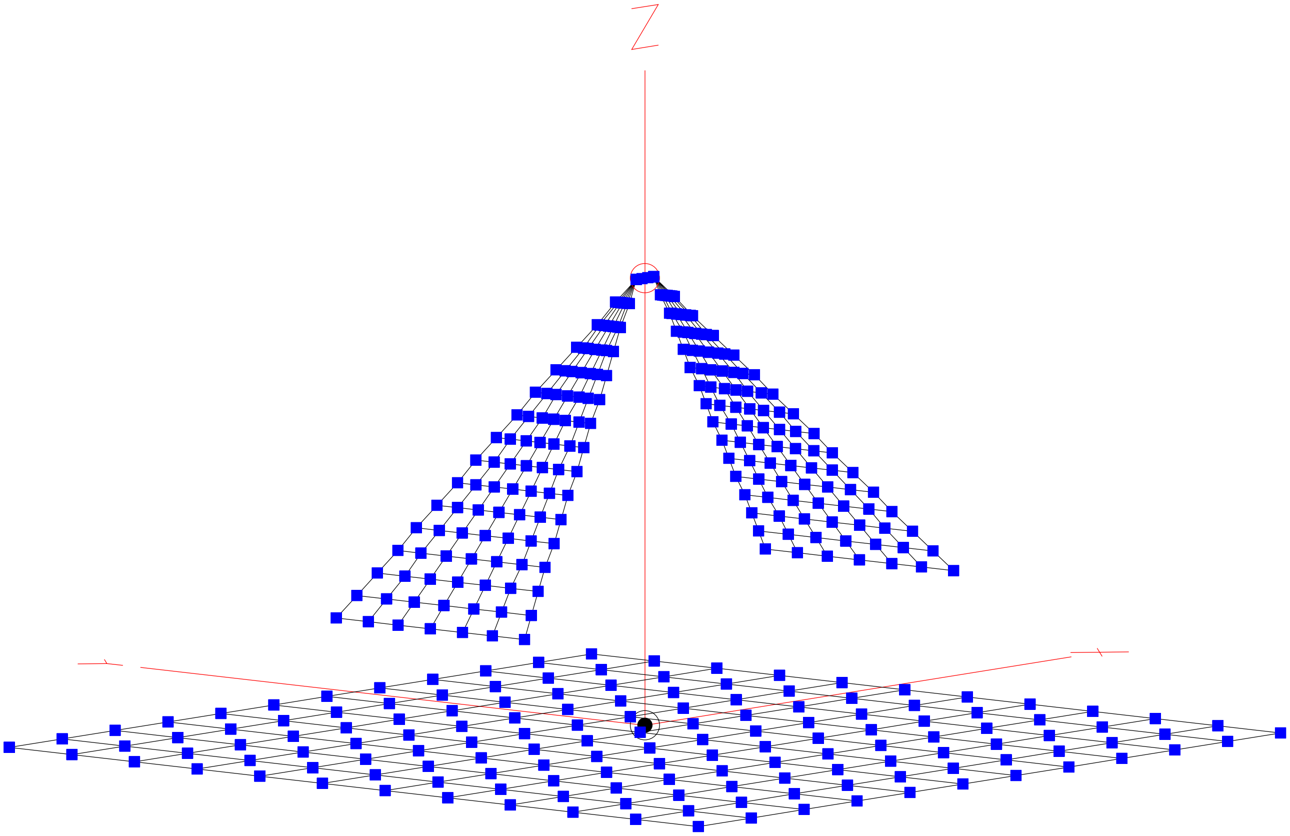

Fig. 33. The NEC4 model of the filled fork antenna over a 3mx3m ground screen.

TABLE XV

MAXIMUM AXIAL RATIO FOR $20^\circ \leq \theta \leq 160^\circ$ FOR THE FILLED FORK ANTENNA

Frequency (MHz)	Maximum Axial Ratio (dB)
20	1.47
38	1.23
50	1.06
74	1.27
80	1.49

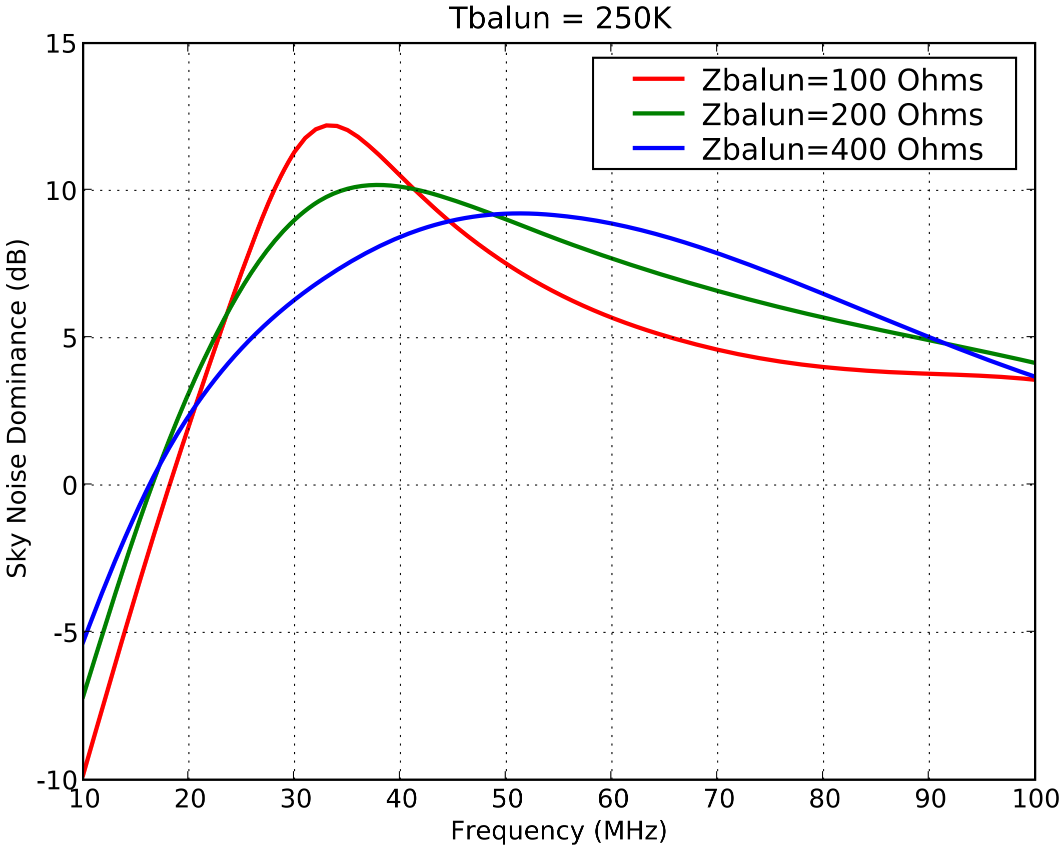

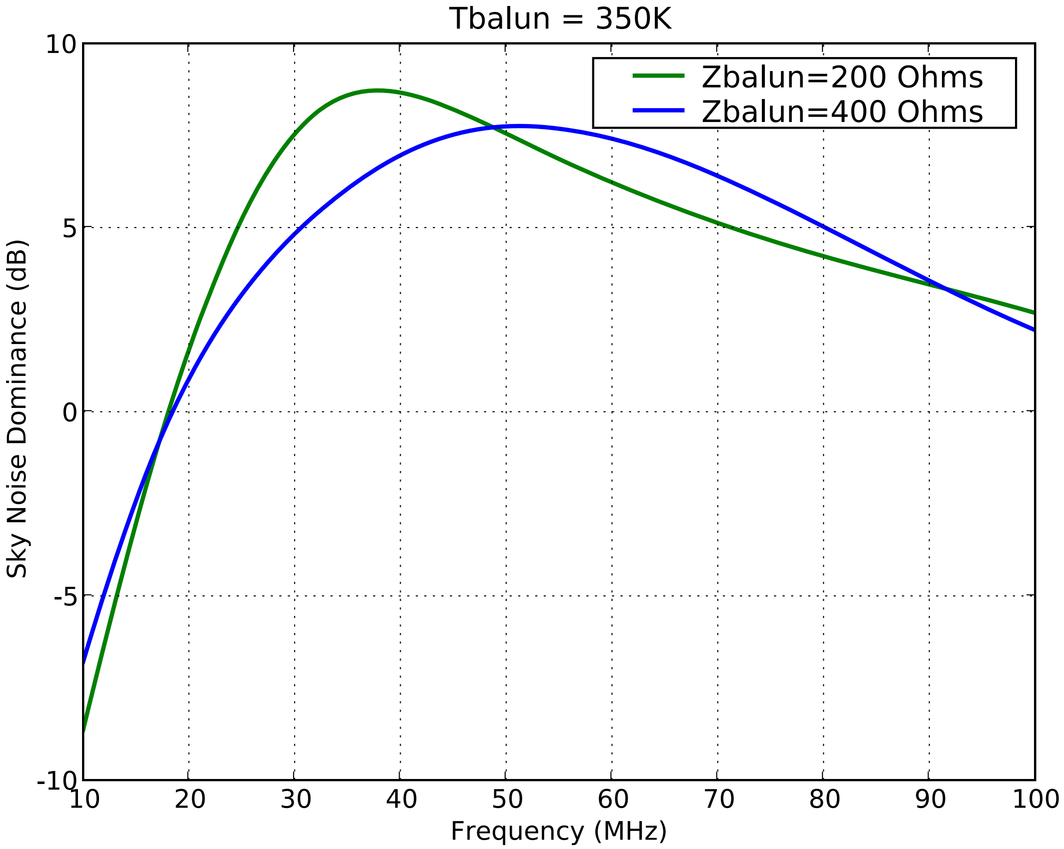

Fig. 34. Simulated sky noise dominance for the filled fork antenna for a 250K noise temperature balun with different input impedances (top). Simulated sky noise dominance for the filled fork antenna for a 350K noise temperature balun with different input impedances (bottom).

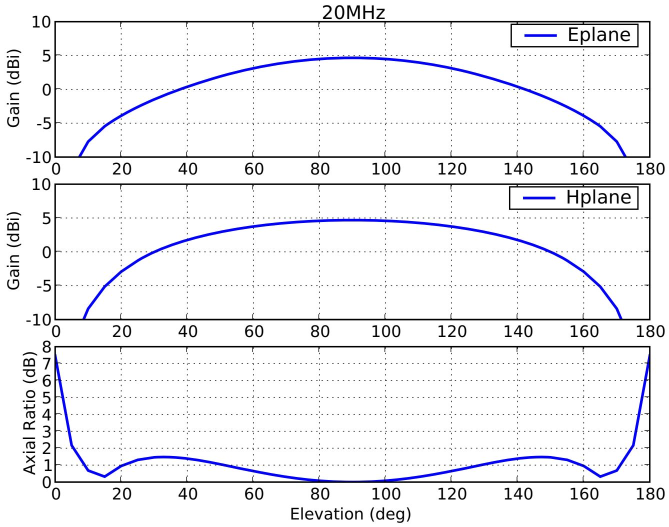

Fig. 35. E- and H- plane beam pattern slices and axial ratios of the filled fork antenna at 20 MHz.

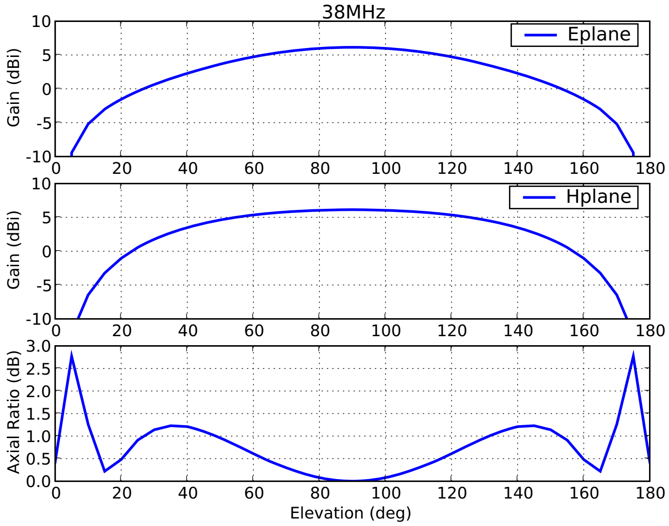

Fig. 36. E- and H- plane beam pattern slices and axial ratios of the filled fork antenna at 38 MHz.

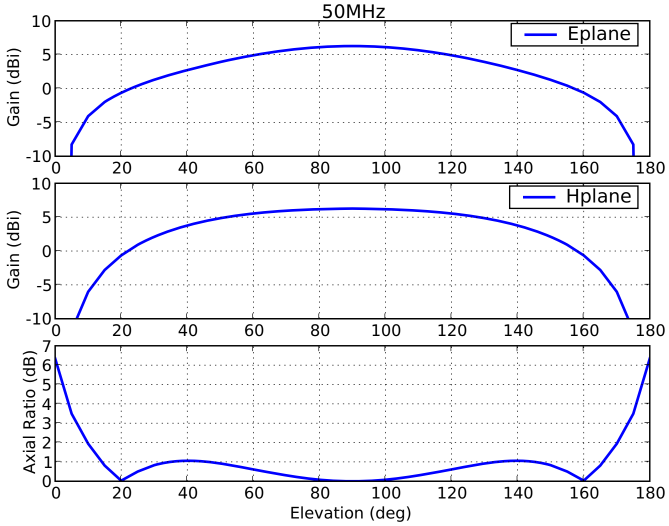

Fig. 37. E- and H- plane beam pattern slices and axial ratios of the filled fork antenna at 50 MHz.

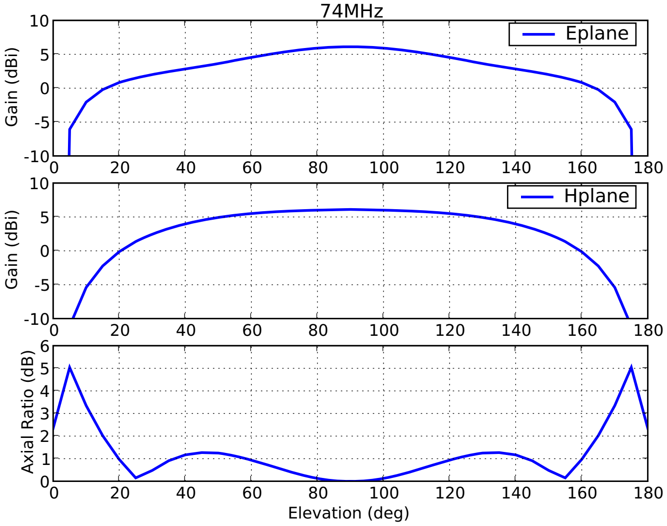

Fig. 38. E- and H- plane beam pattern slices and axial ratios of the filled fork antenna at 74 MHz.

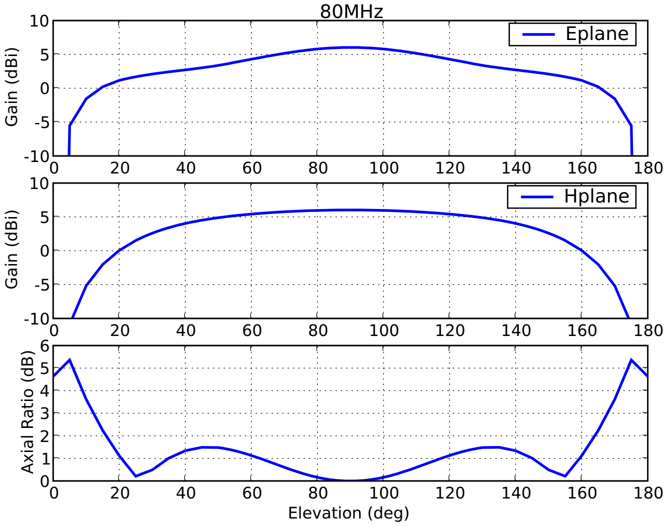

Fig. 39. E- and H- plane beam pattern slices and axial ratios of the filled fork antenna at 80 MHz.

VII. THE BIG BLADE ANTENNA

This section focuses on the big blade antenna. This antenna is the baseline design for the LWA project. The big blade antenna elements have the same dimensions as the Burns dipole in section IV, but are made of sheet aluminum instead of angled aluminum rods. Previously obtained cost estimates indicating that the big blade antenna will likely be prohibitively expensive because of the large amount of sheet aluminum required motivated the development of the Burns and tied fork antennas presented in sections IV and V. The elements in the big blade are also drooped $45°$ and the antenna feed point stands 1.5m off the ground. Further details on the dimensions of the big blade antenna are given in the Appendix.

Figure 40 shows the big blade antenna model as it was simulated in NEC4 over a 3mx3m ground screen. A photograph of a prototype big blade antenna is shown in Figure 41. Figure 42 shows plots of sky noise dominance, and Table XVI gives the 0dB, 3dB, and 6dB frequency ranges for all of the balun noise temperature and input impedance combinations simulated. Figures 43 – 47 show the E- and H-plane beam patterns and axial ratios for five frequencies across the LWA frequency band. Half power beamwidths and maximum axial ratios at all of these frequencies are summarized in Tables XVII and XVIII.

As with the previous antennas in this report, pairing the big blade antenna with the baseline Hicks balun ($Z_{balun} = 100\Omega, T_{balun} = 250K$) results in a limited 6dB sky noise dominance frequency range of 23MHz–64MHz. Simply increasing the input impedance of the balun to 200Ω would appear to yield a significant improvement in 6dB bandwidth, but once again, taking into account the increase in balun noise temperature fromt $250K$ to $350K$ brings the resultant 6dB bandwidth back down, showing once again that increasing the input impedance of the balun is not desirable.

Beam pattern characteristics of the big blade antenna are similar to the Burns and tied fork antennas. Patterns remain fairly symmetric at all five frequencies shown, with sidelobes beginning to form above 50MHz. The advantages of a small ground screen are once again exploited here with the formation of nulls at the horizon, making these antennas less susceptible to RFI coming in from the horizon.

TABLE XVI

FREQUENCY RANGES (IN MHZ) OVER WHICH THE BIG BLADE ANTENNA ACHIEVES 0DB, 3DB AND 6DB SKY NOISE DOMINANCES (D) FOR DIFFERENT PREAMP INPUT IMPEDANCES (Z_{balun}) AND NOISE TEMPERATURES (T_{preamp}).

	$T_{preamp} = 250K$			$T_{preamp} = 350K$		
	$D > 0dB$	$D > 3dB$	$D > 6dB$	$D > 0dB$	$D > 3dB$	$D > 6dB$
$Z_{preamp} = 100\Omega$	18-100	20-100	23-64			
$Z_{preamp} = 200\Omega$	16-100	19-97	23-76	18-100	21-87	25-65
$Z_{preamp} = 400\Omega$	16-100	20-87	29-81	19-100	25-91	34-73

TABLE XVII

E- AND H-PLANE HALF POWER BEAMWIDTHS AT DIFFERENT FREQUENCIES FOR THE BIG BLADE ANTENNA

Frequency (MHz)	E-plane HPBW (deg)	H-plane HPBW (deg)
20	80	100
38	90	100
50	90	100
74	110	100
80	110	100

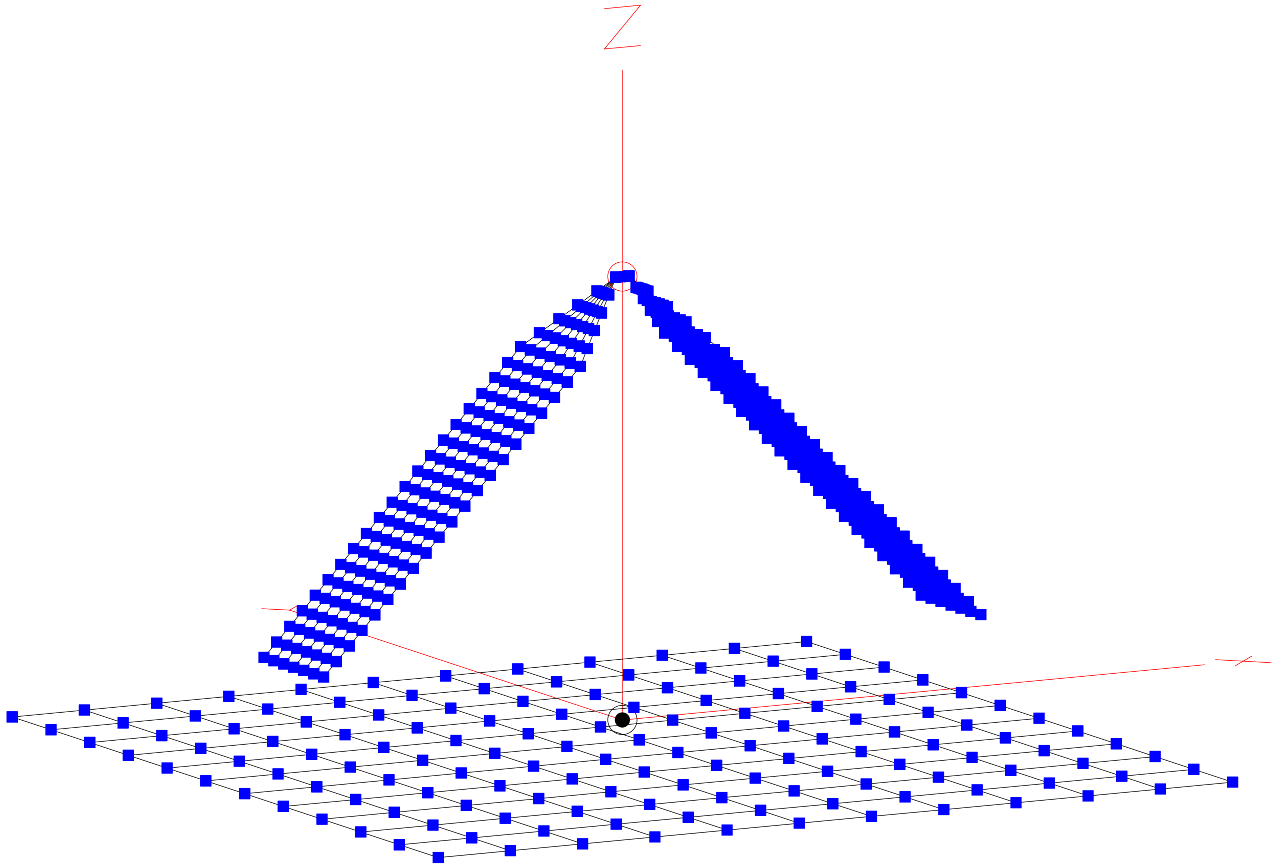

Fig. 40. The NEC4 model of the big blade antenna over a 3mx3m ground screen.

TABLE XVIII

MAXIMUM AXIAL RATIO FOR $20^\circ \leq \theta \leq 160^\circ$ FOR THE BIG BLADE ANTENNA

Frequency (MHz)	Maximum Axial Ratio (dB)
20	0.96
38	0.65
50	1.30
74	2.97
80	3.09

Fig. 41. A photograph of a big blade antenna prototype, modelled in Figure 40.

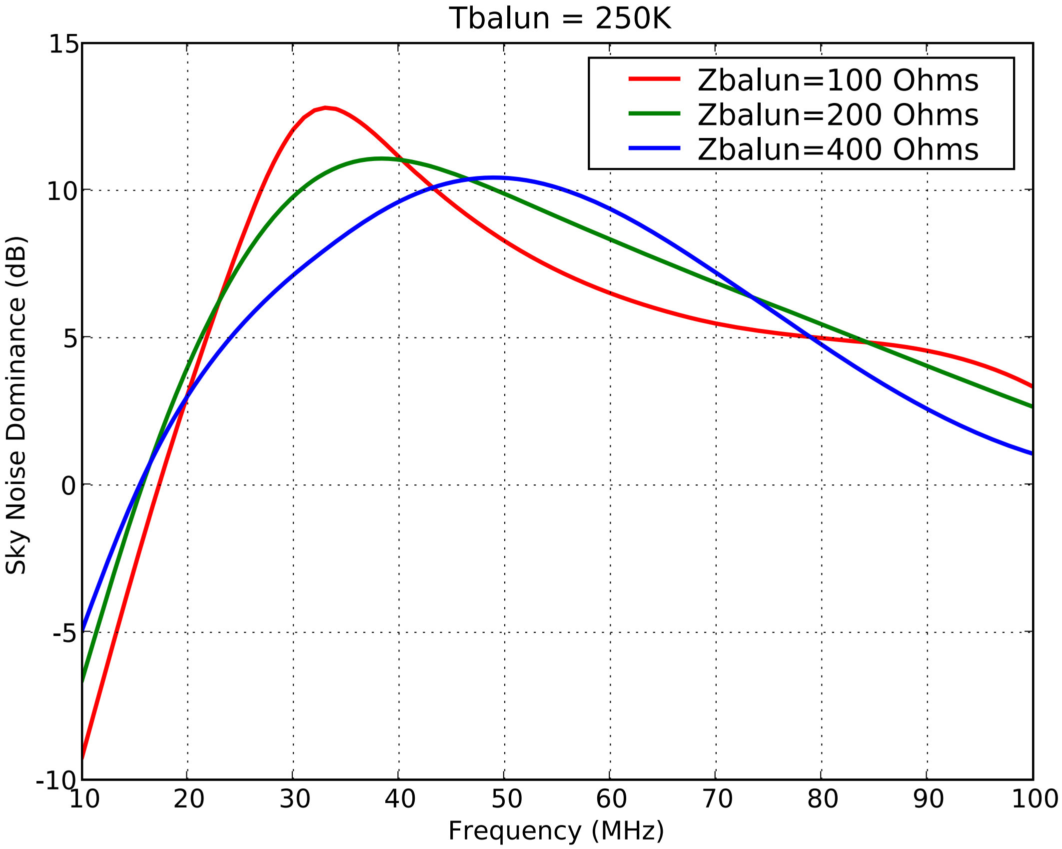

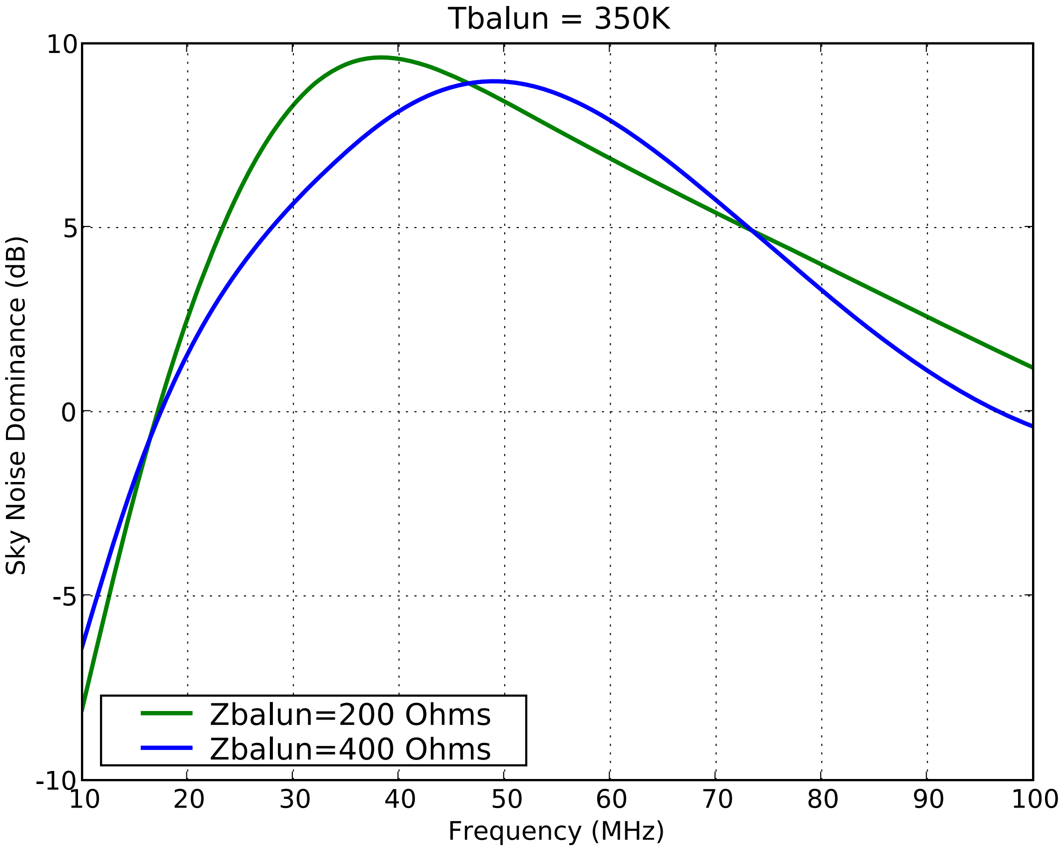

Fig. 42. Simulated sky noise dominance for the big blade antenna for a 250K noise temperature balun with different input impedances (top). Simulated sky noise dominance for the big blade antenna for a 350K noise temperature balun with different input impedances (bottom).

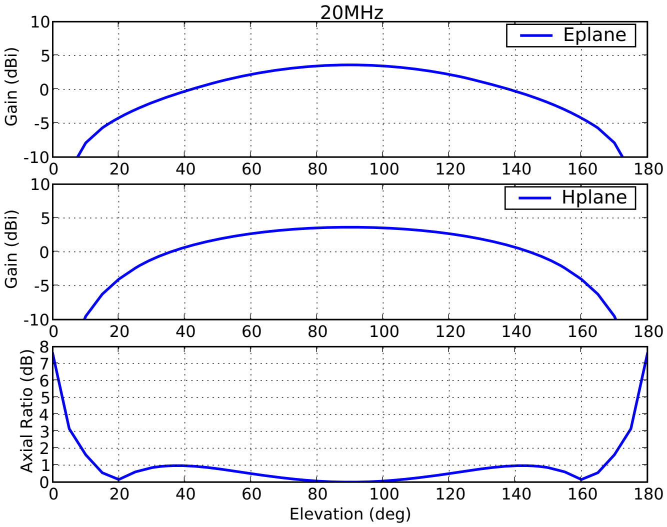

Fig. 43. E- and H- plane beam pattern slices and axial ratios of the big blade antenna at 20 MHz.

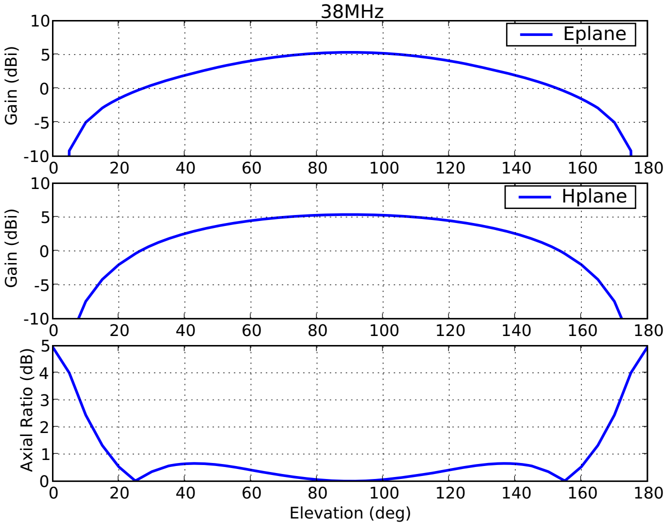

Fig. 44. E- and H- plane beam pattern slices and axial ratios of the big blade antenna at 38 MHz.

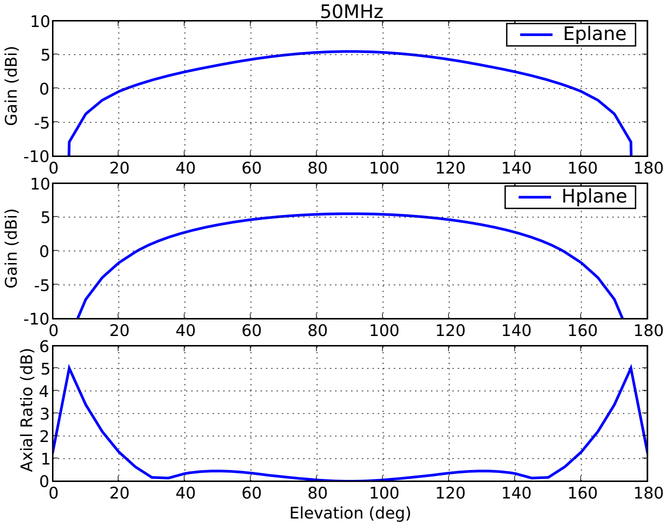

Fig. 45. E- and H- plane beam pattern slices and axial ratios of the big blade antenna at 50 MHz.

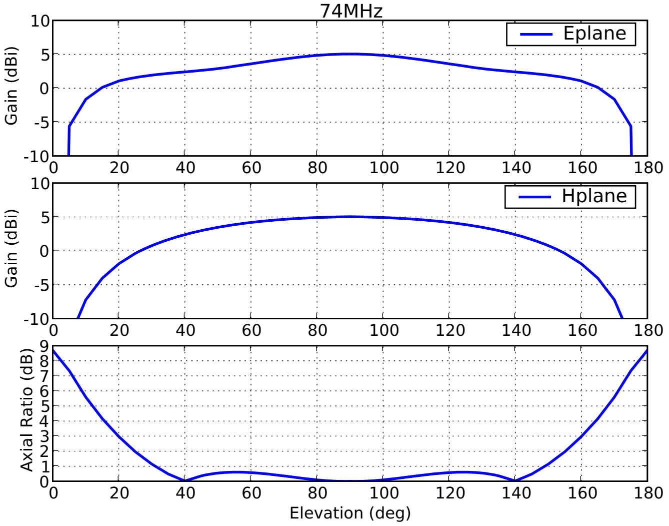

Fig. 46. E- and H- plane beam pattern slices and axial ratios of the big blade antenna at 74 MHz.

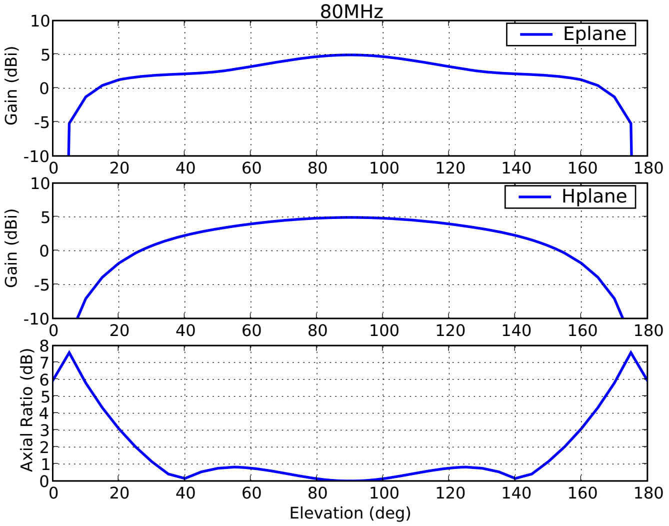

Fig. 47. E- and H- plane beam pattern slices and axial ratios of the big blade antenna at 80 MHz.

VIII. CONCLUSIONS

In this report, we have described the sky noise dominance and beam pattern properties of six potential antenna candidates, on small ground screens, for the first LWA station – LWA-1. This section brings the crucial results from sections II – VII together for a direct comparison of all antennas. Figure 48 shows a plot of sky noise dominance for all antennas when paired with the baseline Hicks balun ($T_{balun} = 250K, Z_{balun} = 100\Omega$). We omit the results for the higher balun noise temperature and impedances here because it was shown in the previous sections that these results offer no improvement over those for the Hicks balun. Figures 49 – 53 show beam patterns for all antennas plotted together.

Based on the simulation results presented, the following conclusions can be drawn:

- Initially, simply increasing the balun input impedance appears to improve the sky noise dominance bandwidths for all antennas. This higher input impedance would be realized by adding transformers at the balun inputs in the circuit design. Tests on these transformers show that these components would have losses of no less than 0.6dB per transformer, translating to a $\sim 100K$ increase in balun noise temperature. Including this higher noise temperature in calculations of sky noise dominance shows that any bandwidth gained by solely increasing the balun input impedance is lost when the higher balun noise temperature is introduced. It would therefore be most advantageous to maintain the original 100Ω input impedance in the LWA balun design.
- Simulation results show that the bowtie antenna has the poorest beam pattern axial ratios of all of the antennas compared in this report, and is therefore not a desirable candidate antenna for the LWA.
- Of the rest of the antennas in this comparison, the Burns and big blade antennas exhibit the smallest axial ratios over the LWA band. The tied fork and filled fork, overall, have wider half power beamwidths with only slightly higher axial ratios. The Burns and big blade antennas also exhibit the widest 6dB sky noise dominance bandwidths, with the tied fork antenna having only slightly less. Cost-wise, the Burns and tied fork antennas are likely to be the most affordable to produce in large numbers, and would therefore be the most attractive candidates for the LWA project.
- Simulations of antennas on ground screens of infinite extent in [2] show that antennas on very large ground screens yield beam patterns with nulls at the horizon in the H-plane, but not in the E-plane, making these antennas susceptible to RFI from low elevation angles. In this report we have shown that the use of small ground screens creates beam pattern nulls in both the E- and H-planes, making the antennas less vulnerable to RFI received at low elevation angels.

Work is in progress with Steve Burns of Burns Industries, Inc. to optimize these antennas for large scale manufacture. Once field measurements of antenna prototypes has been completed and one design has been chosen, prototypes can be purchased from Burns to field test and optimize for structural integrity. The possibility of welding a conducting mesh screen material to an antenna element frame to produce the filled fork antenna, or even an approximation to the big blade antenna are also being explored.

In the meantime, additional follow-up reports are planned for the near future. Prototypes of many of these antennas have already been built and deployed at the LWDA site in order to collect sky noise and drift scan data, and these results will be presented in one report. Another report will compare measured and simulated antenna impedances. A third report will explore the effect of ground screen size on antenna gain, collecting area and beam patterns.

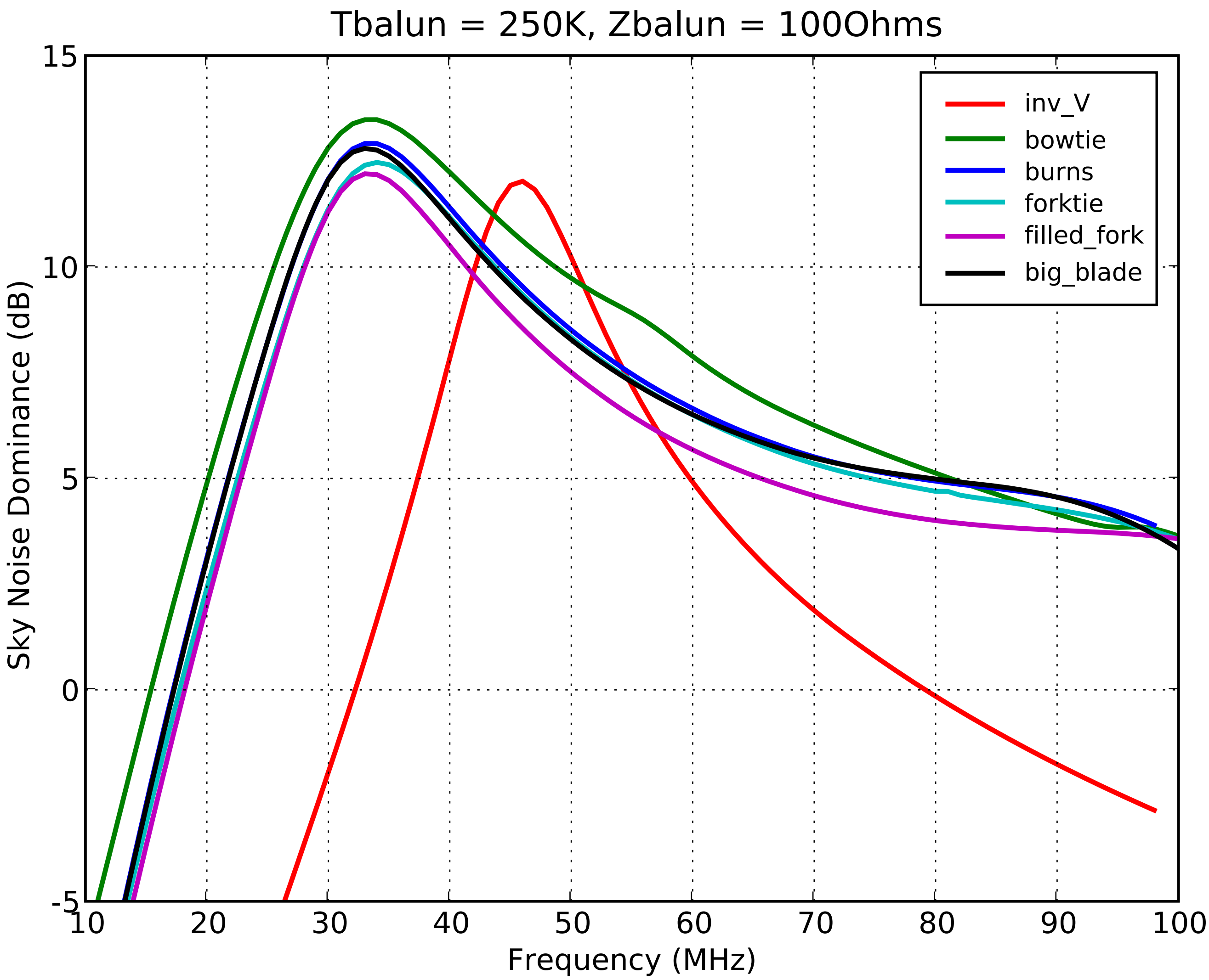

Fig. 48. Sky noise dominance of all antennas when paired with the baseline Hicks balun.

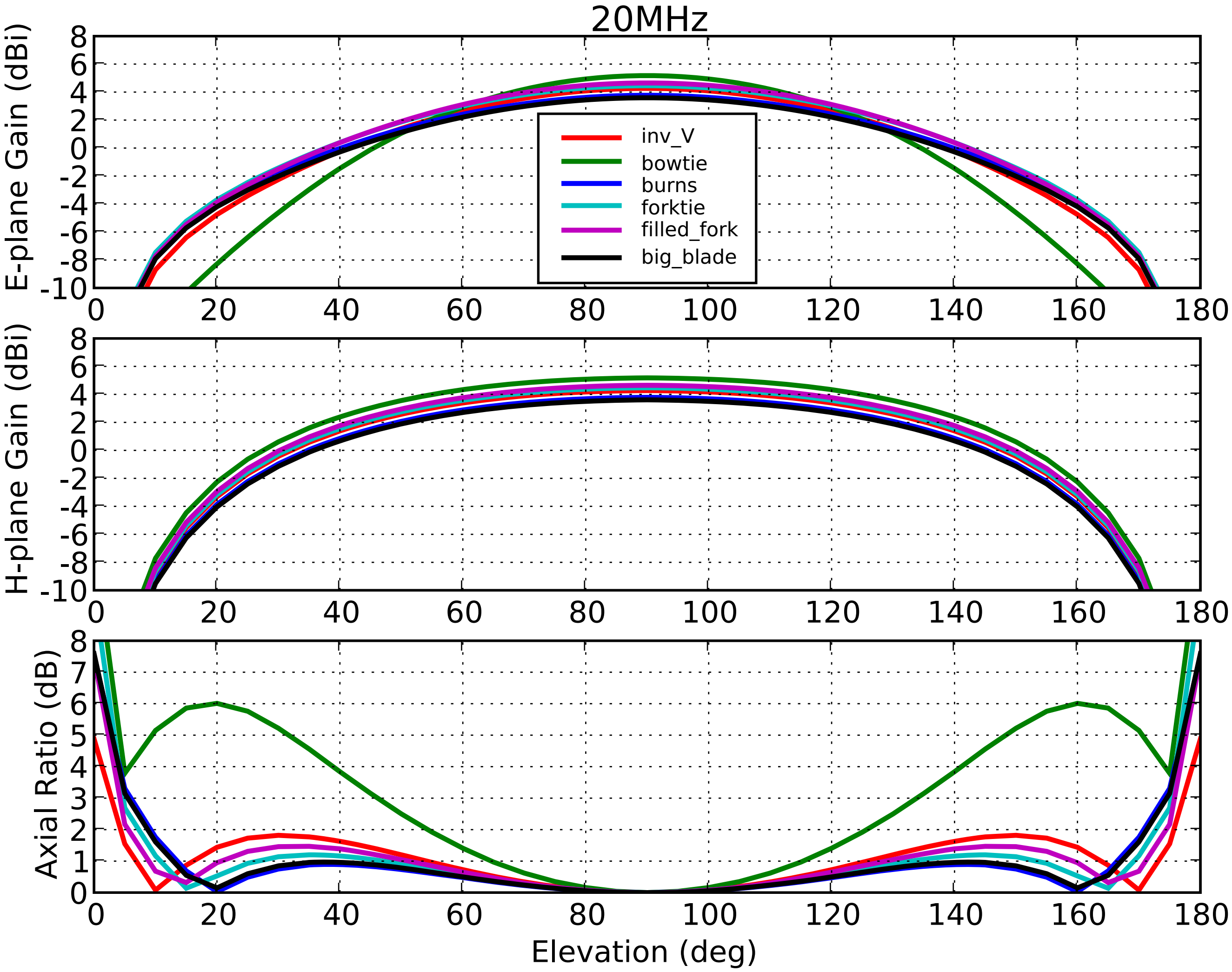

Fig. 49. E- and H- plane beam pattern slices and axial ratios of all antennas at 20 MHz.

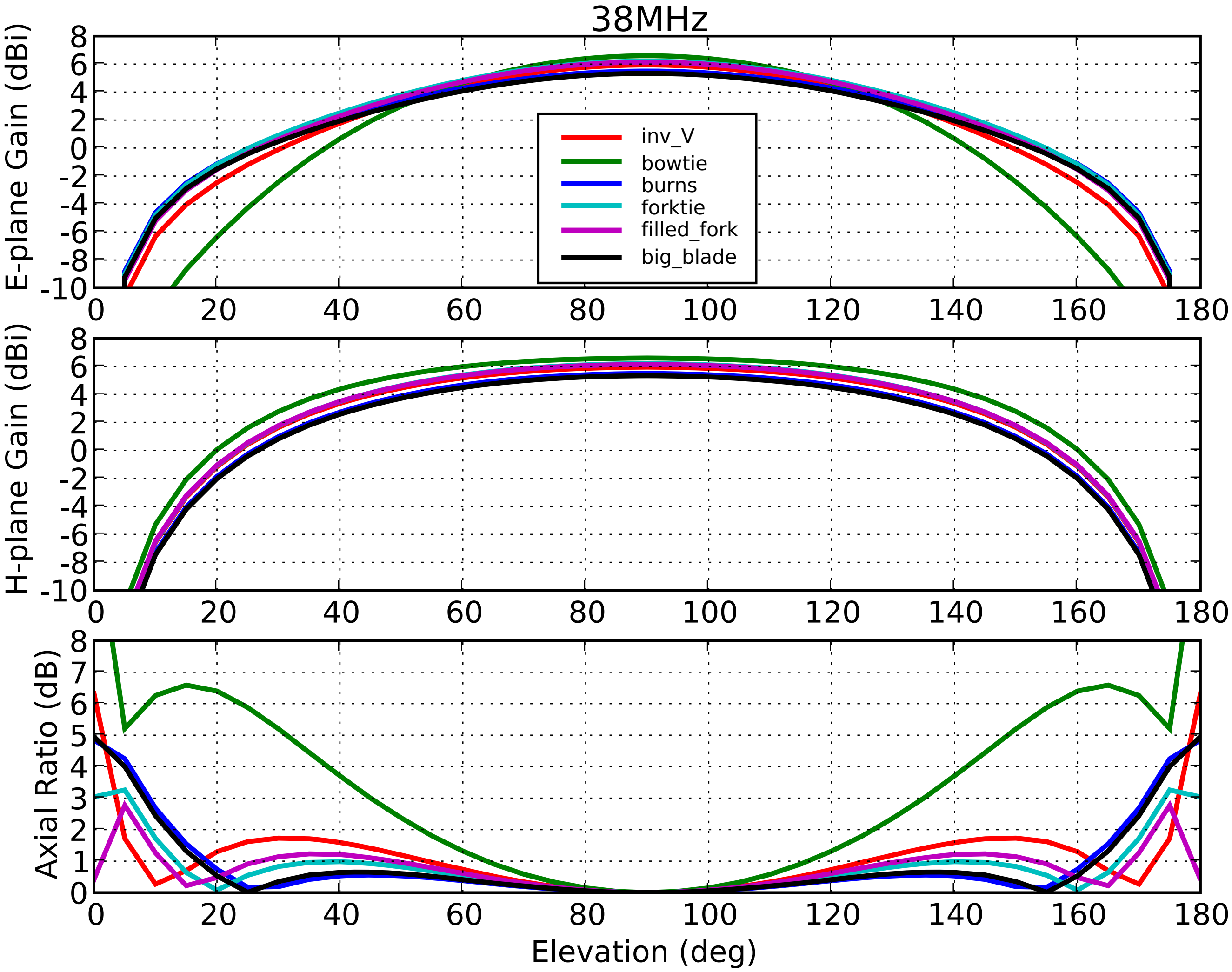

Fig. 50. E- and H- plane beam pattern slices and axial ratios of all antennas at 38 MHz.

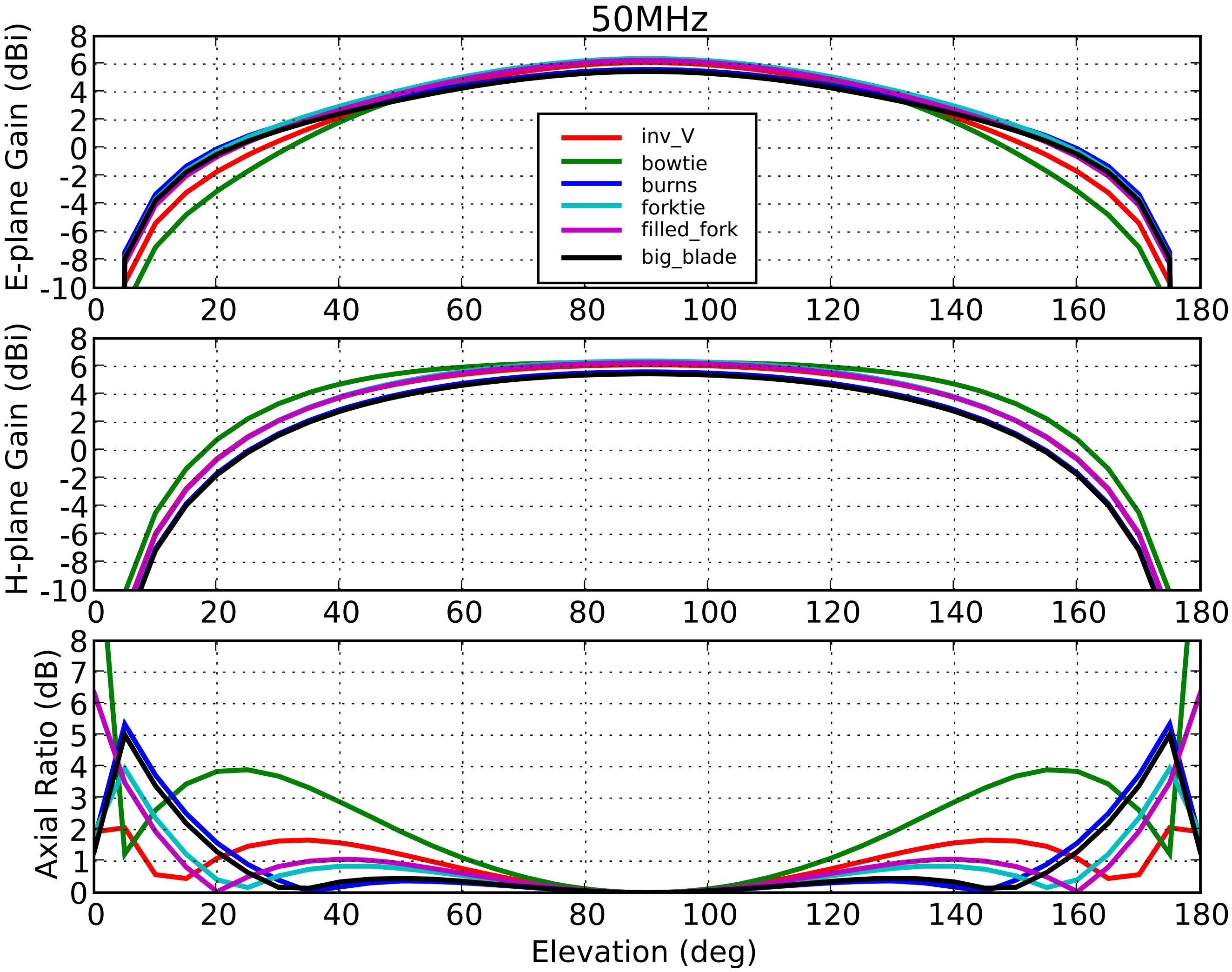

Fig. 51. E- and H- plane beam pattern slices and axial ratios of all antennas at 50 MHz.

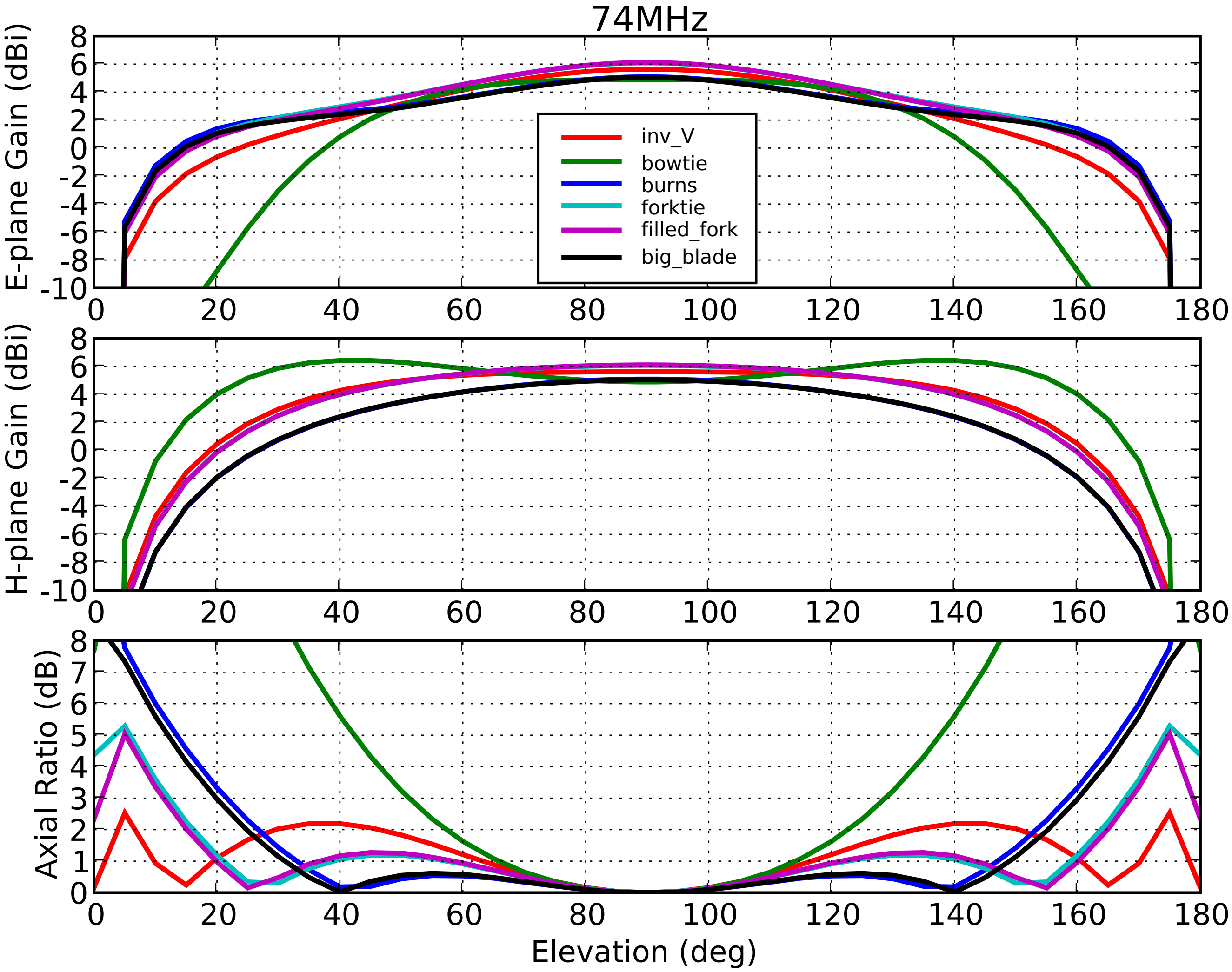

Fig. 52. E- and H- plane beam pattern slices and axial ratios of all antennas at 74 MHz.

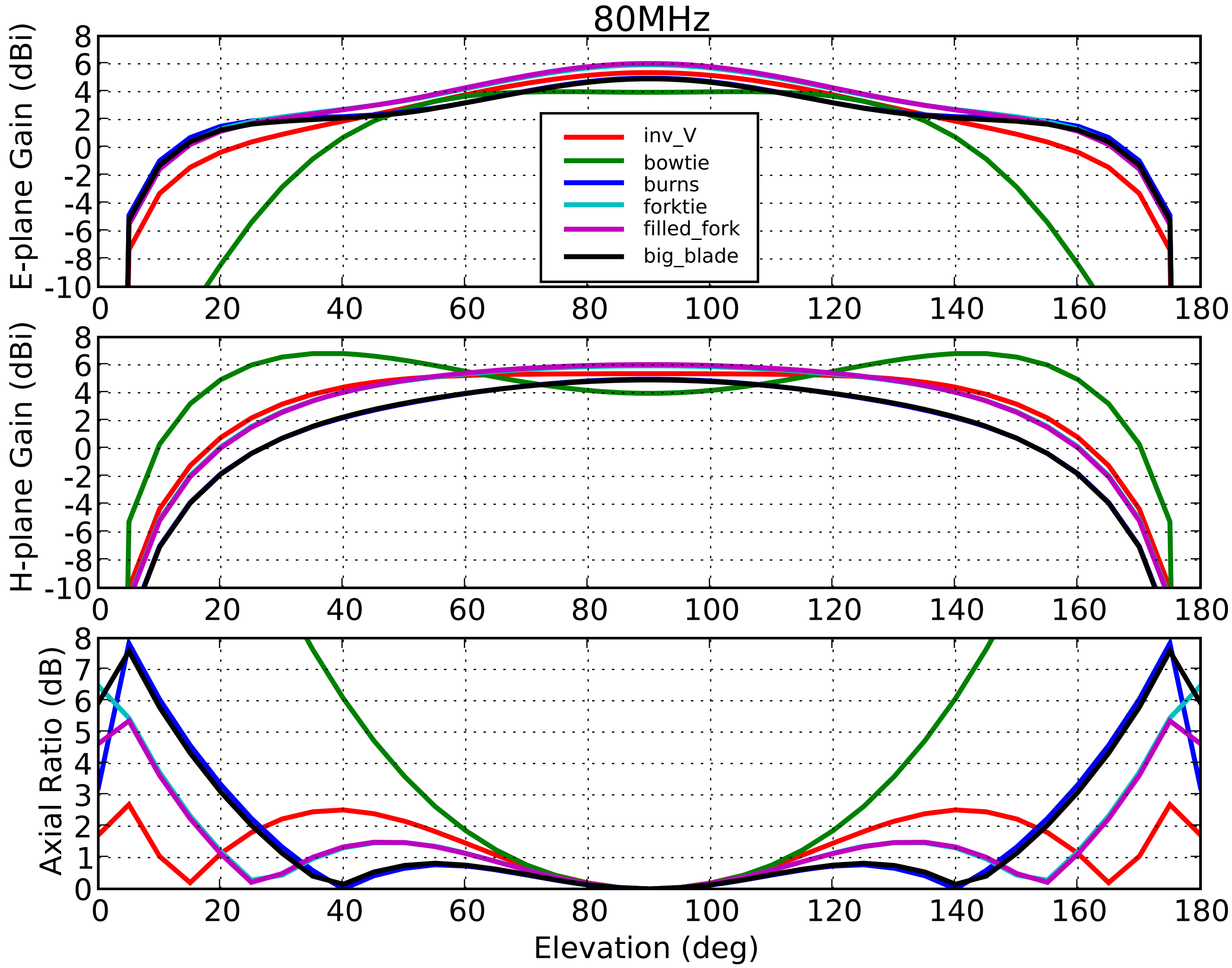

Fig. 53. E- and H- plane beam pattern slices and axial ratios of all antennas at 80 MHz.

ACKNOWLEDGMENT

Basic research in radio astronomy at the Naval Research Laboratory is supported by 6.1 base funding.

APPENDIX

This appendix contains dimensioned drawings of all of the antennas considered in this report. Please note that the drawings are not to scale.

Profile for Inverted-V, Burns,
Tied Fork and Big Blade Antennas

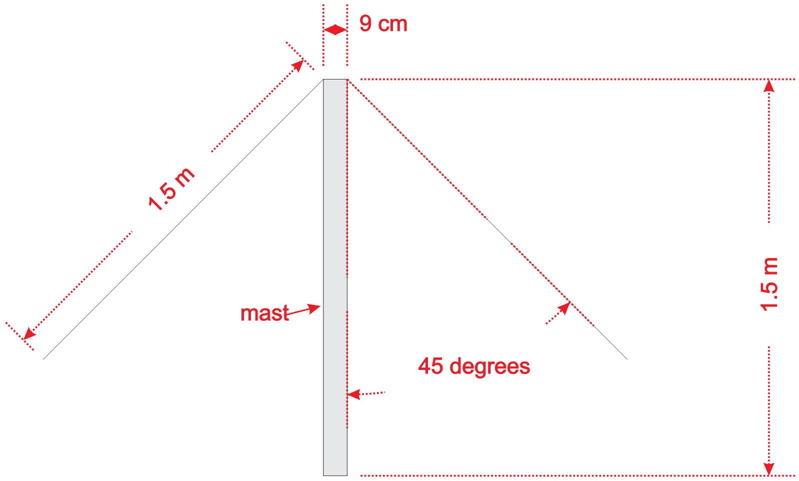

Profile for Bowtie Antenna

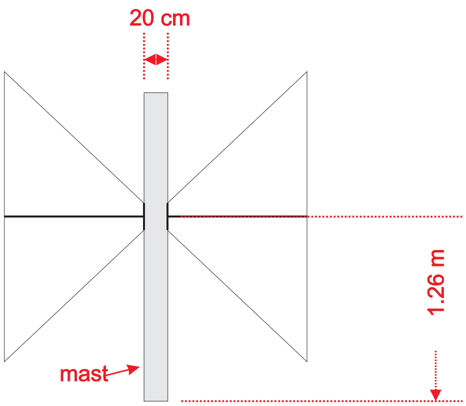

(drawings not to scale)

Antenna Element Dimensions

Inverted-V

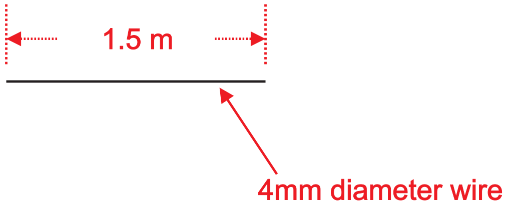

Bowtie

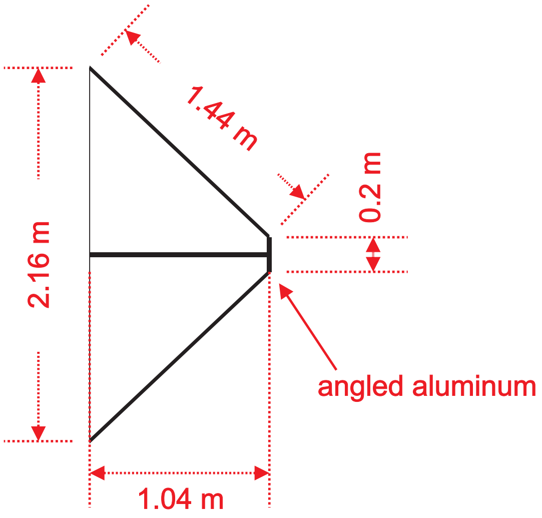

Burns

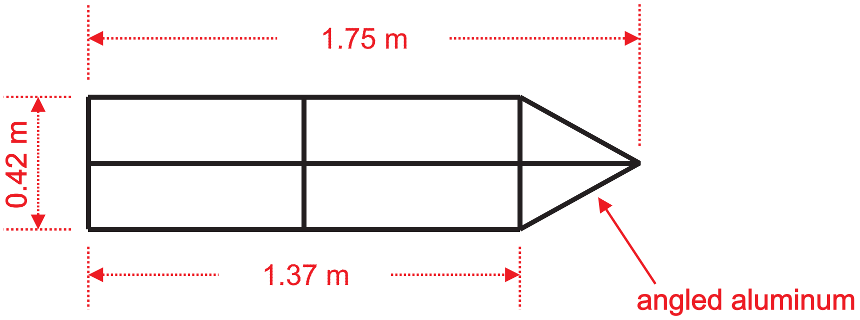

(drawings not to scale)

Tied Fork

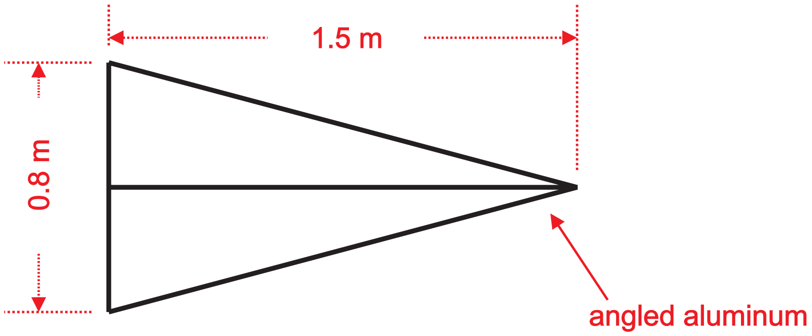

Big Blade

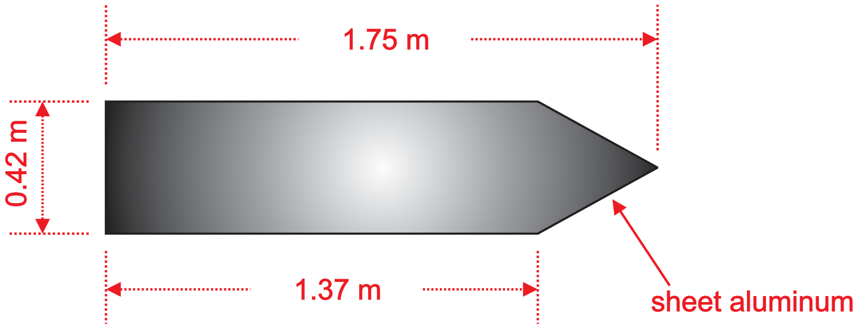

(drawings not to scale)

REFERENCES

[1] N. Paravastu, B. Hicks, and E. e. a. Aguilera, “Impedance Measurements of the Big Blade and Fork Antennas on Ground Screens at the LWDA Site,” *LWA Memo Series (Memo 90)*, June 2007.

[2] A. Kerkhoff, “Comparison of Dipole Antenna Designs for the LWA,” *LWA Memo Series (Memo 102)*, August 2007.

[3] R. Bradley and C. Parashare, “Evaluation of the NRL LWA Active Balun Prototype (Rev.A),” *LWA Memo Series (Memo 19)*, February 2005.

[4] “Communication with B. Hicks, August 2007.”

[5] H. Cane, “Spectra of the Nonthermal Radio Radiation from the Galactic Polar Regions,” *Monthly Notice Royal Astronomical Society*, vol. 189, p. 465, 1979.

[6] “Burns Industries, Inc.,” *http://www.burnsindustriesinc.com*.

[7] N. Paravastu, B. Hicks, P. Ray, and W. Erickson, “A New Candidate Active Antenna Design for the Long Wavelength Aray,” *LWA Memo Series (Memo 88)*, May 2007.

Comparison of Field Measurements on Active Antenna Prototypes on Ground Screens for the Long Wavelength Array

Nagini Paravastu (NRL/ASEE), Paul Ray (NRL), Brian Hicks (NRL),
William Erickson (UMD), Tracy Clarke (Interferometrics/NRL), Ken Stewart (NRL),
Ylva Pihlstrom (UNM), Masaya Kuniyoshi (UNM), Namir Kassim (NRL)
February 5, 2008

Abstract

We present and discuss the results of an antenna and active balun prototyping effort recently performed by members of the Long Wavelength Array project. Four antennas – the Big Blade, the Blade Frame, the 1.7 m Tied Fork and the 1.5 m Tied Fork – were tested with three active baluns – the Hicks–Teletech, the Discrete and the RTA – for a total of six active antenna (antenna/active balun) combinations. Analysis of the data collected included the generation of spectral, sky noise dominance and diurnal power plots for a side-by-side comparison of all of the active antennas that were tested. This analysis shows that the Big Blade antenna paired with the Discrete balun yields the best performance, while the 1.5 m Tied Fork antenna paired with the RTA balun shows the most promise for being a more cost effective alternative. In our conclusion we make comments and recommendations based on these results, and we describe plans to perform one more round of field testing on active antenna prototypes to finalize the antenna and balun designs for the Long Wavelength Array.

I. INTRODUCTION

In late July/early August 2007, a major campaign was undertaken to prototype candidate antennas and active baluns for the Long Wavelength Array (LWA), and test them at the LWDA site in New Mexico. Using the data collected from this work, we perform a side-by-side comparison of the front-runner antenna/active balun (referred to in the rest of this report as the *active antenna*) candidates for the LWA. The subsequent sections of this document show spectral and diurnal power measurements of six active antennas. Based on these results, we draw conclusions about the performance of each active antenna and make a recommendation for a path toward completing the LWA active antenna development program. First, we give a brief description of the antenna and active balun candidates measured and the field measurements that were performed.

A. Antenna and Balun Candidates

Four antennas were used for these measurements. The first, the Big Blade antenna, is the baseline LWA antenna design. Previously obtained cost estimates indicating that the Big Blade would be too expensive for the project motivated the designs of two cheaper alternative geometries. The Blade Frame antenna has the same outer dimensions as the Big Blade, but is made of angle aluminum to decrease weight and wind resistance. The Tied Fork antenna elements are also made from angled aluminum, but are triangular in shape. Two versions of the Tied Fork were built and tested. One had 1.5 m long elements. The other had 1.7 m long elements in order to determine if a Tied Fork antenna with longer elements would yield improved performance at lower frequencies while still maintaining a good response at higher frequencies. Dimensioned drawings of all of these antennas are given in the Appendix. Figures 1, 2, and 3 show photographs of the antenna prototypes at the LWDA site. Measurements of the Big Blade antenna were performed over a 3 m x 3 m ground screen, and measurements of the Blade Frame and Tied Fork antennas were performed over a 7.4 m x 5.8 m ground screen. The ground screens were made from 2”x4” cell size welded wire mesh material.

Three active baluns were used for these measurements – the Hicks–Teletech (HT) balun, the Discrete (DB) balun, and the RTA (RT) balun. Photographs of these baluns are shown in Figures 4, 5, and 6. The Hicks-Teletech balun is the baseline balun design for the LWA project. The Discrete balun was developed in collaboration with NRAO, and has a lower noise temperature and higher gain than the Hick–Teletech balun. The RTA balun was recently developed for the RTA project, and has a roughly equivalent noise temperature to, but higher gain than the Hicks–Teletech balun [1]. Table I summarizes the noise temperatures and gains for each of the baluns. A labelling system was also devised for consistent referral to the baluns in the field and in future documentation. These labels, along with references to LWA memos with design and layout details are also included in Table I.

Using the four antennas and three baluns, six active antennas were constructed for testing. Table II lists all of the antenna-balun combinations that were tested, and gives designations for each one which will be used through the rest of this report to differentiate between the active antennas.

B. Description of Measurements

Spectral power measurements on the active antenna candidates were performed in the 10 – 100 MHz frequency range using the Specmaster spectrum monitoring system [2]. Figure 7 shows a diagram of the measurement system used for all active antennas. The active antennas were connected to the Specmaster system via a 40 m coaxial cable. A second stage amplifier was inserted before the Specmaster input to ensure that power levels detected by the active antennas were well above the noise floor of the spectrum analyzer in the Specmaster system.

Using the data collected, sky noise dominance – the ratio of the sky power detected by the active antenna to the balun noise power – was then calculated for each active antenna. The measurement of one active antenna and the calculation of its sky noise dominance was done as follows:

1) Spectral data were first collected with the active balun inputs terminated with 50 Ω loads. The total power at the balun input, P_{in}^{load}, was then given by Equation 1, where k was Boltzmann's constant, B was the resolution bandwidth of the measurement (which was 51 kHz for all the data presented in this report), T_0 was the physical temperature of the 50 Ω load and was taken to be 290 K, and T_e was the electronic noise temperature of the measurement system, which was taken to the be the noise temperature of the balun under test since a cascade analysis shows that the system noise temperature is dominated by the noise temperature of the balun, and subsequent components in the signal chain raise this value by only a few Kelvin at most (balun noise temperatures are given in Table I).

$$P_{in}^{load} = kT_0B + kT_eB \tag{1}$$

2) The gain, G_{sys}, of the measurement system was then determined using Equation 2, where P_{out}^{load} was the power measured directly at the Specmaster input when the balun inputs were terminated with 50 Ω loads.

$$G_{sys} = \frac{P_{out}^{load}}{P_{in}^{load}} \tag{2}$$

3) Spectral data were then collected with the balun connected to the antenna. The power detected at the antenna feed point, $P_{in}^{antenna}$ was given by Equation 3, where $P_{out}^{antenna}$ was the power directly measured at the Specmaster input when the balun was connected to the antenna.

$$P_{in}^{antenna} = \frac{P_{out}^{antenna}}{G_{sys}} \tag{3}$$

4) The sky noise dominance, D, for each active antenna was then calculated using Equation 4, where P_e is the input electronic noise power, kT_eB.

$$D = \frac{P_{in}^{antenna} - P_e}{P_e} \tag{4}$$

Using the spectral power data collected on the active antenna, drift curves – plots of detected power at one frequency over a 24 hour period – were generated at 25.61 MHz, 38 MHz, 50 MHz, 74 MHz, and 87 MHz. The variation in power levels in these plots is due to the rising and setting of the Galactic center region in the sky over the antenna. Drift curves can be used to compare the dynamic range available from each active antenna at one frequency.

Section II shows plots of measured spectra and calculated sky noise dominance for each of the active antenna candidates considered in this report. Section III shows drift curves for the active antennas at five frequencies in the 10 – 100 MHz frequency range. Section IV compares the calculated sky noise dominance for each active antenna with simulated predictions. Based on all of these plots, we draw conclusions in Section V about the most favorable active antenna candidates, and make recommendations on the next steps that must be taken in the LWA active antenna development program.

TABLE I

LWA ACTIVE BALUN CANDIDATES

Balun	Abbreviation	Designation	Gain	Noise Temperature	Reference
Hicks – Teletech	HT	G250P	24dB	250K	[3]
Discrete	DB	D120P	32dB	120K	[4]
RTA	RT or RTA	G250R	36dB	250K	[5]

TABLE II

LWA ACTIVE ANTENNA CANDIDATES

Antenna	Active Balun	Designation
Big Blade	Hicks – Teletech	BB3HT
Big Blade	Discrete	BB2DB
Big Blade	RTA	BB3RT
Blade Frame	RTA	BDRTA
1.7m Tied Fork	RTA	TFRTA_long
1.5m Tied Fork	RTA	TFRTA_short

Fig. 1. A photograph of the Big Blade antenna over a ground screen.

Fig. 2. A photograph of the Blade Frame antenna over a ground screen.

Fig. 3. A photograph of the Tied Fork antenna over a ground screen. Two versions of this antenna – one that was 1.5m long and one that was 1.7m long – were tested.

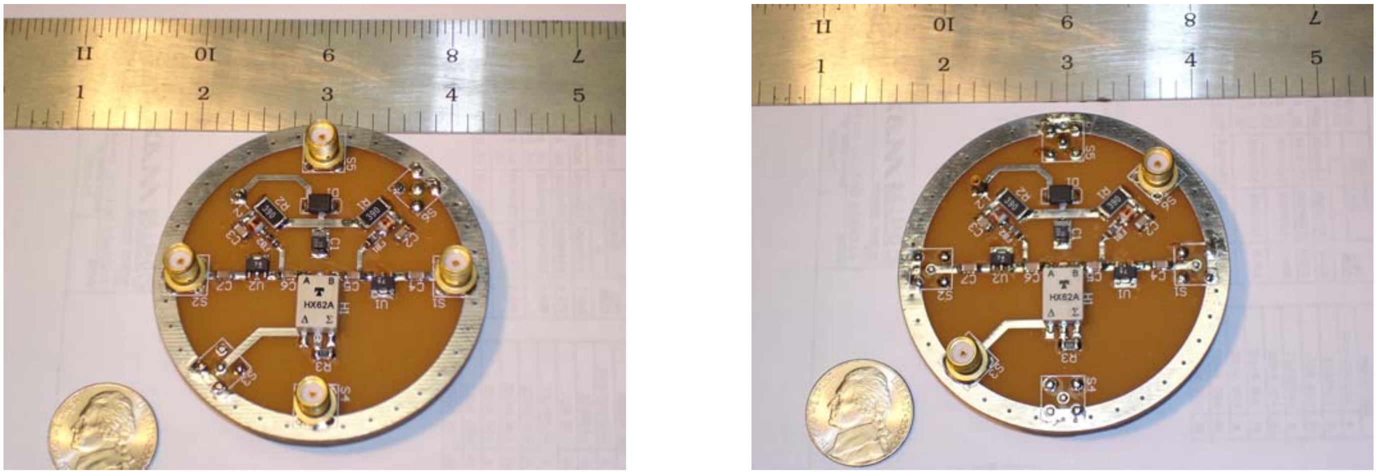

Fig. 4. A photograph of the input side (left) and the output side (right) of a Hicks–Teletech balun.

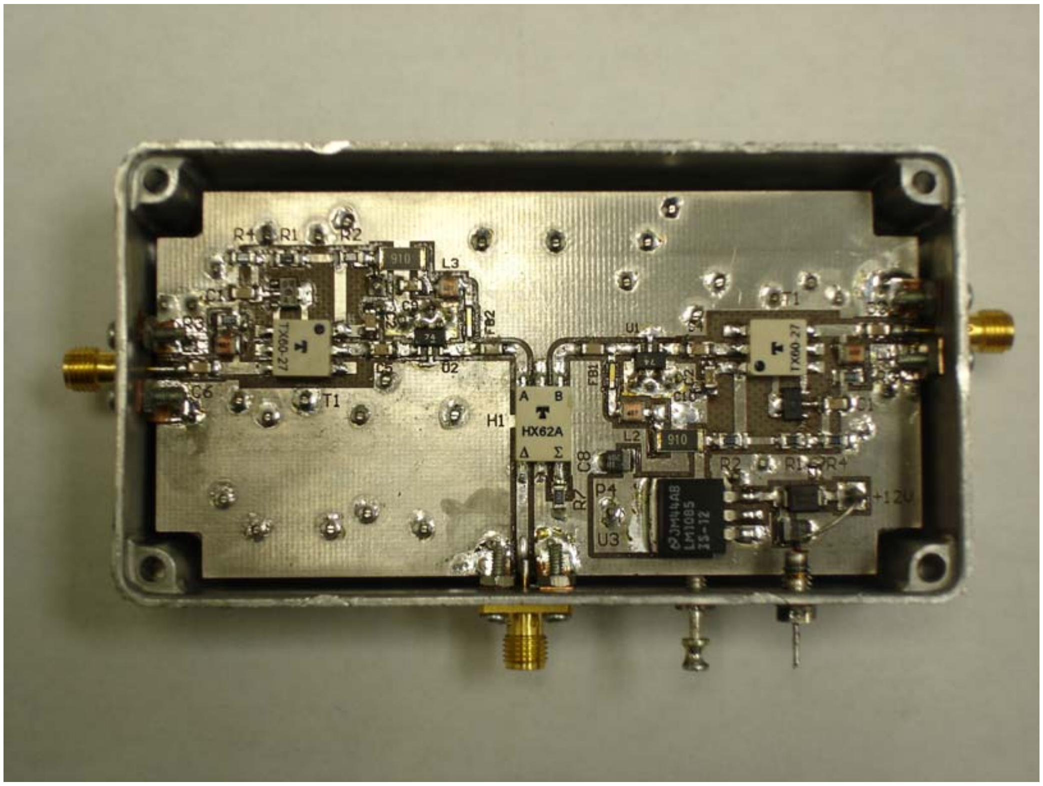

Fig. 5. A photograph of the Discrete balun.

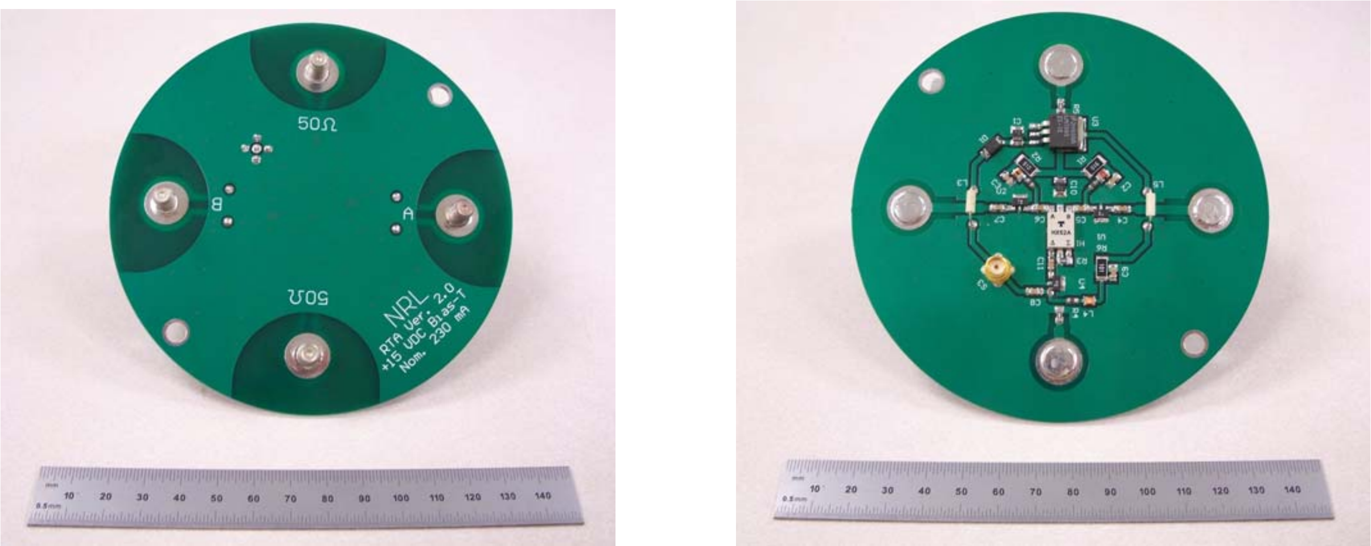

Fig. 6. A photograph of the input side (left) and the output side (right) of the RTA balun.

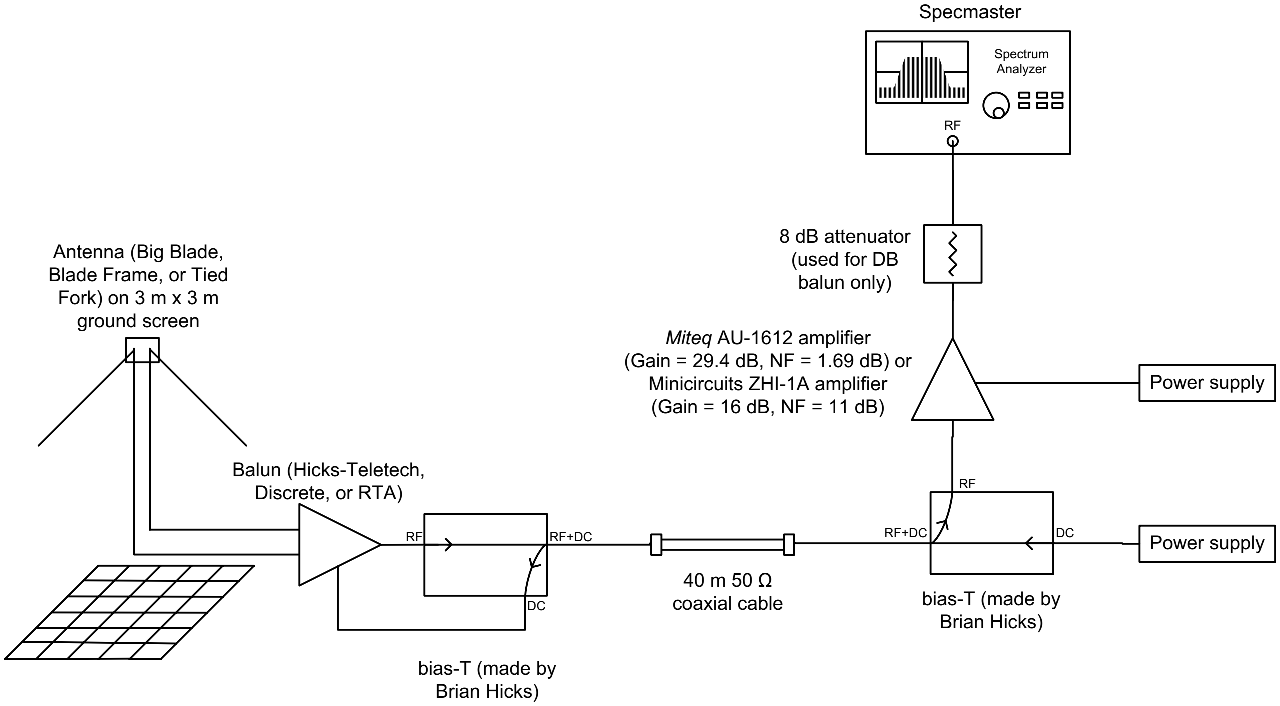

Fig. 7. A diagram of the active antenna measurement system.

II. SKY NOISE DOMINANCE

Figures 8, 9, and 10 show sky noise dominance plots for the Big Blade antenna paired with the Hicks–Teletech balun, the Discrete balun, and the RTA balun respectively. The highest levels of sky noise dominance are achieved with BB2DB. This is not surprising given that the DB balun has half the noise temperature of and 8 dB more gain than the HT balun. BB3RT shows lower sky noise dominance than BB2DB, but still yields better results than BB3HT.

Figures 11, 12, and 13 show measured spectra and sky noise dominance plots for the Blade Frame, 1.7 m Tied Fork, and 1.5 m Tied Fork paired with the RTA balun. All three active antennas achieve at least 5 dB sky noise dominance across the LWA frequency band with TFRTA_long appearing to perform slightly better than BDRTA or TFRTA_short. The goal for the LWA project is to achieve a minimum of 6 dB sky noise dominance across the entire LWA frequency band for the final active antenna design. Table III lists the 6 dB and 10 dB bandwidths for all six active antennas.

TABLE III

ACTIVE ANTENNA SKY NOISE DOMINANCE BANDWIDTHS

Antenna	Active Balun	Designation	D≥6 dB	D≥10 dB
Big Blade	Hicks – Teletech	BB3HT	23 – 72 MHz	29 – 41 MHz
Big Blade	Discrete	BB2DB	19 – 100 MHz	23 – 59 MHz
Big Blade	RTA	BB3RT	22 – 100 MHz	26 – 43 MHz
Blade Frame	RTA	BDRTA	20 – 57 MHz	24 – 42 MHz
1.7 m Tied Fork	RTA	TFRTA_long	18 – 51 MHz	21 – 38 MHz
1.5 m Tied Fork	RTA	TFRTA_short	20 – 58 MHz	25 – 43 MHz

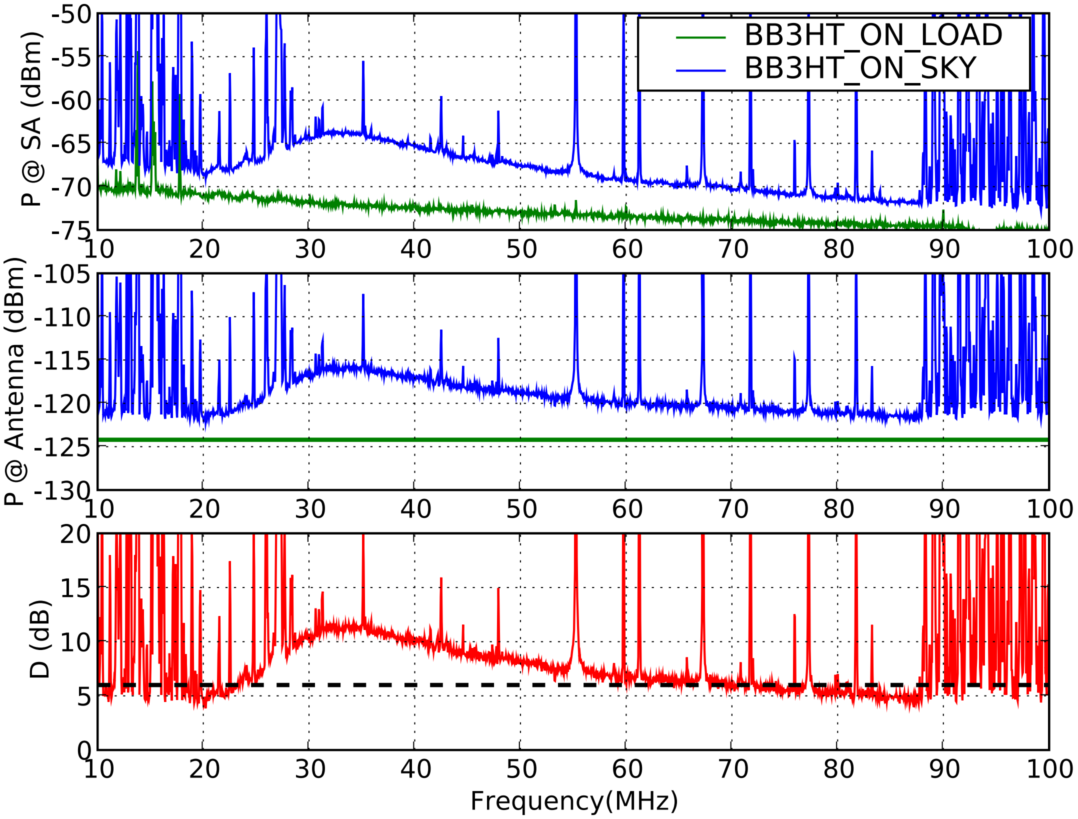

Fig. 8. Measured power for the Big Blade antenna/Hicks–Teletech balun (BB3HT). The power measured at the Specmaster input (P @ SA) is shown on top. The power measured at the antenna feed point (P @ Antenna) is shown in the middle, and the sky noise dominance (D) is shown on the bottom. In the top plot, $P_{out}^{antenna}$ is in blue and P_{out}^{load} is in green. In the middle plot, $P_{in}^{antenna}$ is in blue and P_{in}^{load} is in green. The resolution bandwidth for this measurement was 51 kHz. D = 6 dB is indicated with a dashed black line in the sky noise dominance plot.

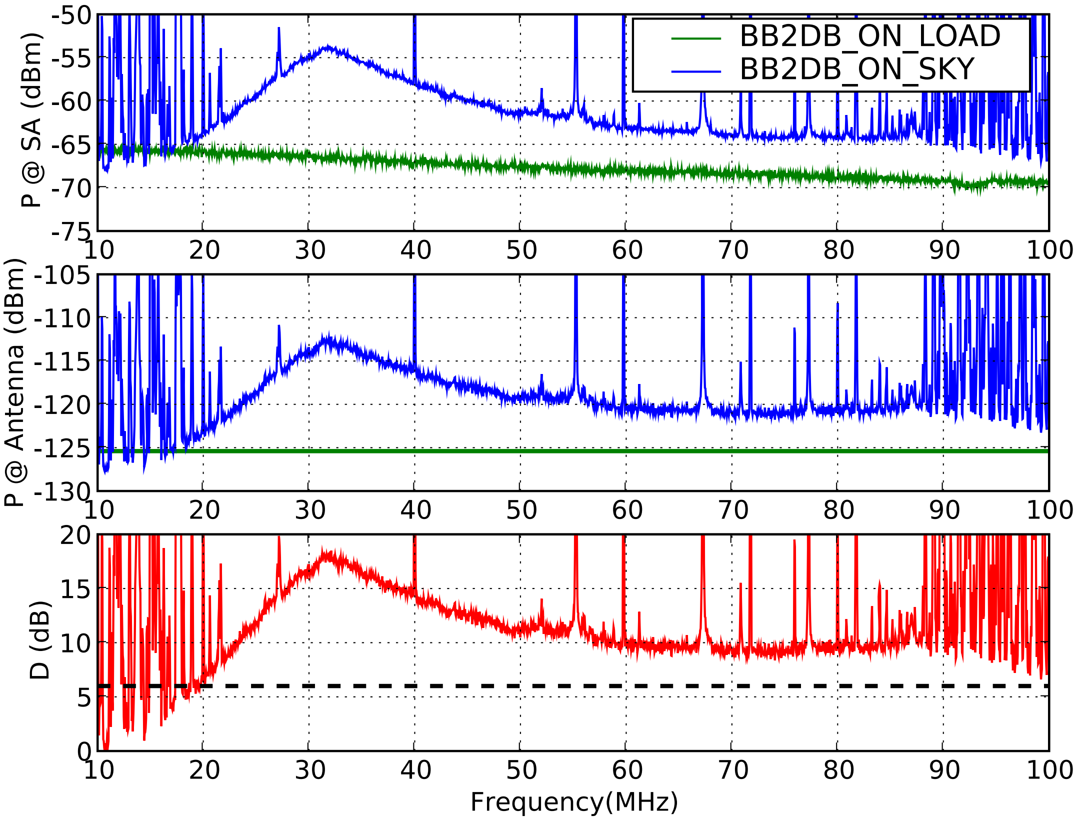

Fig. 9. Measured power for the Big Blade antenna/Discrete balun (BB2DB). The power measured at the Specmaster input (P @ SA) is shown on top. The power measured at the antenna feed point (P @ Antenna) is shown in the middle, and the sky noise dominance (D) is shown on the bottom. In the top plot, $P_{out}^{antenna}$ is in blue and P_{out}^{load} is in green. In the middle plot, $P_{in}^{antenna}$ is in blue and P_{in}^{load} is in green. The resolution bandwidth for this measurement was 51 kHz. D = 6 dB is indicated with a dashed black line in the sky noise dominance plot.

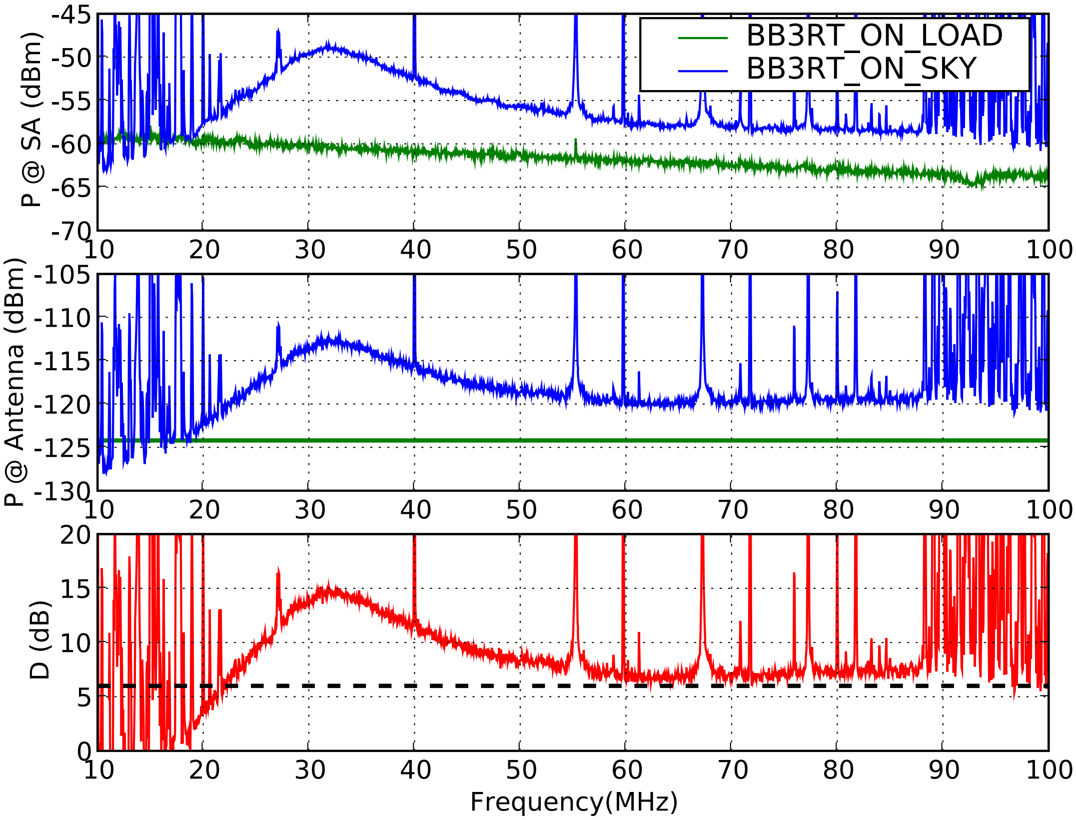

Fig. 10. Measured power for the Big Blade antenna/RTA balun (BB3RT). The power measured at the Specmaster input (P @ SA) is shown on top. The power measured at the antenna feed point (P @ Antenna) is shown in the middle, and the sky noise dominance (D) is shown on the bottom. In the top plot, $P_{out}^{antenna}$ is in blue and P_{out}^{load} is in green. In the middle plot, $P_{in}^{antenna}$ is in blue and P_{in}^{load} is in green. The resolution bandwidth for this measurement was 51 kHz. D = 6 dB is indicated with a dashed black line in the sky noise dominance plot.

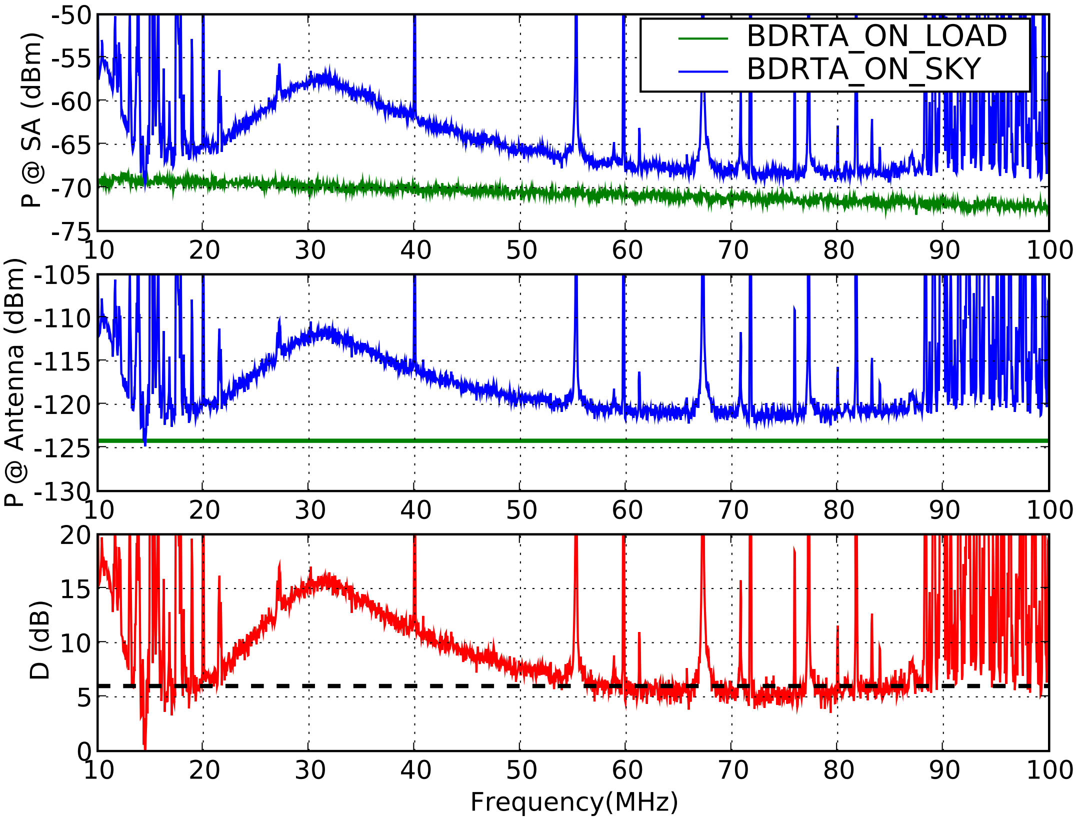

Fig. 11. Measured power for the Blade Frame antenna/RTA balun (BDRTA). The power measured at the Specmaster input (P @ SA) is shown on top. The power measured at the antenna feed point (P @ Antenna) is shown in the middle, and the sky noise dominance (D) is shown on the bottom. In the top plot, $P_{out}^{antenna}$ is in blue and P_{out}^{load} is in green. In the middle plot, $P_{in}^{antenna}$ is in blue and P_{in}^{load} is in green. The resolution bandwidth for this measurement was 51 kHz. D = 6 dB is indicated with a dashed black line in the sky noise dominance plot.

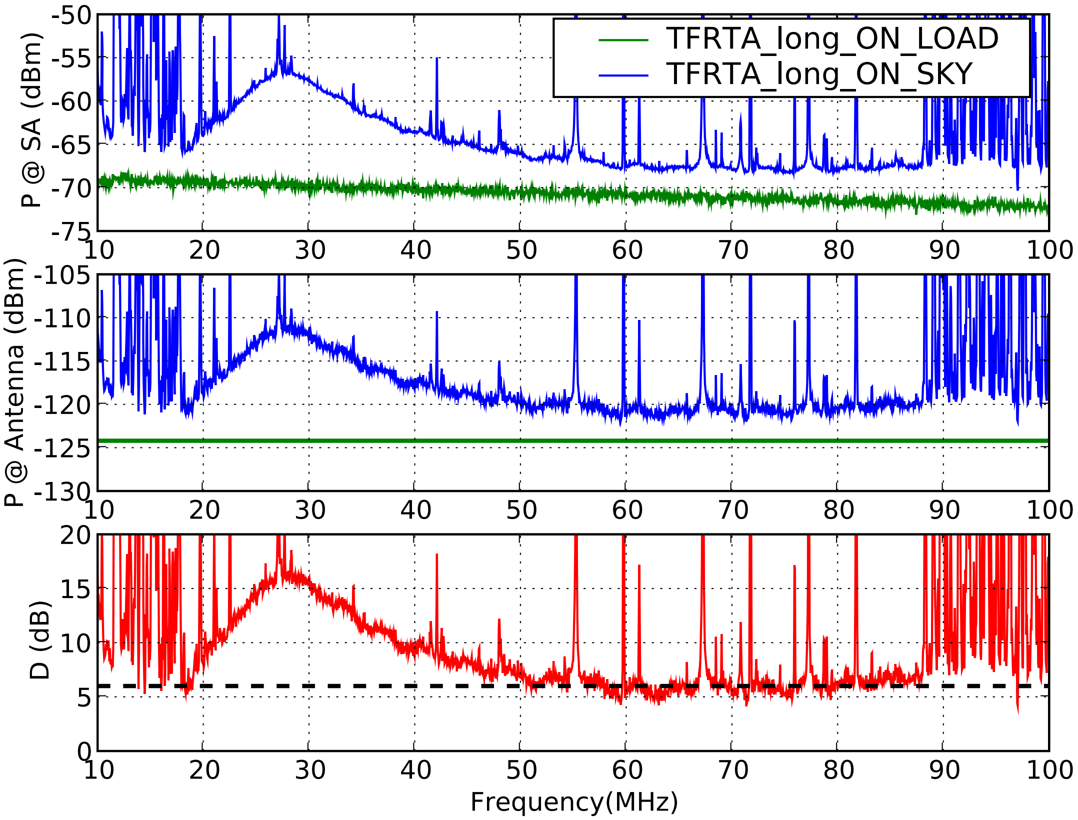

Fig. 12. Measured power for the 1.7 m Tied Fork antenna/RTA balun (TFRTA_long). The power measured at the Specmaster input (P @ SA) is shown on top. The power measured at the antenna feed point (P @ Antenna) is shown in the middle, and the sky noise dominance (D) is shown on the bottom. In the top plot, $P_{out}^{antenna}$ is in blue and P_{out}^{load} is in green. In the middle plot, $P_{in}^{antenna}$ is in blue and P_{in}^{load} is in green. The resolution bandwidth for this measurement was 51 kHz. D = 6 dB is indicated with a dashed black line in the sky noise dominance plot.

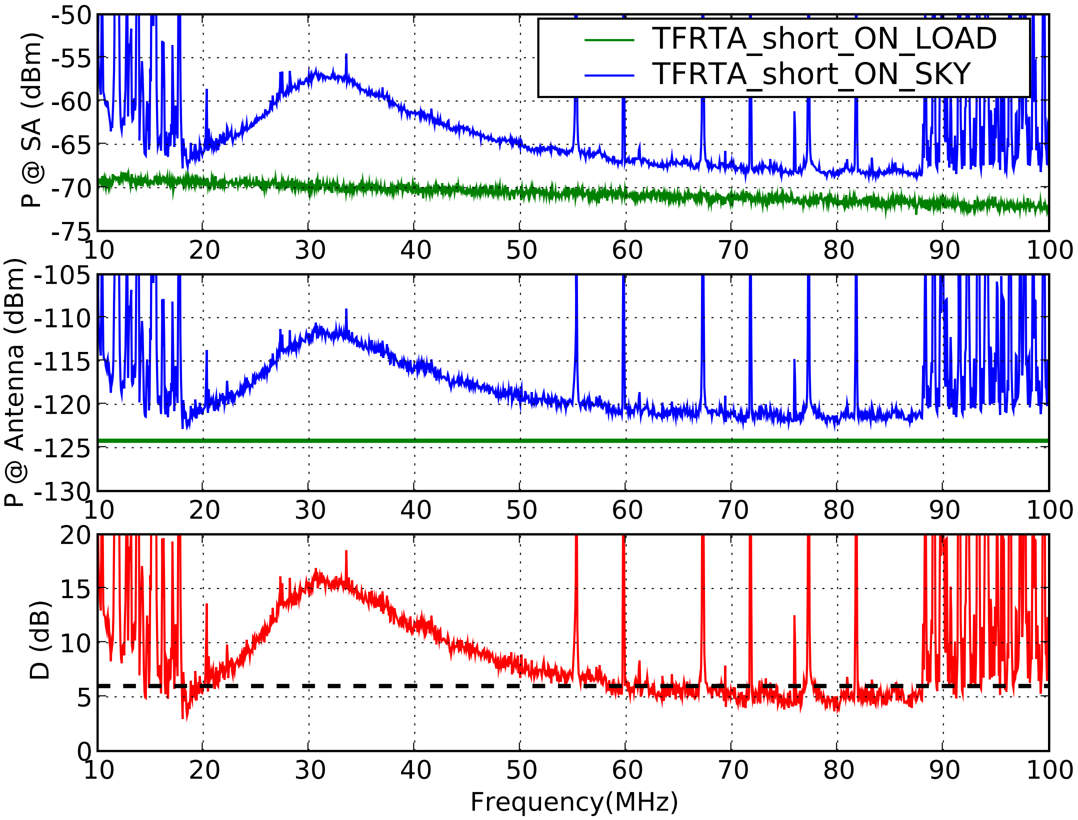

Fig. 13. Measured power for the 1.5 m Tied Fork antenna/RTA balun (TFRTA_short). The power measured at the Specmaster input (P @ SA) is shown on top. The power measured at the antenna feed point (P @ Antenna) is shown in the middle, and the sky noise dominance (D) is shown on the bottom. In the top plot, $P_{out}^{antenna}$ is in blue and P_{out}^{load} is in green. In the middle plot, $P_{in}^{antenna}$ is in blue and P_{in}^{load} is in green. The resolution bandwidth for this measurement was 51 kHz. D = 6 dB is indicated with a dashed black line in the sky noise dominance plot.

III. DRIFT CURVES

Figures 14, 15, 16, 17, and 18 show drift curves for the six active antennas at 25.61 MHz, 38 MHz, 50 MHz, 74 MHz, and 87 MHz respectively. Table IV lists the frequency range and dates of measurement for the data shown in Figures 14 – 18. While all of the active antennas exhibit similar dynamic range at the lower frequencies, differences start appearing around 74 MHz, where the curves for BDRTA and TFRTA_long flatten out at Galactic maximum. Although the cause of this is not certain, one possible explanation can be gleaned from an examination of the beam patterns of the antennas at 74 MHz (shown in Figure 19) and a snapshot of a 74 MHz all sky map taken with the LWDA (shown in Figure 20). The antennas were positioned east-west while they were being measured. Figure 20 shows that at 18 25 hrs LST (Galactic maxiumum), the Galactic center was due south – along the antenna H-planes. The H-plane gains and axial symmetries of the Blade Frame and the 1.7 m Tied Fork are poorer than those of the Big Blade and 1.5 m Tied Fork antennas, resulting in less sky power being coupled in. The next step in this analysis would be to simulate these antenna drift curves using sky models to determine if this explanation is correct. This work is currently in progress.

TABLE IV

ACTIVE ANTENNA DRIFTSCANS

Antenna	Active Balun	Label	Frequency Range	Dates of Measurement
Big Blade	Hicks – Teletech	BB3HT	10 – 100 MHz	July 30 – 31, 2007
Big Blade	Discrete	BB2DB	10 – 100 MHz	August 3 – 6, 2007
Big Blade	RTA	BB3RT	10 – 100 MHz	August 1 – 2, 2007
Blade Frame	RTA	BDRTA	10 – 100 MHz	August 1 – 2, 2007
1.7 m Tied Fork	RTA	TFRTA_long	10 – 100 MHz	August 3 – 6, 2007
1.5 m Tied Fork	RTA	TFRTA_short	10 – 100 MHz	August 15 – 17, 2007

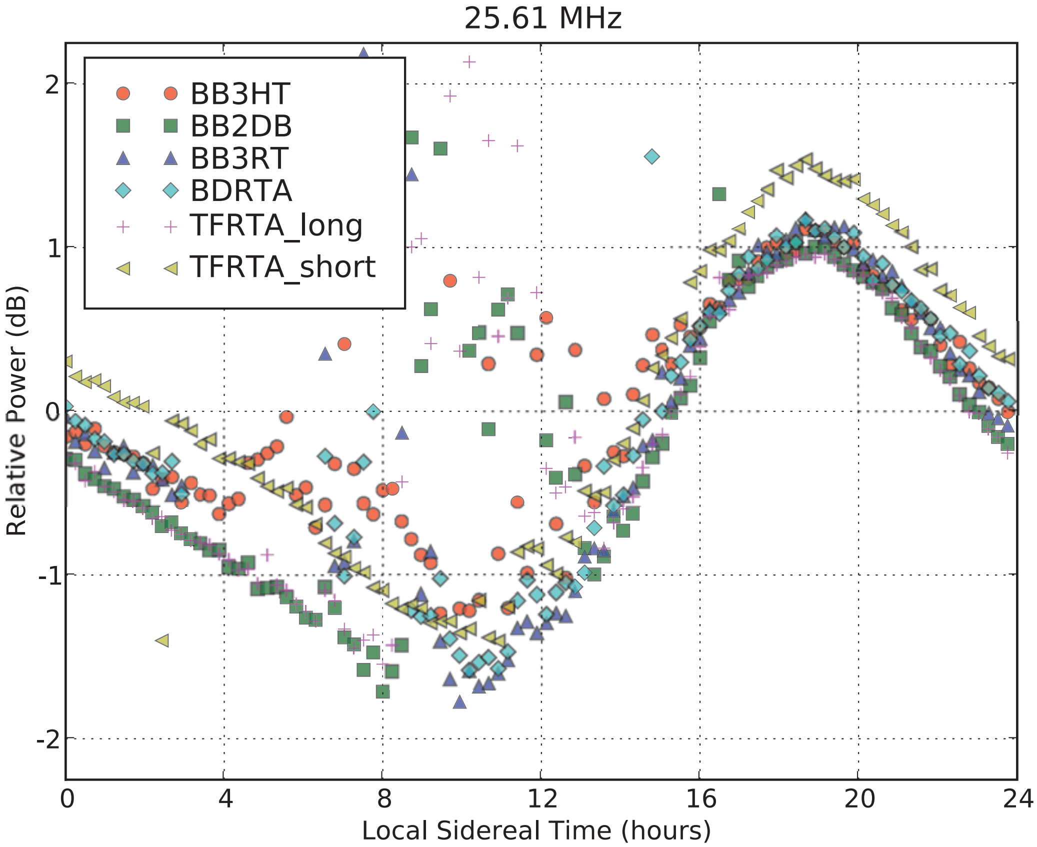

Fig. 14. Drift curves for BB3HT, BB2DB, BB3RT, BDRTA, TFRTA_long, and TFRTA_short at 25.61 MHz.

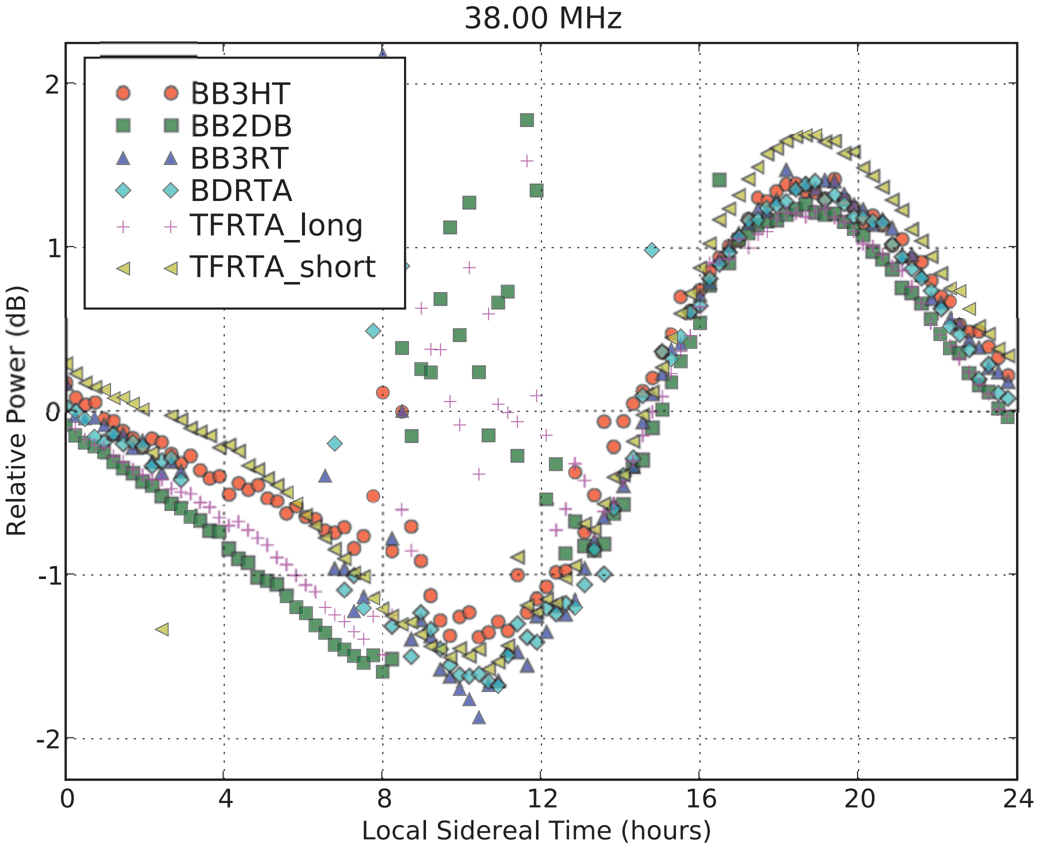

Fig. 15. Drift curves for BB3HT, BB2DB, BB3RT, BDRTA, TFRTA_long, and TFRTA_short at 38 MHz.

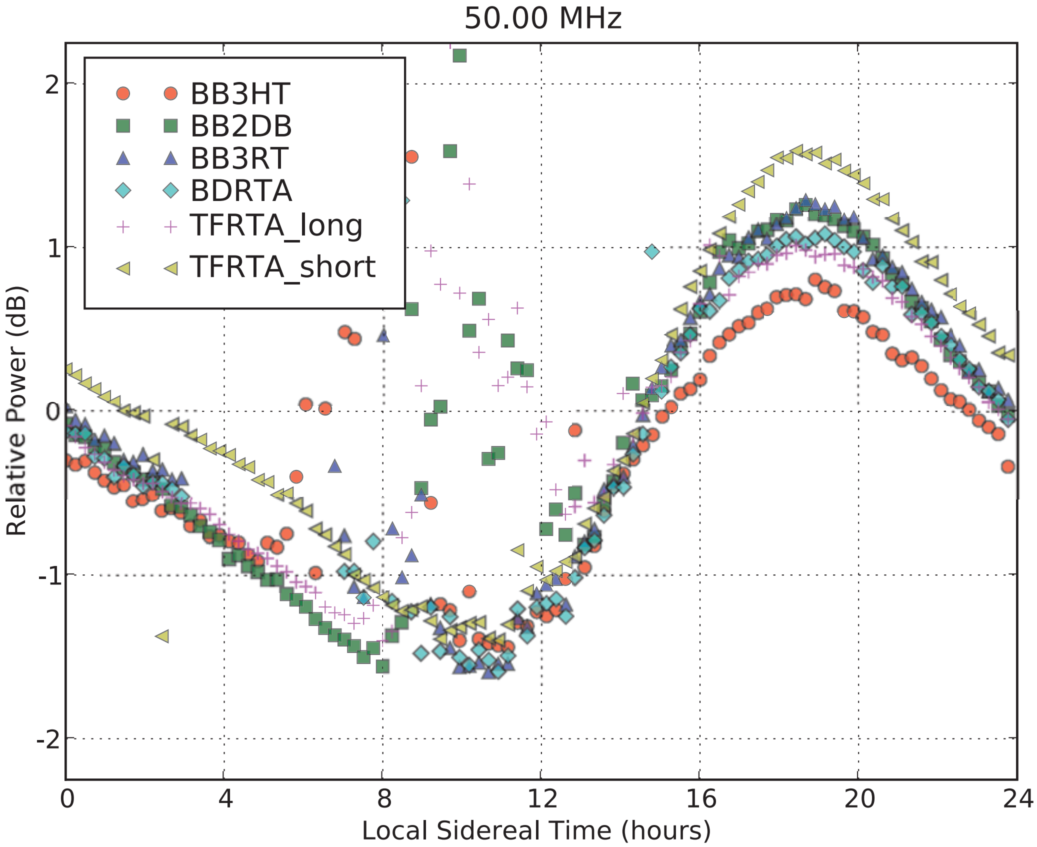

Fig. 16. Drift curves for BB3HT, BB2DB, BB3RT, BDRTA, TFRTA_long, and TFRTA_short at 50 MHz.

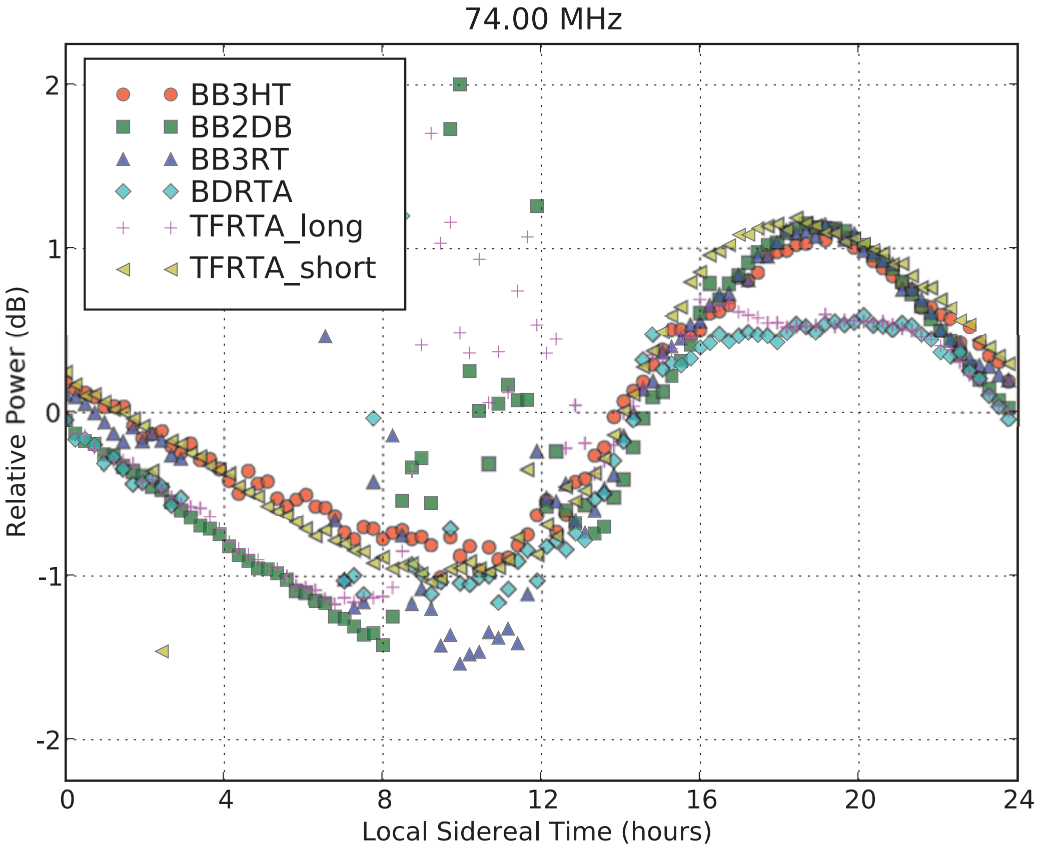

Fig. 17. Drift curves for BB3HT, BB2DB, BB3RT, BDRTA, TFRTA_long, and TFRTA_short at 74 MHz.

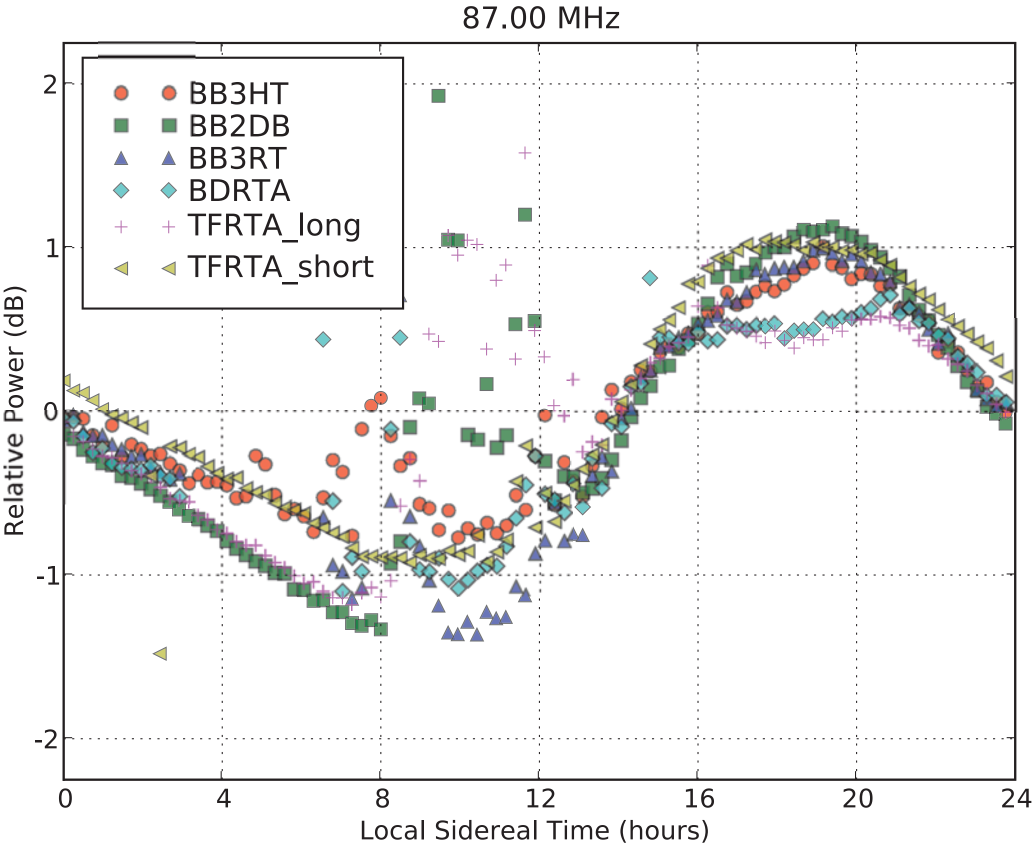

Fig. 18. Drift curves for BB3HT, BB2DB, BB3RT, BDRTA, TFRTA_long, and TFRTA_short at 87 MHz.

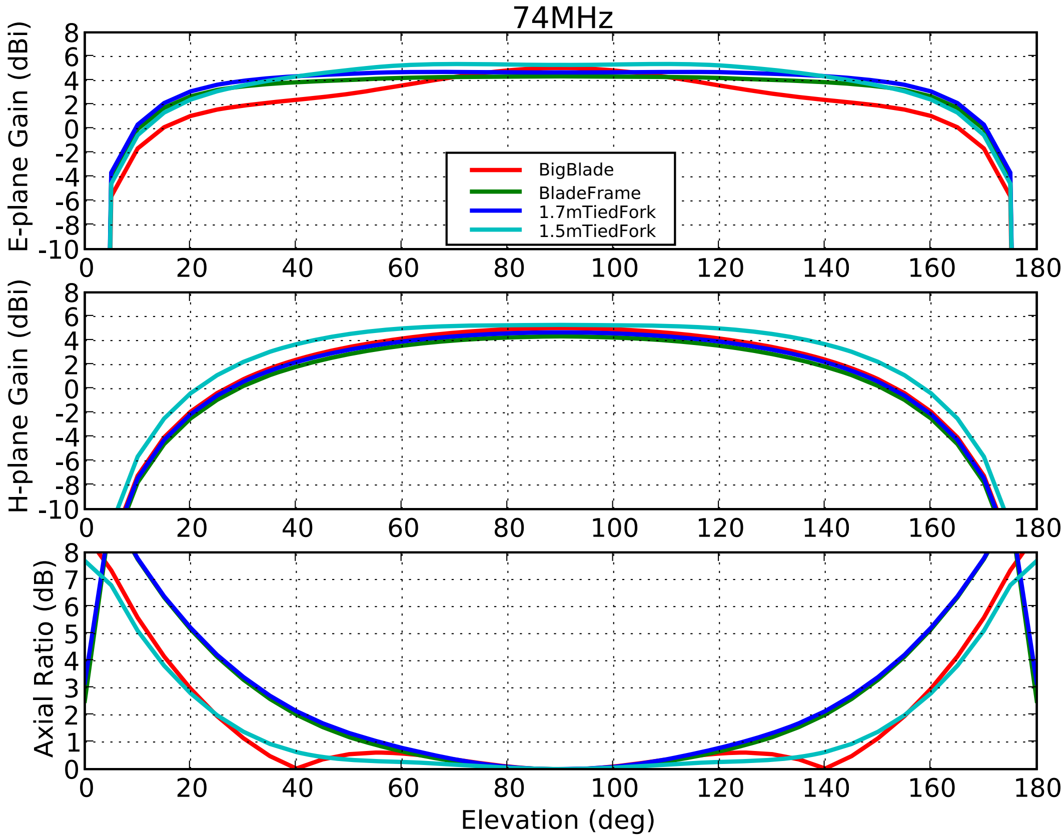

Fig. 19. E- and H-plane beam patterns and axial ratios for the Big Blade, Blade Frame, 1.7 m Tied Fork, and 1.5 m Tied Fork antennas at 74 MHz.

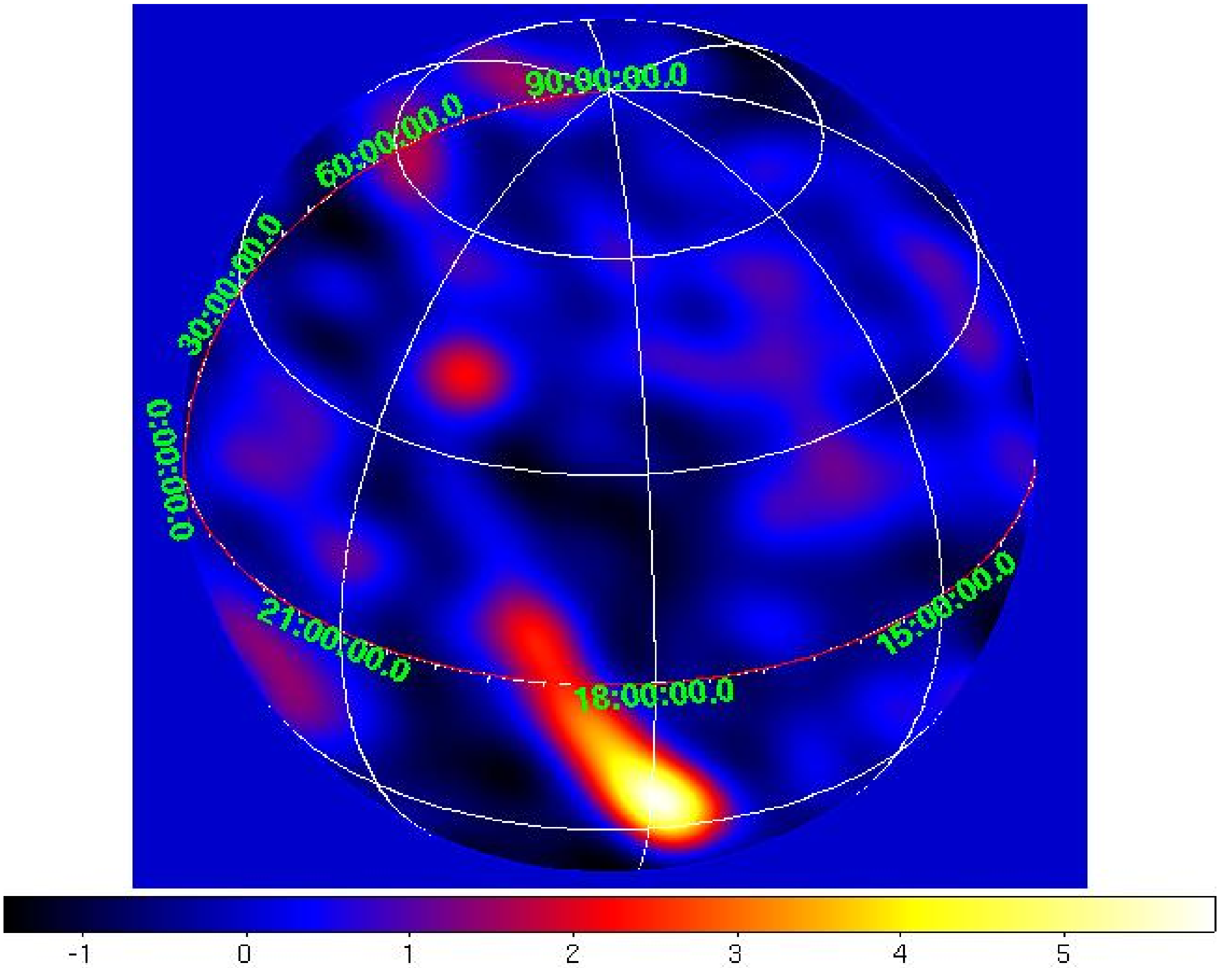

Fig. 20. 74 MHz all sky image taken with the LWDA. The bright source at 18 25 hrs LST is the Galactic center region.

IV. Comparison with Simulation

The ability to accurately simulate and predict the performance of an antenna is a useful tool in determining the viability of a design prior to prototyping. All antennas in this report were modelled in NEC-4, a standard antenna simulation software package. A dielectric constant, ϵ_r, of 13 and a conductivity, σ, of 0.005 S/m were assumed for the Earth ground properties. Using the results of these simulations, predicted sky noise dominance curves were calculated for each active antenna. Figures 21 – 26 show enlarged plots of the measured sky noise dominances first presented in Section II with simulated curves superimposed on each plot. There is good agreement between measurement and simulation for the Big Blade cases (BB3HT, BB2DB, and BB3RT), although the correlation is a bit poorer at higher frequencies for BB2DB and BB3RT. For the Blade Frame, 1.7 m Tied Fork, and 1.5 m Tied Fork antennas (BDRTA, TFRTA_long, and TFRTA_short), the measured response is generally higher and shifted down in frequency compared to the simulated response. This is most probably due to the discrepancies recently discovered between the measured and simulated impedances of these antenna designs. Work is ongoing to determine the reason for this, and to address this problem by improving antenna modelling techniques.

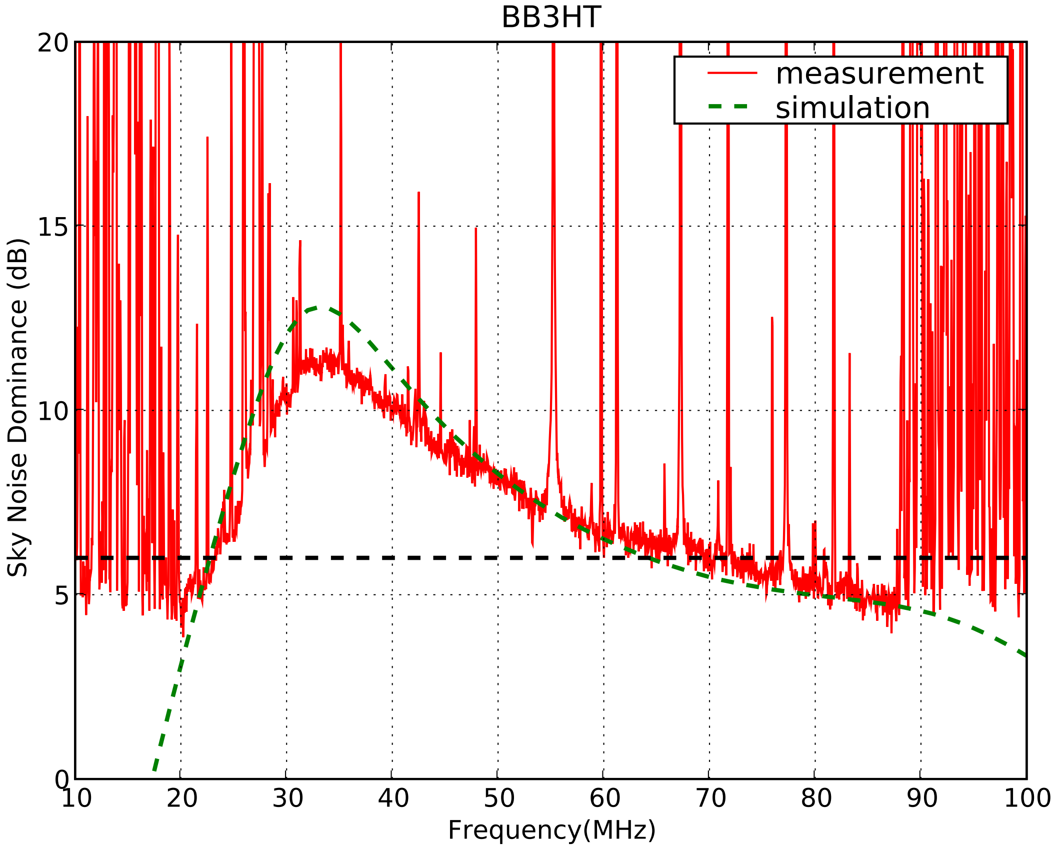

Fig. 21. Measured and simulated sky noise dominance for the Big Blade antenna/Hicks balun (BB3HT).

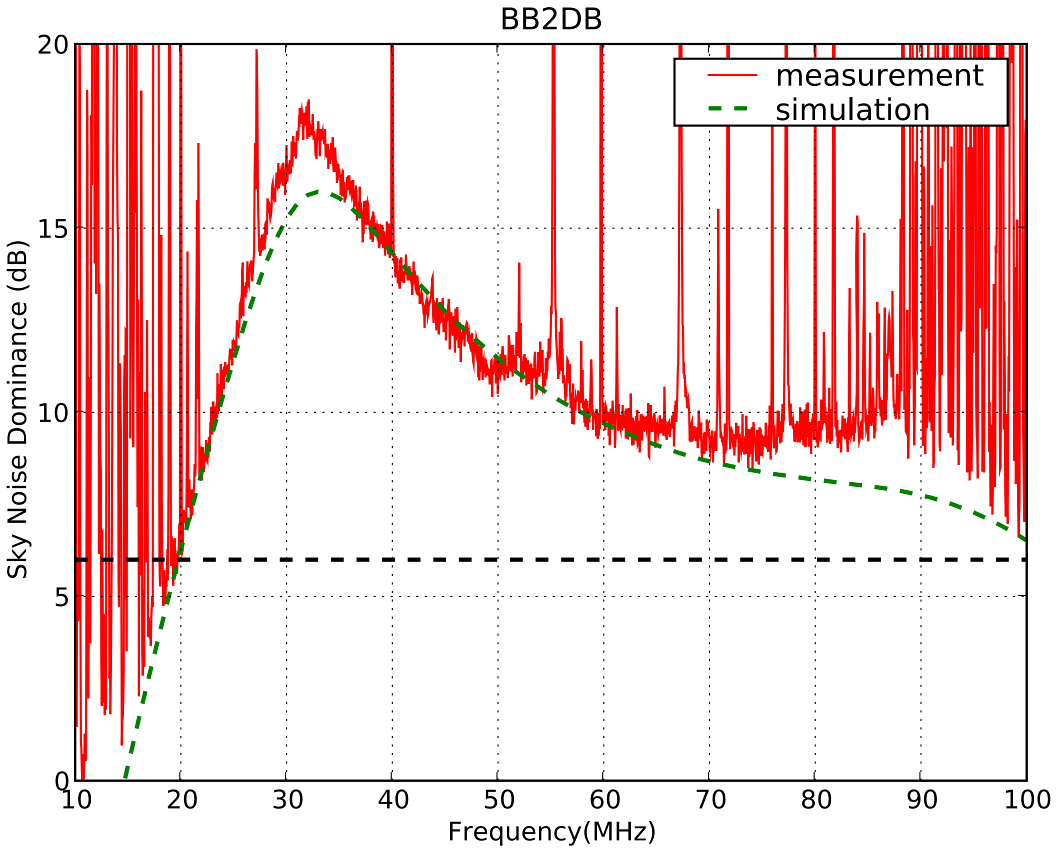

Fig. 22. Measured and simulated sky noise dominance for the Big Blade antenna/Discrete balun (BB2DB).

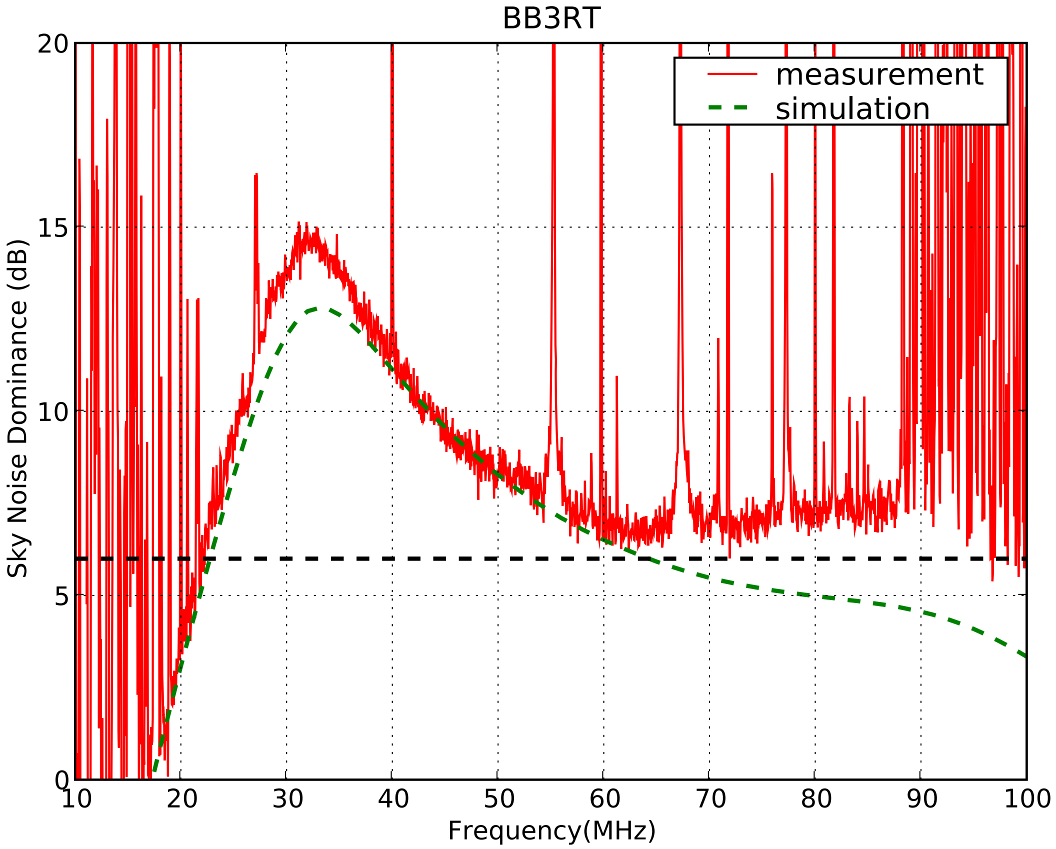

Fig. 23. Measured and simulated sky noise dominance for the Big Blade antenna/RTA balun (BB3RT).

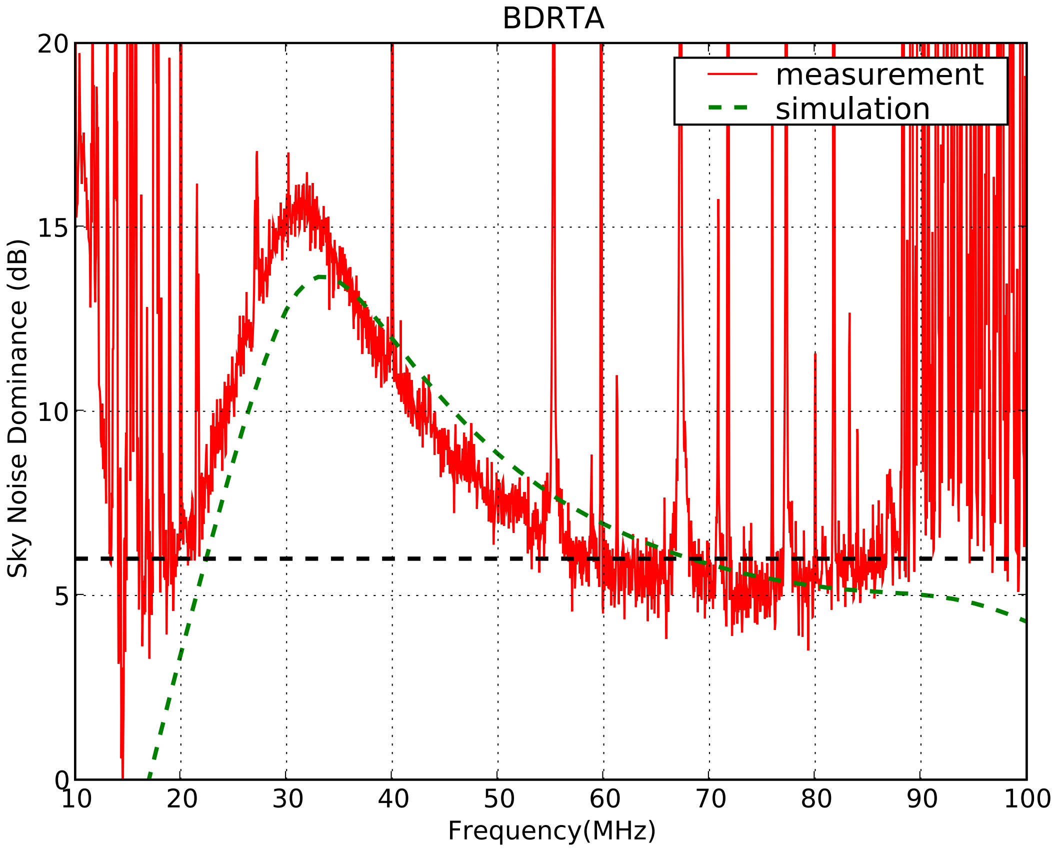

Fig. 24. Measured and simulated sky noise dominance for the Blade Frame antenna/RTA balun (BDRTA).

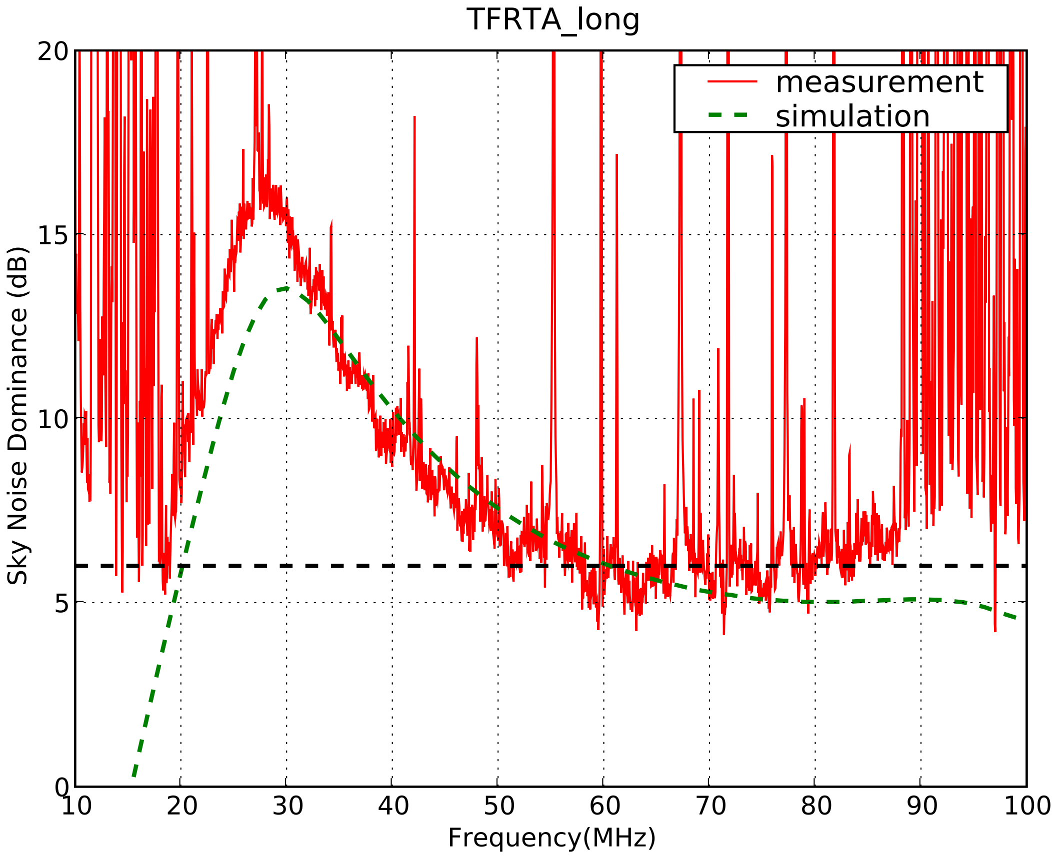

Fig. 25. Measured and simulated sky noise dominance for the 1.7 m Tied Fork antenna/RTA balun (TFRTA_long).

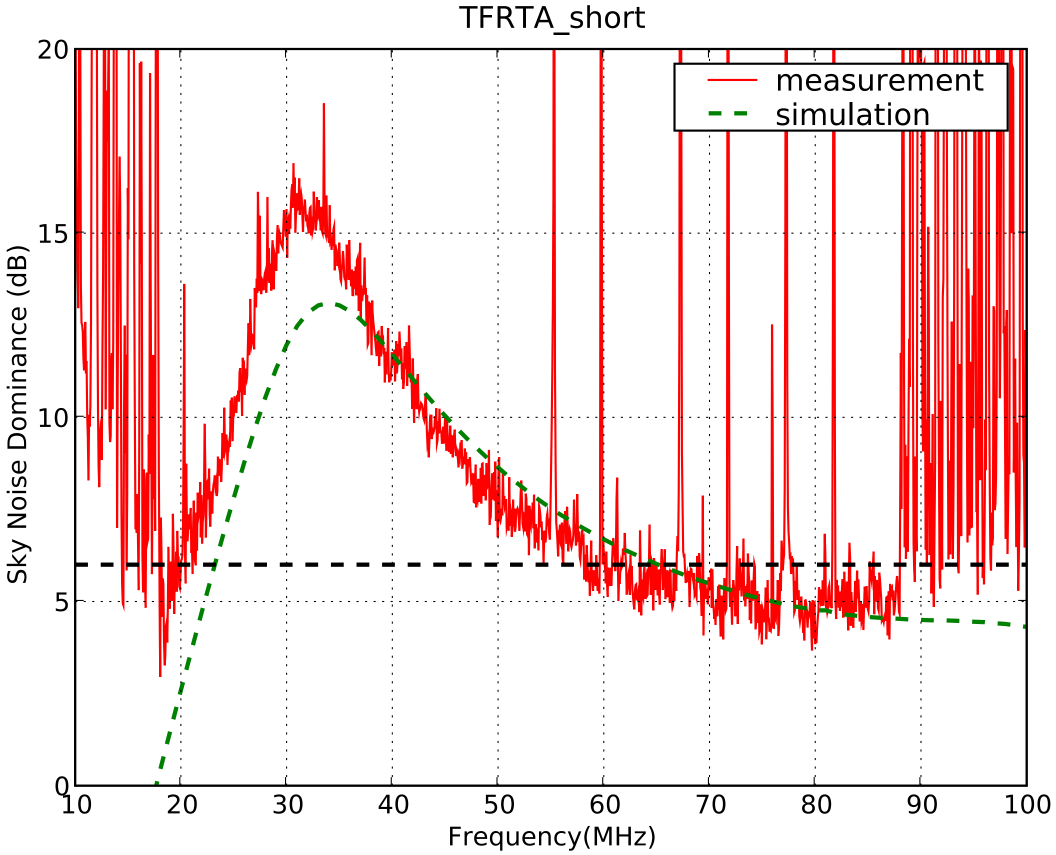

Fig. 26. Measured and simulated sky noise dominance for the 1.5 m Tied Fork antenna/RTA balun (TFRTA_short).

V. CONCLUSIONS

In this report, we have presented measurements of prototype active antenna candidates on ground screens for the Long Wavelength Array. Using the data collected, we have directly calculated the sky noise dominances achieved by each active antenna, and we have created drift curves at five frequencies across the 10 – 100 MHz frequency range. Based on these plots, we make the following comments and conclusions:

- Based on the sky noise dominance plots of the active antennas pairing the Big Blade antenna with the three balun candidates (BB3HT, BB2DB, and BB3RT), both the RTA and the DB baluns display improved performance over the HT balun, with the DB balun yielding the best response of all. It would therefore be worthwhile to consider replacing the HT balun with either the DB or RTA balun in the LWA active antenna design. The DB balun has a more complex circuit layout than the RTA balun, and could therefore be more expensive. Cost-performance tradeoffs between these two baluns must therefore be taken into account in deciding which balun should be chosen to replace the HT balun.
- When the Blade Frame, 1.7 m Tied Fork, and 1.5 m Tied Fork antennas are paired with the RTA balun, TFRTA_long appears to slightly outperform the other two in sky noise dominance. However, a further examination of the drift curves for these antennas reveals a strange "flattening out" at higher frequencies for BDRTA and TFRTA_long. This may be the result of beam pattern deterioration in these two antennas, making them unfavorable for use beyond ~50 MHz. This would make TFRTA_short the most favorable candidate of the three.
- A comparison of measured sky noise dominances with simulated predictions generally shows good agreement for the Big Blade antenna, with room for improvement for the Blade Frame and Tied Fork antennas. It has recently been discovered that simulated impedances of some antenna geometries are not agreeing well with measured values obtained from the antenna prototypes. Since these antenna impedances are used to calculate the simulated sky noise dominance response, improving antenna modelling techniques should enable us to more accurately predict active antenna performance during the antenna modelling stage, prior to prototyping. Work on this is currently in progress.

One more round of testing is scheduled to take place at the LWDA site in February, 2008 on the LWA antenna prototypes. In this round, all active antennas will be tested using the same size ground screens, the same procedures, and the same measurement system to ensure the most accurate side-by-side comparison possible. The 1.5 m Tied Fork/RTA balun will be included in this round of testing. In addition, a 1.5 m Blade Frame antenna/RTA balun (the one considered in this report is 1.75 m) will also be included to determine if shortening the Blade Frame antenna may help eliminate the flattening out in the high frequency drift curves while still maintaining the improved sky noise dominance over the Tied Fork. Finally, we will be performing measurements on "filled" Blade Frame and Tied Fork antennas – with the same outer dimensions as their metal frame counter parts, but with mesh material welded to the frames – paired with RTA baluns to determine if the addition of the metal mesh yields an improvement in performance. We anticipate that this will be the final round of antenna needed to finalize the active antenna design for LWA-1.

ACKNOWLEDGMENT

Basic research in radio astronomy at the Naval Research Laboratory is supported by 6.1 base funding.

APPENDIX

This appendix contains dimensioned drawings of all of the antennas considered in this report. The Big Blade antenna elements were made of 1/8" thick sheet aluminum. The Blade Frame, and Tied Fork antenna elements were made from 1/8" thick 3/4" angle aluminum.

Please note that the drawings are not to scale.

Antenna Profiles

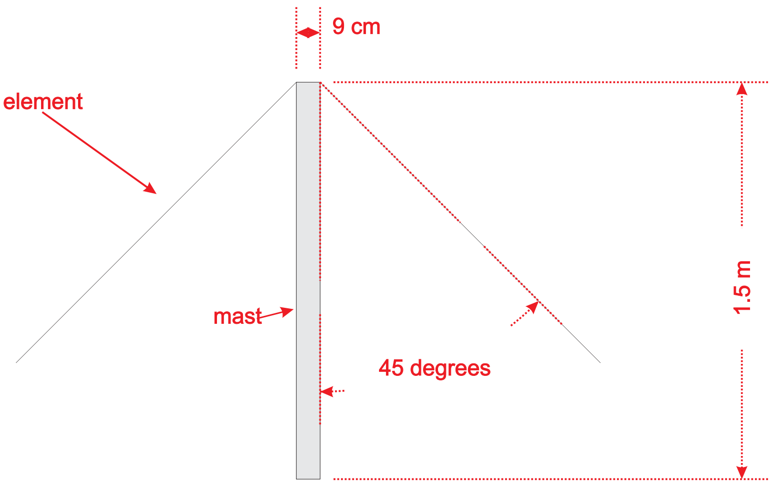

(drawings not to scale)

Antenna Element Dimensions

Big Blade

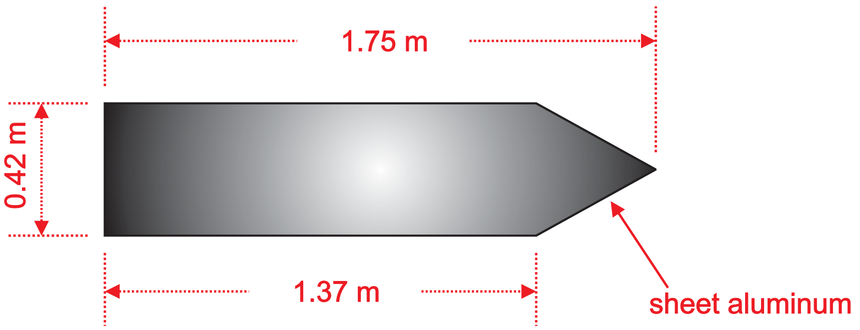

Blade Frame

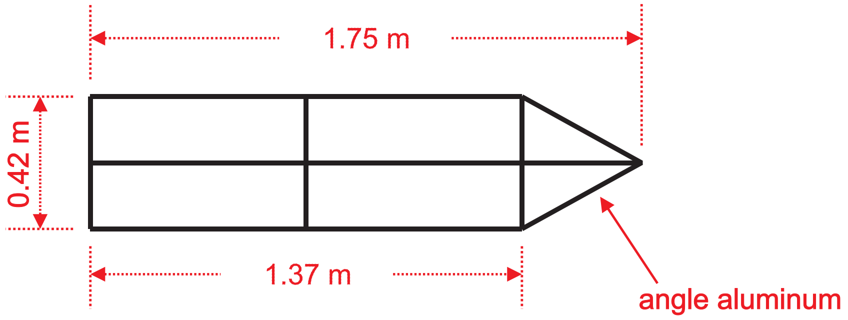

Long Tied Fork

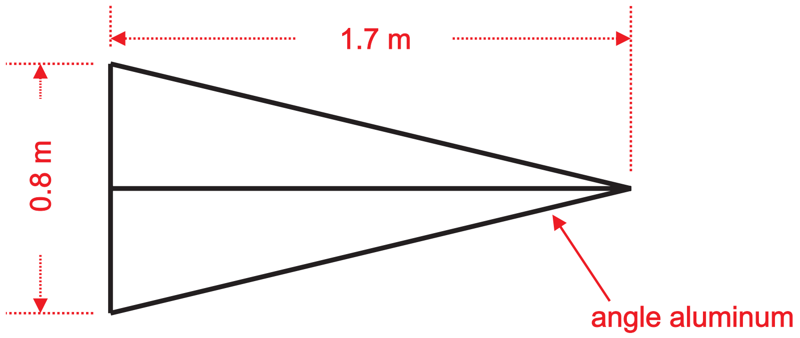

Short Tied Fork

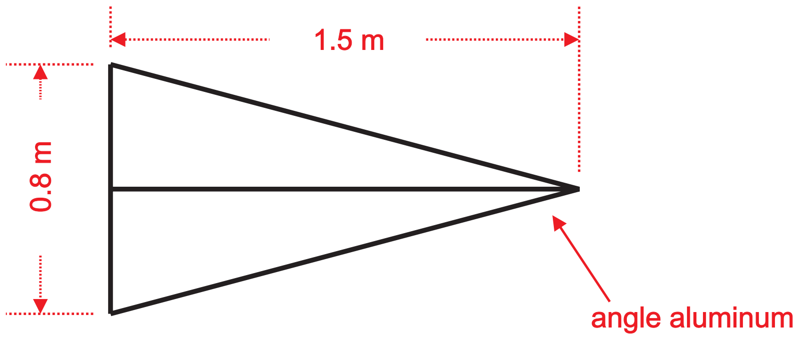

(drawings not to scale)

REFERENCES

[1] N. Kassim, W. Erickson, and P. Ray, “Proposal for a Rapid Test Array (RTA),” *LWA Memo Series (Memo 91)*, June 2007.

[2] B. Hicks, P. Ray, N. Paravastu, R. Duffin, and S. Ellingson, “Specmaster: A Simple Spectrum Monitoring Tool,” *LWA Memo Series (Memo 74)*, January 2007.

[3] R. Bradley and C. Parashare, “Evaluation of the NRL LWA Active Balun Prototype (Rev.A),” *LWA Memo Series (Memo 19)*, February 2005.

[4] N. Paravastu, B. Hicks, R. Bradley, and C. Parashare, “Development and Measurement of a Second Generation Balun Candidate for the LWA,” *LWA Memo Series (Memo 81)*, January 2007.

[5] B. Hicks and N. Paravastu, “The Rapid Test Array Balun (G250R),” *LWA Memo Series (Memo 120)*, January 2008.

LWA Engineering Memo ANT0006
Field Measurements of
Candidate Antenna Designs for LWA-1
June 11, 2008

Nagini Paravastu (NRL/ASEE), William Robbins (ONR Summer Intern),
and Paul Ray (NRL)

Abstract

We report on the current status of impedance measurements on the antenna candidates for LWA-1. We show plots for antenna impedance data collected during an antenna testing campaign at the LWDA site in February, 2008 as well as a second round of measurements done at NRL in June, 2008.

I. INTRODUCTION

In the process of selecting the final antenna design for LWA-1, a prototype of each candidate has been subjected to field tests that include sky spectral measurements (from which sky noise dominance and drift curves could be calculated), and impedance measurements. The data collected from these tests are being compared with simulated predictions and used to perform side-by-side comparisons of the LWA-1 antenna candidates [1], [2]. Through these comparisons, it was determined that the measured antenna impedances do not agree with simulations. We have been working to determine the reasons for this in order to establish confidence in our antenna modeling procedures.

Antenna impedances are measured in the field by connecting an impedance analyzer via a passive power combiner to the antenna elements. In our case, we use a Tele-tech hybrid power combiner, such as the ones being used in the LWDA and G250R active baluns [3], [4]. Through discussions with Aaron Kerkhoff, it was determined that the primary cause of the disagreement between impedance measurement and simulation is the presence the power combiner, which has a non-trivial contribution to the raw measurement data. The properties of the power combiner must therefore be properly accounted for in order to back out the impedance directly at the antenna feed point. Kerkhoff has developed a procedure for this and describes it in [5]. A Python code written to carry out this calculation is given in the Appendix.

II. FIELD MEASUREMENTS

A list of all of the antennas that have been measured, the ground conditions over which they were measured, and designations are given in Table I. For convenience, these antennas will be referred to by their designations in the rest of this report.

The test setup for these measurements is described in [5], and the simulations are described in more detail in [1], [2], and [6].

A. Impedance Measurements at the LWDA Site

The impedances of all antennas listed in Table I (with the exception of TFEG) were measured at the LWDA site in New Mexico in February, 2008. As shown in Figure 1, the output ports of the power combiner (in the blue box) were connected to the antenna elements using 15.24 cm (6 in) long 50 Ω coaxial cables. A 120 m long 50 Ω coaxial cable was used to connect the input of the power combiner to the impedance meter, located inside the LWDA shelter. Before performing the impedance measurements,

TABLE I

ANTENNA DESIGNATIONS

Antenna	Ground	Designation
38 MHz Reference Dipole	7mx6m ground screen	RD38
74 MHz Reference Dipole	7mx6m ground screen	RD74
Big Blade	Earth ground	BBEG
Big Blade	3mx3m ground screen	BBSGS
Big Blade	10mx10m ground screen	BBLGS
Tied Fork	Earth ground	TFEG
Tied Fork	3mx3m ground screen	TFSGS
Blade Frame	3mx3m ground screen	BDSGS
Screen Blade Frame	3mx3m ground screen	SBDSG
Screen Tied Fork	3mx3m ground screen	STFSG
Big Blade	3mx3m ground screen	BBSGS

a calibration was done to compensate for the properties of the 120 m coax. The impedances were therefore measured directly at the power combiner input. An *Array Solutions* AIM 4170 impedance analyzer was used for these measurements and was chosen for its affordability, ruggedness, portability and simplicity.

Figures 2, 3, and 4 show plots of the data that were taken at the site of the reference dipoles, the Big Blades, the Tied Fork, the Blade Frame, the Screen Tied Fork and the Screen Blade Frame. In each plot, the blue curves show the raw measurement, the red curves show the measured antenna impedance after the raw data have been corrected for the properties of the power combiner, and the green curves show simulated predictions from NEC4. In the case of the reference dipole, there is little resemblance between the corrected measured data and simulation. For most of the cases shown in Figures 3 and 4, the measured impedance curves appear narrower than simulation and are downshifted in frequency. In addition, a strong standing wave is evident in all measurements, indicating that the in-field calibration procedure to compensate for the 120 m cable may not have been properly executed, that compensating for such a long cable was beyond the capability of the AIM 4170 impedance analyzer, or that the AIM 4170 is not an appropriate instrument to use for these measurements.

B. Impedance Measurements at NRL

Impedance measurements were reattempted at NRL in June 2008 on TFEG (see Table I). This time around, measurements were performed using both the AIM 4170 as well as an Agilent N3383A vector network analyzer (VNA). A shorter (10 m) 50 Ω coaxial cable was used to connect the power combiner input to the measurement instrument (the AIM or the VNA), and the 15.24 cm long jumpers connecting the power combiner outputs to the antenna elements were replaced with much shorter (3 cm) copper braid.

Both the AIM and VNA data are plotted in Figure 5. As in the previous plots, the blue curves show the raw impedance measurements, the red curves show the corrected data, and the green curves show the simulated predictions. The AIM and VNA data are plotted with solid and dashed lines respectively and are nearly identical, indicating that the problems with the measurements done at the LWDA site were not related to the choice of impedance meter, but were most likely due to the long cable lengths at the power combiner input and output. This time, the shape and amplitudes of the corrected data curves also agree much more closely with the simulated curves, but the measurements are shifted down in frequency by $\sim$20%. While ground properties and parasitics due to connectors used in testing that were not included in the modeling could result frequency shifts of a few percent, the cause of a shift as large as that which was observed has not yet been determined.

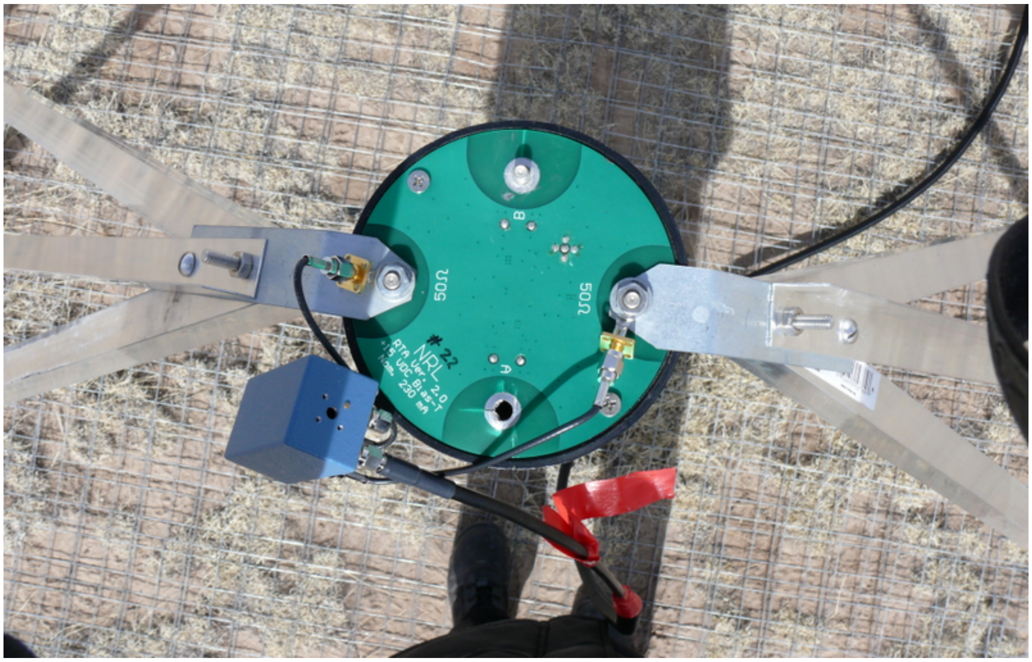

Fig. 1. The Tele-tech hybrid power combiner (in blue box) connected to an antenna for impedance measurements at the LWDA site.

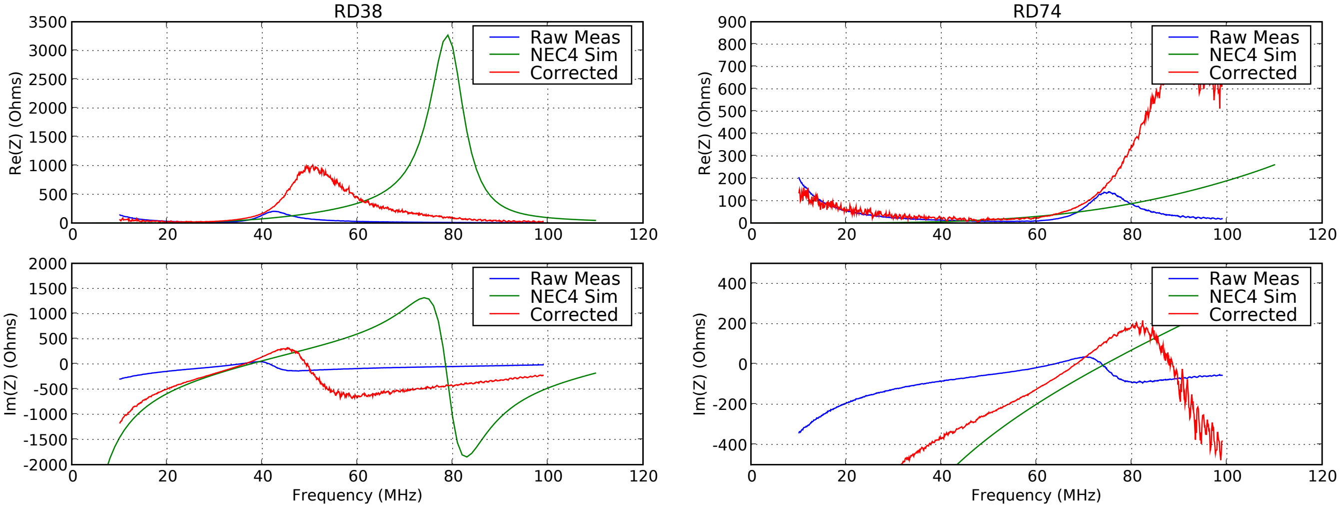

Fig. 2. The raw measured, corrected, and simulated impedances of RD38 (left) and RD74 (right).

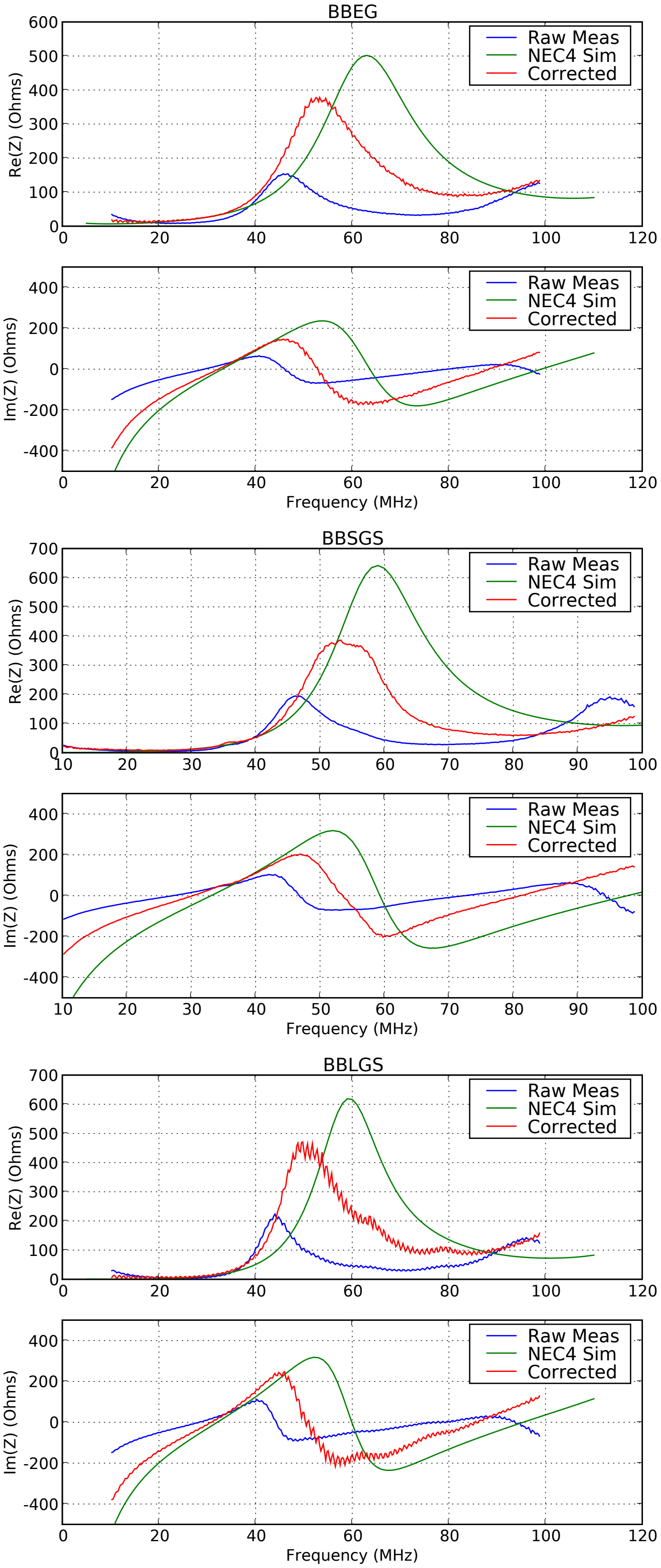

Fig. 3. The raw measured, corrected, and simulated impedances of BBEG (top), BBSGS (middle), and BBLGS (bottom).

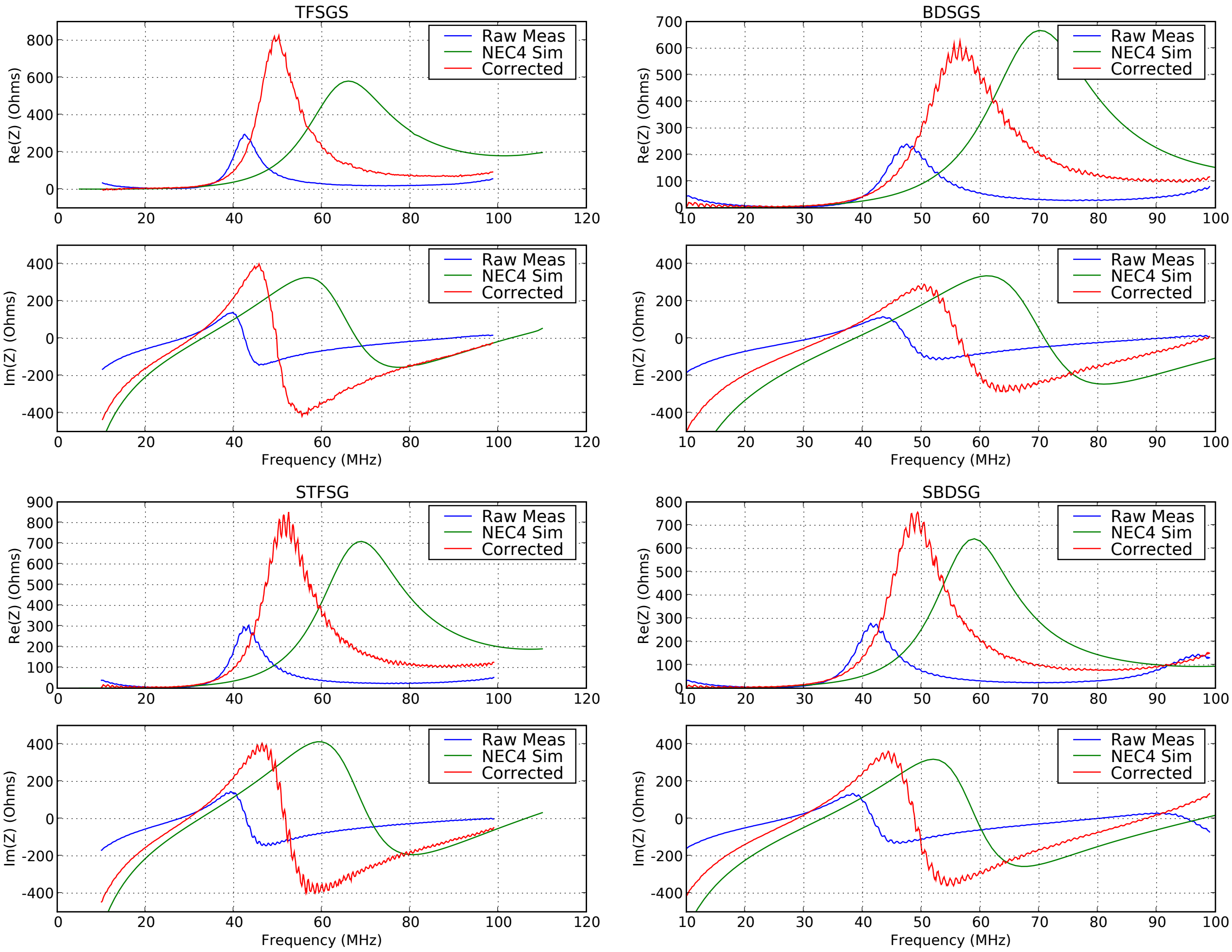

Fig. 4. The raw measured, corrected, and simulated impedances of TFSGS (top left), BDSGS (top right), STFSG (bottom left), SBDSG (bottom right).

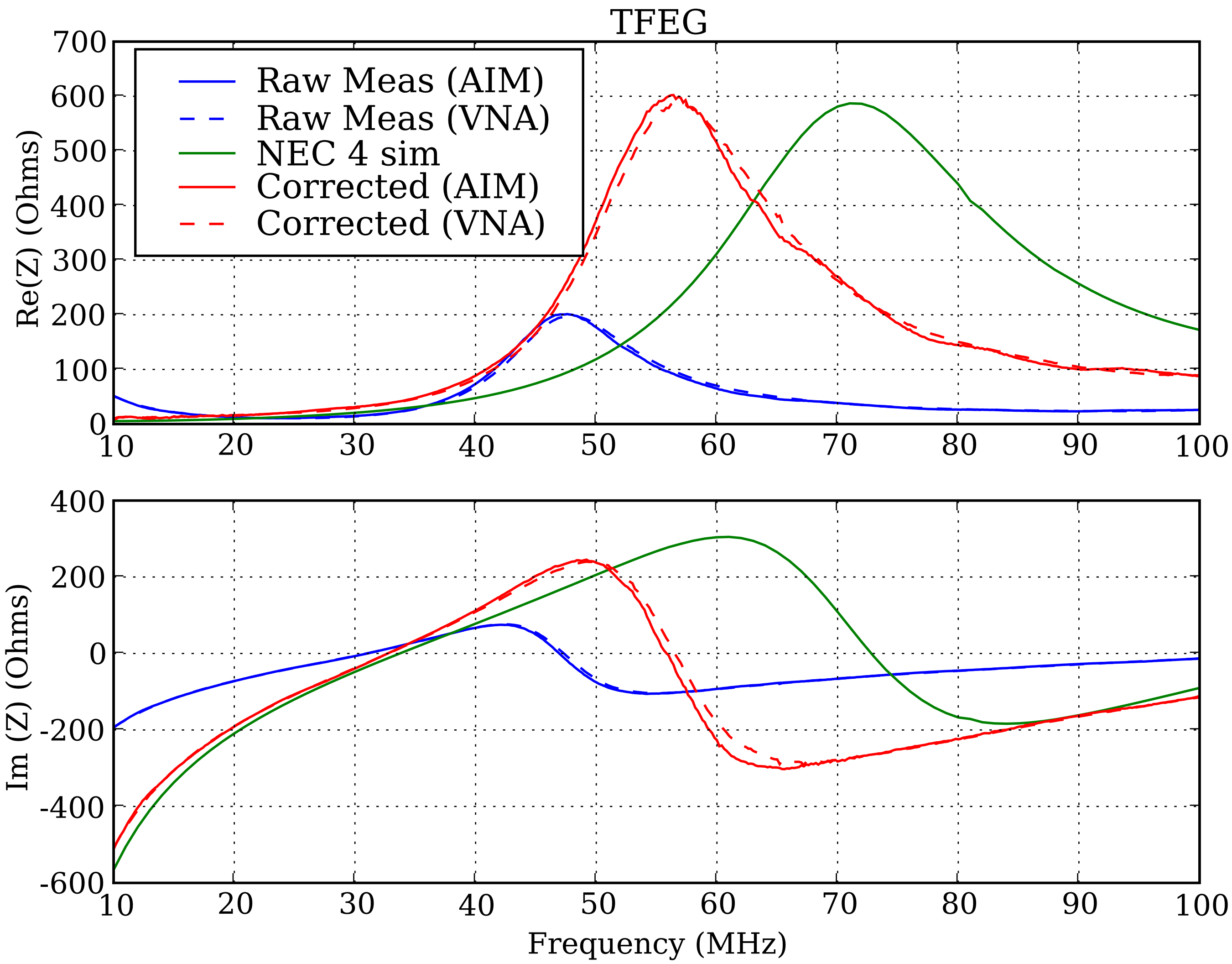

Fig. 5. The raw measured, corrected, and simulated impedances of TFEG.

III. NEC4 SIMULATIONS

In addition to the field measurements, we have been taking a closer look at our antenna modeling techniques. The Tied Fork antenna elements used in these impedance measurements are made of segments angle aluminum which are 3/4 in. (1.9 cm) wide on a side. Because NEC4 can only model wires with circular cross sections, an “effective wire diameter” must be used in the simulations that most closely simulates the properties of the angle aluminum. In Figure 6, the measured TFEG impedance curves (obtained from the AIM 4170) are compared with NEC 4 simulations of TFEG with 25 mm, 50 mm, and 75 mm wire diameters. The full wave resonances of the simulated curves move down in frequency with increasing wire thickness as expected, but the difference in the full wave resonant frequencies between measurement and the 75 mm wire diameter simulation remained high (15%).

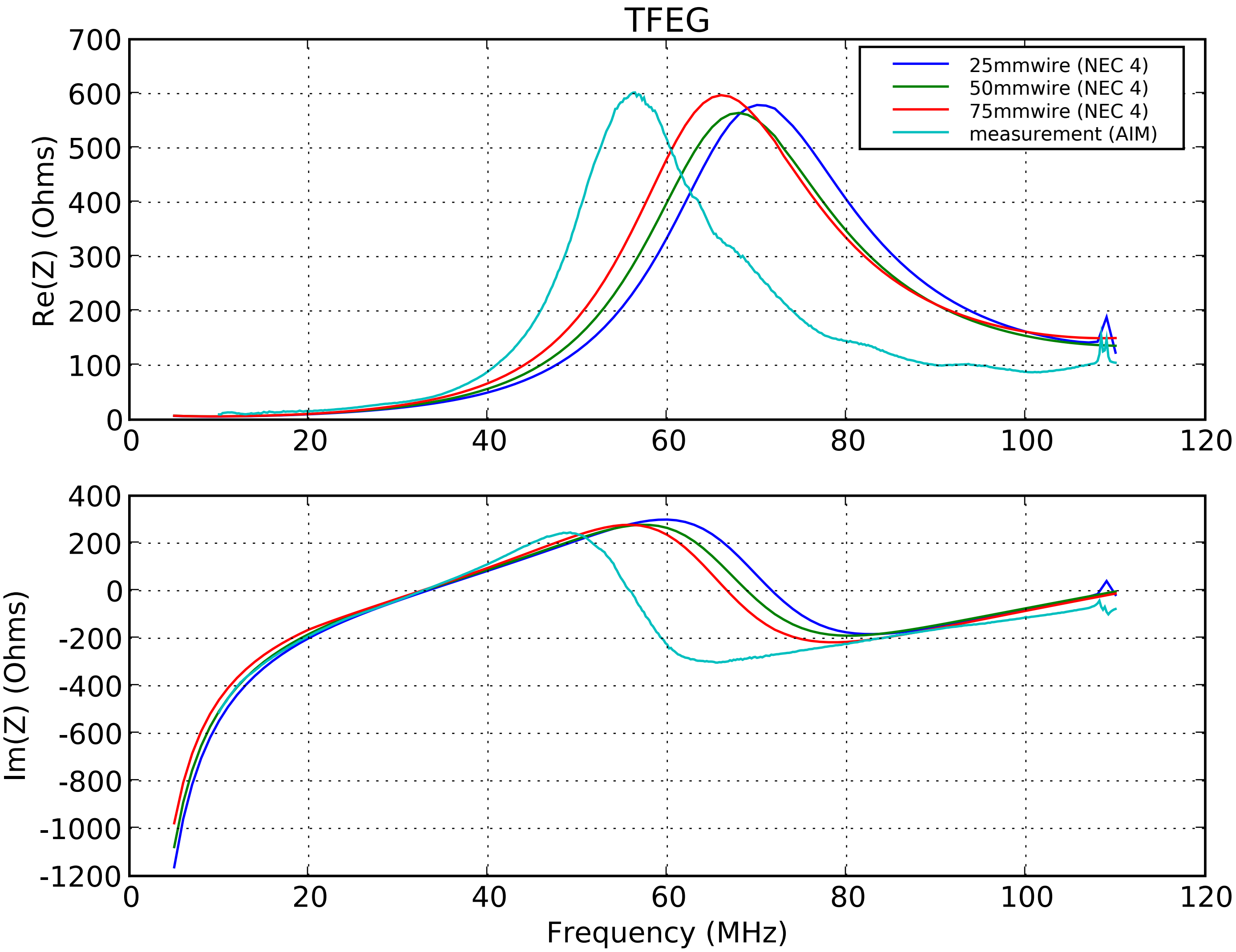

Fig. 6. The corrected (AIM) impedance measurements of TFEG compared with NEC 4 simulations of TFEG using 25 mm, 50 mm, and 75 mm wire diameters.

IV. SUMMARY

We have reported on the most recent progress made in an effort to properly understand and model the feed point impedances of antenna designs that are being considered for LWA-1. An s-parameter extraction procedure developed by Aaron Kerkhoff has been used to take raw impedance measurements obtained in the field and back out the true antenna feed point impedance. So far, we have not been entirely successful, although making some changes to the test setup during the latest round of measurements at NRL has yielded some improvement in our results. We have also been re-examining our modeling techniques to determine if refinements could be made to more accurately simulate our antennas.

APPENDIX

This appendix contains the Python code used to execute Kerkhoff's s-parameter extraction calculation.

```
#!/usr/bin/env python

import sys
import os
import re
from numpy import *
import pylab
from lwda_util import nec_util
from lwda_util.mathutil import to_dB

def cplx_regrid(x,y,newx):
    '''Regrid x,y data onto a new x axis grid points.
    y is a COMPLEX array, so it interpolates the real and imag parts
    separately.'''
    if newx.min() < x.min():
        raise ValueError, 'x.min(%f) must be smaller than newx.min(%f)'
% (x.min(), newx.min())
    if newx.max() > x.max():
        raise ValueError, 'x.max(%f) must be larger than newx.max(%f)'
% (x.max(), newx.max())

    r = interp(newx,x,y.real)
    i = interp(newx,x,y.imag)

    return array([complex(rr,ii) for rr,ii in zip(r,i)])

class s3p_file:
    '''Read in a set of 3-port S-parameter matrices from a file.
    Expects format as written directly by network analyzer (3
lines/meas)
    Returns an object with a list of frequencies in freqs_Hz
    and a list of 3x3 matrices in smats.'''
#!S3P File: Measurements: <S11,S12,S13>, <S21,S22,S23>, <S31,S32,S33>:
    def __init__(self, infile):
        freqlist = []
        matlist = []
        cnt = 0
        for line in file(infile):
            if (line[0] == '!') or (line[0] == '#'):
                print line,
                continue
            X = array([float(i) for i in line.split()])
            if cnt == 0:
                freqlist.append(X[0])
                s11 = complex(X[1],X[2])
                s12 = complex(X[3],X[4])
                s13 = complex(X[5],X[6])
                cnt = 1
            elif cnt == 1:
                s21 = complex(X[0],X[1])
                s22 = complex(X[2],X[3])
                s23 = complex(X[4],X[5])
                cnt = 2
            elif cnt == 2:
                s31 = complex(X[0],X[1])
                s32 = complex(X[2],X[3])
                s33 = complex(X[4],X[5])
```

```
                cnt = 0

matlist.append(matrix([[s11,s12,s13],[s21,s22,s23],[s31,s32,s33]]))
        self.freqs_Hz = array(freqlist)
        self.smats = matlist

def cnv3to2ports(s):
    '''Convert a 3-port S-parameter matrix to an equivalent 2-port
model.'''
    s2p = matrix([[s[0,0], (s[0,1]-s[0,2])/2.0],
    [s[1,0]-s[2,0], (s[1,1]+s[2,2]-s[1,2]-s[2,1])/2.0 ]])
    return s2p

def s2t(s):
    '''Convert 2-parameter S-matrix to a T-matrix as on
    page 14 of Agilent App Note AN154.'''
    t = matrix([[-1.0*(s[0,0]*s[1,1]-s[0,1]*s[1,0])/s[1,0],
s[0,0]/s[1,0]],
    [-1.0*s[1,1]/s[1,0], 1.0/s[1,0] ]])
    return t

def t2s(t):
    '''Convert 2-parameter T-matrix to an S-matrix as on
    page 14 of Agilent App Note AN154.'''
    s = matrix([[t[0,1]/t[1,1], (t[0,0]*t[1,1]-t[0,1]*t[1,0])/t[1,1]],
    [1.0/t[1,1], -1.0*t[1,0]/t[1,1]]])
    return s

def gamma_from_Z(Z,Z0=50.0):
    '''Compute the reflection coefficient gamma from an impedance Z
(which can be an array).
    Assumes Z0=50 ohms, unless overridden by the Z0 keyword parameter.
    '''
    return (Z-Z0)/(Z+Z0)

if __name__ == "__main__":

    # Setup parameters

    # Reference impedance of transmission lines
    Z0 = 50.0
    # Characteristic impedance of transmission line from dipole
terminal
    # to balun input
    Z0k = 100.0 # For NRL measurements
    # Z0k = 100.0 # For field measurements at site
    # Cable length (cm)
    # L = 8.0 # For NRL measurements
    L = 15.2 # For field measurements at site
    # Speed of light (cm/s)
    c = 2.99792E10

    # Read 3-port S-parameter matrices
    s3p = s3p_file('ports12and3_v3.s3p')
    fidx = where(s3p.freqs_Hz > 74000000.0)[0][0]
    print "Index :",fidx
    print "Freq %f: " % s3p.freqs_Hz[fidx]
```

```
    print "Smatrix :"
    print s3p.smats[fidx]
    print "Smatrix(dB):"
    # Need 2.0 to show dB power ratios
    print 2.0*to_dB(abs(s3p.smats[fidx]))

    # Convert to 2-port representation
    freqs_Hz = s3p.freqs_Hz
    freqs_MHz = freqs_Hz/1.0E6
    s2pmats = [cnv3to2ports(s) for s in s3p.smats]
    print "2-port model"
    print s2pmats[fidx]
    print "2-port Smatrix(dB):"
    # Need 2.0 to show dB power ratios
    print 2.0*to_dB(abs(s2pmats[fidx]))

    # Convert to a T matrix
    tmats = [s2t(s) for s in s2pmats]
    print "T-matrix"
    print tmats[fidx]

    print "And back to S-matrix"
    print t2s(tmats[fidx])
    print "...as dB"
    print 2.0*to_dB(abs(t2s(tmats[fidx])))

    # Compute S matrix for cable
    Z0kbar = Z0k/Z0
    lambda0 = c / freqs_Hz
    betaL = 2.0*pi*L/lambda0
    scab1 = 1j*(Z0kbar**2-
1.0)*sin(betaL)/(2.0*Z0kbar*cos(betaL)+1j*(Z0kbar**2+1)*sin(betaL))
    scab2 =
2.0*Z0kbar/(2.0*Z0kbar*cos(betaL)+1j*(Z0kbar**2+1)*sin(betaL))
    scabs = [matrix([[sc1, sc2],[sc2,sc1]]) for sc1,sc2 in
zip(scab1,scab2)]
    tcabs = [s2t(s) for s in scabs]

    # Combine T-matrices from hybrid and cable
    Ttots = [tm*tc  for tm,tc in zip(tmats,tcabs)]

    # Convert back to an S matrix
    Stots = [t2s(t) for t in Ttots]
    print "Stotal"
    print 2.0*to_dB(abs(Stots[fidx]))

    # Read measured impedances
    antenna_meas_file = 'TFSGS.csv'
    freqs_MHz_meas,ReZ_meas,ImZ_meas =
pylab.load(antenna_meas_file,unpack=True,skiprows=5,usecols=(0,2,3),del
imiter=',')
    Z_meas = array([complex(r,i) for r,i in zip(ReZ_meas,ImZ_meas)])
    idx = (freqs_MHz_meas < 99.0) & (freqs_MHz_meas > 10.0)
    freqs_MHz_meas = freqs_MHz_meas[idx]
    Z_meas = Z_meas[idx]

    # Read simulated impedances
```

```
    antenna = 'BDSGS'
    nec = nec_util.NECImpedance('%s.NEC' %antenna)

    # Convert measured impedances into gammas
    gamma_meas = gamma_from_Z(Z_meas,Z0=50.0)

    # First, need to map S parameters onto measured frequency grid
(freqs_MHz_meas)
    s11 = array([s[0,0] for s in Stots])
    s12 = array([s[0,1] for s in Stots])
    s21 = array([s[1,0] for s in Stots])
    s22 = array([s[1,1] for s in Stots])
    s11_r = cplx_regrid(freqs_MHz,s11,freqs_MHz_meas)
    s12_r = cplx_regrid(freqs_MHz,s12,freqs_MHz_meas)
    s21_r = cplx_regrid(freqs_MHz,s21,freqs_MHz_meas)
    s22_r = cplx_regrid(freqs_MHz,s22,freqs_MHz_meas)

    # Now, use them to compute gamma_ant
    gamma_ant = (s11_r - gamma_meas)/(s11_r*s22_r-s11_r*gamma_meas -
s12_r*s21_r)
    if 0:
        pylab.figure(2)
        pylab.plot(freqs_MHz_meas,gamma_ant.real,'g')
        pylab.plot(freqs_MHz_meas,gamma_meas.real,'b')
        pylab.plot(freqs_MHz_meas,gamma_ant.imag,'g.')
        pylab.plot(freqs_MHz_meas,gamma_meas.imag,'b.')
        pylab.grid(1)

    # Compute Z_ant
    Z_ant = 2.0*Z0*(1.0+gamma_ant)/(1.0-gamma_ant)

    pylab.figure(1)
    pylab.subplot(211)
    pylab.plot(freqs_MHz_meas,Z_meas.real,label='Raw Meas')
    pylab.plot(nec.freqs,nec.z.real,label='NEC4 Sim')
    pylab.plot(freqs_MHz_meas,Z_ant.real,label='Corrected')
    pylab.ylabel('Re(Z) (Ohms)')
    pylab.grid(1)
    pylab.legend()
    pylab.title('%s' %antenna)
    pylab.subplot(212)
    pylab.plot(freqs_MHz_meas,Z_meas.imag,label='Raw Meas')
    pylab.plot(nec.freqs,nec.z.imag,label='NEC4 Sim')
    pylab.plot(freqs_MHz_meas,Z_ant.imag,label='Corrected')
    pylab.xlabel('Frequency (MHz)')
    pylab.ylabel('Im(Z) (Ohms)')
    pylab.grid(1)
    pylab.ylim((-500.0,500.0))
    pylab.legend()
    #pylab.savefig('%s.eps' %antenna)
    pylab.show()
```

REFERENCES

[1] N. Paravastu, "LWA Engineering Memo ANT0004 - Big Blade Measurement Plots," *LWA Engineering Memo Series (ANT0004)*, April 2008.

[2] ——, "LWA Engineering Memo ANT0006 - Field Measurements of Candidate Antenna Designs for LWA-1," *LWA Engineering Memo Series (ANT0006)*, April 2008.

[3] R. Bradley and C. Parashare, "Evaluation of the NRL LWA Active Balun Prototype (Rev.A)," *LWA Memo Series (Memo 19)*, February 2005.

[4] B. Hicks and N. Paravastu, "The Rapid Test Array Balun (G250R)," *LWA Memo Series (Memo 120)*, January 2008.

[5] A. Kerkhoff, "S Parameter Extraction Approach to the Reduction of Dipole Antenna Measurements," *LWA Memo Series (Memo 137)*, February 2008.

[6] N. Paravastu, "LWA Engineering Memo ANT0005 - Measurement and Simulation of 38 MHz and 74 MHz Resonant Dipoles," *LWA Engineering Memo Series (ANT0005)*, April 2008.

ANT0015: Pattern measurements from the two-element interferometer

Jake Hartman, Apr 15, 2009

Abstract. We present a comparison of the observed antenna patterns of the Burns prototype antennas with the patterns simulated using NEC. By measuring the fringe amplitudes of bright radio sources as they cross the sky, we can calculate the effective area of the antennas in the directions of the sources. From these effective area measurements, we constructed an approximate antenna pattern, defined over the entire sky. This pattern matches reasonably well with the simulations. The most notable difference is that the gain of the real antennas near the zenith and perpendicular to the direction of polarization (at all altitudes) is 0.3–0.5 dB higher than the NEC simulations for the 73.8 MHz and 80.0 MHz patterns. By comparing the ratio of fringe amplitudes of the observed sources, we were able to measure their relative flux densities. We found that the flux ratio of Cas A / Cyg A was 1.05 ± 0.03, and that the spectrum of Cas A has hardened since 1965, in agreement with other observations.

Background.

During the September 2008 trip to the LWDA site, two Burns prototype antennas were setup as an interferometer, using the LWDA backend as a correlator. The baseline of the interferometer is 390 m long, running 8° north of east. See LWA Engineering Memo STD0004 for full details.

We have taken 96 days of data with this configuration over the past four months. A single "data run" is six sidereal days long, divided evenly between the N/S and E/W polarizations and three frequency bands, centered around 62.5 MHz, 73.8 MHz, and 80.0 MHz. Each frequency band is 2.3 MHz wide.

The initial analysis of these data is described in LWA Engineering Memo STD0012. By analyzing the phases of the fringes from the four brightest radio sources (Cas A, Cyg A, Tau A, and Vir A), we fit the baseline between the antennas and the cable delays for the two polarizations. The residuals of the fringe phases relative to our best fits were typically 0.09 wavelengths, although the 80.0 MHz data was consistently somewhat noisier. Nearly all the instances in which there were significant differences between a source's expected and predicted fringe phases could be explained by the interference with the fringes from another source.

Measurement of the antenna gains from the fringe amplitudes.

Just as the phases of the fringes encode information about the baseline and cable delays of the interferometer, the fringe amplitudes can be used to measure the gain patterns of the antennas. If the direction of a source aligns with a high-gain direction of the antenna pattern, then the resulting interferometric fringes will have a relatively high amplitude. As bright radio sources traverse the sky over the course of a sidereal day, we can measure the relative gains associated with their paths to produce a rough antenna pattern, which can be compared with simulations. Of course, the paths of the brightest four radio sources does not fully cover altitude / azimuth space, but it should be sufficient to identify any large discrepancies between the simulations and physical antennas.

The measurement of the fringe amplitudes follows the same fringe-stopping procedure described in STD0012. For a small frequency band (5 LWDA channels, 97 kHz width) centered at a frequency of ν, let $V(t)$ be the complex visibility measured by the interferometer. For a baseline $\mathbf{b}$, a cable delay of Δt, and a source direction vector of $\mathbf{s}(t)$, we fringe stop $V(t)$ by subtracting out the expected phase shift introduced by the source direction:

$$V_{\mathrm{stopped}}(t) = V(t)\exp(-2\pi i \nu\, [\mathbf{s}(t) \cdot \mathbf{b} / c + \Delta t\,])\ .$$

To minimize the impact of sources interfering, we remove data for which the fringe rate of the targeted source is within 1 mHz of Cas A or Cyg A. Substantial RFI contaminates the 80.0 MHz band, so for it we also remove data when the fringe rates are within 1 mHz of zero drift. We chose altitude thresholds for each source based on their observed phase scatter near the horizon: 5° above the horizon for Cas A; 10° for Cyg A; and 20° for Tau A and Vir A.

The power received from the direction $\mathbf{s}(t)$ is proportional to the amplitude of the fringe: $P(\mathbf{s}(t)) = k_{\nu,\mathrm{pol}}\, V_{\mathrm{stopped}}(t)$, where $k_{\nu,\mathrm{pol}}$ is some constant gain factor for each frequency and polarization. These powers are averaged over 1200 s intervals to reduce noise. If the flux density of the source (integrated over the interferometer beam) is S_ν, then the effective area of the antenna in the direction of the source is $A(\mathbf{s}) = P(\mathbf{s}) / S_\nu\, \Delta\nu$.

Choosing values for S_ν is not trivial. There are limited observations at these frequencies, and previous measurements of flux density may not be directly applicable to due differences in beam size. After a good bit of discussion among the LWA team at the NRL, we decided to use the following approximate flux densities. For Cyg A, we used the flux densities given in Baars et al. (1977; A&A 61, 99). For Cas A and Tau A at 73.8 MHz, we used the flux densities derived from the VLSS images (provided by Aaron Cohen): Cas A, 17.52 kJy; and Tau A, 1.81 kJy. These VLSS flux densities are calibrated relative to Cyg A using the Baars et al. (1977) Cyg A model. The VLSS-derived flux density for Vir A was 1.41 kJy, which seemed too low based on my preliminary results. Most likely the VLSS beam, which is smaller than our interferometer's beam, resolved out some of the flux from Vir A, by far the most extended of our four sources. Instead, we used a flux density of 2.08 kJy for Vir A at 73.8 MHz, from Kassim et al. (2007; ApJS 172, 686).

Freq.	62.5	73.8	80.0
Cas A	19.75	17.52	16.53
Cyg A	18.77	17.09	16.30
Tau A	1.89	1.81	1.77
Vir A	2.40	2.08	1.94

Table 1. Flux densities (in kJy) used for our initial antenna pattern fits. Uncertainties in absolute flux density are on the order of 10%, although their relative uncertainties are considerably smaller.

To estimate the flux densities at 62.5 MHz and 80.0 MHz, we used these power law indices: −0.72 for Cas A and −0.58 for Cyg A, from the models given in Baars et al. (1977); −0.27 for Tau A, from Bietenholz et al. (1997; ApJ 490, 291); and −0.86 for Vir A. The Vir A index is also from Baars et al. (1977). Although its model only claims to be valid down to 400 MHz, the spectrum from Kühr et al. (1981; A&AS 45, 367) shows that the spectral index is approximately constant down to low frequencies.

The resulting flux densities are listed in Table 1. Uncertainties are on the order of 10% for the VLSS-derived values. However, the uncertainties are dominated by absolute flux calibration, and errors in their flux ratios should be considerably smaller. A potentially greater problem is the large beam of our interferometer, which may lead to us picking up additional flux, most notably unresolved emission from the Galactic plane. This issue is discussed in more detail at the end of this report.

Simulated antenna patterns.

We are interested in comparing the observed gain patterns with simulations. Additionally, we use the simulations to normalize our areas. Because the gains $k_{\nu,\mathrm{pol}}$ are unknown, we set these constants to minimize the difference between the observed and simulated areas. In theory, we could also normalize our observed patterns by requiring $\int A(\mathbf{s})\, d\Omega = \lambda^2$, but the observations do not have sufficient sky coverage to perform this integral over the necessary 4π sr.

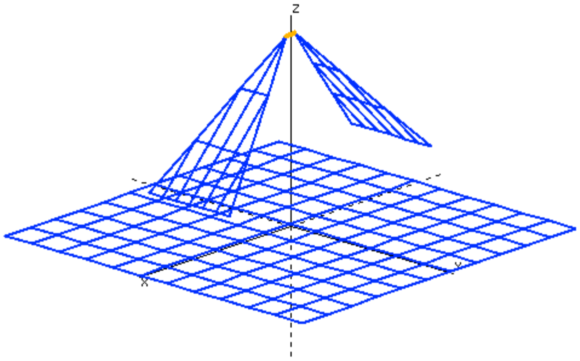

Figure 1. Structure of the simulated antenna and 3 m x 3 m ground screen.

We used the NEC model THV_SGS.NEC, created by N. Paravastu, to simulate the Burns prototype antennas over a 3 m x 3 m ground screen and realistic earth ground parameters. Figure 1 shows the conducting wires of this model. We then used NEC 4.1 to simulate the antenna pattern over a grid of 1° steps in azimuth and altitude for each of the three frequency bands.

The output of these NEC simulations gives dB gains at each of the alt/az grid positions. For a more physical measure of the pattern, we convert them to effective areas. If $U(\theta, \varphi)$ defines the gain for an azimuth of θ and an altitude of φ, then the associated area is

$$A_e(\theta, \phi) = \frac{\lambda^2}{4\pi} \cdot \frac{U(\theta, \phi)}{\langle U(\theta, \phi) \rangle}$$

for a wavelength of λ. The areas calculated using NEC are in reasonable agreement with theory for a simple half-wave dipole; see LWA memo 65 (S. Ellingson, "Use of NEC-2 to Calculate Collecting Area") for details. Our simulated antennas have maximum effective areas in the vertical direction of 10.04 m^2, 7.05 m^2, and 5.89 m^2 for 62.5 MHz, 73.8 MHz, and 80.0 MHz, respectively. For any chosen azimuth, the simulated areas monotonically decrease to zero as the altitude decreases from zenith to horizon.

Measured patterns I — Observed effective areas for individual source tracks and polarizations

The figures on the next three pages compare the initial results of our observations with the simulations. They represent 16 days of measurement for each combination of polarization and frequency.

The top plots show the simulated antenna patterns and observed relative gains over the whole sky. The contours show the simulation results, giving lines of constant effective area in steps of 1 m^2. The colored circles show the observed areas for the four sources, color coded with Cas A in red, Cyg A in green, Tau A in blue, and Vir A in purple. The area of each circle is proportional to the effective area implied by the fringe amplitudes as the sources cross the sky, rising on the left half of the graph and setting on the right. Each circle represents the average of many amplitude measurements in order to reduce scatter.

The lower plots present the same data with effective area as their Y-axes, so the simulated and observed areas can be more meaningfully compared. The black lines give the simulation results; the crosses show the observations. Area measurements with similar altitudes have been grouped and averaged, and the vertical error bars give the standard deviation within each group. There is a 1-to-1 correspondence between the crosses in the lower plots and the circles in the top plots.

The 80.0 MHz band has significantly more RFI than the other two bands, and when the fringe rates are near zero (around 30° altitude for Cas A and 20° altitude for Cyg A) the data are not usable. The RFI is worst in 80.70-80.93 MHz; within this band none of the data are usable, with noise dominating even when the fringe rate is far from zero.

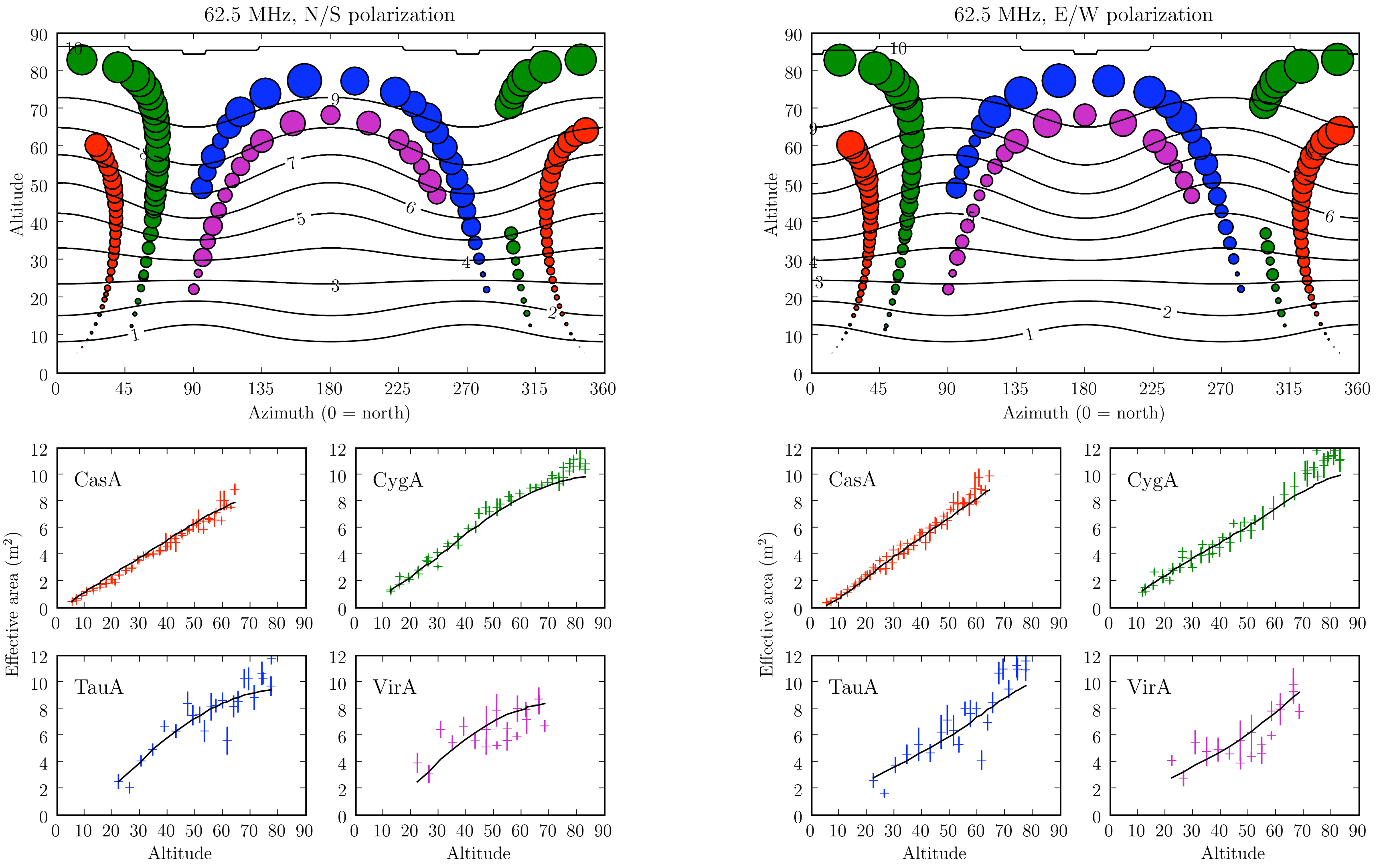

Figure 2. Observed effective areas for individual sources and polarizations at 62.5 MHz.

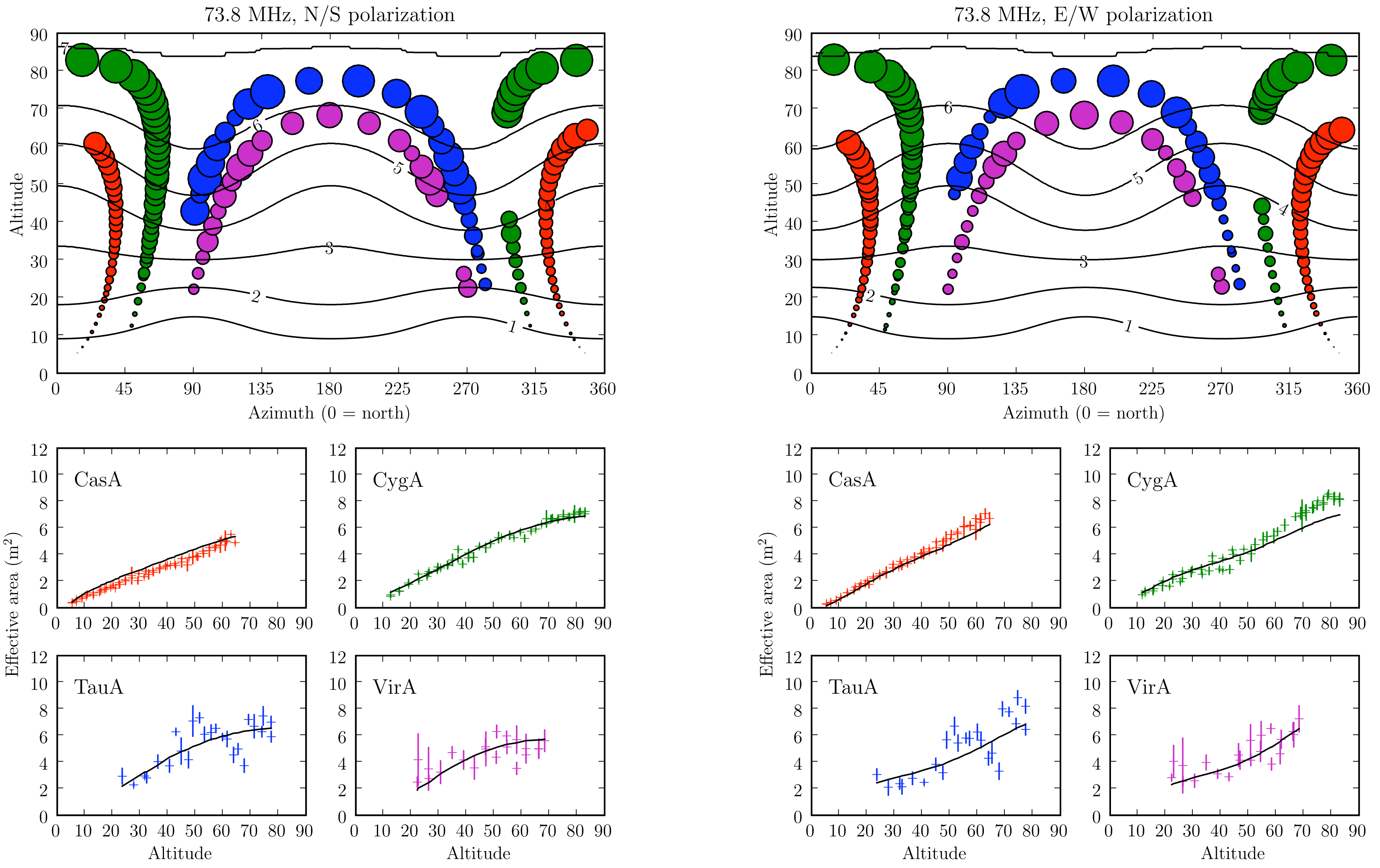

Figure 3. Observed effective areas for individual sources and polarizations at 73.8 MHz.

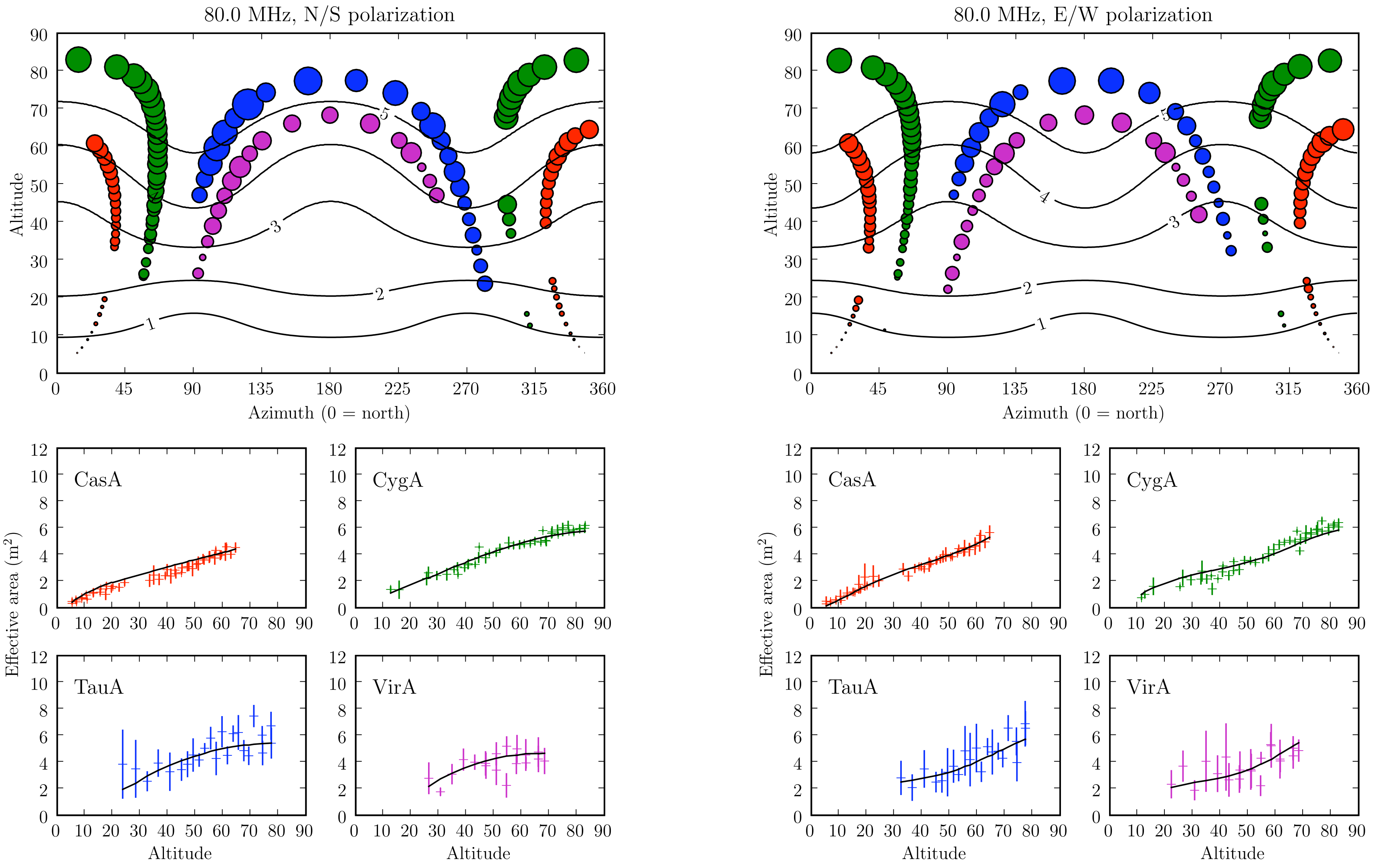

Figure 4. Observed effective areas for individual sources and polarizations at 80.0 MHz.

Generally the observed patterns are a good match to the simulations, which demonstrates that both the NEC model and the assumed source flux densities are reasonable. There are some notable differences, however. At altitudes greater than ~70°, the areas derived from the Cyg A fringes are 10–15% greater than expected in the E/W polarization, suggesting that the simulation is underestimating the gain near the zenith in the direction perpendicular to the axis of polarization. Additionally, the areas derived from the Cas A fringes in the N/S polarization are systematically low. However, it is unclear whether these discrepancies are due to unexpected features of the antenna pattern or are artifacts of a single source and polarization.

Measured patterns II — Combining the sources and polarizations to measure the overall patterns

To reconstruct a complete antenna pattern from our observations, we need to combine the fringe data from all the sources and polarizations. Since many regions of the pattern are crossed by multiple sources, this approach allows us to much better constrain systematic errors due to incorrect source fluxes or other source- or polarization-specific problems.

We divided the 90° × 90° spherical octant into tiles that are roughly 5° × 5°. Figure 5 illustrates our tiling scheme. Due to the square symmetry of the antenna, only 90° of azimuth needs to be considered. This symmetry assumption allows us to reflect all the source tracks across the direction of polarization; shift the azimuths of the source tracks for the E/W polarization data by 90° so all the data define 0° azimuth along the direction of polarization; and then fold all the resulting azimuths into the 0–90° interval. Each fringe amplitude measurement gets mapped into the tile corresponding to its source's position at the time of measurement. Clearly some tiles will remain empty, as the source trajectories don't cover the whole sky. As usual, we discard measurements that are contaminated by interference between sources or RFI.

The data support these assumptions of symmetry. Because the antennas are oriented along the cardinal directions, the rising and setting halves of the source tracks cover the same point in our folded pattern, but do so on opposite sides of the antenna. The agreement between these two sets of fringe amplitudes is generally good. If the antenna lacked reflective symmetry across the plane separating east from west, this would not be the case. Meanwhile, the combination of the two polarizations tests the 90° rotational symmetry of the antenna. The polarizations can be directly compared in tiles that contain points from both, and the resulting gains are also typically in good agreement.

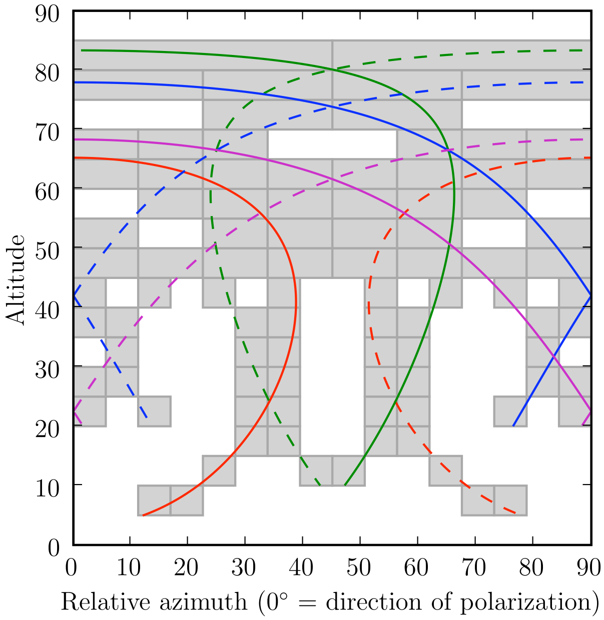

Figure 5. The tiling scheme and source tracks used in our pattern analysis. Each tile covers roughly 5° × 5° of sky, and only tiles that have significant fringe data are shown. The source tracks are colored as before: Cas A = red; Cyg A = green; Tau A = blue; Vir A = purple. Solid lines indicate data from the N/S polarization; dashed lines indicate E/W data. The tracks have been reflected across the azimuths of antenna symmetry, as described in the text. Cutoffs at low altitudes are due to the poor quality of fringe data near the horizon.

For each tile, we then averaged the difference in gain relative to the NEC simulation. (By making these gains relative to a model rather than a constant, we mostly correct for any gain gradient across a single tile.) We also took the standard deviation of these relative gains as a measurement of the uncertainty for each tile, although the distribution of gains within a tile is not at all Gaussian, so any statistics derived from these uncertainties need to be taken with a grain of salt. (Comparing the scatter within a tile against the tile-to-tile variation, these standard deviations overestimate the uncertainties; in other words, there is a lot of scatter within each tile — more so than the scatter between adjacent tiles.) Nevertheless, these uncertainties still provide useful measures of goodness when fitting models to the relative gains of the tiles.

The next step is to smooth the relative gains and interpolate them over the entire sky to produce a useful antenna pattern. We fit a limited set of spherical harmonics to the tiles' relative gains and uncertainties. We used a basis of 16 harmonics: up to the degree $n = 6$, and using only non-negative, even orders (i.e., $m = 0, 2, \dots, n$) due to the square symmetry. These harmonics do a good job of smoothing over scatter, preserving the general trends of the relative gain pattern, and not usually introducing noticeable artifacts. For the 62.5 MHz and 73.8 MHz patterns, the resulting models were well-behaved. For 80.0 MHz, the initial fit blew up to a high gain at the horizon (where there is no data to constrain it), so a boundary condition holding the horizon gains to near the NEC model was added.

Figure 6 shows the tiled gain measurements and the resulting antenna patterns.

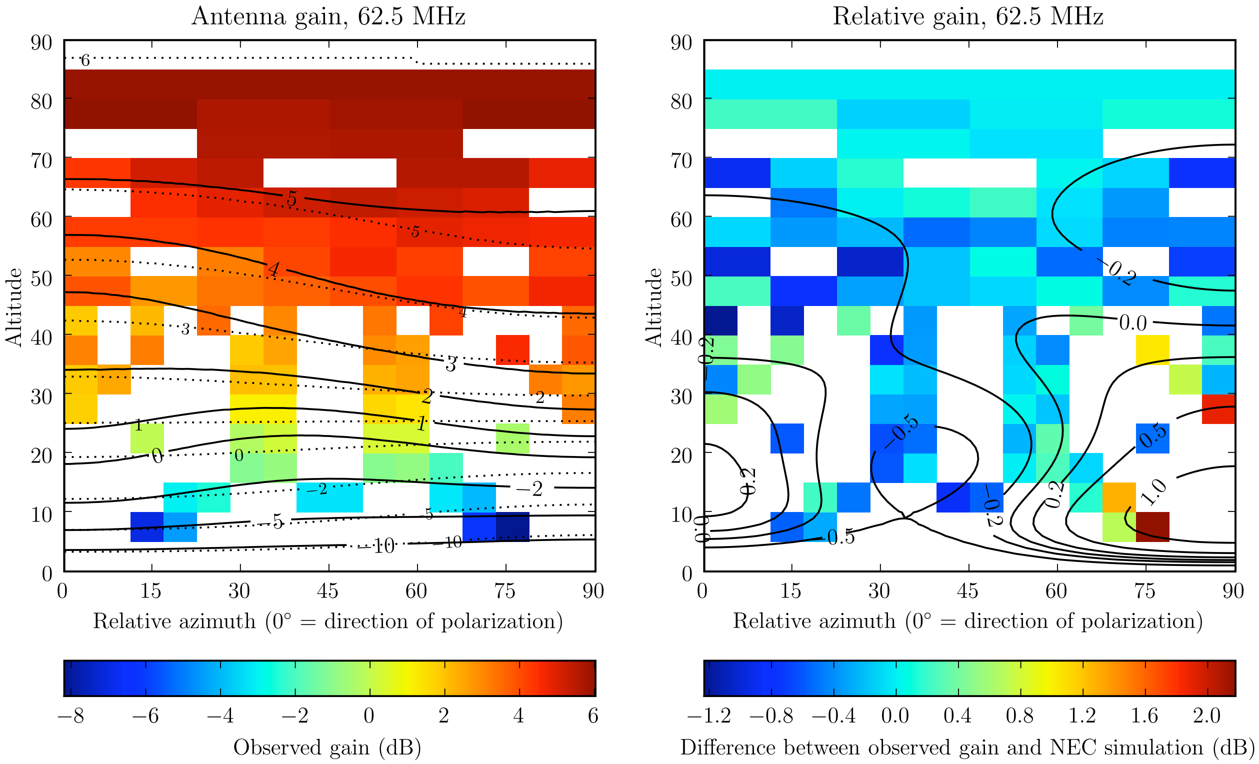

Figure 6. The antenna patterns for the Burns prototype antennas, measured at 62.5 MHz, 73.8 MHz, and 80.0 MHz. The colored tiles in the left-hand plots show the overall antenna pattern, with gains relative to the mean gain; tiles in the right-hand plot shows the gains relative to the NEC simulations. Solid contour lines show the smoothed and interpolated patterns from the best-fit spherical harmonic models. For comparison, in the overall pattern plots the NEC simulation results are shown by the dotted contours.

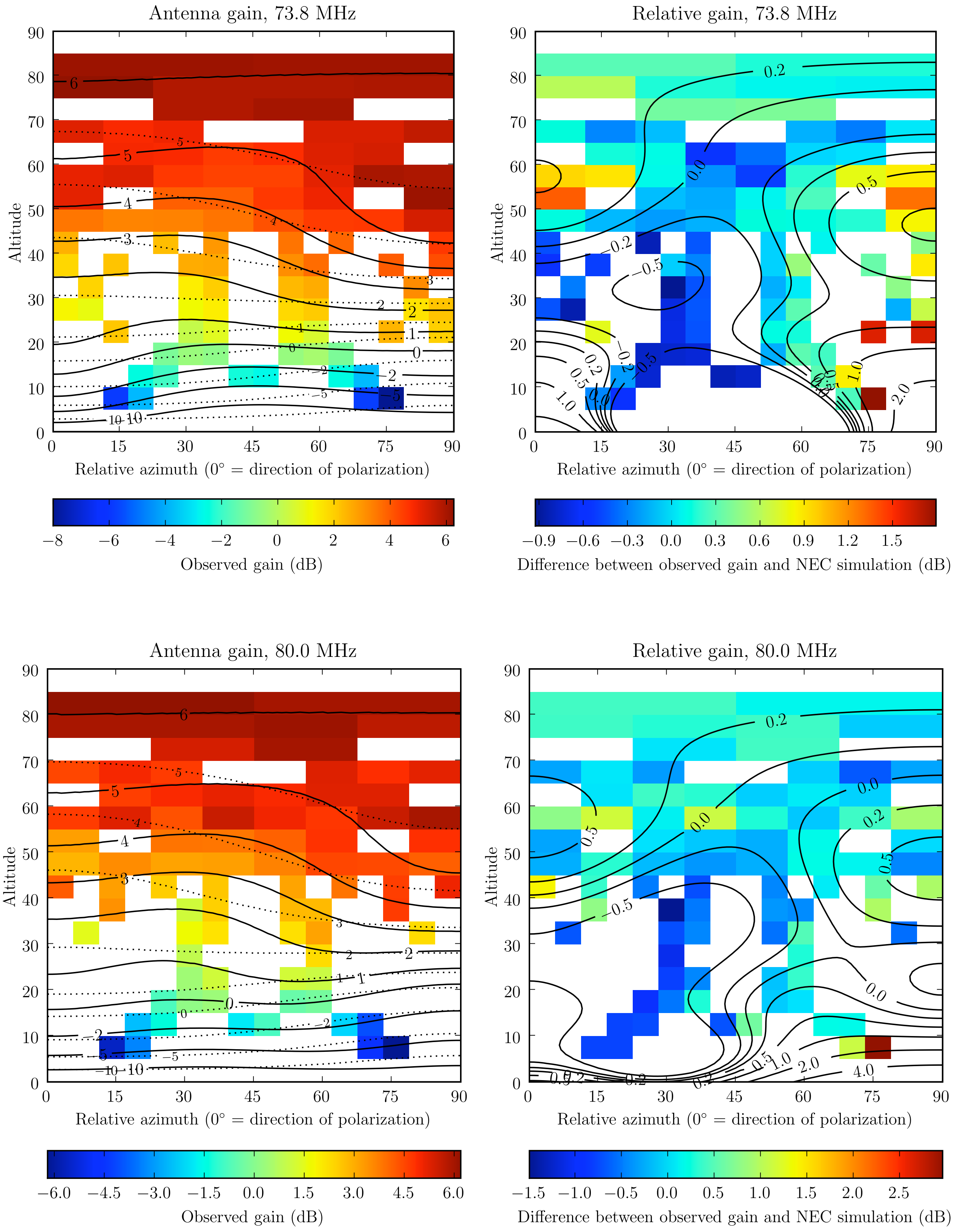

Figure 6, continued.

	Freq. (MHz)	Initial (kJy)	Measured (kJy)	Difference (σ)
Cas A	62.5	19.75	19.28 ± 0.77	−0.61
	73.8	17.52	17.70 ± 0.62	+0.29
	80.0	16.53	17.32 ± 0.80	+0.99
Cyg A	62.5	18.77	—	—
	73.8	17.09	—	—
	80.0	16.30	—	—
Tau A	62.5	1.89	2.04 ± 0.14	+1.09
	73.8	1.81	1.73 ± 0.15	−0.53
	80.0	1.77	1.96 ± 0.25	+0.76
Vir A	62.5	2.40	2.29 ± 0.39	−0.27
	73.8	2.08	2.16 ± 0.17	+0.46
	80.0	1.94	2.00 ± 0.15	+0.38

Table 2. Measured flux densities of Cas A, Tau A, and Vir A, compared with their initial values. All flux densities are relative to Cyg A.

Measurement of the flux density of Cas A.

The flux densities used during the fitting of the antenna pattern came from various sources (see Table 1 and the associated text), which in general do not have the same beam pattern as our interferometer. Although we do not expect the interferometer to resolve these sources, it is still worth measuring the observed flux densities to ensure that they agree with our assumptions. Additionally, the brightness of Cas A at low frequencies is somewhat uncertain, as it has been changing (generally but not necessarily monotonically decreasing) over time as the supernova remnant expands (Helmboldt & Kassim 2009; arXiv: 0903.5010, submitted to AJ). Our data provide a new measurement of this source.

All flux densities are calibrated relative to Cyg A. To minimize uncertainties due to the antenna pattern, we only used tiles which the other sources shared with Cyg A. This allows us to directly calculate the ratio of the sources' flux densities from the ratio of their fringe amplitudes. For each source there are 4–6 tiles shared with Cyg A, so we can estimate the uncertainty in a source's flux ratio from the scatter among these tiles. This method yields the results shown in Table 2. The agreement between the initial and observed flux densities is generally good. Arguably, the agreement is too good: the hypothesis that the observed values are equal to the initial values has a reduced χ^2 statistic of 0.45, lower than expected. Most likely this measure of the tile-to-tile scatter includes substantial systematic noise, which increases the uncertainty estimates.

The Cas A / Cyg A ratio is of astrophysical interest, as this source is changing over time. Because the flux densities of the other sources agreed with their initial values, we held them fixed at their initial values and only fit Cas A. This provided somewhat higher accuracy, since we could compare the fringe amplitudes of Cas A with Tau A and Vir A as well as Cyg A to provide more measurements. (Although the flux ratios with these dimmer two sources were generally not as accurate.)

The resulting Cas A flux density measurements are 19.61 ± 0.54 kJy at 62.5 MHz; 17.86 ± 0.55 kJy at 72.5 MHz; and 17.41 ± 0.84 kJy at 80.0 MHz. At 73.8 MHz, the Cas A / Cyg A ratio is 1.05 ± 0.03, measured during 2008/09/07 – 2009/02/05. This figure is slightly higher than the last 73.8 MHz VLA observation, taken on 2006/10/27, of 0.99 ± 0.01 (Helmboldt & Kassim 2009). Cas A also appears to be hardening. The 62.5 MHz flux is substantially lower than expected, and calculating a spectral index from these three frequency measurements gives –0.52 ± 0.19. Once again, this uncertainty estimate is most likely high, as the linear fit from which it derives has a χ^2 statistic of 0.09 for 1 degree of freedom; a less conservative estimate of –0.5 ± 0.1 is reasonable. For comparison, Baars et al. (1977) reports an index based on 1965 data of –0.72 at 74 MHz.

Improvements for future pattern measurement strategies.

As mentioned earlier, the orientation of the antennas along the cardinal directions results in the rising and setting trajectories of the sources covering the same part of the pattern due to the symmetry of the antennas. For initial measurements, this orientation provided the advantage of testing assumptions of antenna symmetry. However, once this symmetry is confirmed, it is advantageous to rotate the antennas relative to the cardinal directions, thereby separating the rising and setting trajectories and providing better coverage of the sky. Figure 7 shows the improvement in coverage. An angle of 22.5° provides the highest coverage, increasing it from 47% to 64% for these four sources when observing from New Mexico latitudes. (These numbers depend somewhat on the tiling scheme, but not strongly.)

Future ability to measure the antenna patterns depends entirely on the presence of the LWDA backend at the site. We feel that the results discussed in this memo provide a strong argument for not removing it. The Burns prototype antennas that we have measured will be replaced with revised antennas during the upcoming April 21–24 trip to the site, and we plan to take pattern measurements of those antennas as well. Additionally, our configuration is currently the only instrument capable of monitoring the flux density of Cas A. Frequent monitoring of this source is critical for understanding the unusual patterns of brightness variation reported in Helmboldt et al. (2009).

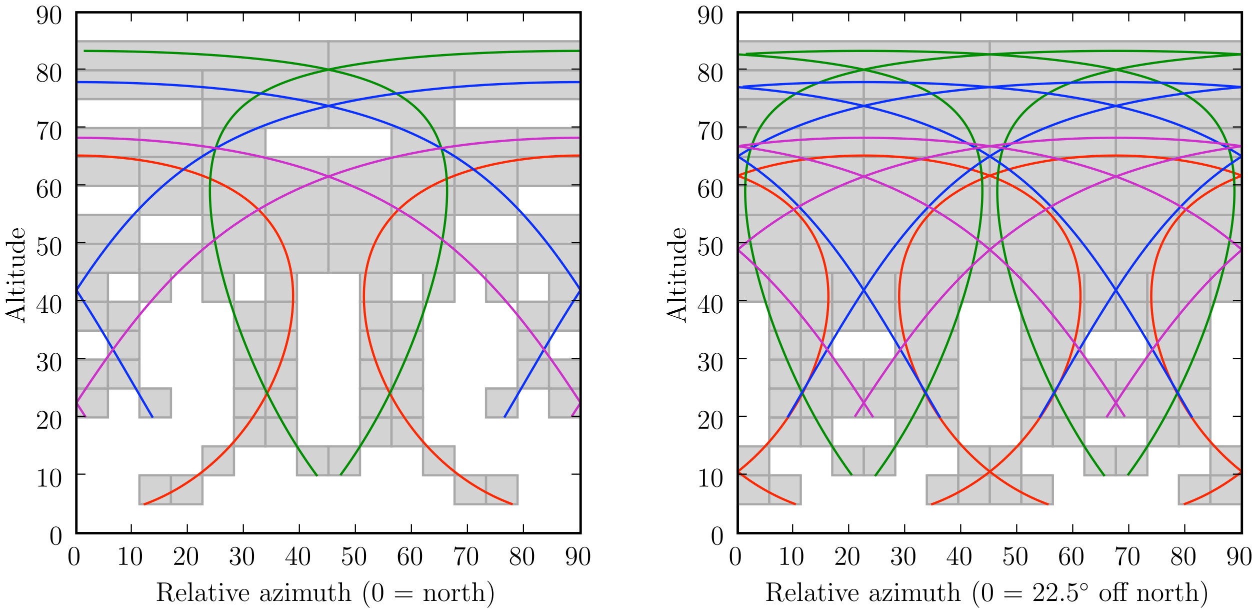

Figure 7. Difference in pattern coverage for antennas aligned with the cardinal directions (left) vs. antennas offset from the cardinal directions by 22.5°. The lines indicate the sky trajectories of the four brightest sources (using the same coloration as before) wrapped onto the 90°-wide antenna pattern. Rotating the antenna increases the maximum possible sky coverage from 47% to 64%.

LWA Antenna Feedpoint Separation

Ken Stewart, Brian Hicks

4 February 2009

Earlier antenna simulations assumed a feedpoint separation i.e., the distance between the dipole arms, of 9.5 cm with an arm length of 1.5 m. The current antenna design requires a separation of 17.4 cm to accommodate the larger dielectric hub on which the arms are mounted. The figures below show calculations for three different cases: 1) the original model, 2) increased feedpoint separation with dipole arms of the same length, and 3) increased feedpoint separation with the dipole arms shortened to keep the overall length of the antenna the same as in the original model.

Fig. 1 shows the impedance mismatch efficiency, or the fraction of power transferred from the antenna into the front end electronics, for these three cases. Case 2 is slightly worse than the original design between 33 and 77 MHz, but better elsewhere. Case 3 improves the impedance match slightly between 30 and 35 MHz, but makes it worse at frequencies > 45 MHz.

The effect of these design changes on the calculated sky noise dominance is shown in Fig. 2. Increasing the feedpoint distance without changing the arm length (case 2) decreases the sky noise dominance slightly between 40 and 75 MHz compared to the original design, but improves it below 30 MHz. Shortening the arms (case 3) decreases the sky noise dominance for all frequencies > 45 MHz and remains approximately the same below 25 MHz. Compared with the original model, case 2 is ~ 0.8 dB lower above 40 MHz and ~ 2 dB better below 30 MHz.

Because the larger feedpoint separation improves the antenna performance at low frequencies with only a small decrease at high frequencies, we recommend that the length of the dipole arms remain at the original design length of 1.5 m.

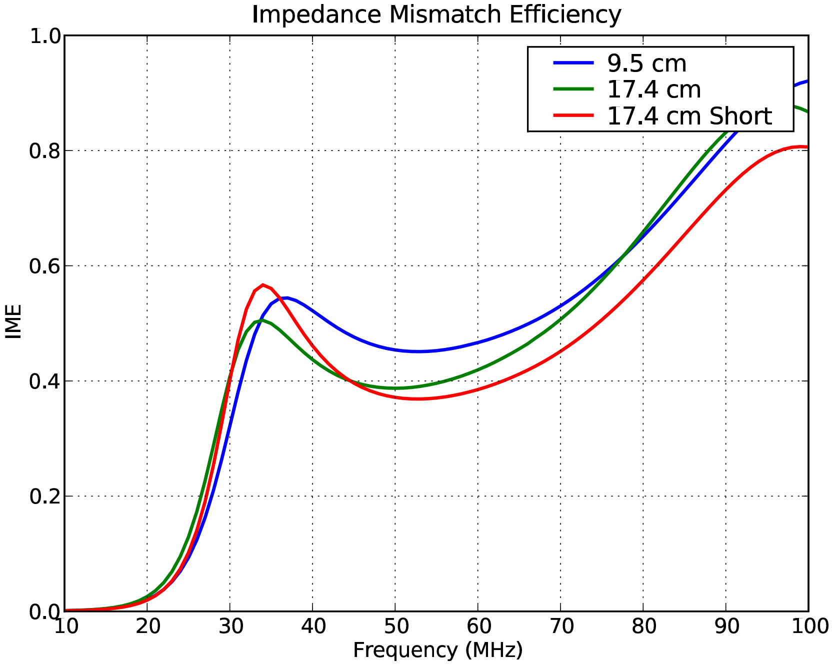

Figure 1: Impedance mismatch efficiency for antenna + ground screen model

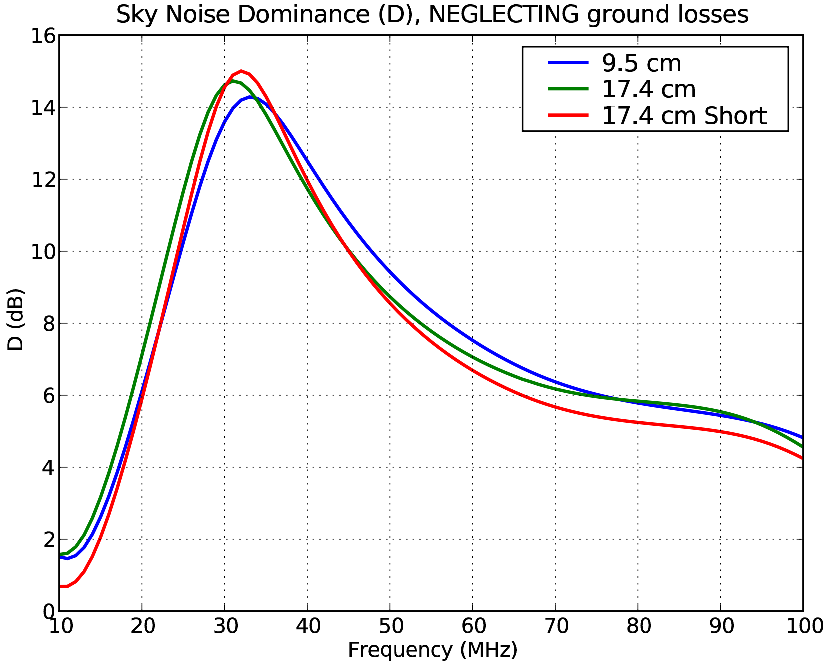

Figure 2: Sky noise dominance for antenna + ground screen model

LWA-1 ANTENNA DIMENSIONS

2009 September 11

Paul Ray, Steve Burns, Art Haines, Brian Hicks

This report contains final dimensioned drawings of the antennas as built for LWA-1.

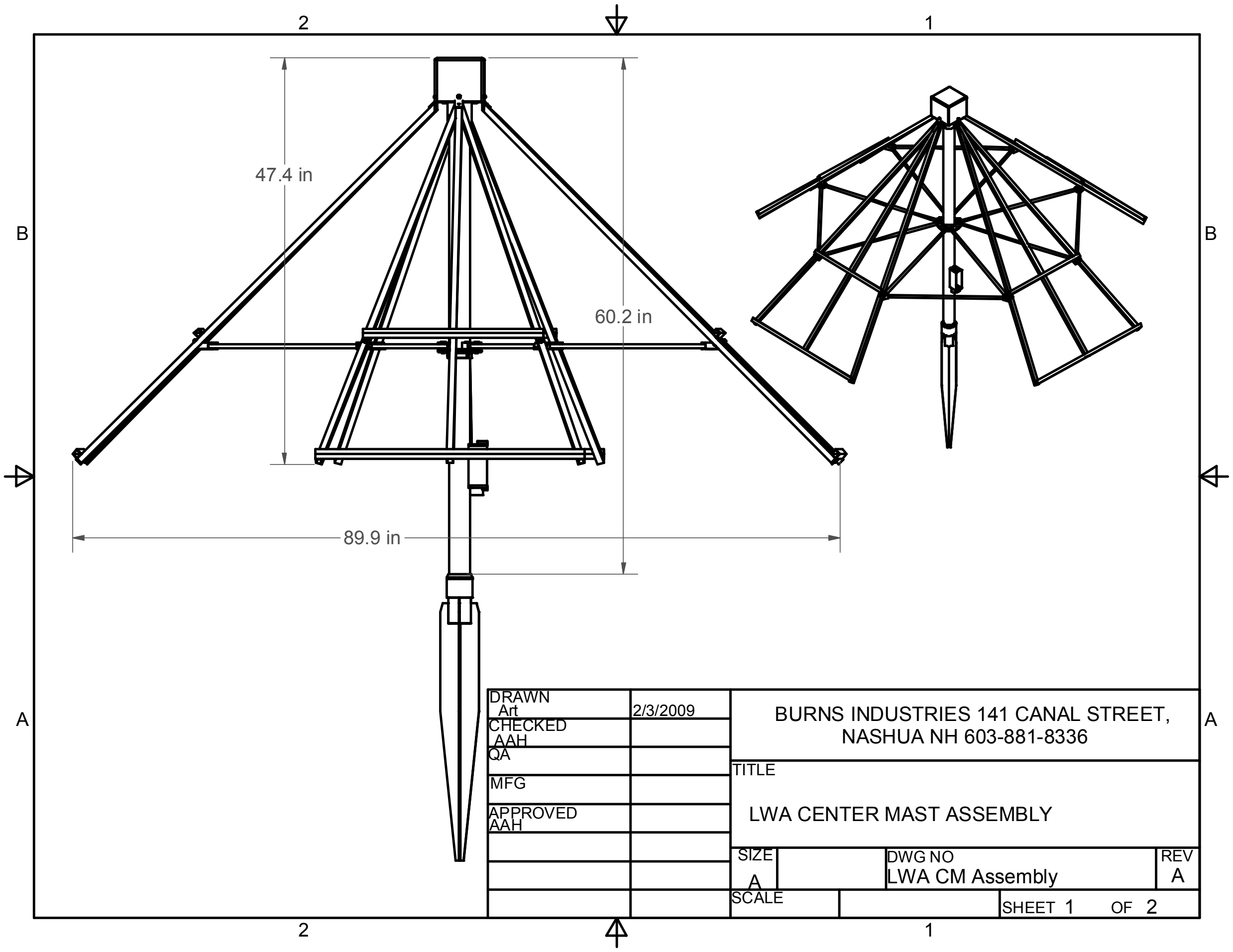

2 1

B

Parts List

IT	Q	PART NUMBE	DESCRIPTION
1	1	LWA10-114	EXTRUSION 1
2	1	LWA10-115	EXTRUSION 1 LEFT
3	1	LWA10-116	EXTRUSION 2
4	1	LWA10-117	EXTRUSION 3
5	1	LWA10-118	EXTRUSION 7
6	1	LWA10-119	TAB

REVISION HISTORY

ZONE	REV	DESCRIPTION	DATE	APPROVED
1	1	Released for production	3/12/2009	Art

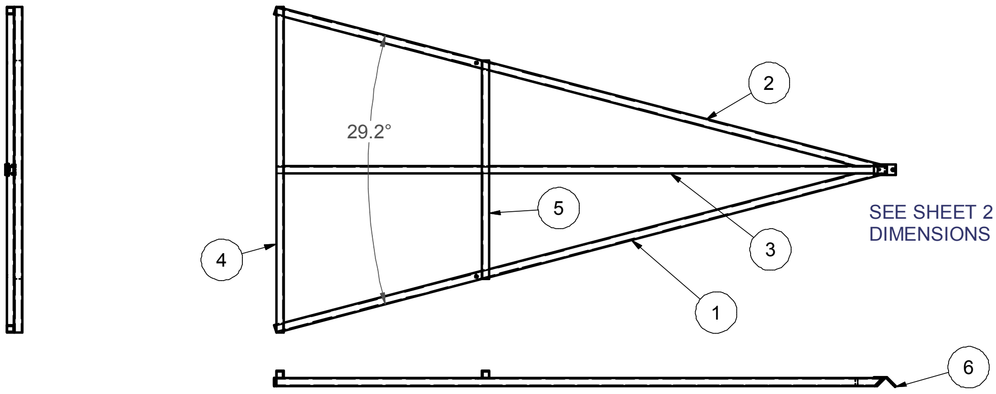

SEE SHEET 2 FOR DIMENSIONS

A

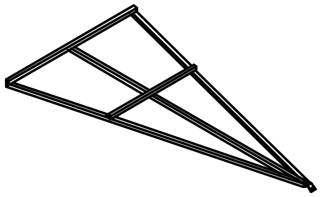

DIMENSIONS IN cm/inches

DRAWN Art	7/15/2008
CHECKED AAH	
QA	
MFG	
APPROVED AAH	

BURNS INDUSTRIES 141 CANAL STREET,
NASHUA NH 603-881-8336

TITLE

LWA ELEMENT

SIZE	DWG NO	REV
A	element A	B

SCALE

SHEET 1 OF 2

2 1

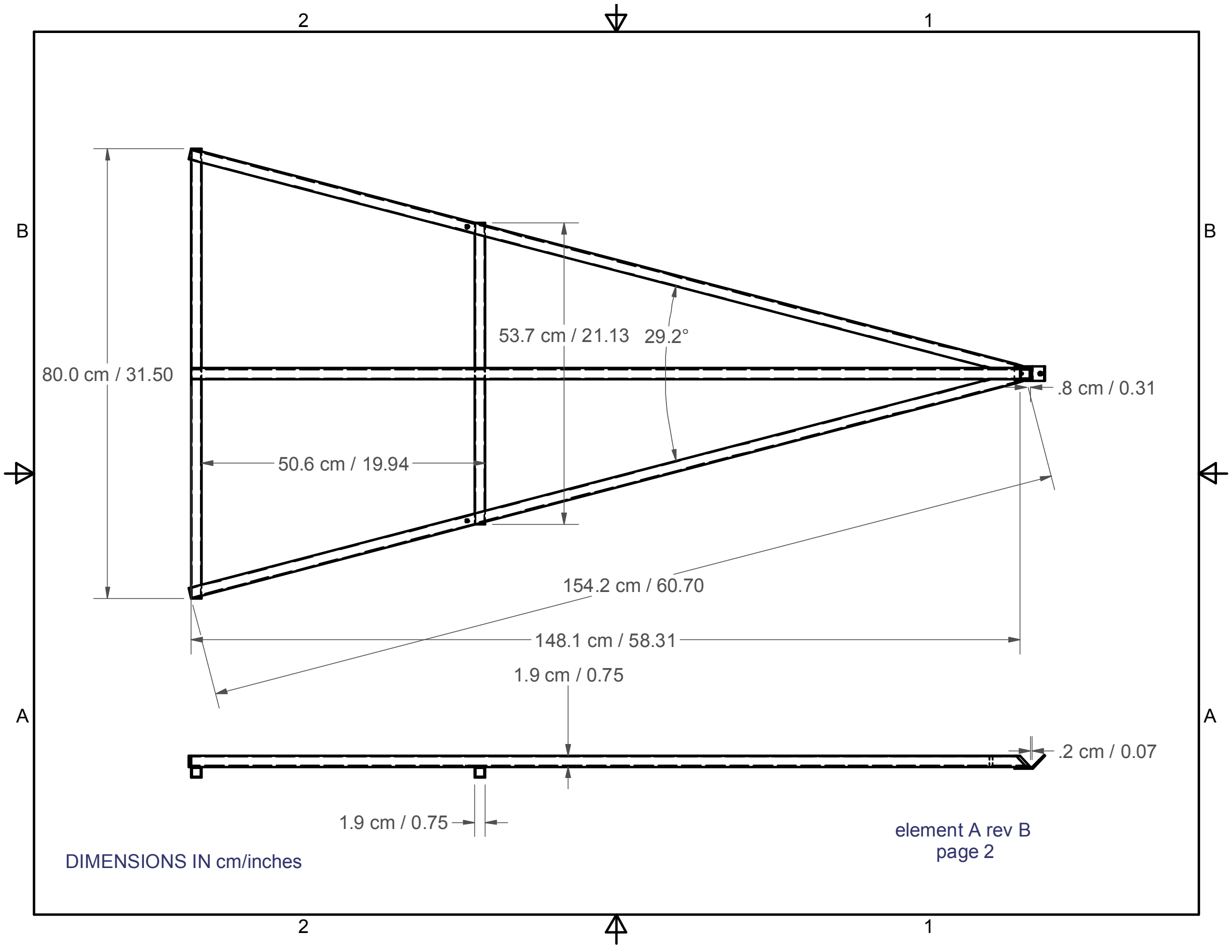
2
1
B
B
80.0 cm / 31.50
53.7 cm / 21.13
29.2°
.8 cm / 0.31
50.6 cm / 19.94
154.2 cm / 60.70
148.1 cm / 58.31
1.9 cm / 0.75
A
A
.2 cm / 0.07
1.9 cm / 0.75
element A rev B
page 2
DIMENSIONS IN cm/inches
2
1